ABSTRACT

Title of Document: MODELING OF GAS TURBINE - SOLID OXIDE FUEL CELL SYSTEMS FOR COMBINED PROPULSION AND POWER ON AIRCRAFT.

Daniel Francis Waters,
Doctor of Philosophy, 2015

Directed By: Associate Professor, Christopher P. Cadou,
Department of Aerospace Engineering

This dissertation investigates the use of gas turbine (GT) engine integrated solid oxide fuel cells (SOFCs) to reduce fuel burn in aircraft with large electrical loads like sensor-laden unmanned air vehicles (UAVs). The concept offers a number of advantages: the GT absorbs many SOFC balance of plant functions (supplying fuel, air, and heat to the fuel cell) thereby reducing the number of components in the system; the GT supplies fuel and pressurized air that significantly increases SOFC performance; heat and unreacted fuel from the SOFC are recaptured by the GT cycle offsetting system-level losses; good transient response of the GT cycle compensates for poor transient response of the SOFC. The net result is a system that can supply more electrical power more efficiently than comparable engine-generator systems with only modest (<10%) decrease in power density. Thermodynamic models of SOFCs, catalytic partial oxidation (CPOx) reactors, and three GT engine types (turbojet, combined exhaust turbofan, separate exhaust turbofan) are developed that account for equilibrium gas phase and electrochemical reaction, pressure losses, and heat losses in ways that capture 'down-the-channel' effects (a level of fidelity necessary for making meaningful performance, mass, and volume estimates). Models are created in a NASA-developed environment called Numerical Propulsion System Simulation (NPSS). A sensitivity analysis identifies important design parameters and translates uncertainties in model parameters into uncertainties in overall performance. GT-SOFC integrations reduce fuel burn 3-4% in 50 kW systems on 35 kN rated engines (all types) with overall uncertainty <1%. Reductions of 15-20% are possible at the 200 kW power level. GT-SOFCs are also able to provide more electric power (factors ≥3 in some cases) than generator-based systems before encountering turbine inlet temperature limits. Aerodynamic drag effects of engine-airframe integration are

by far the most important limiter of the combined propulsion/electrical generation concept. However, up to 100-200 kW can be produced in a bypass ratio = 8, overall pressure ratio = 40 turbofan with little or no drag penalty. This study shows that it is possible to create cooperatively integrated GT-SOFC systems for combined propulsion and power with better overall performance than stand-alone components.

MODELING OF GAS TURBINE - SOLID OXIDE FUEL CELL SYSTEMS FOR COMBINED PROPULSION AND POWER ON AIRCRAFT.

By

Daniel Francis Waters

Dissertation submitted to the Faculty of the Graduate School of the
University of Maryland, College Park, in partial fulfillment
of the requirements for the degree of
Doctor of Philosophy
2015

Advisory Committee:
Associate Professor Christopher P. Cadou, Chair
Associate Professor David Akin
Associate Professor James Baeder
Associate Professor Kenneth Yu
Professor Michael Zachariah, Dean's Representative
Professor Gregory Jackson, Graduate Faculty Special Member

Dedication

To my family for giving me the drive, opportunity,

support, and confidence to achieve great things.

Acknowledgements

I would first and foremost like to thank Annie for being there every day to keep my eye on the prize and to provide the unflagging love and support needed in this long but rewarding process.

Thank you to the United States Navy and specifically the Naval Air Warfare Center Aircraft Division for financially supporting parts of this work under Master contract N0042198H1116.

Thank you to the SMART Scholarship for Service Program and the Naval Air Warfare Center Aircraft Division – Patuxent River for financially supporting the completion of my studies.

Thank you to my advisor, Dr. Chris Cadou, for providing me with the perfect balance of freedom to follow my instincts and guidance to keep me on the rails.

Thank you to Dr. Jackson for being an invaluable resource for me through your guidance and insight into the world of fuel cells.

Last but not least, I would like to thank my friends and colleagues at the university. Thank you to Andrew, Camilo, Fernando, and John for being a midday outlet to clear my head. Thank you to Daanish for co-ruling the lab with me these past four years, and thank you to Shyam, Anand, and Kiran for helping me learn the ropes in the beginning.

Table of Contents

List of Tables

List of Figures

Nomenclature

Abbreviations:

AFC	…….....	alkaline fuel cell
APU	…….....	auxiliary power units
CEA	…….....	Chemical Equilibrium with Applications
CFD	…….....	computational fluid dynamics
CPOx	…….....	catalytic partial oxidation
DGM	…….....	Dusty Gas Model
GDC	…….....	gadolinium doped ceria
GT	…….....	gas turbine
GT-SOFC	…….....	gas turbine / solid oxide fuel cell
HALE	…….....	high altitude, long endurance
HP	…….....	high pressure
HPC	…….....	high pressure compressor
HPT	…….....	high pressure turbine
IR	…….....	internal reforming
JP-5	…….....	jet propellant – 5, naval jet fuel variant
LSM	…….....	lanthanum strontium manganite
LP	…….....	low pressure
LPC	…….....	low pressure compressor
LPT	…….....	low pressure turbine
MEA	…….....	membrane electrode assembly
NASA	…….....	National Aeronautics and Space Administration
NPSS	…….....	Numerical Propulsion System Simulation
PEMFC	…….....	proton exchange membrane fuel cell
SL	…….....	sea level conditions
SLS	…….....	sea level static
SOFC	…….....	solid oxide fuel cell
TIT	…….....	turbine inlet temperature
UAV	…….....	unmanned air vehicles
YSZ	…….....	yttria stabilized zirconia

Symbols:

A	…….....	area; empirical pre-exponential factor
A^*	…….....	choked flow area
A_{ref}	…….....	combustor reference flow area
AFR	…….....	air-to-fuel ratio
AR	…….....	wing aspect ratio
b	…….....	wing span
BPR	…….....	bypass ratio
C_B	…….....	blade chord
C_D	…….....	drag coefficient
C_{Dmin}	…….....	drag coefficient at minimum lift
C_L	…….....	lift coefficient

C_{Lmin} ..... minimum lift coefficient
C/S ..... turbomachinery blade solidity
C_f ..... skin friction coefficient
C_{max} ..... higher heat capacity of the hot and cold streams
C_{min} ..... lower heat capacity of the hot and cold streams
C_{noz} ..... nozzle coefficient
C_p ..... specific heat capacity at constant pressure
C_x ..... constant value
d , D ..... diameter
D_h ..... hydraulic diameter
D_{kl}^e , $D_{k,Kn}^e$ ..... effective binary and Knudsen diffusion coefficients
E ..... endurance; activation energy
f ..... fineness
F ..... Faraday constant; force, thrust
FC ..... fuel cell
FF ..... pressure drag form factor
g ..... molar specific Gibbs energy; acceleration due to gravity
G ..... Gibbs free energy
h ..... specific enthalpy; height
HTR ..... turbomachinery hub-to-tip ratio
i , i_0 ..... current density, exchange current density
k ..... thermal conductivity
K ..... lift induced drag factor; rotor/stator blade volume factor
L ..... length
L^+ ..... non-dimensional duct length
m ..... mass
$\dot{m}$ ..... mass flow rate
M ..... Mach number
n_e ..... number of electrons transferred in reaction
$n_{O,k}$ ..... number of oxygen atoms present in species *k*
$n_{O,k}^*$ ..... number of oxygen atoms to fully oxidize species *k*
N ..... number/quantity; shaft speed
N_k ..... molar flux of species *k*
NTU ..... dimensionless parameter number of transfer units
Nu ..... Nusselt number
OPR ..... overall pressure ratio
$\%Ox$ ..... percent fuel oxidation
P , p ..... pressure or partial pressure
Pr ..... Prandtl number
q' ..... heat transfer per unit length
Q_f ..... fuel heating value
Q , $\dot{Q}$ ..... heat transfer, heat transfer rate
r ..... radius
R ..... gas constant; resistance; range
Re ..... Reynolds number

s ……..... specific entropy
S ……..... area, wing area
SF ……..... safety factor
S_v ……..... external surface area per unit volume of solid
S_{wet} ……..... wetted area
t ……..... thickness
t_{res} ……..... flow residence time
T ……..... temperature; torque
$TSFC$ ……..... thrust specific fuel consumption
U ……..... overall heat transfer coefficient
U_T ……..... rotor tip speed
v ……..... specific volume; flow or vehicle velocity
V ……..... volume; voltage / electric potential
w ……..... width
w_{act} ……..... active/channel width
W ……..... weight; molecular weight
$\dot{W}$ ……..... work rate, power
$[X_k]$ ……..... molar concentration of species *k*
Y^*_{max} ……..... turbine loading parameter
z^* ……..... non-dimensional length parameter
α ……..... turbomachinery blade aspect ratio; catalyst parameter
α_f , α_r ……..... forward/anodic and reverse/cathodic asymmetric factors
β ……..... geometry dependent catalyst parameter
γ ……..... ratio of specific heats
γ_0 ……..... sticking probability
Γ ……..... surface site density
δ ……..... thickness, clearance, incremental distance
δx ……..... incremental length along x-axis
δy ……..... incremental length along y-axis
Δ ……..... change or difference in/between property values
ε ……..... heat exchanger effectiveness
ϵ ……..... duct aspect ratio
ζ ……..... electric power fraction
η ……..... efficiency
η_{act} ……..... activation overpotential
η_{ohm} ……..... ohmic overpotential
μ ……..... flow viscosity
μ^0 ……..... standard state chemical potential
ν ……..... stoichiometric coefficient
π ……..... pressure ratio
π_{max} ……..... maximum stage pressure ratio
ρ ……..... density
σ ……..... stress, material strength
τ ……..... tortuosity; turbomachinery blade taper ratio
τ_{max} ……..... allowable stress limit of shaft

ϕ ……..... porosity
ω ……..... angular velocity of the shaft

Subscripts:

– ……..... property moving in the backward direction
+ ……..... property moving in the forward direction
0 ……..... initial value; baseline; stagnation property
$\sqrt{A}$ ……..... reference length scale is square root of flow area
a ……..... anode property/ value
AB ……..... afterburner
actual ……..... real value (relative to theoretical)
air ……..... air property
amb ……..... ambient property
B ……..... turbomachinery blade
bolt ……..... hardware, mounting bolt property
bp ……..... bypass
BP ……..... blade pull
c ……..... corrected property; cathode property; cold side property
c, comp ……..... compressor
C, case ……..... case, casing property
cell ……..... cell or fuel cell property
ch ……..... channel
choked ……..... choked flow property
comb ……..... combustor, combustion zone
core ……..... engine core
cross ……..... cross sectional
cruise ……..... cruise conditions
D ……..... turbomachinery disc
diff ……..... diffuser
div ……..... fuel cell interconnect divider
dome ……..... burner dome, fuel manifold, fuel nozzles, etc.
e.gen. ……..... electrical generation
el ……..... electrolyte property
elec ……..... electric, electrical
entry ……..... entry value
exh ……..... exhaust property
exit ……..... exit value
ext ……..... fuel cell interconnect exterior wall
f, fuel ……..... fuel property
fin ……..... final values
free ……..... free stream property
ft ……..... flame tube
gen ……..... generator
gross ……..... gross value
h ……..... hot, hot side property
H ……..... hub property

HW	.....	hardware
in, inlet	.....	inlet, inflow property; inlet element
ini	.....	initial values
ins	.....	insulation
k	.....	property of species k
M	.....	median property
Map	.....	property from performance map
mech	.....	mechanical property
mixer	.....	engine flow mixer
net	.....	net value
nozzle	.....	nozzle
oper	.....	operating value
out, outlet	.....	outlet, outflow property
p, pore	.....	porous material or foam pore property
pass	.....	passage, bypass
prop	.....	propulsion, propulsive
r	.....	turbomachinery rotor
ram	.....	ram air, ram compression
reac	.....	reaction
ref	.....	reference value
rep	.....	repeat, property of repeating channel
rev	.....	reversible
s	.....	isentropic value; spacer property; turbomachinery stator
S	.....	reference length scale of S_V^{-1}
seg	.....	segment, segment property
shaft	.....	engine shaft
stage	.....	turbomachinery stage property
stoich	.....	stoichiometric value
surf	.....	surface property, to/from surface
t, turb	.....	turbine
T	.....	total property; tip property
target	.....	target/design value
th	.....	thrust
throat	.....	nozzle throat property
unit	.....	single unit property
w, wall	.....	wall, wall property
zones	.....	combustion zones

Superscripts:

BV	.....	Butler-Volmer equation
e	.....	electrical
i	.....	ionic
0	.....	standard state value

Chapter 1: Introduction

1.1 Motivation

1.1.1 High Electric Demand Air Vehicles

The electrical demands on air vehicles' power and energy systems are substantially increasing due to recent trends such as the replacement of hydraulic actuators and controls with electrical ones, growing sensor and telemetry payloads, and the introduction of new devices like in-flight entertainment systems (or even directed energy weapons).

A survey of air vehicles' electric power demands is illustrated in Figure 1 which compares estimates of electric power fraction (ζ) in various aircraft for which information is available [1].

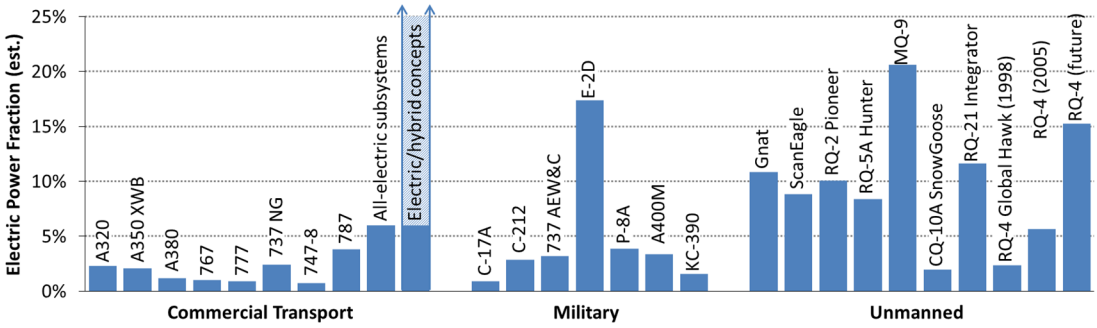

Figure 1. Estimated electric power fraction in various commercial, military, unmanned aircraft.

The electric power fraction is defined as the ratio of electrical power demand to total power demand (propulsive and electrical) on the vehicle at cruise:

$$\zeta = \frac{\dot{W}_{elec}}{\dot{W}_{elec} + \dot{W}_{prop}} \tag{1}$$

where $\dot{W}_{elec}$ is the electric power and $\dot{W}_{prop}$ is the propulsive power. Cruise propulsive power (the product of thrust and cruise velocity) is estimated by reducing the sea level rated engine power (or thrust) by the cruise altitude density ratio (ρ_{cruise}/ρ_{SL}) and assuming reduced throttle to 60% of available power/thrust.

Figure 2. Clockwise from top left: E-2 Hawkeye, RQ-4 Global Hawk, MQ-9 Reaper, Boeing 787[1].

While electric power fractions are relatively small ($1\% < \zeta < 2.5\%$) in today's commercial airliners, the Boeing 787 (a 'more electric aircraft') has a larger electric power fraction (approximately 4%) that may be indicative of future trends. In the 787, electrically-powered cabin pressurization systems, pumps, and anti-icing systems [2] replace engine-driven ones. Future aircraft could have even higher electric power fractions ranging from $\zeta \approx 6\%$ for aircraft with all-electric subsystems [3] up to

[1] Image sources, all accessed 3/16/2015:
E_2 Hawkeye (http://www.navy.mil/view_image.asp?id=44686)
RQ-4 Global Hawk (http://www.af.mil/News/Photos.aspx?igphoto=2000581685)
MQ-9 Reaper (http://www.af.mil/News/Photos.aspx?igphoto=2000649518)
Boeing 787 (http://boeing.mediaroom.com/index.php?s=20291&item=982)

$\zeta = 100\%$ for the large all-electric transport aircraft concepts envisioned by NASA [4]. Electric power fractions in existing manned military aircraft are comparable to those in commercial transport aircraft with the exception of the E-2D airborne early warning aircraft ($\zeta \approx 17\%$), notable for its large circular radar dome. Electric power fractions in unmanned air vehicles (UAVs) are substantially higher than in commercial aircraft, presumably because of large sensor and communications payloads. Electric loads will likely continue to increase as UAV technology matures: at its introduction in 1988, the RQ-4 Global Hawk was equipped with a 10 kW generator which was upgraded to 25 kW in 2005 [5]. Another upgrade to 75 kW is anticipated in the future [6]. Overall, the data indicate an upward trend in electrical power demand on aircraft. As this demand grows relative to propulsion, the efficiency of the electrical power generation process has an increasingly important influence on vehicle range, endurance, and operational capability.

The standard methods for providing electrical power on turbine-powered aircraft are either mechanical generators driven by the high pressure shaft or smaller stand-alone turbine-based auxiliary power units (APUs) [1,5]. However, both are relatively inefficient because fuel passes through the Brayton cycle to produce mechanical power as an intermediate step before conversion to electrical power. Fuel cells offer a direct and more efficient means of converting fuel to electrical power: up to 50-60% in systems without heat recovery cycles [7] vs. 20-40% for a typical gas turbine (GT) [8,9].

1.1.2 Range and Endurance

To illustrate the impact of improving electrical generation efficiency, consider Eq. (2) which presents the general form of endurance (E) and range (R) equations for a fuel burning vehicle:

$$E = \int_{m_{fin}}^{m_{ini}} \frac{dm}{\dot{m}_f} \; ; \quad R = \int_{m_{fin}}^{m_{ini}} v \frac{dm}{\dot{m}_f} \tag{2}$$

In these expressions, $\dot{m}_f$ is the mass flow rate of fuel, v is vehicle velocity, m_{ini} is the initial vehicle mass, and m_{fin} is the final vehicle mass. The dependence on $\dot{m}_f$ is clear in these equations. Now, consider the mass flow rate of fuel for a combined propulsive/electrical system:

$$\dot{m}_f = (TSFC)F_{th} + \frac{\dot{W}_{elec}}{Q_f \eta_{elec}} \tag{3}$$

where $TSFC$ is thrust specific fuel consumption of the propulsion cycle, F_{th} is the thrust force, Q_f is the fuel heating value, $\dot{W}_{elec}$ is the electric power, and η_{elec} is the electrical generation efficiency.

A modified form of the Breguet range equation [10] can be derived which incorporates the fuel used for electric power generation. The traditional assumptions for the Breguet equation (level flight, constant velocity, constant L/D [11]) are applied and constant electric power is assumed. Based on these assumptions, the range of the vehicle:

$$R = \frac{v(L/D)}{(TSFC)g} \ln\left(\frac{(TSFC) + \frac{v}{Q_f \eta_{elec}} \left[\frac{\zeta_{ini}}{1 - \zeta_{ini}} \right]}{\frac{(TSFC)}{(m_{ini}/m_{fin})} + \frac{v}{Q_f \eta_{elec}} \left[\frac{\zeta_{ini}}{1 - \zeta_{ini}} \right]} \right) \tag{4}$$

where g is the acceleration due to gravity and ζ_{ini} is the initial electric power fraction of the vehicle. The initial (and not instantaneous) power fraction is used so that electric power is constant and does not vary with thrust. For zero electric power fraction, this equation reduces back to the standard form Breguet equation. Further details of this derivation can be found in Appendix A.

The equation can be alternately written in terms of the overall efficiency at which the engine produces thrust power ($\eta_F = vF_{th}/\dot{m}_f Q_f$):

$$R = Q_f \eta_F \frac{(L/D)}{g} \ln\left(\frac{\frac{1}{\eta_F} + \frac{1}{\eta_{elec}}\left[\frac{\zeta_{ini}}{1-\zeta_{ini}}\right]}{\frac{1}{\eta_F\left(m_{ini}/m_{fin}\right)} + \frac{1}{\eta_{elec}}\left[\frac{\zeta_{ini}}{1-\zeta_{ini}}\right]} \right) \tag{5}$$

Because flight velocity was assumed to be constant, the endurance of the vehicle is simply the range over velocity:

$$E = \frac{(L/D)}{(TSFC)g} \ln\left(\frac{(TSFC) + \frac{v}{Q_f \eta_{elec}}\left[\frac{\zeta_{ini}}{1-\zeta_{ini}}\right]}{\frac{(TSFC)}{\left(m_{ini}/m_{fin}\right)} + \frac{v}{Q_f \eta_{elec}}\left[\frac{\zeta_{ini}}{1-\zeta_{ini}}\right]} \right) \tag{6}$$

These equations are only applicable for the specific assumptions listed, but they make apparent the dependencies of vehicle performance on various parameters. Efficiencies are clearly of great importance but so is L/D. This implies that increased drag (which lowers L/D) will have a strongly negative impact on range and endurance.

To better understand the effects of drag, a detailed drag polar can be assumed instead of the simplified assumption of constant L/D. Assuming level flight (thrust equals drag) and drag coefficient is of the form $C_D = C_{Dmin} + K(C_L - C_{Lmin})^2$ [12]:

$$\dot{m}_f = \left((TSFC) + \frac{v}{Q_f \eta_{elec}}\left[\frac{\zeta}{1-\zeta}\right] \right) \frac{1}{2}\rho v^2 S \left[C_{Dmin} + K\left(\frac{(m_0 + m_{elec})g}{\frac{1}{2}\rho v^2 S} - C_{Lmin} \right)^2 \right] \tag{7}$$

where S is wing area, g is the acceleration due to gravity, m_{elec} is the mass of the electrical conversion system, and m_0 is all remaining aircraft mass. The addition of m_{elec} increases the drag force (thus the thrust requirement) thereby accounting for the penalty of adding mass to the aircraft. Equation (7) also accounts for the splitting of power generated at different efficiencies ($TSFC$ for the propulsion cycle efficiency, η_{elec} for the overall electrical generation efficiency). With a fuel cell, $\eta_{elec} = \eta_{FC}$ which accounts for the efficiency of converting fuel to electricity (including any losses from fuel processing). With a mechanical generator, $\eta_{elec} = \eta_{e.gen.}$ which accounts for both the efficiency of converting fuel to shaft power and the efficiency of converting shaft power to electricity. A 'relative' fuel mass flow rate can be defined as the ratio of $\dot{m}_f$ at a particular electric power fraction to $\dot{m}_f$ at zero electric power fraction (i.e., when the system produces only thrust):

$$\dot{m}_f{}' = \left(1 + \frac{v}{(TSFC)Q_f\eta_{elec}}\left[\frac{\zeta}{1-\zeta}\right]\right)\frac{\left[C_{Dmin} + K\left(\frac{(m_0 + m_{elec})g}{\frac{1}{2}\rho v^2 S} - C_{Lmin}\right)^2\right]}{\left[C_{Dmin} + K\left(\frac{m_0 g}{\frac{1}{2}\rho v^2 S} - C_{Lmin}\right)^2\right]} \quad (8)$$

Further details of the derivation of this equation can be found in Appendix A.

Figure 3 shows $\dot{m}_f'$ as a function of electric power fraction (assuming: $Mach\ (M) = 0.5$ at 16.8 km (55 kft) altitude [ρ = 0.147 kg/m^3, v = 147.5 m/s], $TSFC$ = 16.8 g/s/kN, Q_f = 44 MJ/kg, $\eta_{e.gen.}$ = 0.4, η_{FC} = 0.6, aircraft specifications for HALE UAV from Table 18, $m_{elec} = 0$). Figure 4 shows the percent improvement (i.e., reduction) of fuel flow rate in the fuel cell-based system compared to the generator-based one. It is clear that the system-level benefit of fuel cells' higher electrical conversion efficiency increases with electric power fraction. However, it is

also important to note the potentially important factors that are not accounted for in this simple analysis: The electrical system mass is neglected ($m_{elec} = 0$) so the range estimate is an upper bound of what could be achieved. Also, any coupling effects between the engine and the fuel cell are neglected.

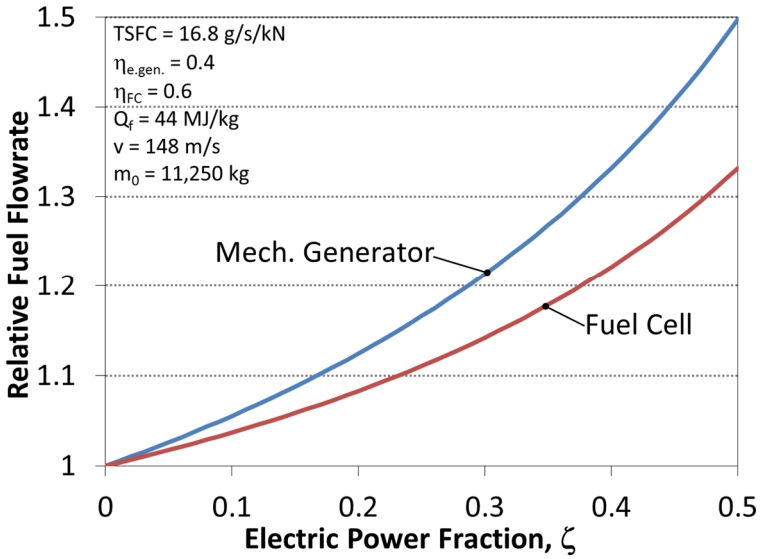

Figure 3. Relative fuel flow rate vs. electric power fraction.

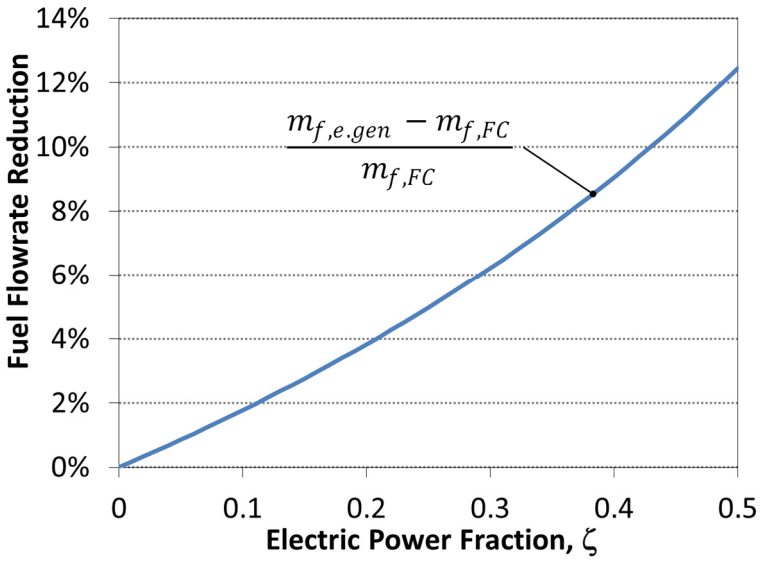

Figure 4. Percent fuel flow rate improvement vs. electric power fraction.

1.1.3 Fuel Cells for Airborne Power

While fuel-cell based APUs are being studied [13,14], they are not in widespread use. One of the main reasons for this is that the fuel cell reactor (or stack) requires a relatively complex system of pumps, blowers, sensors, controllers, and often fuel processors/reformers to deliver the appropriate reactants, maintain proper operating temperatures, and manage starting and shutdown transients. These additional components (referred to as 'balance of plant') add complexity, cost, and consume most of the efficiency advantage of the electrochemical approach over the heat engine. They also lower specific power substantially: The specific power of a stand-alone fuel cell is on the order of hundreds of W/kg [15] whereas that of modern heat engines is on the order of thousands of W/kg [16].

A potentially promising way to exploit fuel cells' high thermodynamic efficiency while minimizing balance of plant and specific power penalties is to integrate a catalytic partial oxidation (CPOx) reactor and solid oxide fuel cell (SOFC) into a heat engine's flow path. At least one study has shown, through chemical kinetic modeling, that a short contact time partial oxidation reactor is the most efficient choice for jet fuel reforming in aerospace applications [17]. An example GT-CPOx-SOFC integration is illustrated in Figure 5 and Figure 6.

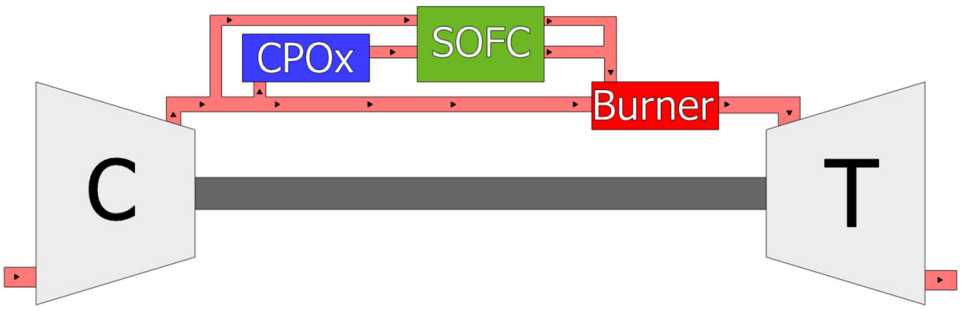

Figure 5. Schematic layout of a simple turbojet GT-SOFC.

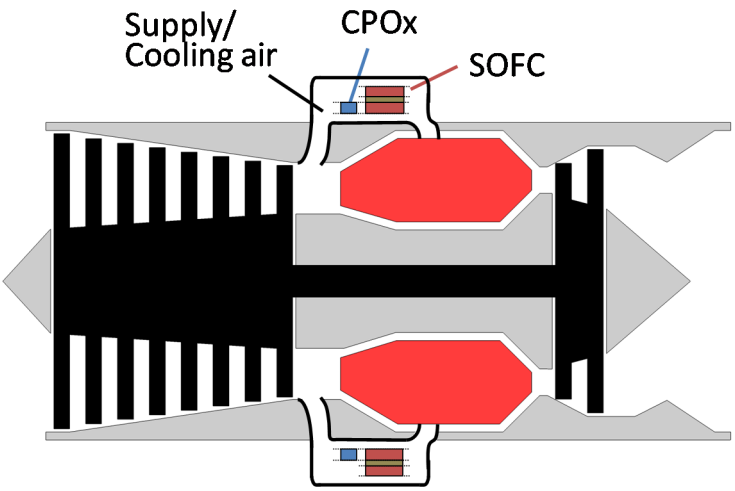

Figure 6. Simplified engine layout of a turbojet GT-SOFC. SOFC in annular duct around engine.

The potential complications arising from introducing ceramic SOFC materials into a GT engine upstream of the burner and turbine should not be overlooked or underestimated. In designing a system for operation in the field, careful consideration must be given to the prevention of fractured ceramic materials from reaching and damaging the engines turbines. However, the potential benefits of the GT-SOFC suggested by Figure 3 and Figure 4 are substantial enough to justify further investigations and future investments in R&D necessary to address and overcome these problems.

The GT-SOFC system offers several considerable advantages. The engine supplies air, fuel, and maintains CPOx/SOFC temperature thereby eliminating the need for separate systems and the associated balance of plant losses. The SOFC operates at elevated pressure which improves its efficiency and power density. The engine's combustor consumes unreacted fuel exiting the SOFC enabling it to operate at relatively low fuel utilization without incurring system-level efficiency penalties. Finally, the rapid temporal response of the Brayton cycle could permit significant improvements in transient response over comparable 'free-standing' SOFC systems.

1.2 Gas Turbine Engines

1.2.1 Fundamentals of Operation

The Brayton cycle is a thermodynamic cycle that can be used to describe the operation of a class of engines that includes gas turbines [18]. The ideal Brayton cycle is described by the following series of four processes [19]:

1. Isentropic compression
2. Isobaric heat addition
3. Isentropic expansion
4. Isobaric heat rejection

The working fluid is compressed, heated, expanded, and cooled. All processes are reversible in the ideal cycle. In the most general sense, the physical means of compression/expansion (cylinder, centrifugal or axial turbomachinery) and heat addition (heat exchangers, internal or external combustion) is inconsequential. The general P-v (pressure - specific volume) and T-s (temperature - entropy) diagrams [20] of this cycle are illustrated in Figure 7.

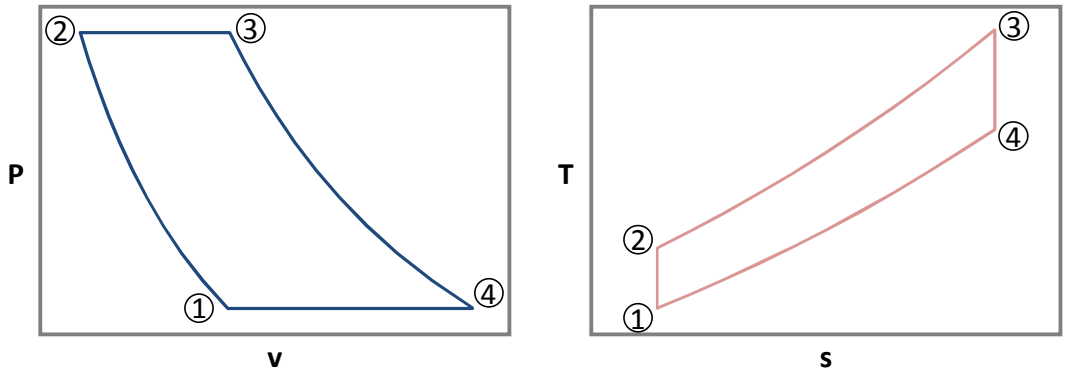

Figure 7. P-v and T-s diagrams of the ideal Brayton cycle.

The specific work of the ideal Brayton cycle (where all processes except heat addition are isentropic) is defined as the net work per unit mass of working fluid and is usually expressed using temperatures at various stages in the cycle for a calorically perfect gas [18]:

$$Net\ Work = C_p(T_3 - T_2) - C_p(T_4 - T_1) \tag{9}$$

T_1 is fixed by the ambient temperature, and T_2 and T_4 are constrained by the assumption of isentropic flow. This leaves maximizing T_3 via heat addition as the primary way to increase the specific work of the cycle [19]. Because T_3 is the highest temperature in the cycle, the limit on specific work is typically set by material properties and cooling limitations.

The efficiency of the ideal Brayton cycle is the ratio of the ideal net work to heat addition. This can be expressed in terms of temperature for a calorically perfect gas [18]:

$$\eta = \frac{Net\ Work}{Heat\ Addition} = \frac{C_p(T_3 - T_2) - C_p(T_4 - T_1)}{C_p(T_3 - T_2)} \tag{10}$$

Again, the relationships between the temperatures are known because all processes are assumed to be isentropic and because $P_1 = P_4,\ P_2 = P_3$. This leads to the following constraint on temperature ratios [19]: $T_4/T_3 = T_1/T_2$. This allows the efficiency to be rewritten in terms of the temperature or pressure ratio of the compression process:

$$\eta = 1 - \frac{T_1}{T_2} = 1 - \frac{1}{(P_2/P_1)^{(\gamma-1)/\gamma}} \tag{11}$$

The importance of this is that cycle efficiency is a monotonically increasing function of the compression ratio (i.e., higher compression ratio always leads to higher efficiency).

It can also be shown [19] that for a fixed inlet temperature, T_1, and fixed heater/burner exit temperature, T_3, there exists an optimum pressure ratio that maximizes specific work:

$$\left[\frac{P_2}{P_1}\right]_{max\ work} = \left(\frac{T_3}{T_1}\right)^{\frac{\gamma}{2(\gamma-1)}} \tag{12}$$

The gas turbine engine is an implementation of the open Brayton cycle using turbomachinery on a common shaft for the compression and expansion processes and internal combustion for the heat addition. An open Brayton cycle vents the working fluid after the expansion process instead of performing the heat rejection process.

Compression in a gas turbine engine is typically achieved via a centrifugal or axial flow compressor. This real (i.e., non-ideal) compression process is characterized by an isentropic efficiency that relates the amount of work required for an isentropic process to the amount required in the real process [10]:

$$\eta_c = \frac{h_{02s} - h_{01}}{h_{02} - h_{01}} \tag{13}$$

where h_0 is the total enthalpy and the subscript 's' denotes conditions resulting from isentropic processes.

Expansion in a gas turbine engine is typically achieved via an axial flow turbine. This real expansion process is characterized by an isentropic efficiency similar to that of a compressor [10]:

$$\eta_t = \frac{h_{03} - h_{04}}{h_{03} - h_{04s}} \tag{14}$$

The turbine drives one or more compressor components via a common shaft.

Heat addition in a gas turbine engine is accomplished via the burning of fuel in a combustor. Combustors are typically can type (several 'cans' with separate air and fuel flows), can-annular type (similar to can but all are contained in an annular flow passage), or annular (combustion and air passages are completely annular). Can type combustors are common in older engine designs but are seldom seen in modern engines [10]. In real combustors, flameholding is necessary [10,18,19] which inevitably introduces a pressure drop. This means that the heat addition is neither reversible nor truly isobaric.

Non-idealities also arise from the other components of the gas turbine engine. Inlets and diffusers introduce pressure losses (usually less than a few percent for simple inlets at subsonic Mach numbers). Similarly, nozzles also introduce losses although they too are typically small. Even shafts introduce non-ideality, primarily through bearing friction.

1.2.2 Engine Types

There are several types of gas turbine engine flow paths (Figure 8):

1. A turbojet engine has a single flowpath passing through the engine core (compressor, combustor, turbine) and nozzle. It generates thrust by accelerating the exhaust flow through a single nozzle.

2. A low bypass ratio mixed exhaust turbofan engine has two flowpaths. One path passes through the entire engine core while the other bypasses the combustor and turbine. It generates thrust by accelerating both flows through a single nozzle.
3. A high bypass ratio separate exhaust turbofan engine has also two flowpaths. One passes through the inner portion of the fan and engine core while the other only passes through the outer portion of the fan. The flowpaths exit through separate thrust-producing nozzles.
4. A turboprop engine has one flowpath through the engine core and a second through the propeller. The propeller is driven by the engine shaft and generates the bulk of the thrust. The engine flowpath generates additional thrust by accelerating the flow through the nozzle.
5. A turboshaft engine has one flowpath through the engine core and a power turbine. It generates power directly via the power turbine which is attached to a shaft that is separate from the gas generator turbine. The engine does not generate significant levels of thrust directly.

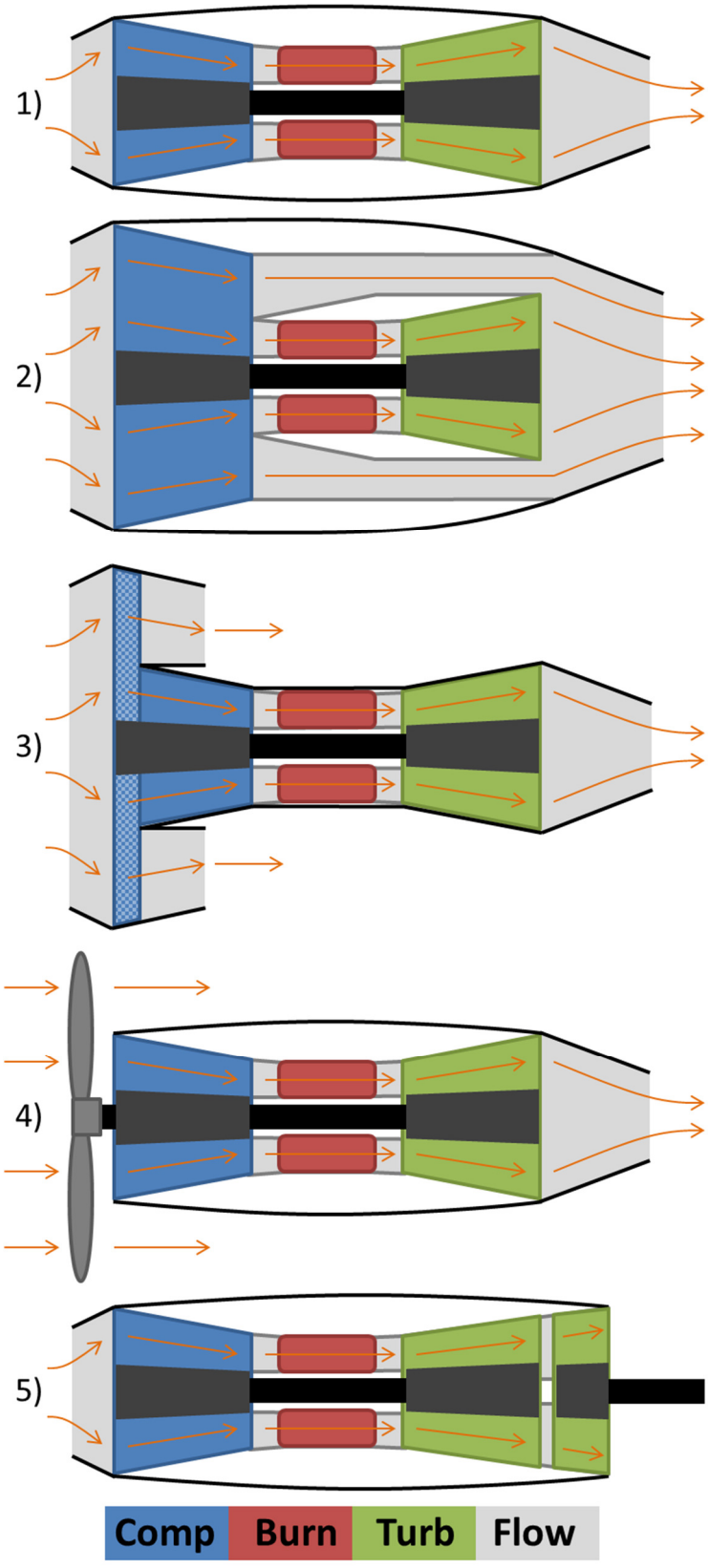

Figure 8. Different types of gas turbine engines: (1) turbojet, (2) low BPR turbofan, (3) high BPR, (4) turboprop, (5) turboshaft.

1.3 Fuel Cells

1.3.1 Fundamentals of Operation

A combustion process converts chemical potential energy stored in molecular bonds directly into heat. This is accomplished via exothermic reactions which create relatively low enthalpy products from higher enthalpy reactants [21]. Combustion-based power cycles convert thermal energy into mechanical energy in order to do useful propulsive work. To produce electrical energy through a combustion based process, one must convert chemical potential energy to thermal energy to mechanical energy and *then* to electrical energy. In contrast, fuel cells convert chemical potential energy directly into electrical energy (along with some heat due to inefficiencies). There, of course, will be mechanical losses in a fuel cell system, but these are associated with the balance of plant components (pumps, blowers, etc.) and are absent from the physical process of generating electrical power from fuel energy.

There is an interesting contrast between the temperature dependencies of ideal heat engines and ideal fuel cells. The maximum possible efficiency of any heat engine is the Carnot efficiency [22]:

$$\eta_{carnot} = 1 - T_L/T_H \tag{15}$$

where T_L and T_H are the temperatures of the low and high temperature reservoirs in the power cycle. The Carnot efficiency is a specific example of a "second law efficiency" [22] which bounds the maximum efficiency allowed by the second law of thermodynamics (i.e., assuming completely reversible processes). Carnot efficiency of 100% is impossible (would require T_L at absolute zero or an infinite T_H) but it can

be maximized by raising T_H as high as possible. The maximum efficiency possible of any fuel cell is given by a general form of the second law efficiency [22]:

$$\eta_{fc,max} = W_{max}/-\Delta H = \Delta G/\Delta H \tag{16}$$

where W_{max} is the maximum work output, ΔG is the change in Gibbs free energy, and ΔH is the change in enthalpy. Because a fuel cell can operate at a single temperature there is no temperature ratio as there was for a heat engine.

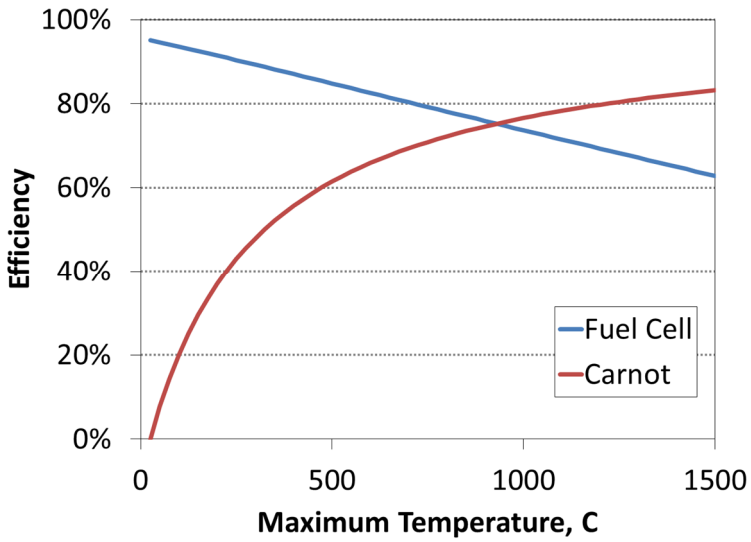

Figure 9. Comparison of ideal fuel cell and heat engine efficiencies vs. temperature.

Figure 9 compares the maximum theoretical efficiency of heat engines and fuel cells as a function of temperature (T_H in the case of the heat engine, cell operating temperature for the fuel cell). The heat engine curve is simply Eq. (15) assuming $T_L = 298\ K$. The fuel cell curve is based on calculation of Gibbs energy and enthalpy for a fuel cell at 1 atm with an oxidizer stream of air and a fuel stream of 80% hydrogen and 20% water vapor. The figure illustrates the opposite trends of the two types of systems with respect to temperature as fuel cell maximum efficiency is peak at low temperature and heat engine maximum efficiency is peak at high temperature.

In closing, however, it is important to remember that the maximum theoretical efficiency will never be achieved by a real system, and that ultimately comparisons between fuel cells and heat engines must be made based on efficiencies that can be achieved in practice, not in theory.

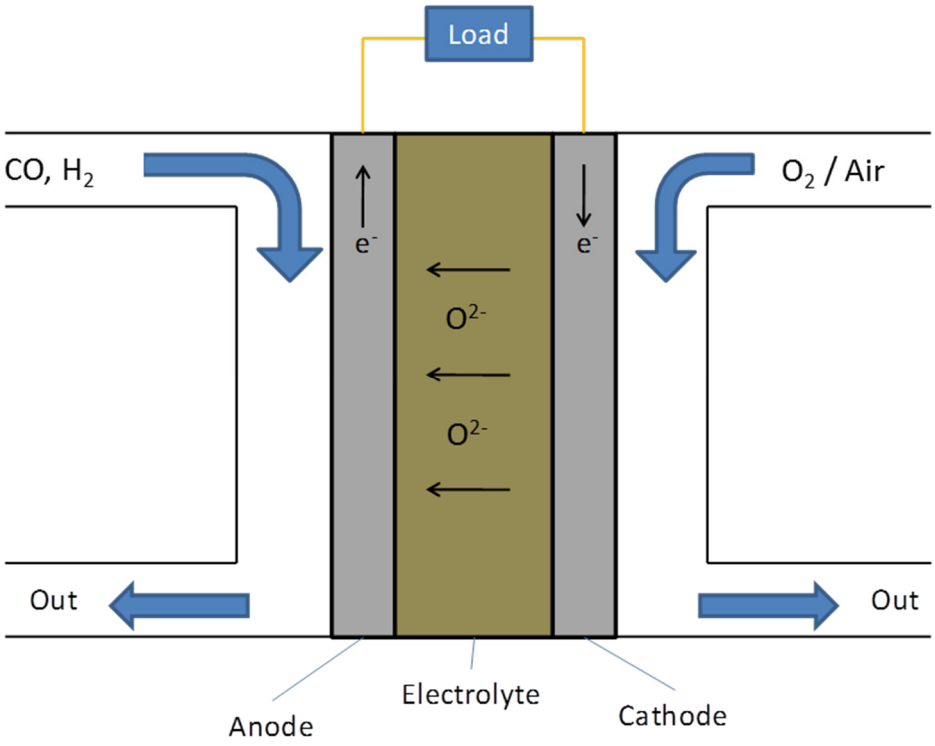

Figure 10. Solid oxide fuel cell.

Figure 10 is a schematic illustration of a solid oxide fuel cell. Hydrogen, carbon monoxide, or a hydrogen carrier (i.e., fuel) enters at the anode side and oxidizer (i.e., O_2 or air) enters at the cathode side. Partial reactions occur at the anode and cathode, and O^{2-} ions are transported across the electrolyte to complete the process. The type of ion varies among fuel cell types. For a PEM fuel cell, protons (H^+) are exchanged whereas for SOFCs it is O^{2-}. Electrons are drawn from the anode to the cathode through a load to produce the useable work of the cell. The overall reaction in a fuel cell is identical to the combustion reaction of the same reactants ($fuel + oxidizer \rightarrow$

$products$), and the overall energy release is likewise a function of the enthalpy difference between reactants and products. However, the objective in a fuel cell is not to release heat but to drive an electrochemical process from which electrical work can be extracted. The fuel, the oxidizer, and the electrolyte material used to perform the reaction all vary with fuel cell type and particular application.

In the case of solid oxide fuel cells which are the interest of this work, the following reaction occurs at the cathode [22]:

$$\text{Cathode:} \quad O_2 + 4e^- \rightarrow 2O^{2-} \tag{17}$$

where e^- denotes an electron. The ionized oxygen diffuses across the electrolyte to the anode. The electrolyte membrane must have very specific properties that enable it to transport O^{2-} ions without transporting the reactant streams or conducting electricity [23]. The reaction at the anode side is given by:

$$\text{Anode:} \quad H_2 + O^{2-} \rightarrow H_2O + 2e^- \tag{18}$$

The electrons produced by this reaction are conducted through the load attached to the cell and returned to the cathode. The power produced by the cell is the electron current times the electrical potential across the cell. All chemical potential energy not converted to electricity becomes waste heat.

Electrolyte material choices vary by fuel cell type. In fact, fuel cells are typically classified by their electrolyte material. Alkaline fuel cells (AFC) are named for the alkaline solution which saturates a porous medium to form the electrolyte [24]. Proton exchange membrane fuel cells (PEMFC) utilize an electrolyte membrane permeable to hydrogen ions but not gases [25]. Solid oxide fuel cells (SOFC) employ ceramics such as yttria stabilized zirconia (YSZ) as the porous electrolyte medium to

transmit oxygen ions [23]. As a result of their unique compositions and operating conditions, each cell type has its own strengths and limitations.

The pressure dependence of fuel cell operation can be understood by inspecting the partial derivative of the reversible cell voltage, V_{rev}, with respect to pressure at constant temperature [22]:

$$\left(\frac{\partial V_{rev}}{\partial P}\right)_T = -\frac{1}{nF}\left(\frac{\partial \Delta g}{\partial P}\right)_T = -\frac{\Delta v}{nF} \tag{19}$$

where n is the number of electrons participating in the fuel cell reaction, F is the Faraday constant, Δg is the change in Gibb's free energy, and Δv is the change in specific volume of the gaseous species in the reaction. Assuming ideal gases, the equation can be rewritten [22]:

$$\left(\frac{\partial V_{rev}}{\partial P}\right)_T = -\frac{\Delta NRT}{nF}\frac{1}{P} \tag{20}$$

where ΔN is the change in moles of gas species from the fuel cell reaction and R is the universal gas constant. According to this relationship, for reactions with $\Delta N < 0$ (which is the case for most fuel cell reactions including those relevant to this work) the reversible voltage will increase as pressure increases because the partial derivative is greater than zero. Fuel cell systems can take advantage of this effect by operating at elevated pressure to increase efficiency and/or power density. Relative to a lower pressure system, an elevated pressure fuel cell can produce the same power with lower current density (i.e., higher voltage and efficiency) or produce more power with the same current density. Note, however, that because the derivative is inversely proportional to the pressure, there are diminishing returns as pressure is increased to very high levels.

1.3.2 Challenges

Because of the elevated temperature of the air leaving a gas turbine compressor, low temperature fuel cells such as proton exchange membrane fuel cells (PEMFC) and alkaline fuel cells (AFC) are not viable options for the type of gas turbine integration considered in this work. The most common types of high temperature fuel cells are SOFCs and molten carbonate fuel cells (MCFC) [22]. MCFCs use a molten mixture of alkali carbonates as an electrolyte [26] which leads to bulkier assemblies than SOFCs which use solid electrolytes. Additionally, the stresses of 'freeze-thaw' thermal cycling of the electrolyte during start/stop transients makes MCFCs best suited to ground based, stationary, continuously operating applications [26]. This leaves SOFCs as the only logical choice for gas turbine integration.

Despite the potential benefits, the task of implementing fuel cell technology for vehicle applications is no simple matter. Most challenges in developing effective fuel cell systems are rooted in the very specific physical properties demanded of the anode, cathode, and electrolyte materials [27]. Ideal materials must withstand contamination, repeated duty cycles, potentially large temperature fluctuations, and various physical stresses all without experiencing significant performance degradation. This is in addition to the specific electrochemical, conductive, and diffusive properties demanded of the material in order to function as an electrolyte. The specific and stringent requirements on fuel cell materials often lead to issues of cost and availability (e.g., rare and very expensive platinum). Additionally, difficult issues arise with attempts to find cost effective methods to scale up the production of porous ceramics [27].

Thermal management is an important and challenging aspect of solid oxide fuel cell design [22]. Firstly, it is important to maintain a sufficiently high temperature to enable the efficient transport of oxygen ions across the electrolyte (a more difficult process than transporting the much smaller hydrogen ions present in proton exchange membrane fuel cells). Secondly, the rates of heating and cooling as well as the spatial thermal gradients must be limited to reduce the likelihood of fracturing the ceramic SOFC materials.

Contamination and poisoning are always a concern with fuel cells. Chloride ion poisoning has been studied in relation to the presence of HCl in coal syngas [28]. HCl concentrations as low as 20 ppm were shown to degrade SOFC performance. Sulfur is a very concerning contaminant for aerospace applications because of the preference for liquid hydrocarbon fuels. Syngas from hydrocarbon fuels can contain relatively high levels (hundreds of ppm) of H_2S and other sulfur compounds [29], and sulfur levels of only a few ppm can deactivate Ni catalysts. H_2S is among the most studied anode contaminants [29].

Goodenough and Huang [30] reviewed alternative anode materials for SOFCs. They discuss recent developments in double perovskites $Sr_2Mg_{1-x}Mn_xMoO_{6-\delta}$ that show high sulfur tolerance. Sun and Stimming [31] also reviewed advances in SOFC anodes noting several examples of ongoing research on Ni free materials that show increased sulfur tolerance. Gong et al. [32] reviewed SOFC anode materials with a specific focus on sulfur tolerance. Thiospinels and metal sulfides, metal cermets (SSZ, ceria, doped ceria oxides), and mixed ionic and electronic conductors, MIEC, (perovskites and lanthanum vanadate) are discussed. Materials showed sulfur

tolerances ranging from tens to hundreds of ppm. Kurokawa et al. [33] showed that a ceria nanoparticle infiltrated Ni-YSZ anode is capable of tolerating 40 ppm of sulfur. Sengodan et al. [34] showed sulfur tolerance up to 30 ppm using conventional Ni-YSZ anodes with a sulfur tolerant nanocoating. Ouweltjes et al. [35] showed that Ni-GDC (nickel and gadolinium doped ceria, GDC) exhibited a significant decrease in Ni degradation. Kurokawa et al. [36] showed that ceria- and ruthenium-infiltrated yttria-doped $SrTiO_3$ tolerated H_2S levels of the 10-40 ppm. Trembly et al. [37] studied a three layered anode of Ni-GDC, GDC, and Ni. Sulfur levels of 200-240 ppm cause degradation that may stabilize at 10-12% after several hundred hours. Aguilar et al. [38] identify $La_{0.7}Sr_{0.3}VO_3$ anodes as having particularly high tolerance to H_2S (up to 10% and over 5000 times greater than Ni based options). Cheng et al. [39] demonstrated SOFC effectiveness using strontium doped lanthanum vanadate, $La_{0.7}Sr_{0.3}VO_3$, anodes in the presence of high concentrations (5%) of H_2S. Chan et al. [40] undertook an analytical study of the sulfur tolerance of CeO_2. Cheng et al. [41] studied the stability of various candidate sulfur resistant materials (metal carbides, borides, nitrides, silicides, sulfides, complex oxides, etc.) using thermodynamic principles.

These studies are representative of the large amount of research being done to address the issue of sulfur poisoning in SOFC anodes. There is still progress left to be made for the development of functional SOFCs capable of using hydrocarbon fuels. Significant advances will be necessary in either development of sulfur tolerant anodes, desulfurizing of fuels, or development of sulfur free fuel options.

Another challenge of developing fuel cell systems is the relatively large, heavy, costly and power consuming balance-of-plant systems needed to operate a fuel cell stack. For example, among commercially available products from Ballard Power Systems [42] a stack alone weighs between 0.8 and 9 kg per kW but a full system (with balance-of-plant) weighs between 15 and 110 kg per kW. Also, balance-of-plant can account for greater than half the cost of a fuel cell system [27].

1.3.3 Solid-Oxide Fuel Cell

As stated above, SOFCs are named for the solid oxide ceramic materials used as the electrolyte. The electrolyte must transmit oxygen ions, but have very low permeability to reactant gases and very low electron conductivity. YSZ, the most common SOFC electrolyte, is composed of zirconia (ZrO_2) doped with roughly 8 to 12% by mole of yttrium (Y) [22]. The doping replaces Zr atoms in the crystalline structure with Y atoms, which creates vacancies through which O^{2-} ions may be transmitted [23]. The mechanism by which the ions move is only effective at high operating temperatures, and even then the ion conductivity is an order of magnitude smaller than for aqueous electrolytes used in other cell types. The ion conductivity of YSZ is approximately 0.02 S/cm at 800°C and rises to 0.1 S/cm at 1000°C [22]. Because of this, SOFCs must operate at high temperature and the electrolyte layer must be kept as thin as possible. A side benefit of high temperature is resistance to catalyst poisoning.

The cathode material must be porous to allow the diffusion of reactants and must also be a good electron conductor. The material must additionally be resistive to the highly oxidizing cathode environment, which rules out most metals. A common

choice for SOFC cathodes is strontium doped lanthanum manganite, a p-type semiconductor [22]. It has the appropriate diffusive and conductive properties, and also acts as a catalyst for the reaction.

The anode material must similarly be porous and conductive, but the catalytic properties must be suitable for the fuel-side reaction. Because the anode environment is not oxidizing, metals and other materials not suitable for the cathode can be used. A popular choice for the anode material is YSZ combined with approximately 35% by volume of nickel [22]. Nickel is an effective reaction catalyst and provides for the conduction of electrons. The YSZ provides the porous structure and allows for a highly stable interface with the YSZ electrolyte [23].

Because many metals have melting points near or below the operating ranges of SOFCs, materials choices are limited. Common conductors aluminum (660°C) and copper (1084°C) [21] will melt if exposed to the temperatures in many SOFCs. The cathode side flow is also a strongly oxidizing environment (high temperature and oxygen rich) [26] that will attack aluminum and copper conductors. Although high operating temperature presents a challenge, it also has its benefits. Carbon monoxide (CO) poisoning, a very common problem in low temperature fuel cells, is not a concern in SOFCs owing to the high temperatures. In contrast, low temperature cells require CO levels below 100 ppm [43] which can be particularly problematic when using hydrocarbon fuels. SOFCs have no such requirement.

1.3.4 Catalytic Partial Oxidation Reactor

A catalytic partial oxidation (CPOx) reactor is a type of fuel reformer commonly used to prepare fuel for use with SOFCs [29] among other applications. A typical

CPOx construction consists of a porous alumina foam coated in catalyst material [44-46]. The alumina foam is a ceramic material "prepared as positive images of corresponding plastic structures" [47]. These foams exhibit relatively high bed porosities of 80-90% which makes them an appealing option for applications where pressure drop minimization is important [47]. Platinum [45] and rhodium [29,46] are options for catalyst coatings. Well designed CPOx reactors operate near chemical equilibrium (assuming high temperature operation with active catalyst) [23,29].

As the name implies, CPOx reactors facilitate the partial oxidation of hydrocarbons through the use of a catalyst to produce a syngas (synthesis gas) mixture of smaller, more reactive molecules. The partial oxidation reaction has the desired products of hydrogen (H_2) and carbon monoxide (CO) as opposed to a complete oxidation reaction with the desired products of water (H_2O) and carbon dioxide (CO_2). The partial oxidation (Eq. (21)) and complete oxidation (Eq. (22)) of methane are contrasted below:

$$CH_4 + \frac{1}{2}O_2 \rightarrow CO + 2\,H_2 \tag{21}$$

$$CH_4 + \frac{3}{2}O_2 \rightarrow CO_2 + 2\,H_2O \tag{22}$$

The partial oxidation of larger hydrocarbons can be more generally expressed:

$$C_xH_y + \frac{x}{2}O_2 \rightarrow x\,CO + \frac{y}{2}H_2 \tag{23}$$

where x and y are the numbers of carbon and hydrogen atoms in the hydrocarbon molecule, respectively.

1.4 Gas Turbine / Fuel Cell Hybrid Systems

1.4.1 Advantages of System Coupling

A gas turbine / solid oxide fuel cell hybrid system is capable of taking advantage of a number of beneficial coupling effects between the two systems:

- The GT engine provides air to the fuel cell, eliminating the need for blowers or air pumps
- The air provided by the GT engine is pressurized, allowing higher efficiency and power density than atmospheric pressure fuel cells
- The pressurization process heats the air provided
- Heat in the CPOx and fuel cell exhaust is recovered through the Brayton cycle
- Unreacted fuel from the fuel cell is recovered in the Brayton cycle
- The faster transient response of the Brayton cycle could improve the overall transient response of the system relative to conventional stand-alone SOFCs

1.4.2 Challenges

One challenge facing the design of GT-SOFCs for combined propulsion and power on aircraft is the impact of pressure drop through the CPOx/SOFC assembly on the GT's overall performance. The CPOx catalyst is supported on a porous alumina foam material. This design is preferred for its relatively low pressure drop [47] compared to alternatives such as packed beds, but losses are still significant. The SOFC flow paths are long, narrow (just a few mm wide) channels which will also experience pressure drop from frictional losses. Extraction, turning, and reintroduction of air flows will cause additional pressure loss. It is important to the

operation of the physical system that the pressure drop across the CPOx/SOFC assembly be limited to less than or equal to the pressure drop across the GT burner/combustor at the desired flow rates. Otherwise, the SOFC will receive insufficient flow or the GT engine must incur additional losses that will lower overall system performance.

Another challenge is designing the physical integration of the fuel cell exhaust paths with the GT burner/combustor. Required modifications could add mass to the combustor or disrupt its flow. Flow disruptions could contribute to undesired modes of turbulent flow or combustion instability. It is also unknown how conventional combustors might respond to the injection of low molecular weight fuel species such as CO and H_2, though this could perhaps have beneficial effects (e.g., increased mixing and reaction rates).

Finally, there are potentially serious complications arising from discharging the SOFC exhaust into the GT engine upstream of the turbine. The SOFC contains ceramic materials which are less durable than the metal structures of typical GT system components. If these ceramic components fracture due to impact, thermal cycling, etc. the pieces could carried into the combustor and turbine. Any solid debris impacting the turbine blades would likely cause physical damage that at a minimum would lower turbine efficiency and in a worst case scenario could cause engine failure. There are a number of possible strategies to combat this problem. 'Ruggedized' fuel cell designs could reduce the possibility of ceramic fractures, but this would almost certainly add mass and volume to the system. Physical screens or filters could trap debris but likely at the cost of increased pressure losses. Perhaps the

best strategy would be some sort of centrifugal separator which could be as simple as a flow bend with a particle trap (Figure 11) to separate out larger particles not fully entrained in the flow. In any case, this is an important problem that will warrant increased attention as this technology matures.

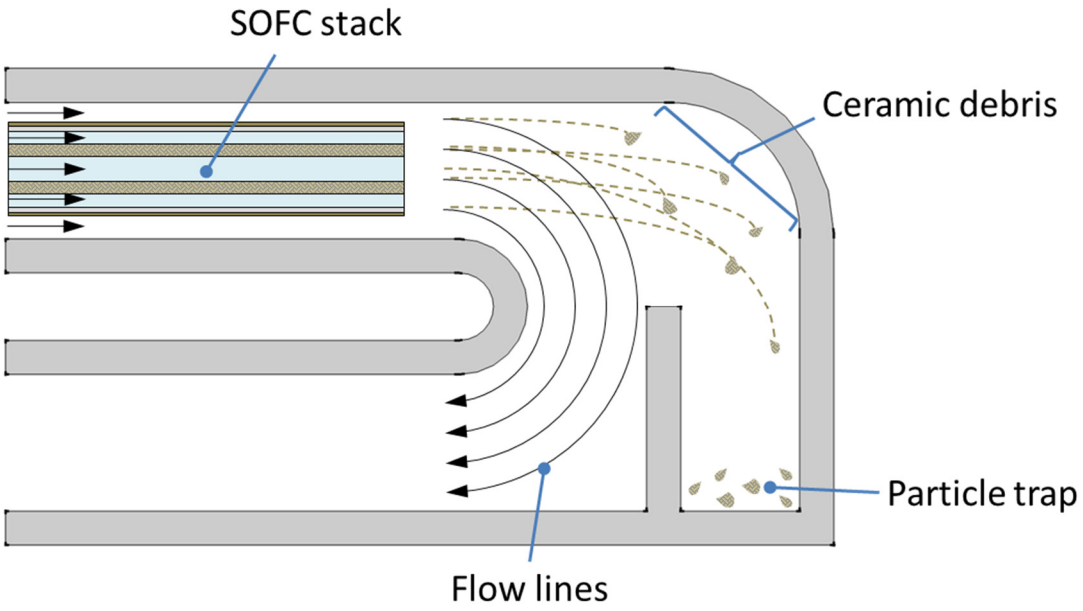

Figure 11. Conceptual ceramic particle trap.

1.4.3 Review of Research on Ground Based Systems

A number of studies have investigated integrated GT-SOFC systems for large-scale stationary power generation [48-56] and at least one has considered a similar system with a molten carbonate fuel cell [57]. Natural gas [48,51,54], methane [49,52,53,57], and syngas [55,56] are typical fuels. Some use internal reforming SOFCs [48-51] while others use external fuel reformers [52-55]. Power levels range from 5 kW [54] to 2.4 MW [49].

Calise et al. [48] simulated an internal reforming (IR) SOFC running on natural gas for the purpose of optimizing operating costs. Compressors and turbines are modeled via scaled performance maps. SOFC performance modeling is validated

against Siemens Westinghouse SOFC data. Estimated plant electrical efficiency is roughly 68%, a number which the authors describe as “remarkably high”. A “thermoeconomic” model is developed to evaluate the costs associated with the system configuration. The authors emphasize the importance of system level optimization over stack optimization as gas turbine and balance of plant losses are significant.

Haseli et al. [49] simulated an IR-SOFC running on methane and focused on the irreversibilities in the system. Compressors and turbines are modeled assuming constant efficiencies. Findings show that increasing turbine inlet temperature reduces thermal efficiency but raises the specific power of the overall cycle. The authors also identify an optimum compression ratio, balancing improved SOFC performance against higher rates of entropy production. Estimated thermal efficiencies for GT-SOFC systems are on the order of 60%. The irreversibility in the system is dominated by the SOFC and combustor (each accounting for roughly 30% of the total).

Abbasi and Jiang [50] simulated an IR-SOFC and stressed a multidisciplinary approach to the system modeling. Compressors and turbine modeling methods are not clearly stated, but they are seemingly modeled with constant efficiencies. Internal reforming is assumed and not modeled. This work includes a model of the power conditioning system. It also models the transient response of the system to changes in demand loads.

Chan and Tian [51] simulated an IR-SOFC running on natural gas. Compressors and turbines are modeled assuming constant efficiencies. The SOFC modeling is based on a Siemens-Westinghouse design. Findings show that increasing operating

pressure raised system efficiency, but increasing fuel flow (at constant utilization rate) decreases system efficiency. The study estimates greater than 60% electrical efficiency and greater than 80% system efficiency with waste heat recovery.

Palsson et al. [52] simulated an SOFC with a pre-reformer running on methane for combined power and heat generation. A two dimensional fuel cell model is developed in this work and validated against the literature. Other components are modeled using standard unit operation models in the Aspen Plus^{TM} software package. Results show an optimum pressure ratio for maximizing system efficiency. The study estimates roughly 60% electrical efficiency and greater than 85% system efficiency.

Costamagna et al. [53] simulated a steam reforming system running on natural gas fuel. Compressors and turbines are modeled via experimental performance maps. A zero-dimensional (no spatial temperature or concentration gradients) SOFC model is developed and used in this study. The modeled engine is a recuperated micro gas turbine. On- and off-design analysis is presented for this hybrid model. The study estimates greater than 60% efficiency for on-design operation. Efficiencies of greater than 50% are predicted at power levels as low as 30% of design.

Lim et al. [54] built and tested a 5 kW class planar SOFC with pre-reformer running on natural gas. The Forschungszentrum Julich made stack was designed to operate at 3.5 atm absolute pressure. The authors tested the stack as a stand-alone pressurized fuel cell unit and as a hybrid GT-SOFC system with a micro gas turbine. The study demonstrates the improved efficiency and power density from the stack during high pressure operation. It also demonstrates successful operation of a combined GT-SOFC system.

Suther et al. [55] simulated a steam reforming system running on user defined syngas mixture as fuel. Reformer, combustor, compressors, turbine, and all other non SOFC components are modeled using standard Aspen Plus™ thermodynamic models. A zero-dimensional (no spatial temperature or concentration gradients) SOFC model is developed and used in this study. A key finding is that increasing SOFC temperature and pressure both increase efficiency, but higher pressure increases cycle specific work while higher temperature decreases it. The study also shows that the optimum fuel utilization factor is dependent on the GT cycle efficiency.

Zhao et al. [56] simulated a coal syngas fed SOFC coupled with an ideal, irreversible GT model and used an optimization algorithm in MATLAB. The fuel cell model is simplified to assume uniform structure temperature while allowing a gas temperature gradient across the SOFC. The study investigates the importance of current density, operating temperature, fuel utilization factor, GT efficiencies, and heat transfer parameters.

Leto et al. [57] simulated an internal reforming molten carbonate fuel cell running on natural gas fuel. Fuel cell and reformer models are developed in this work. Other components are modeled using predefined blocks in the IPSE Pro™ software package. Estimated efficiency is roughly 60%. The authors investigate partial load performance and the sensitivity of the system to fuel utilization, current density, operating pressure, air flow, steam/methane ratio, and component efficiencies. Performance is improved by raising operating pressure and current density. 75% fuel utilization ratio balances the performance of the fuel cell and gas turbine systems.

Veyo et al. [58] investigated the conceptual design of GT-SOFC systems. The study predicts an increase from 45% electrical generation efficiency in atmospheric pressure SOFC systems to as high as 59% in pressurized GT hybrid systems.

1.4.4 Review of Research on Auxiliary Power Units

Investigations of GT-SOFC systems for airborne applications generally falls into two categories: auxiliary power unit (APU) applications and high altitude, very long (multiple days) endurance UAVs. The APU application is separate from the main propulsion of the aircraft and is designed as a direct replacement for existing APU technology. The high altitude application takes advantage of the unique low power, very long endurance nature of that type of mission that places a premium on system efficiency. APUs are discussed below, and very long endurance UAVs are discussed in the following section.

Daggett et al. [59] review a wide range of topics regarding the potential for fuel cell and hybrid fuel cell APUs for aircraft. The authors identify the primary benefits of the system as removing load from aircrafts' main engines and greatly increasing electrical generation efficiency. They also point out the technology challenges that must be overcome for the technology to reach necessary performance levels: low technology readiness level, low specific power, reforming and sulfur content of jet fuel, durability, safety, and cost. It is worth noting that since the 2003 publication of this paper, significant advancements have been made in several of these areas.

A NASA team investigated a steam reforming GT-SOFC for use as an APU that consumed Jet-A fuel [60-63]. All of these NASA studies model the system using the Numerical Propulsion System Simulation software. Freeh et al. [60] detail the bulk

(i.e., zero dimensional) SOFC model that calculates electrochemistry for the whole fuel cell based on exit properties. The model is validated against experimental data. The reformer is modeled assuming equilibrium chemistry. Compressors and turbines are modeled with performance maps for off-design analysis. Initial studies with this model simulated a 200 kW system (186 kW from SOFC, 14 kW from shaft powered generator) with estimated 40% thermal efficiency and 65% electrical efficiency. Tornabene et al. [61] lay out a detailed mass estimation method for the GT-SOFC hybrid system including estimates for compressor, pumps, turbine, heat exchangers, reformer, combustor, fuel cell, and other associated parts and piping. The fuel cell mass model involves the piece-wise summation of all SOFC components including anodes, electrolytes, cathodes, interconnects, and mounting rods and plates. Steffen et al. [62] simulated an APU system for a 300 passenger commercial aircraft. The simulated system delivers 440 kW (289 kW from SOFC, 151 kW from shaft powered generator) with estimated 62% thermal efficiency. The study illustrates the importance of cell geometry in achieving high system specific power. The system mass of an initial configuration with gas channels formed by the metallic interconnect layer is 1396 kg. The mass is dramatically reduced to 720 kg using a corrugated support anode that forms the gas channels. Freeh et al. [63] investigated off-design performance of the hybrid system. The GT cycle off-design performance is estimated using compressor and turbine performance maps. At sea level full power conditions, the estimated mass was increased by 37% because the SOFC stack size increased due to the fraction of electricity coming from shaft power dipping from 36% at cruise full power to 2.5% at sea level. At reduced power (250 kW) cruise, roughly 33% of

electricity comes from shaft power. System thermal efficiency is 42% at sea level and 73% at cruise.

Eelman et al. [64] modeled proton exchange membrane fuel cell (PEMFC) and SOFC hybrid concepts for commercial aircraft power. The systems utilize steam reformers. The study looked at 370 kW systems for both fuel cell types. The SOFC system provides 70% to 75% efficiencies. The PEMFC system provides 35% to 45% efficiencies. Aircraft integration approaches (aircraft center vs. tail cone locations) are also considered. The authors concluded that SOFC concepts show greater potential due to higher efficiency but that PEMFCs are more technologically ready in the near term.

Rajashekara et al. [8,65] modeled a steam reforming GT-SOFC APU system. The system delivers 440 kW running on commercial jet fuel. The split between SOFC and generator power is not specified. Details of the mass estimation method are not given, but the modeled system slightly exceeded the target mass of 880 kg. System efficiency is estimated at 61% at sea level and 74% at altitude. The authors predict that GT-SOFC systems will be competitive in the 100 kW to 10 MW power range.

Braun et al. [66] modeled an autothermal reforming GT-SOFC APU system using Jet-A fuel. The system is sized to produce 300 kW. The study investigates two system architectures: one focused on more near term practical integration and the second focused on tighter system integration and higher performance but with higher technological risks. The second configuration is estimated at 53% and 70% efficiency on the ground and at cruise, respectively. The study shows that SOFC APU systems

are capable of significant fuel burn reductions (5% to 7%) and emission reductions (up to 70%). This is in spite of the lower specific power of these systems.

Although some of these studies report efficiencies upwards of 70% or more, the bulk of the other studies surveyed here suggest these efficiency estimates may be overly optimistic.

1.4.5 Review of Research on All Electric UAVs

As mentioned previously, high altitude, very long (multiple days) endurance UAVs are a target for GT-SOFC use. The unique mission requirements of low propulsion power and exceptionally long endurance place a premium on system efficiency. The specific power of the energy system becomes relatively less important in these missions.

A NASA study by Himansu et al. [67] modeled 20 kW and 50 kW hydrogen fueled GT-SOFC systems for a fully electric UAV performing high altitude (50 to 70 kft), very long duration (10 days or more) missions. The study shows that there exists an optimum cell operating voltage for minimum system mass (including fuel mass). The optimum voltage trends higher for longer design mission durations due to the increased importance of efficiency. The study includes detailed trade studies of system mass as a function of fuel cell voltage, mission duration, and system losses.

Aguiar et al. [68] modeled 140 kW hydrogen fueled GT-SOFC systems for a fully electric UAV performing high altitude (50 to 65 kft), low speed (Mach 0.25 to 0.35), very long duration (1 week) missions. The study shows that, for this mission, it is advantageous to use multiple fuel cell stacks (fuel flow in parallel, air flow in series with intercoolers) as opposed to a single larger stack. Efficiency of a single stack

system is estimated at 54% and that of a multi-stack system is estimated at 66%. The improvement is due to reduction of required air flow and an increase in turbine inlet temperature. However, the study is directed at minimizing fuel mass only. Fuel cell mass is not estimated.

1.4.6 Summary of GT-SOFC Literature Review

The following table summarizes several key elements from the works referred to in the preceding literature review. The system size, fuel cell type, fuel type, model fidelity, and predicted efficiencies are included for easy comparison between studies.

Table 1. Literature review summary.

Ground based:

Reference	Platform	Size	Reformer / FC	Fuel	FC model	GT model	Efficiency	Notes
Calise et al. [42]	MATLAB	1.5 MW	IR-SOFC	natural gas	validated against data	scaled performance maps	$\eta_{elec} = 68\%$, $\eta_{sys} > 90\%$	cost optimization
Haseli et al. [43]	MATLAB	2.4 MW	IR-SOFC	methane	zero-D	constant efficiencies	$\eta_{sys} = 60\%$	focus on the irreversibilities
Abbasi and Jiang [44]		132 kW	IR-SOFC		zero-D	constant efficiencies		power conditioning; transient response
Chan and Tian [45]		2.1 MW	IR-SOFC	natural gas	zero-D, validated against data	constant efficiencies	$\eta_{elec} = 62\%$ $\eta_{sys} = 84\%$	
Palsson et al. [46]	Aspen Plus	500 kW	pre-reformer, SOFC	methane	2-D, validated against literature	Aspen Plus std. models	$\eta_{elec} = 60\%$ $\eta_{sys} = 86\%$	combined power and heat generation
Costamagna et al. [47]	MATLAB	300 kW	steam reformer, SOFC	natural gas	zero-D	performance maps	$\eta_{sys} > 60\%$	on- and off-design analysis
Lim et al. [48]	Experiment	5 kW	pre-reformer, SOFC	natural gas				working GT-SOFC
Suther et al. [49]	Aspen Plus		steam reformer, SOFC	syngas	zero-D	Aspen Plus std. models		
Zhao et al. [50]	MATLAB			coal syngas	zero-D	ideal GT	$\eta_{sys} = 50\text{-}60\%$	
Leto et al. [51]	IPSE Pro	140 kW	IR molten carbonate	natural gas	zero-D	IPSE Pro std. models	$\eta_{sys} = 60\text{-}70\%$	
Veyo et al. [52]		300 kW, 1 MW		natural gas			$\eta_{sys} = 59\%$	

APUs:

Freeh et al. [54]	NPSS	200 kW	steam reformer, SOFC	Jet-A	zero-D,validated against data	performance maps	$\eta_{sys} = 40\%$, $\eta_{elec} = 65\%$	
Steffen et al. [56]	NPSS	440 kW, 1396 kg	steam reformer, SOFC	Jet-A	zero-D	performance maps	$\eta_{sys} = 62\%$	
Freeh et al. [57]	NPSS	440 kW	steam reformer, SOFC	Jet-A	zero-D	performance maps	$\eta_{sys} = 73\%$	on- and off-design analysis
Eelman et al. [58]	MATLAB	370 kW	steam reformer, PEM and SOFC	jet fuel			SOFC: $\eta_{sys} > 70\%$ PEM: $\eta_{sys} > 35\%$	aircraft integration approaches
Rajashekara et al. [59]		440 kW, >880 kg	steam reformer, SOFC	jet fuel	zero-D		SL: $\eta_{sys} = 61\%$ cruise: $\eta_{sys} = 74\%$	
Braun et al. [60]	UTRC proprietary	300 kW	autothermal reforming SOFC	Jet-A			SL: $\eta_{sys} = 53\%$ cruise: $\eta_{sys} = 70\%$	

All-electric:

Himansu et al. [61]	MATLAB	20 kW, 50 kW	SOFC	H_2	zero-D	constant efficiencies		
Aguiar et al. [62]		140 kW	SOFC	H_2		constant efficiencies	single: $\eta_{sys} = 54\%$ multi: $\eta_{sys} = 66\%$	multiple stacks: fuel in parallel, air in series

1.5 Numerical Propulsion System Simulation

1.5.1 Overview

The analysis of GT-SOFC systems presented in this work is performed using the Numerical Propulsion System Simulation (NPSS) code developed by the National Aeronautics and Space Administration (NASA) [69,70]. NPSS was chosen for this work because it is specifically designed for GT analysis and is well suited for expansion to incorporate other complicated thermodynamic systems. Additionally, NPSS is currently in use as a modeling tool by engine manufacturers which would make it relatively seamless to blend this tool with manufacturer's engine specific gas turbine modeling in the future.

NPSS makes it relatively simple to assemble a wide variety of flow components into many different system arrangements. The NPSS package comes with a library of standard components for GT systems like turbines, compressors, combustors, etc. New components may be defined in almost any level of detail desired by the user. 'Interpreted' components are defined using the NPSS coding language which is object oriented and similar in most respects to C++. These user defined components can be as simple as table lookup or as complex as linking to external CFD simulations. The NPSS element structure has built-in flow port data structures that store and pass flow information (composition, temperature, pressure, enthalpy, etc.) between linked components. NPSS also has several built-in thermodynamics packages which execute functions to determine the flow state based on some combination of pressure, temperature, enthalpy, and entropy. The modeling presented in this work utilizes the Chemical Equilibrium with Applications (CEA) [71]

thermodynamics package which performs chemical equilibrium calculations each time these built-in functions are called. Other thermodynamics package options include a limited chemical equilibrium calculation ('JANAF' package) and simple gas property lookup ('GasTable' package).

1.5.2 Solution Method

To model complicated thermodynamic systems such as GTs and GT-SOFCs, one must define a set of equations describing the operation of the system. To solve for stable operating points one must additionally define an array of differentiable functions (the dependent conditions) of several (independent) variables.

There are many methods available [72-74] for solving systems of nonlinear equations. In fact, there are essentially infinite variations upon methods which one could use (though of course not all are practical). It is not the intent of this section to conduct an exhaustive review of solution methods but rather to summarize some of those most relevant to the type of problem investigated in this work: finding solutions to strongly coupled, highly nonlinear systems of several equations.

Genetic algorithms are not considered here because they are typically used for optimization and machine learning problems [75], though they have been considered for solving nonlinear systems (e.g., Refs. [76-78]).

For models of complex systems like gas turbines and fuel cells, it will generally not be possible to explicitly calculate solutions to system level equations which are strongly interrelated and dependent on complex underlying calculations. Therefore, iterative methods are required that begin with an initial guess and calculate successively better approximations (often using function derivatives or their

approximations) until a solution is found. The size of the problem (i.e., number of equations) and the computational cost of evaluating the functions and their derivatives are primary factors influencing the choice of solver [79]. For systems of relatively few equations with low function computation cost, methods like finite differenced Newton's method that update by calculating a partial derivative matrix (Jacobian) via finite differencing are preferred because the relatively large number of calculations per equation per iteration is made acceptable by the low overall computational cost of the problem. In contrast, for problems that are sufficiently large (CFD problems can have thousands of equations) or for which the function calculation is very expensive, calculation of derivatives at every iteration is undesirable. There are methods termed 'inexact Newton methods' [74] that update without calculating or approximating the derivatives. Others, like Broyden's method [72,74,79], approximate the derivatives without the costly finite differencing. These types of methods require a preconditioner to perform well (typically a matrix close to the inverse of the Jacobian, which can be difficult when the Jacobian is unknown). Other methods reduce computational cost by calculating derivatives for only the first iteration or only when certain criteria are met. Examples include 'simplified Newton's method' [72] which simply reuses the derivatives from the first iteration and hybrid methods which approximate updates to the initial Jacobian at subsequent iterations (via Broyden's method, for example).

It is this final example which is used in the current work. Other methods could certainly also be effective, but a modified Newton's method with Broyden updates is well suited to this application. The problem is relatively small (several equations) so

methods specialized for large systems are not appropriate. The function calculation cost is large, so generating Jacobians at each iteration is impractical. Calculating a Jacobian for the first iteration provides the high quality starting point of a finite differenced Newton method, but Broyden updates subsequently allow the benefits of improved computational efficiency. Refer to Appendix B for a more analytical discussion of Newton's and Broyden's methods.

The NPSS solver requires the user to define a set of independent variables and dependent conditions. Any parameter in the system can be defined as an independent variable which is controlled and varied by the solver. The solver adjusts the values of the independent variables at each iteration using the Jacobian matrix in order to converge a solution that meets all of the dependent conditions. Dependent conditions are defined by equalities that the solver attempts to satisfy. These equalities can take the form of driving a dependent parameter to a preset value, driving two dependent parameters to equal each other, or any number of more complex forms. One example of an independent-dependent relationship is varying rotation speed to match the power of compressors and turbines on the same shaft. The number of independents and dependents must be equal.

The solver utilizes the previously described quasi-Newton's method to converge solutions of the system. Perturbations of the independent variables are used to form a Jacobian matrix of partial derivatives that describes the complex set of interrelationships between the independents and dependents. For each iteration, the solution algorithm approximates the correction to each independent variable required to drive the residuals to zero based on the Jacobian and the error in the dependent

conditions. Following the first iteration, a new Jacobian is formed only when certain convergence criteria are not met [69]. User controlled variables define the maximum number of iterations or Jacobians to attempt before considering the convergence failed.

1.5.3 Challenges

Solving complex and highly nonlinear systems presents formidable numerical challenges. While CFD solvers regularly handle thousands or even millions of variables simultaneously, the task is greatly facilitated by the similarity of the equations and the sparse nature of the problem [80]. The types of systems of interest here do not have those advantages. Each dependent condition is typically affected to varying degrees by most, if not all, of the independent variables (i.e., the system is not sparse). Solving the system requires simultaneously satisfying equalities in several (in this work, up to 13) dissimilar functions in a multi-dimensional parameter space where the functions are highly nonlinear.

The NPSS solver is appropriate for this effort because of its proven track record in solving problems involving gas turbine integration. A major issue inherent to all Newton type solvers is the need for good initial approximations of the independent variables [72]. Initial values for the variables that do not produce a thermodynamically consistent approximation of the system or are simply not close enough to the converged solution will lead to divergence. To overcome this challenge, it is often necessary to begin from a known initial state that produces a valid solution and then gradually progress toward increasingly different target states (e.g., beginning with a known solution for a low power system and incrementally

increasing power instead of attempting a solution for a high power system directly). While this could be a significant impediment to performing system-level optimizations over large parameter spaces, it is less important in the context of this work.

1.5.4 Implementation of CEA

As mentioned previously, NPSS supports many different types of thermodynamic calculations. The most suitable for this work involves determining flow states via chemical equilibrium calculations. This is accomplished by an implementation of NASA's CEA code. The CEA calculation is based on a minimization of Gibbs' free energy. This produces a solution at the minimum free energy state, irrespective of the activation energy or chemical kinetics of the reactions required to reach that state. A summary of how this is done and what equations are involved can be found elsewhere [71].

The CEA thermodynamics package is needed because detailed species output is required for the electrochemistry calculations. It also performs the equilibrium calculations used to simulate the catalytic partial oxidation reaction and the water-gas shift reaction. Unfortunately, because of the relatively computationally intensive minimization of Gibbs free energy, CEA is computationally slower than the other thermodynamic packages which lack the detailed output needed in this study. Computational speed is improved by reducing the number of species considered from the more than 2000 available in the base package to only the approximately 250 that are potentially relevant to hydrocarbon combustion in air (i.e., combinations of C, H, O, and N). The CEA package is capable of multiple types of equilibrium calculations

including but not limited to: constant temperature and pressure, constant enthalpy and pressure, constant entropy and pressure.

1.6 Objective and Approach

The objective of this work is to evaluate the efficacy of integrating CPOx reactors and SOFCs directly into an air vehicle's main gas turbine engine(s) as a means to reduce fuel consumption and improve range and endurance. This is accomplished by developing 'intermediate fidelity' models of various types of gas turbine/SOFC hybrids. Models of the individual subsystems (gas turbines, CPOx reactors, and solid oxide fuel cells) are tested as separate systems before being incorporated into the overall GT-SOFC system model. The 'intermediate fidelity' models include detailed representations of the electrochemistry, pressure and heat losses, and account for 'down-the-channel' performance of the CPOx and SOFC but not the detailed aspects of fluid flow (velocity profiles in the channel, etc.). Mass models are also developed that permit estimation of system energy density and the effects of added systems on aircraft drag. System performance is evaluated by comparing total fuel mass flow rates (as a proxy for range/endurance) at constant speed and altitude flight conditions. The modeling tools are used to perform several studies:

- Comparison of performance of an individual fuel cell operating in the actual engine environment (delivered air temperature and pressure) at multiple altitude and throttle conditions

- Evaluation of potential fuel burn reduction in UAVs and regional jet transport applications made possible by GT-SOFC integrations compared to GT-generator systems with multiple configurations and conditions:
    - Turbojet, low BPR turbofan, and high BPR turbofan integrations
    - Low, medium, and high engine overall pressure ratios (OPR)
    - High altitude (16.8 km) and mid-altitude (10.7 km) flight conditions
- Sensitivity analysis of performance (fuel burn) to system parameters
- Evaluation of the uncertainty in model predictions based on uncertainties in the model assumptions
- Investigation of the impact of external fuel cell assembly drag on the predicted performance of systems accomplished by performing:
    - An initial study of short, radially expanding SOFC configurations
    - A more refined study of a more thoughtfully integrated GT-SOFCs that are less obstructive and higher performing

Chapter 2: Component Modeling

2.1 Overview of Modeling in NPSS

The basic NPSS structure is to define a series of component elements which can be linked to generate models of any number of systems. The ease of linking components makes NPSS a relatively fast and easy environment for developing system models and investigating various systems and configurations.

'Fluid Ports' and 'Bleed Ports' are types of 'Flow Stations' in NPSS that pass flows into and out of a component. Each Flow Station stores the state of the fluid stream. This includes, but is not limited to: temperature, pressure, enthalpy, entropy, composition, flow rate, viscosity, molecular weight, specific heat capacity, ratio of specific heats, velocity, Mach number, flow area, etc. A Fuel Port passes a stream of fuel with specific mass flow and properties. It differs from a Fluid Port in that it stores just a limited set of properties specific to a fuel (heating value, reference enthalpy, carbon-to-hydrogen ratio, etc.). Shaft Ports input or extract shaft power into the component, changing the amount of energy present in the flows.

The Fluid Output Port of any component is easily linked to a Fluid Input Port using the NPSS 'linkPorts' command. Bleed, Fuel, and Shaft Ports are linked similarly. Linking ports between components is the numerical means by which a fluid stream passes through the system.

Figure 12 illustrates a simple NPSS model (a simplified turbojet) and its relationship with the system solver. In this simple example, Fluid Ports are linked between the Inlet Start, Inlet, Compressor, Burner, Turbine, Nozzle, and Flow End

components. Bleed Ports and Shaft Ports are linked between the Compressor and Turbine. Fuel Ports are linked between the Fuel Start and Burner components.

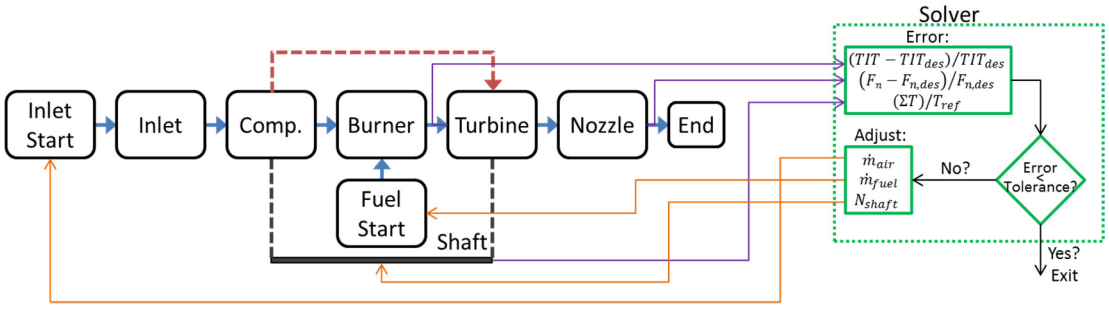

Figure 12. NPSS model schematic with simple turbojet and solver.

A simple solver setup is shown with three independent variables (air mass flow, fuel mass flow, and shaft speed (N_{shaft})) and three dependent conditions (turbine inlet temperature (TIT=target), thrust (F_n=target), and net shaft torque (ΣT=0)). The model runs and sends information about the dependents to the solver. The solver calculates errors in the dependent conditions. If the errors are within tolerance, the solver exits. Else, adjustments to the independent variables are calculated and returned to the model, and the model is run again. For more information on the operation of the system solver, see Section "1.5.2 Solution Method" and Refs. [69] and [70].

System components are modeled in NPSS using the NPSS interpreted code language which is heavily based on C++. Each component satisfies the basic conservation equations for mass and energy in addition to any other equations specific to the type of component being modeled. Many models of basic components are included in the NPSS software release. The current work uses some of these pre-existing models and develops new component models for additional elements.

A generic element (Figure 13) has any number of ‘Fluid Input Ports’, ‘Fluid Output Ports’, ‘Bleed In Ports’, ‘Bleed Out Ports’, ‘Fuel Ports’, and ‘Shaft Ports’. The component performs various operations on the incoming fluid and fuel streams to simulate the function of the modeled component.

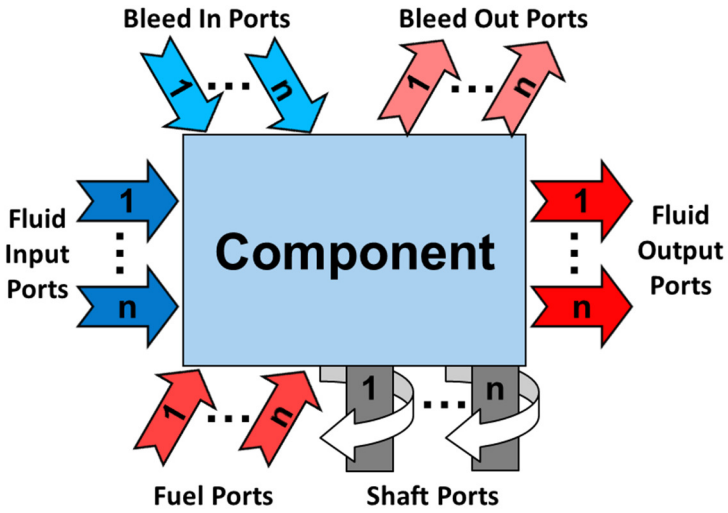

Figure 13. Generic element diagram.

There are several commands in NPSS that execute the functions of the thermodynamic package. The command ‘setTotalSP’ sets the fluid state using a constant entropy, constant pressure equilibrium calculation carried out by CEA. The command ‘setTotal_hp’ sets the fluid state using constant enthalpy, constant pressure equilibrium calculation. The command ‘setTotalTP’ sets the fluid state using a constant temperature, constant pressure equilibrium calculation. For more information on CEA and its implementation in NPSS, see Section “1.5.4 Implementation of CEA” and Refs. [69] and [70].

The ‘standard’ components described in Section 2.2 are all included in the NPSS software release. The descriptions provided here do not necessarily cover functionality that is not used in the current work. The components described in

Section 2.3 have all been created or modified for this research. The 'Solid-Oxide Fuel Cell' element is a heavily modified and improved version of a model developed in earlier research [81-83]. The 'Catalytic Partial Oxidation Reactor' element is completely new for this work. More detail on each component is included in the following sections.

2.2 Standard NPSS Components

2.2.1 Ambient Element

The AmbientNASA (hereinafter referred to as 'Ambient') element is used to calculate flight condition properties based on user defined inputs. It is a non-flow element meaning that it does not start, terminate, or modify a flow and it has no fluid ports. The Ambient element defines the flight conditions which are then referenced by an Inlet Start element (described in a later section).

The element calculates the flight conditions based on internally defined atmospheric profiles including 'Standard' day (defined by U.S. Standard Atmosphere, 1962 [84]), 'Hot', 'Cold', 'Polar', 'Tropical' days (defined by MIL-STD-210A [85]), and a number of extreme temperature profiles (defined by MIL-HDBK-310 [86]).

The element accepts a variety (literally dozens of combinations) of inputs to determine the flight condition. The required inputs are typically a set of three parameters: one defines altitude/pressure level (altitude, static pressure, or total pressure), a second defines relative temperature (temperature difference from the profile, static pressure, or total pressure), and a third defines speed (Mach number, airspeed, or total temperature/pressure to implicitly define Mach number).

The outputs of the element include (but are not limited to) altitude, pressure, temperature, Mach number, airspeed, and dynamic pressure.

There are no independent variables or dependent conditions for this element.

Parameters (used in this work): 'Standard' day, altitude, Mach number, temperature difference from standard day.

2.2.2 Bleed Element

The Bleed element was created to allow for the extraction and reintroduction of bleed flows in gas turbine engines. It is illustrated schematically in Figure 14. The user can add as many bleed ports as necessary to each bleed element.

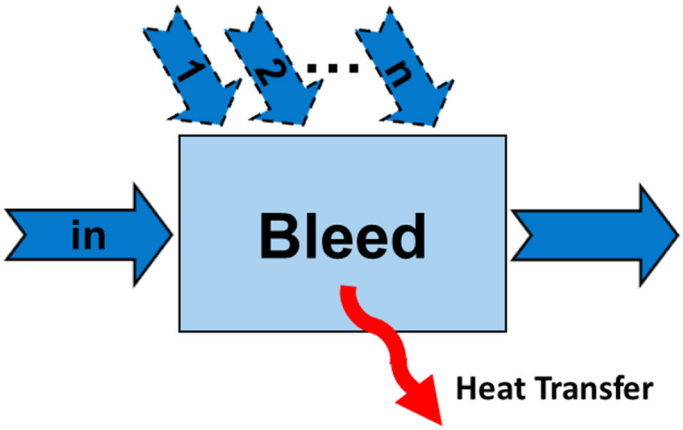

Figure 14. Bleed element diagram.

The Bleed element will accept any number of user created bleed ports into the element in addition to the standard fluid inlet and outlet ports. Mass and energy are conserved by requiring the total mass and enthalpy summed across all inlets to equal the values summed across all outlets. The conservation of energy additionally allows for heat transfer, $\dot{Q}$, in or out of the component.

$$\sum_{j}^{N_{OUT}} \dot{m}_j = \sum_{i}^{N_{IN}} \dot{m}_i \tag{24}$$

$$\sum_{j}^{N_{OUT}} \left(\dot{m}_j h_{T,j}\right) = \sum_{i}^{N_{IN}} \left(\dot{m}_i h_{T,i}\right) + \dot{Q} \tag{25}$$

where N_{IN} and N_{OUT} are the total number of inlets and outlets respectively, and h_T is the total specific enthalpy at the port. The NPSS command 'setTotal_hp' is used to set enthalpy and pressure and calculate all other fluid properties at each port including the output flow. The command sets the fluid state using input total specific enthalpy and pressure of the flow.

There are no independent variables, dependent conditions, or input parameters for this element.

2.2.3 Burner Element

The BurnerNASA (hereinafter referred to as 'Burner') element was designed to calculate the performance of a standard burner/combustor in gas turbine engines. The Burner element is always used in conjunction with a Fuel Start element (described in a later section) which supplies the fuel stream conditions.

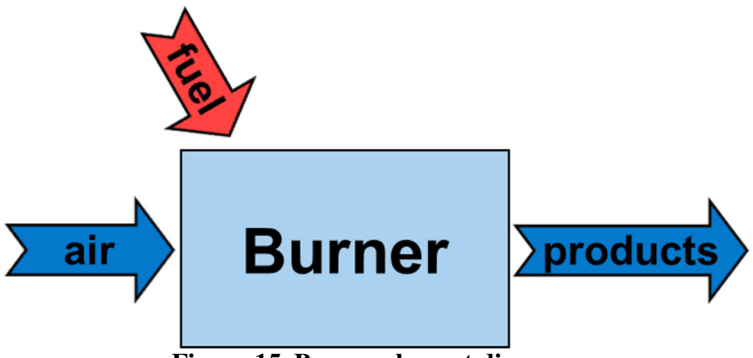

Figure 15. Burner element diagram.

The burner mixes the incoming fuel and air streams and performs combustion-related calculations. The fuel stream conditions are specified in the Fuel Start element. A pressure drop is applied in the burner before the combustion calculation. The nature of the combustion calculation depends on the chosen thermodynamics package. In this work the CEA thermodynamics package is used so the calculation is based on chemical equilibrium. The element allows the user to input either fuel mass flow (used in this work), fuel-to-air ratio, or combustor exit temperature by specifying one of several operating modes. The element also enables one to specify combustion efficiency (actual/ideal heat release), heat loss, and pressure drop due to heat release (Rayleigh flow) in addition to other pressure drop, but these are not used in the current work. Heat loss is assumed to be negligible, Rayleigh pressure drop is considered part of the input pressure drop mentioned previously, and the combustion efficiency calculation is incompatible with the CEA thermodynamics package.

There are no independent variables or dependent conditions for this element.

Parameters (in this work): fractional pressure drop, fuel mass flow rate.

2.2.4 Compressor Element

The Compressor element raises the pressure of gaseous flows based on user inputs to define pressure ratio and efficiency. The pressure ratio and efficiency are either assigned directly or they can be looked up in a user-defined compressor performance map (pressure ratio and efficiency as functions of corrected mass flow and corrected speed). The actual performance maps used in this work can be found in Appendix C. An example compressor map is shown in Figure 17 where the colored lines show contours of constant efficiency and the black lines are contours of constant corrected

speed. It is also necessary to define an operating line parameter in order to uniquely define a steady state operating condition on the performance map for a particular mass flow or shaft speed. This operating point parameter directly corresponds to the concept of an operating line on the compressor map [18] which defines the positions on the map for normal compressor operation.

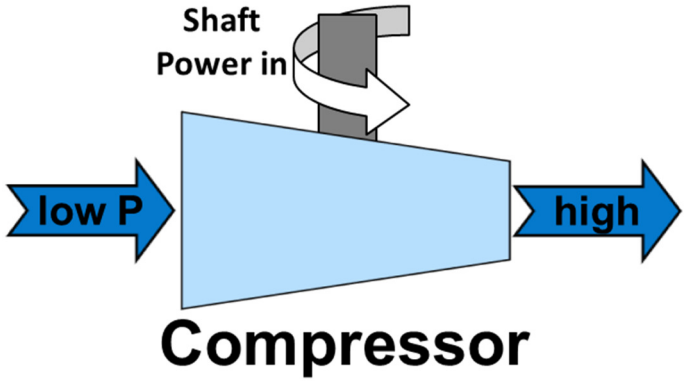

Figure 16. Compressor element diagram.

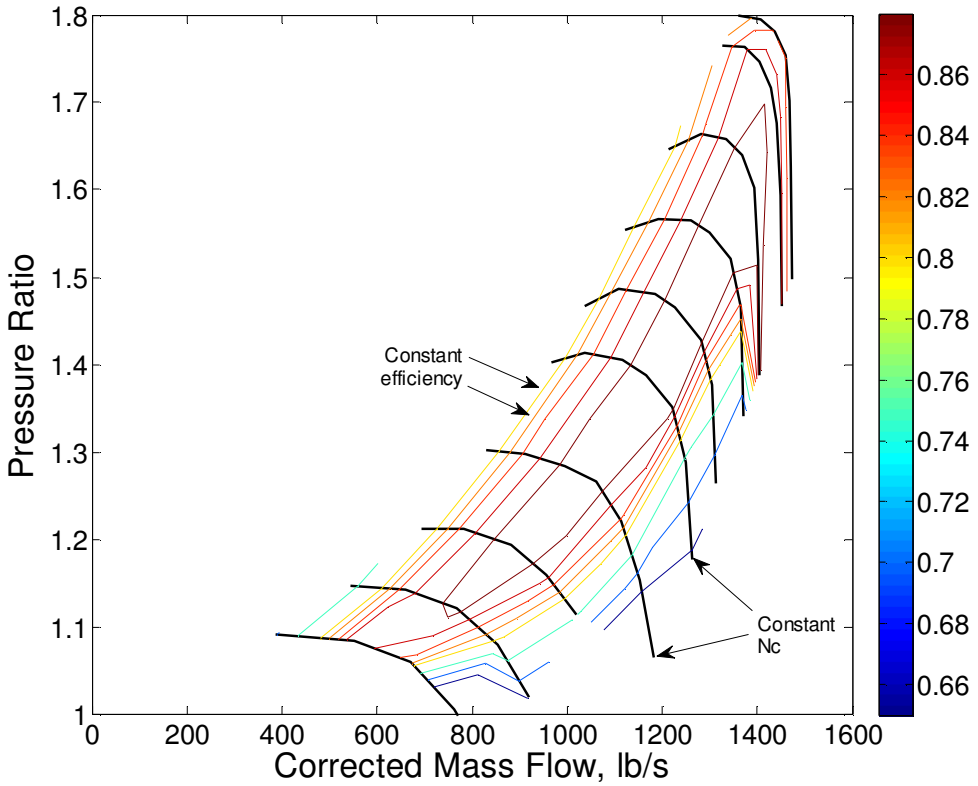

Figure 17. Example compressor performance map.

In addition to the performance map, the element also has inputs for 'design point efficiency' and 'design point pressure ratio'. In 'On-Design' mode, the element treats the design values as fixed and scales the input performance map to match the design values. This process is illustrated in Figure 18 where the purple dot denotes the design point. In the example, the source performance map has a design pressure ratio of 1.75, design corrected mass flow of 1400 lb/s, and design efficiency of 87%. The map is then scaled to a user input design point of 1.5 pressure ratio and 89% efficiency. The map is additionally scaled such that the corrected mass flow of the engine is set to be the design value. In the example, the corrected mass flow of the engine at the design condition is 1000 lb/s, thus the map is scaled accordingly. The scaling is simply performed linearly on all three axes. This manner of scaling allows a single performance map to provide realistic performance estimates for engines at a wide range of conditions. In off-design mode, the map becomes fixed and the compressor operates away from the design point.

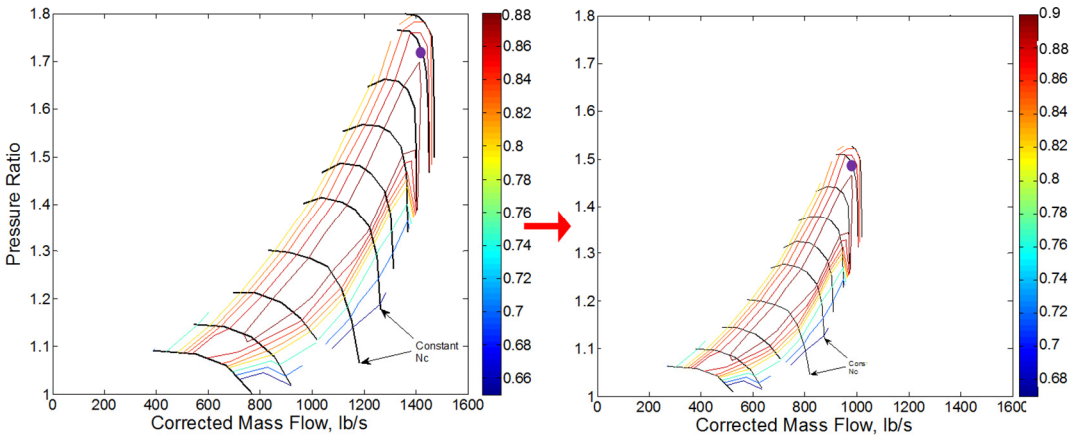

Figure 18. Compressor performance map scaling.

The element sets the outlet mass flow and composition equal to those present at the inlet and sets the outlet pressure based on the pressure ratio, π_c.

$$P_{T,out} = P_{T,inlet}\pi_c \tag{26}$$

The exit enthalpy is determined using the definition of the isentropic efficiency [18]:

$$h_{T,out} = \frac{h_s - h_{T,inlet}}{\eta_s} + h_{T,inlet} \tag{27}$$

where η_s is the isentropic efficiency, h_T is the total specific enthalpy, and h_s is the specific enthalpy assuming that the compression process occurs isentropically. The latter is determined using the NPSS command 'setTotalSP' which returns the enthalpy in a fluid with a known inlet entropy state and a known exit pressure. The exit state is determined at the known exit pressure and enthalpy using the NPSS command 'setTotal_hP'. The power input to the compressor is calculated based on the change in enthalpy across the component:

$$\dot{W} = \dot{m}\left(h_{T,out} - h_{T,inlet}\right) \tag{28}$$

Independent variable:

- Operating line parameter, *RlineMap*

Dependent condition:

- Match corrected mass flow

$$\dot{m}_{c,actual} = \dot{m}_{c,calculated} \tag{29}$$

Parameters (in this work): Design pressure ratio, design efficiency, design operating line parameter, design corrected speed (as a percentage), performance map (see Appendix C).

2.2.5 Duct Element

The DuctNASA (hereinafter referred to as 'Duct') element models pressure drops and heat losses in ducts.

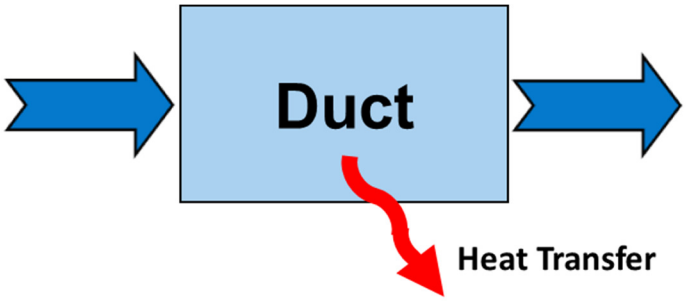

Figure 19. Duct element diagram.

Pressure drop and heat loss can be represented in a variety of ways: lossless (i.e., exit pressure and enthalpy equal inlet pressure and enthalpy), user-specified pressure loss (fractional) and heat loss rate, or other user-specified calculation functions. This work, uses user-specified values:

$$P_{T,out} = P_{T,inlet}\left(1 - \frac{\Delta P}{P}\right) \tag{30}$$

$$h_{T,out} = h_{T,inlet} - \dot{Q}/\dot{m} \tag{31}$$

where P_T and h_T are total pressure and enthalpy, respectively.

There are no independent variables or dependent conditions for this element.

Parameters (in this work): fractional pressure drop, $(\Delta P/P)$, heat loss rate $(\dot{Q})$.

2.2.6 Flow End Element

The Flow End element is very simple and only serves to terminate a flow path. Because every fluid port must be linked, the end of a flow path must be connected to a Flow End which has an inlet, but no outlet ports.

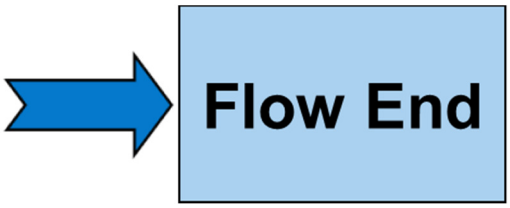

Figure 20. Flow End element diagram.

No calculations are performed by this element.

There are no independent variables, dependent conditions, or input parameters for this element.

2.2.7 Fuel Start Element

The Fuel Start element is used to initiate a fuel stream.

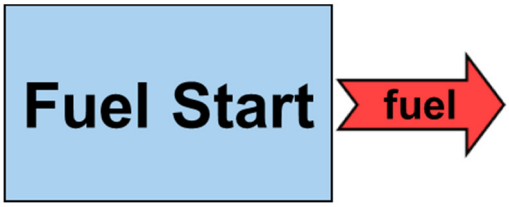

Figure 21. Fuel Start element diagram.

The element creates a stream of fuel based on user specified inputs. The inputs required depend on the thermodynamics package. For the CEA thermodynamics package used in this work, the user specifies the fuel type by name and the fuel enthalpy at standard conditions. Depending on the user selected operating mode of the model, fuel flow rate can be specified in this component or in a connected Burner element. The latter is done in this work.

There are no independent variables or dependent conditions for this element.

Parameters (in this work): 'JP-5' fuel, fuel enthalpy at standard conditions.

2.2.8 Inlet Element

The Inlet element calculates the performance of a gas turbine inlet.

Figure 22. Inlet element diagram.

The ram recovery is specified by user input. This can be an input value (as in this work) or an input calculation function. The ram pressure recovery, π_{inlet}, is defined as the fraction of total pressure in the freestream that is 'recovered' in the inlet.

$$P_{T,out} = P_{T,free}\pi_{inlet} \tag{32}$$

The element also calculates the ram drag, F_{ram}. This is the force that results from decelerating the freestream flow.

$$F_{ram} = \dot{m}_{air}v_{free} \tag{33}$$

There are no independent variables or dependent conditions for this element.

Parameter: ram recovery value (π_{inlet}).

2.2.9 Inlet Start Element

The InletStartNASA (hereinafter referred to as 'Inlet Start') element is designed to initiate an air stream to an engine.

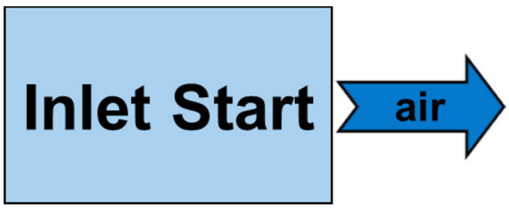

Figure 23. Inlet Start element diagram.

The Inlet Start element is used in conjunction with an Ambient element (described previously). The properties of the air stream are not defined in this element, but instead they are referenced from the associated Ambient element. The properties read in include (but are not limited to) altitude, pressure, temperature, Mach number, airspeed, and dynamic pressure.

There are no independent variables or dependent conditions for this element.

Parameters: Ambient element name, air mass flow.

2.2.10 Nozzle Element

The NozzleNASA (hereinafter referred to as 'Nozzle') element is designed to calculate the performance of engine nozzles.

Figure 24. Nozzle element diagram.

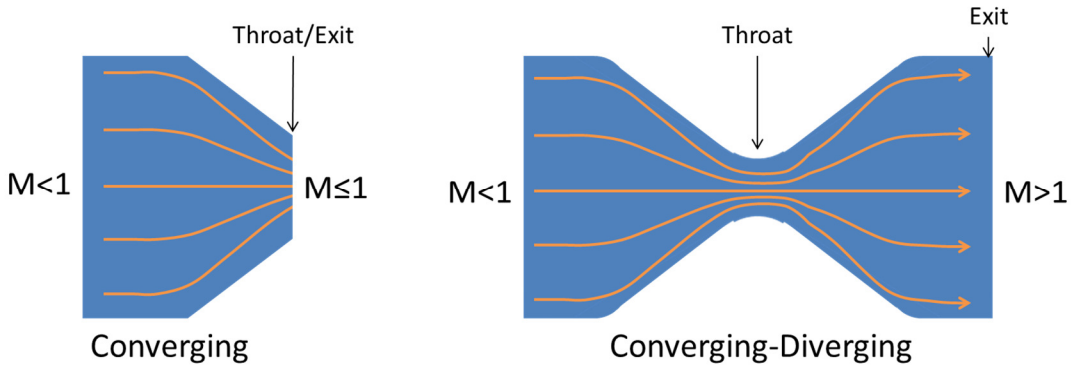

Figure 25. Converging and converging-diverging nozzle geometries.

The element can calculate performance for different types of nozzles: convergent or convergent-divergent, fixed or variable geometry. The ambient pressure is referenced from a specified Ambient element. Choked throat conditions are determined by setting the flow station Mach number to 1.0 and using the NPSS 'setTotal_hP' function to determine the overall flow state. The function iteratively calculates static flow properties from the known total properties and specified Mach number. The flow is determined to be choked when the ambient pressure is greater than the calculated pressure at the throat, $P_{amb} > P_{choked}$. If the flow is not choked, the exit flow will be subsonic even for a converging-diverging nozzle.

Typically, the user sets a model to first run in 'On-Design' mode followed by a number of runs in 'Off-Design' mode. In 'On-Design' mode, the exit flow conditions are determined by setting the flow station pressure to P_{exit} and using the NPSS 'setStaticPs' function (which iterates on the flow exit Mach number to match pressure) to determine the overall flow state. The exit area is determined by this same calculation as the area necessary to satisfy the pressure and Mach conditions. In 'Off-Design' mode for a fixed geometry nozzle, the exit area remains fixed and exit Mach and pressure are calculated by NPSS as a function of that flow area. In either case, the gross thrust can then be calculated:

$$F_{gross} = \dot{m}_{exit} v_{exit} C_{noz} + (P_{exit} - P_{amb}) A_{exh} \tag{34}$$

where C_{noz} is a nozzle coefficient (ratio of actual force produced by flow momentum to the theoretical, $= F_{actual}/(\dot{m}v)$) and A_{exit} is the nozzle area at the exit plane. For a variable area nozzle (assumed in this work), the exhaust and ambient pressures are explicitly matched so that the final term in the equation vanishes.

In 'On-Design' mode, the throat area is calculated to achieve choked flow for the mass flow entering the nozzle element. In 'Off-Design' mode, the throat area (determined by an 'On-Design' run or a user input value) is a fixed parameter and the mass flow rate into the component must be adjusted by the system level solver in subsequent iterations of the entire model. This is accomplished by changing the flow rate of air into the entire engine or by changing a Splitter element bypass ratio to alter the air flow rate through a particular engine flowpath.

Independent variable:

- None, but the dependent below usually pairs with either a Splitter element bypass ratio or an Inlet Start air mass flow.

Dependent condition:

- Physical throat area matches calculated choked flow area ('Off-Design' only)

$$A_{throat} = A_{choked} \tag{35}$$

Parameters: None in this work.

2.2.11 Shaft Element

The Shaft element is designed for use with gas turbine engine models specifically to perform component matching operations among the compressors and turbines linked to the Shaft.

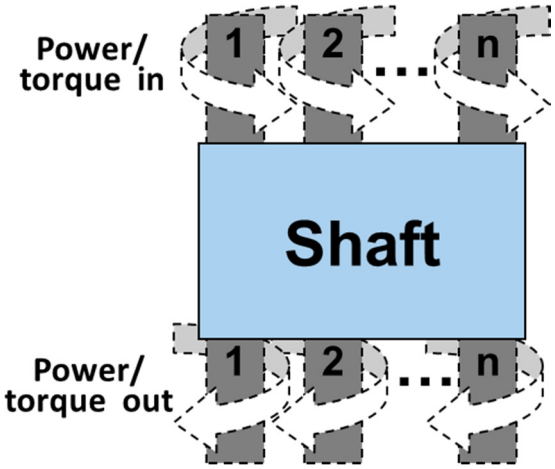

Figure 26. Shaft element diagram.

Every compressor and turbine element in a gas turbine engine has a shaft output port that must be linked to a Shaft element. Any number of torque producing components may be linked to a particular Shaft element, but all must share the same physical shaft in the actual system. In the case of multiple concentric shafts (as in this work), more than one Shaft element is required. The element performs the necessary

calculations to assure the net torque on the shaft is zero for steady state operations. The torque balance is achieved by varying the shaft rotation speed until Eq. (36) is satisfied.

Independent variable:

- Shaft rotation speed, N_{mech}

Dependent condition:

- Zero net torque

$$\sum (Torque)_{component} = 0 \tag{36}$$

There are no input parameters for this element in steady state operation.

2.2.12 Splitter Element

The SplitterNASA (hereinafter referred to as 'Splitter') element allows for a flow to be divided into two different streams. The composition, pressure, and temperature are assumed to remain constant through the element.

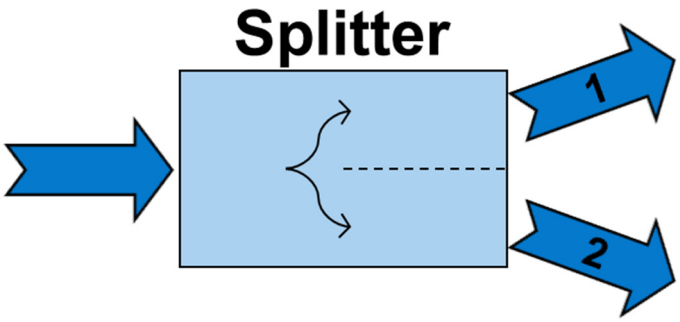

Figure 27. Splitter element diagram.

The ratio of the exit mass flows is termed the bypass ratio (BPR, Eq. (37)). BPR is a parameter that may be set by the user or the system level solver. Keeping the pressure, temperature, and composition constant guarantees that energy is conserved in the splitter.

$$BPR = \frac{\dot{m}_{out,2}}{\dot{m}_{out,1}} \tag{37}$$

$$\dot{m}_{inlet} = \dot{m}_{out,1} + \dot{m}_{out,2} \tag{38}$$

$$\dot{m}_{out,1} = \frac{\dot{m}_{inlet}}{1 + BPR} \tag{39}$$

$$\dot{m}_{out,2} = \frac{\dot{m}_{inlet}}{1 + 1/BPR} \tag{40}$$

Independent variable:

- Bypass ratio, *BPR*

Dependent conditions:

- None, but usually pairs with a Nozzle element area dependent.

Parameters: Design bypass ratio.

2.2.13 Turbine Element

The Turbine element is used for expanding and extracting work from gaseous flows based on user inputs to define pressure ratio and efficiency.

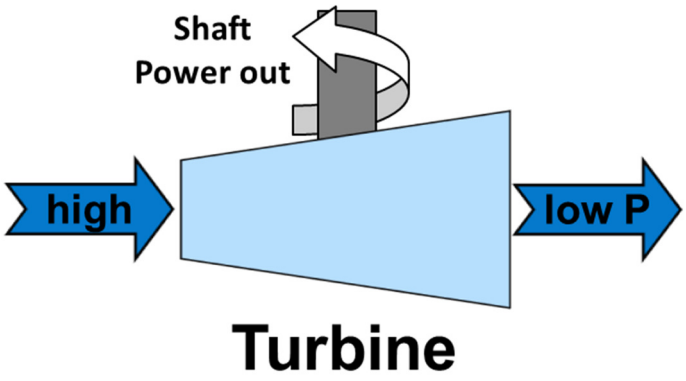

Figure 28. Turbine element diagram.

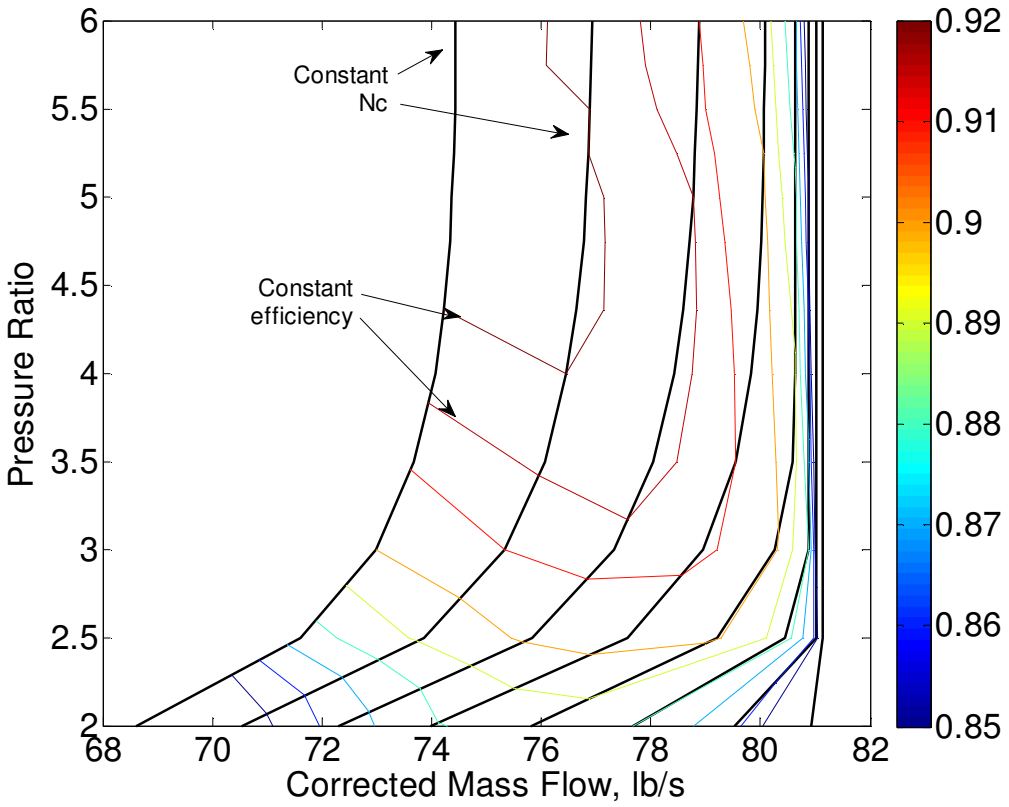

Figure 29. Example turbine performance map.

The pressure ratio and efficiency are either assigned directly or they can be looked up in a user-defined turbine performance map (pressure ratio and efficiency as functions of corrected mass flow and corrected speed). The actual performance maps used in this work can be found in Appendix C. It is also necessary to define a turbine map parameter in order to uniquely define a steady state operating condition on the performance map for a particular mass flow or shaft speed. In addition to the performance map, NPSS also accepts inputs for design point efficiency and design point map parameter. While in 'On-Design' mode, NPSS linearly scales the performance map to match the specified design point values and the turbine corrected mass flow and corrected shaft speed. This scaling process is directly analogous to the process for compressor map scaling discussed in Section "2.2.4 Compressor Element"

and Figure 18. In 'Off-Design' mode, the performance map remains fixed and the turbine operates away from the design point.

The Turbine element assigns the inlet mass flow to the outlet flow and computes the outlet pressure based on the pressure ratio across the turbine, π_t:

$$P_{T,out} = P_{T,inlet}/\pi_t \tag{41}$$

The actual exit enthalpy is determined using the definition of the isentropic efficiency [18]:

$$h_{T,out} = h_{T,inlet} - \left(h_s - h_{T,inlet}\right)\eta_s \tag{42}$$

where η_s is the isentropic efficiency, h_T is the total specific enthalpy, and h_s is the specific enthalpy assuming that the compression process occurs isentropically. The latter is determined using the NPSS command 'setTotalSP' which returns the flow state (including enthalpy) in a fluid with a known entropy state and known pressure. The exit state is computed at the exit pressure from Eq. (41) and enthalpy from Eq. (42) using the NPSS command 'setTotal_hP'.

The power extracted by the turbine is calculated from the enthalpy change from inlet to exit:

$$\dot{W} = \dot{m}\left(h_{T,inlet} - h_{T,out}\right) \tag{43}$$

Independent variable:

- Turbine map parameter, *parmMap*

Dependent condition:

- Match corrected mass flow

$$\dot{m}_{c,actual} = \dot{m}_{c,calculated} \tag{44}$$

Parameters: Design efficiency, design geometric parameter.

2.3 Developed NPSS Components

2.3.1 CPOx/SOFC Assembly Overview

The following subsections present the components developed specifically for this work to represent the CPOx/SOFC assembly. For the convenience of the reader, fig illustrates how all of the components are linked together to form the assembly.

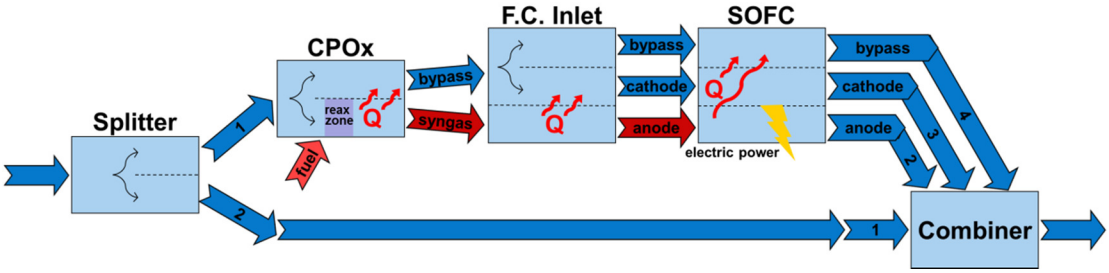

Figure 30. CPOx/SOFC assembly diagram.

A splitter separates a portion of the flow into the CPOx/SOFC assembly pathway. The air enters the CPOx element where some participates in the partial oxidation reaction and some bypasses directly to the fuel cell inlet. The bypass air is divided between a cathode channel flow and a bypass/cooling flow. The partial oxidation products (syngas) pass to the anode channel. The anode, cathode, and bypass flows pass to the corresponding pathways in the SOFC element. The anode and cathode channels participate in the electrochemical reaction producing electrical power. The bypass/cooling flow absorbs heat from those channels. The anode, cathode, and bypass exit flows then are recombined with the second air flow from the Splitter element.

2.3.2 Combiner Element

The Combiner element was developed to combine several flow streams.

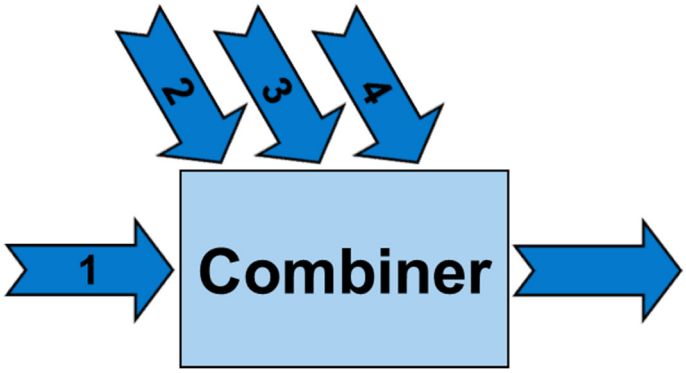

Figure 31. Combiner element diagram.

It is similar in function to a Bleed element except that it is hard-coded to accept one primary inlet and three secondary inlets (four total) and one outlet. Mass and energy are conserved by requiring that the total mass flow and enthalpy summed across the inlets equals the values at the outlet (see Eqs. (24) and (25)).

There are no independent variables, dependent conditions, or input parameters for this element.

2.3.3 Catalytic Partial Oxidation Reactor Element

The Catalytic Partial Oxidation (CPOx) reactor element is used to simulate the catalytic breakdown of larger hydrocarbon molecules into the desired fuel species for the fuel cell, CO and H_2.

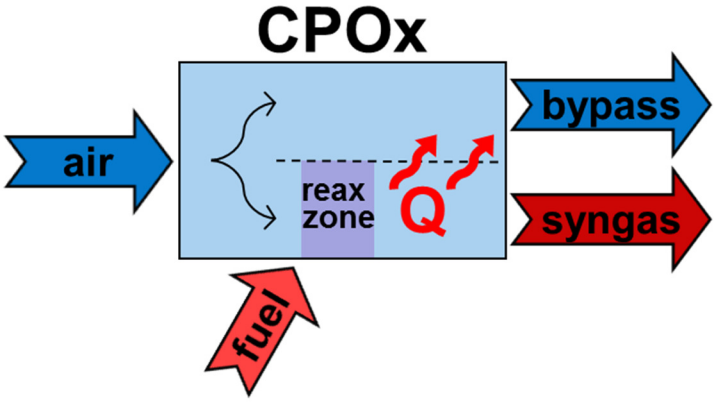

Figure 32. Catalytic Partial Oxidation Reactor element diagram.

Internally, the CPOx element divides the incoming air into reaction and bypass/cooling pathways. The element models a single CPOx unit out of many (N_{CPOx}) with the reaction air and fuel flows reduced proportionally ($\dot{m} = \dot{m}/N_{CPOx}$). The single unit CPOx products are multiplied by N_{CPOx} (implicitly assuming all units operate identically) at the exit.

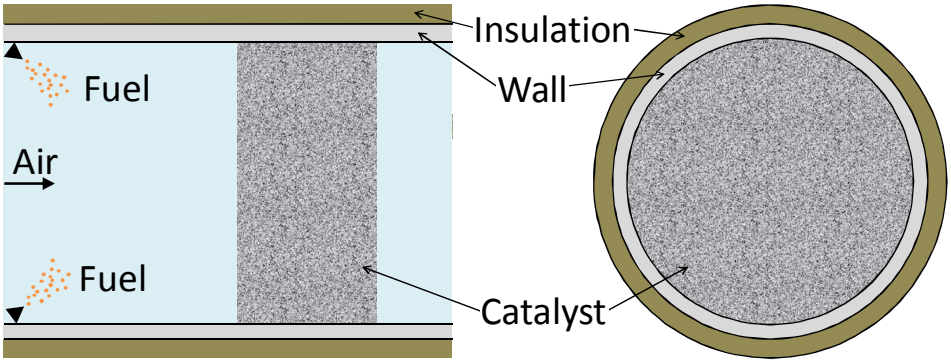

Figure 33. Illustration of the assumed CPOx reactor element geometry.

An illustration of the physical geometry being simulated by the CPOx model is shown in Figure 33. The geometry is simple, with a fuel/air mixture in a circular tube passing through an alumina foam catalyst.

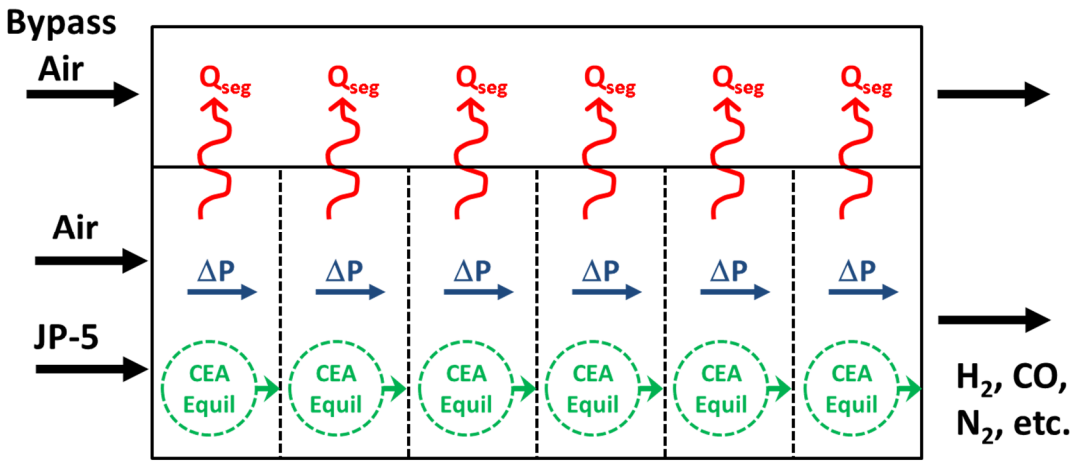

Figure 34. Illustration of the CPOx reactor element modeling structure.

The CPOx is modeled by dividing the reactor into a number (N_{seg}) flow-wise segments. Pressure drop and heat loss are calculated in each segment by enforcing conservation of mass, momentum, and energy in each segment. This also ensures that these are conserved for the reactor as a whole. The heat loss from the interior CPOx flow is transferred to the bypass/cooling flow surrounding the CPOx units. This division is illustrated in Figure 34.

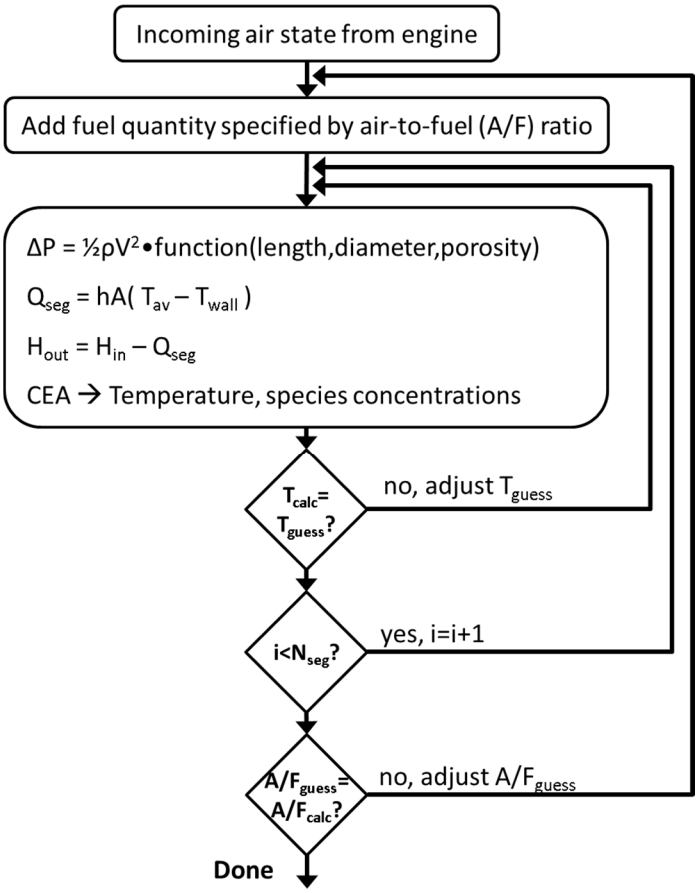

Figure 35. Illustration of CPOx reactor element calculation and looping procedure.

The calculation and looping procedure within the element is illustrated in Figure 35. The incoming air state is determined by the operation of the engine. Fuel is added to an air-to-fuel ratio (AFR) set by an initial guess. Then the pressure drop, heat loss, and equilibrium composition and heat release in the segment are calculated. Details of

these calculations are found below. The innermost loop iterates on the segment exit temperature until energy is conserved:

$$\dot{m}_{in}h_{T,in} - \dot{m}_{out}h_{T,out} - \dot{Q}_{loss} = 0 \quad (45)$$

where 'out' and 'in' denote segment exit and entrance values. Exit temperature is adjusted to satisfy this equality because of the dependence on exit enthalpy. The additional dependence of heat loss on temperature necessitates an iterative solution as the 'guessed' segment exit temperature and the calculated exit temperature are driven toward convergence. Once energy conservation is satisfied, the segment number is incremented until the end of the channel is reached. Based on the resulting exit temperature of the final segment, the minimum air-to-fuel ratio necessary to avoid soot formation is calculated. The goal is to run the system at the minimum AFR for no soot formation at all times. The outermost loop iterates on the air-to-fuel ratio until it converges (i.e., the value no longer changes between iterations).

The assumption of local equilibrium in each reactor element is reasonable since well-designed CPOx reactors operate near chemical equilibrium (assuming high temperature operation with active catalyst) [23,29]. Therefore equilibrium calculations are used to determine the heat release and chemical composition in each segment. The CPOx is assumed to consist of a catalytically active ceramic foam where the heat and pressure loss are determined using the approach of Richardson et al. [44,45,87,88].

Pressure drop in a ceramic foam can be described by the Forscheimer equation [45,87-89]:

$$dP/dL = [\alpha S_V^2 \mu(1-\phi)^2/\phi^3]v + [\beta S_V \rho(1-\phi)/\phi^3]v^2 \quad (46)$$

where dP/dL is the pressure drop, $\phi = (volume\ of\ voids)/(total\ volume)$ is the porosity, μ is the flow viscosity, ρ is the flow density, and v is the 'superficial' flow velocity. The external surface area per unit volume of solid is modeled as [45,87,88]:

$$S_V = 4\phi/\left[d_p(1-\phi)\right] \tag{47}$$

The parameters α and β depend on the catalyst geometry [87]. They are calculated per the results of Twigg and Richardson [87]:

$$\alpha = 9.73 \times 10^2 d_p^{0.743}(1-\phi)^{-0.0982} \tag{48}$$

$$\beta = 3.68 \times 10^{-4} d_p^{-0.7523}(1-\phi)^{0.07158} \tag{49}$$

where d_p is the foam pore diameter in meters.

The heat transfer rate through the catalyst foam is determined via a Nusselt number correlation [44]:

$$Nu = h/\left(k_f S_V\right) = C_1 \phi T^3 + C_2 Re_S \tag{50}$$

where Re_S is the Reynolds number with length scale S_V^{-1}. The coefficient parameters are highly dependent on the properties and structure of the foam. For the present work, the correlation of Peng and Richardson [44] for 30-PPI α-alumina foam with 6%wt γ-alumina washcoat has been adopted ($C_1 = 6.88 \times 10^{-11}, C_2 = 0.0601$).

The heat transfer modeling in the CPOx currently incorporates radial but not axial conduction within the catalyst support. At the present level of modeling fidelity, this was deemed an acceptable simplification due to the use of equilibrium chemistry which is most strongly dependent on CPOx exit temperature (currently controlled via the CPOx assembly insulation thickness). However, if future modeling efforts incorporate finite rate chemistry, axial conduction will need to be included to achieve accurate temperature profiles within the catalyst.

There are no system level independent variables or dependent conditions for this element. However, recall that air-to-fuel ratio and segment temperatures are solved for internally to satisfy soot avoidance criteria and energy conservation, respectively.

Parameters: fuel mass flow, number of identical CPOx units, number of flow-wise segments, various physical parameters (listed below).

Table 2: CPOx reactor physical parameters.

Parameter	Value	Units
Wall		
Thickness, t_w	0.1585	cm
Thermal conductivity, k_w	29.91	W/m-K
Insulation		
Thickness, t_{ins}	0.1067	cm
Thermal conductivity, k_{ins}	0.0997	W/m-K
Catalyst		
Length, l_{cat}	2.54	cm
Cross section area, A_{cross}	0.1129	cm^2
Porosity, ϕ	0.83	
Foam pore diameter, d_p	0.021	cm

2.3.4 Fuel Cell Element

The SolidOxideFC (hereinafter referred to as 'Fuel Cell' or 'SOFC') element is used to simulate the conversion of syngas fuel into electricity in a solid oxide fuel cell.

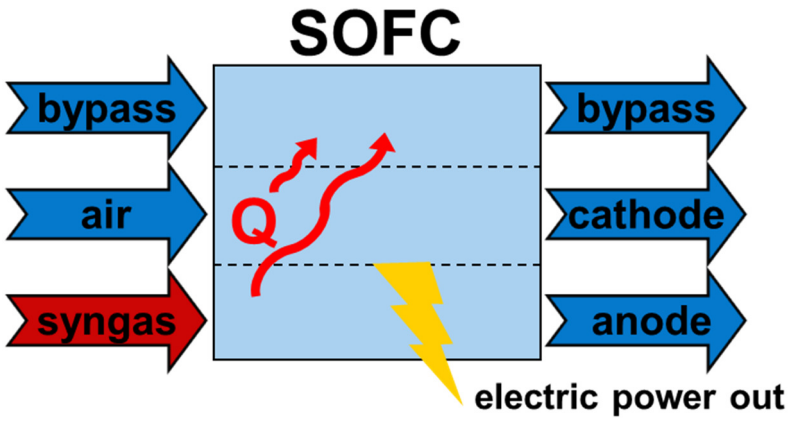

Figure 36. Solid-Oxide Fuel Cell element diagram.

Figure 37 illustrates an example of an annular arrangement of fuel cell channels integrated with a gas turbine engine (in this instance, a turbojet).

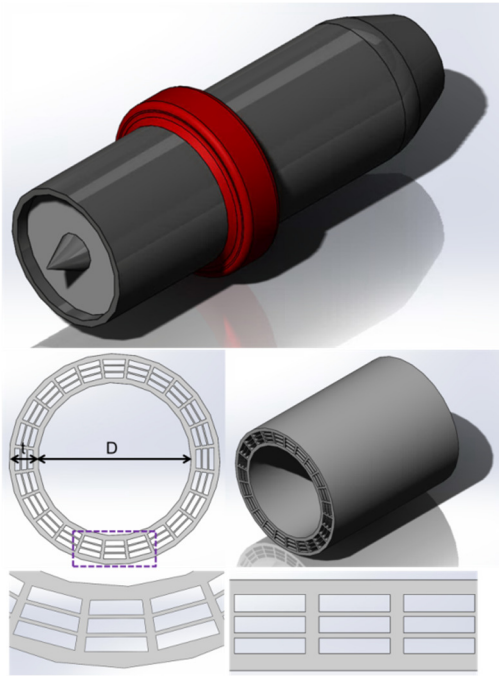

Figure 37. Annular Solid-Oxide Fuel Cell arrangement. Top: GT-SOFC integration; Middle: down channel and isometric views of SOFC; Bottom: actual and approximate channel shapes.

In the modeling, the number of radially stacked channels can greatly exceed what is shown in the illustration. The figure shows how the annular array of fuel cell channels is integrated with the engine, wrapping its circumference. Although the individual fuel cell channels will each have a small amount of curvature, in this work they are modeled as being planar. This assumption is justified by the large diameter to thickness (D/t) ratio of the annulus which results in surfaces that are nearly flat.

The NPSS element models a single planar anode/cathode pair out of many (N_{FC}) with both flows reduced proportionally $(\dot{m} = \dot{m}/N_{FC})$. The single channel anode and cathode flows are multiplied by N_{FC} (implicitly assuming all channels operate identically) at the exit.

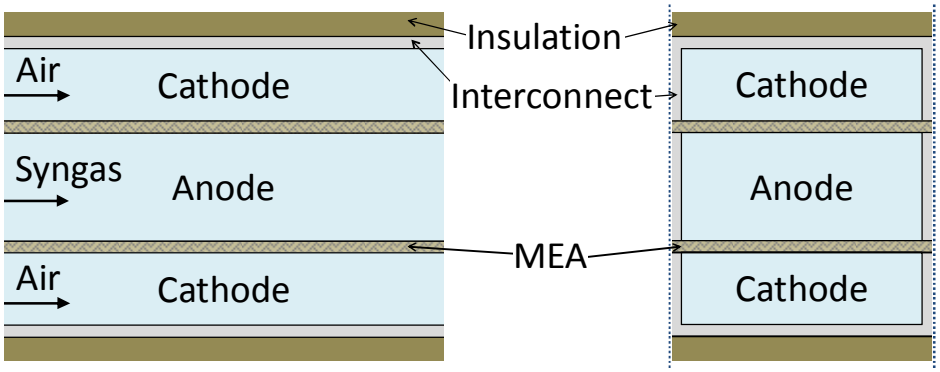

Figure 38. Illustration of the assumed SOFC geometry (cross section and down channel view).

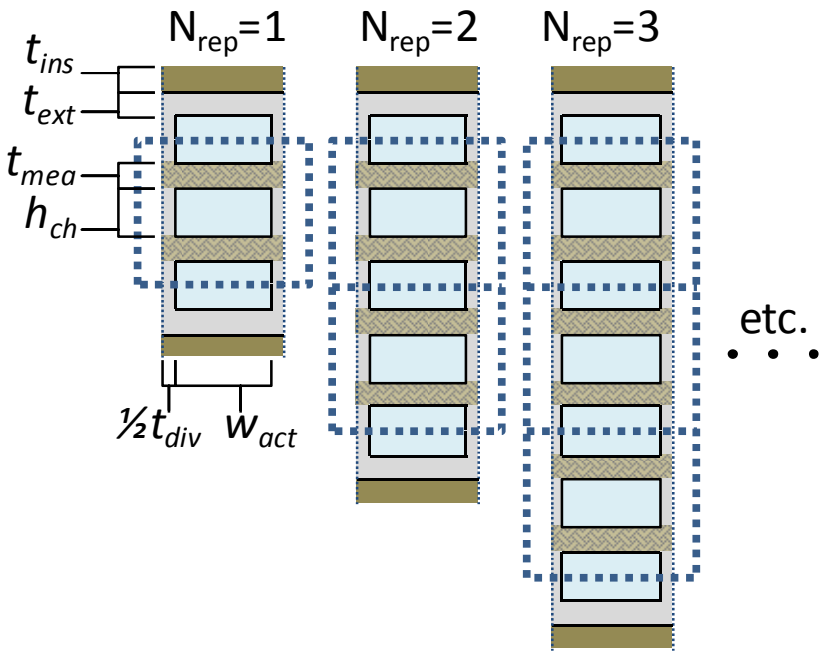

Figure 39. Illustration of the radially extendable SOFC geometry.

An illustration of the physical geometry of the circumferentially repeating fuel cell unit being simulated by the SOFC model is provided in Figure 38. At a minimum, there is one central anode channel with cathode channels on either side. The repeating units combine to form a ring around the engine, which (as explained above) can be approximated in simulations as planar because the radius of curvature is much greater than thickness of the unit.

The circumferentially repeating fuel cell unit is also expandable to include any number of radially repeating channel – membrane electrode assembly (MEA) units. This expandability is illustrated in Figure 39. All interior channels have the same height. The exterior cathode flow channels have half the airflow rate of interior channels and are 65% the height of the interior channels. The exterior channel height is chosen to result in approximately the same pressure drop as the central channels. The insulation thickness is denoted t_{ins}, exterior interconnect wall thickness is t_{ext}, vertical interconnect divider thickness is t_{div}, active/channel width is w_{act}, and channel height is h_{ch}.

The physical properties of the membrane electrode assembly used in these simulations are summarized in Table 5. Other MEA parameters used in the calculation of the ohmic and activation overpotentials are summarized in Table 6 and Table 4, respectively. The values of these parameters are drawn from the literature [90-93] and are representative of a yttria stabilized zirconia (YSZ) electrolyte, a porous nickel-YSZ (Ni-YSZ) anode, and a porous lanthanum strontium manganite-YSZ (LSM-YSZ) cathode. These are the most common material choices in SOFC MEA's [29,92,94]. In this work, an iron based metallic interconnect material is assumed. Ceramic interconnects are required for high temperature (>850^{o}C) cells [92,96], but those materials are less durable and less conductive than metals.

Like the CPOx, the solid oxide fuel cell model is divided into flow-wise segments. Electrochemistry, pressure drop, and heat loss are calculated in each segment. Conservation of mass and energy are enforced for each segment and consequently the fuel cell as a whole. The heat loss from the SOFC anode and

cathode flows is transferred to the bypass/cooling flow surrounding the SOFC units. This division is illustrated in Figure 40. In the figure, there is a single anode flow and a single cathode flow because only a single pair is modeled and all other channels are assumed to perform identically. The figure shows two bypass air flows to improve clarity of how each channel loses heat to the bypass, but in fact only one bypass flow stream is modeled in the SOFC element.

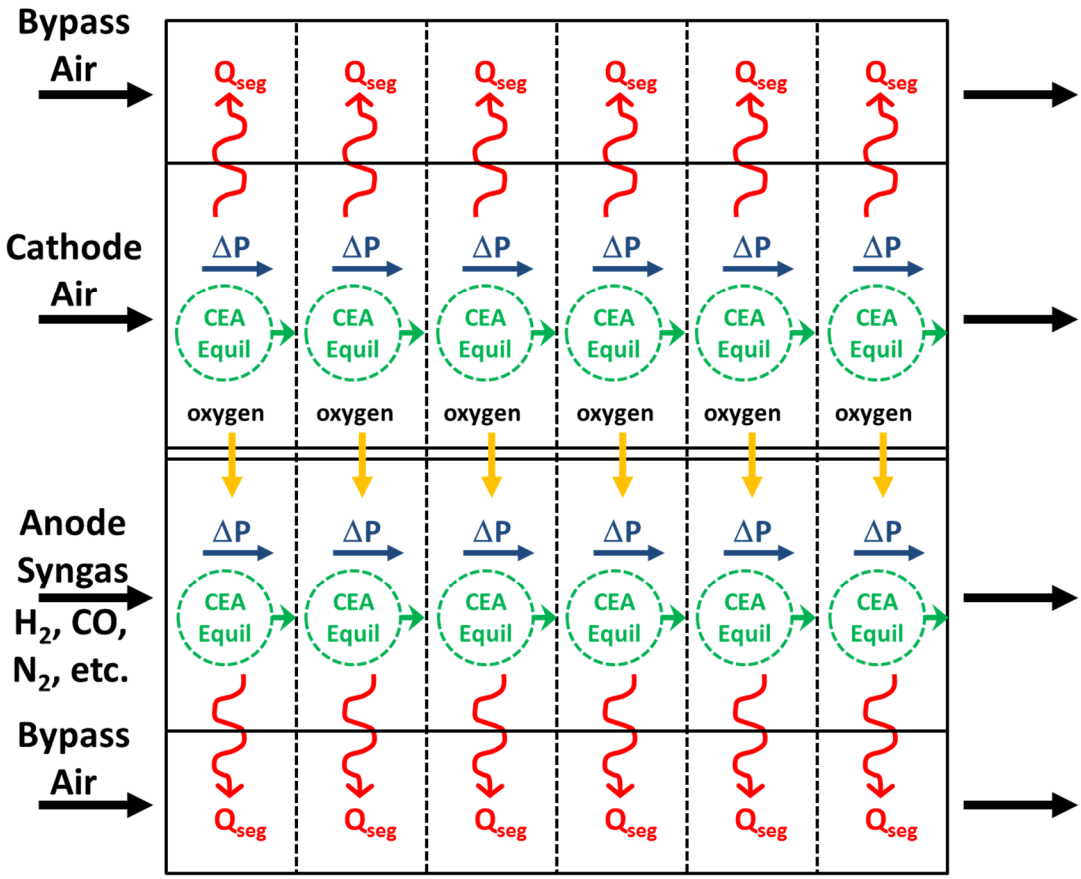

Figure 40. Illustration of the SOFC element modeling structure.

The calculation and looping procedure within the element is illustrated in Figure 41. The incoming air and syngas flows are determined by the operation of the engine and the CPOx and FC Inlet elements upstream. The pressure drop, heat loss, electrochemistry and gas phase chemistry are calculated in the segment. Note that

assuming equilibrium gas phase chemistry may tend to over-predict the rate of reforming which in practice is limited by chemical kinetics. While this is a non-trivial simplification that can lead to overestimates of fuel cell power densities, it is necessary given present limitations on computational speed.

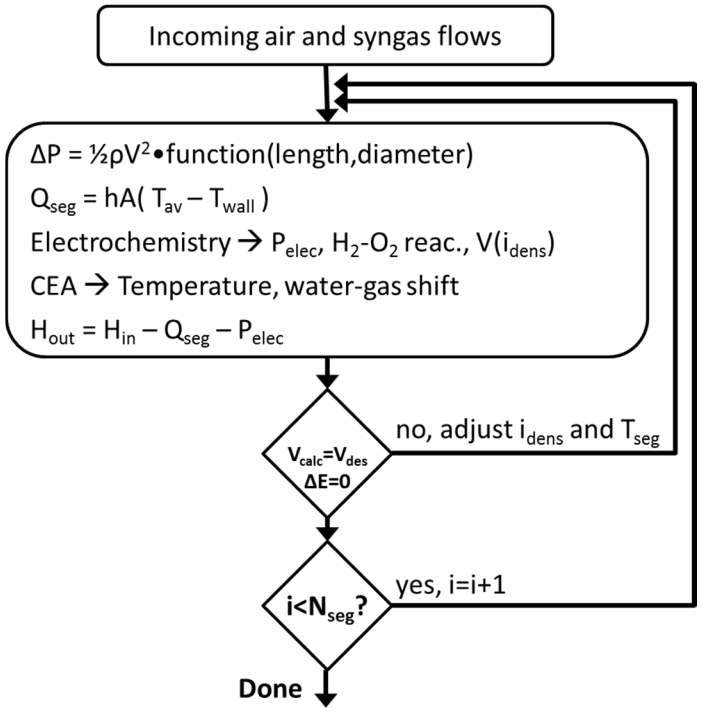

Figure 41. Illustration of SOFC element calculation and looping procedure.

The innermost loop iterates on the segment exit temperature and the segment current density until energy is conserved and cell voltage reaches the design value. Energy conservation is enforced via the following equality:

$$\dot{m}_{a,in}h_{T,a,in} + \dot{m}_{c,in}h_{T,c,in} = \dot{m}_{a,out}h_{T,a,out} + \dot{m}_{c,out}h_{T,c,out} + \dot{Q}_{loss} + \dot{W}_{elec} \qquad (51)$$

where ‘a’ and ‘c’ denote anode and cathode, ‘out’ and ‘in’ denote segment exit and entrance values, $\dot{Q}_{loss}$ is the heat loss to the bypass/cooling flow, and $\dot{W}_{elec}$ is the electric power extracted. Exit temperature and current density are both adjusted to satisfy this equality because of the interdependence of both with exit enthalpy, heat

loss, cell voltage, and electric power. The strong interdependence of relevant quantities necessitates an iterative solution as the 'guessed' segment exit temperature and current density and the calculated values are driven toward convergence. Once the energy and voltage conditions are satisfied, the segment number is incremented until the end of the channel is reached.

The SOFC model is based largely on the approach of Zhu and Kee, et al. [23,29,90,91,94,96-98]. The operating potential of the cell, V_{cell}, is determined by finding the reversible potential, V_{rev}, and subtracting off several overpotentials (denoted as η) which account for irreversible losses in the reaction process [23,29,90,91]:

$$V_{cell} = V_{rev} - \eta_{ohm} - \eta_{act,a} - \eta_{act,c} \tag{52}$$

where η_{ohm} is the ohmic overpotential, η_{act} is the activation overpotential, and the subscripts 'a' and 'c' denote the anode and cathode, respectively. The reversible cell potential is found via the Nernst equation which evaluates the change in chemical potential that results from the electrochemical reaction in the cell [23,29]:

$$V_{rev} = -\Delta G^0_{reac}/(n_e F) - [RT/(n_e F)] \ln\left(\Pi\, p_k^{\nu_k}\right) \tag{53}$$

In this expression, ΔG^0_{reac} is the standard state change in Gibbs free energy due to the electrochemical reaction, n_e is the number of electrons transferred in the reaction, p_k is the partial pressure in atmospheres of species k that participates in the reaction, and ν_k is the stoichiometric coefficient of species k. ΔG^0_{reac} is a function of the standard state chemical potentials, μ^0_k, of the participating species [23,29]. The temperature dependent values of μ^0_k, equivalent in this case to molar specific Gibbs free energy (g^0_k), are found using polynomial fits:

$$\frac{\mu_k^0}{RT} = \frac{h_k^0}{RT} - \frac{s_k^0}{R} = C_0(1 - \ln T) - C_1\frac{T}{2} - C_2\frac{T^2}{6} - C_3\frac{T^3}{12} - C_4\frac{T^4}{20} + \frac{C_5}{T} - C_6 \qquad (54)$$

The polynomial coefficients (C_0 to C_6) used in this work are found in Table 3.

Table 3: Thermodynamic polynomial fit coefficients.

Temperature:	200 – 1000 K			1000 – 6000 K		
Species:	H_2	O_2	H_2O	H_2	O_2	H_2O
C_0	2.3443311e0	3.7824564e0	4.1986406e0	3.3372792e0	3.2825378e0	3.0339925e0
C_1	7.9805208e-3	-2.9967342e-3	-2.0364341e-3	-4.9402473e-5	1.4830875e-3	2.1769180e-3
C_2	1.9478151e-5	9.8473020e-6	6.5204021e-6	4.9945678e-7	-7.5796667e-7	-1.6407252e-7
C_3	2.0157209e-8	-9.6812951e-9	-5.4879706e-9	-1.7956639e-10	2.0947056e-10	-9.7041987e-11
C_4	-7.3761176e-12	3.2437284e-12	1.7719782e-12	2.0025538e-14	-2.1671779e-14	1.6820099e-14
C_5	-9.1793517e2	-1.0639436e3	-3.0293727e4	-9.5015892e2	-1.0884577e3	-3.0004297e4
C_6	6.8301024e-1	3.6576757e0	-8.4903221e-1	-3.2050233e0	5.4532313e0	4.9667701e0

Because the flow is assumed to be in chemical equilibrium in each flow segment, V_{rev} can be computed using any global oxidation reaction [90,94]. For simplicity, the oxidation of H_2 is considered:

$$V_{rev} = -\left(\mu^0_{H_2O,a} - \mu^0_{H_2,a} - \frac{1}{2}\mu^0_{O_2,c}\right)/(2F) - [RT/(2F)]\ln\left(\frac{p_{H_2O,a}}{p_{H_2,a}p_{O_2,c}^{1/2}}\right) \qquad (55)$$

The concentration overpotential is not calculated explicitly here because V_{rev} is the reversible potential of the electrolyte membrane (not the same as the reversible potential based on the channel flow) [91]. The concentrations of species in the active region used to calculate V_{rev} are determined by considering transport of chemical species through the electrolyte using the Dusty Gas Model (DGM) [23,29,90,91,94,95,98] developed by Mason and Malinauskas [99]:

$$\sum_{l\neq k}\frac{[X_l]N_k - [X_k]N_l}{[X_T]D^e_{kl}} + \frac{N_k}{D^e_{k,Kn}} = -\nabla[X_k] - \frac{[X_k]}{D^e_{k,Kn}}\frac{B_g}{\mu}\nabla p \qquad (56)$$

where $[X_k]$ is the molar concentration of species k, $[X_T] = p/RT$ is the total molar concentration, N_k is molar flux of species k, D^e_{kl} and $D^e_{k,Kn}$ are effective binary and Knudsen diffusion coefficients, B_g is the permeability constant, and μ is the mixture

viscosity. In fuel cell electrodes, normal diffusion and Knudsen diffusion are often comparable in magnitude so it is important to consider both. Effective diffusion coefficients are modified by ϕ/τ, the porosity-to-tortuosity ratio:

$$D_{kl}^{e} = \frac{\phi}{\tau} D_{kl} \tag{57}$$

$$D_{k,Kn}^{e} = \frac{4}{3} r_p \frac{\phi}{\tau} \sqrt{8RT/(\pi W_k)} \tag{58}$$

where r_p is the average pore radius and W_k is the molecular weight of species *k*. The Kozeny-Carman relationship [95,100] is used to describe the permeability of porous media formed by closely packed spheres of constant diameter:

$$B_g = \phi^3 d_p^2 / [72\tau(1-\phi)^2] \tag{59}$$

where d_p is the diameter of the packed spheres. Use of this expression is an idealization of porous electrode structure [95].

Summing the DGM equation over all species causes the binary diffusion term to vanish exactly, allowing the pressure gradient to be written [95]:

$$\nabla p = -\frac{\sum_k N_k / D_{k,Kn}^{e}}{(1/RT) + (B_g/\mu)\sum_k [X_k]/D_{k,Kn}^{e}} \tag{60}$$

Re-writing molar concentrations as mole fractions ($[X_k] = p\, x_k/RT$) and applying the simplest numerical approximation of the gradient (first order forward difference) gives the following expression for the pressure gradient:

$$\frac{p_+ - p_-}{\delta} \approx -\frac{(RT)\sum_k N_k / D_{k,Kn}^{e}}{\left[1 + p_-(B_g/\mu_-)\sum_k x_{k,-}/D_{k,Kn}^{e}\right]} \tag{61}$$

In this expression, '+' denotes properties evaluated deeper into the electrode. Once the pressure gradient is known, a similar approximation of the DGM equation allows

the calculation of each species' concentration gradient. Rewriting in terms of mole fractions and applying the simple numerical approximation:

$$\frac{x_{k,+} - x_{k,-}}{\delta} \approx -\frac{RT}{p_-}\left(\sum_{l \neq k} \frac{x_{l,-}N_k - x_{k,-}N_l}{D_{kl}^e} + \frac{N_k}{D_{k,Kn}^e}\right) - \left(\frac{1}{p_-} + \frac{B_g}{D_{k,Kn}^e \mu_-}\right) x_{k,-} \nabla p \tag{62}$$

The electrode is also divided into segments. Some experimentation is necessary to determine the number of segments (N_{FC}) required to resolve the diffusion profiles.

The ohmic overpotential, η_{ohm}, represents the combined loss from driving charge through the electrodes and electrolyte in the form of Ohm's law [23,29,95]:

$$\eta_{ohm} = i_e R_{tot} = i_e (R_{el} + R_a + R_c) \tag{63}$$

where R_{el}, R_a, and R_c are resistance terms of the electrolyte, anode, and cathode, respectively. The total resistance is usually dominated by the electrolyte term [23,29]. The temperature dependent conductivities can be expressed in an Arrhenius exponential form [90,91,94,95,101]. Based on these relationships, the ohmic overpotential can be written:

$$\eta_{ohm} = i_e \left[\frac{\delta_{el}}{A_{el}^i T^{-1} \exp\left(-E_{el}^i/RT\right)} + \frac{\delta_a}{A_a^e T^{-1} \exp(-E_a^e/RT)} + \frac{\delta_c}{A_c^e T^{-1} \exp(-E_c^e/RT)}\right] \tag{64}$$

where δ is the thickness, A is an empirical pre-exponential factor, and E is the activation energy. Subscripts '*a*', '*c*', and '*el*' denote the anode, cathode, and electrolyte. Superscripts '*i*' and '*e*' denote ion or electrical conductivity.

The activation overpotentials of the anode and cathode, $\eta_{act,a}$ and $\eta_{act,c}$, account for the energy needed to overcome the activation energy barrier of charge transfer

reactions at the electrode-electrolyte interfaces [23,29,91]. The relationship is described by the Butler-Volmer equation [23,29,90,91,95,98]:

$$i_e = i_0 \left[\exp\left(\frac{\alpha_f n_e^{BV} F \eta_{act}}{RT} \right) - \exp\left(-\frac{\alpha_r n_e^{BV} F \eta_{act}}{RT} \right) \right] \tag{65}$$

where i_0 is the exchange current density, n_e^{BV} is the number of electrons in the charge transfer reaction (typically $n_e^{BV} = 1$) [95], and α_f and α_r are the forward/anodic and reverse/cathodic asymmetric factors.

The Butler-Volmer equation can be written specifically for the SOFC anode as [90,91]:

$$i_e = i_{0,\mathrm{a}} \left[\exp\left(\frac{\alpha_{f,a} F \eta_{act,a}}{RT} \right) - \exp\left(-\frac{\alpha_{r,a} F \eta_{act,a}}{RT} \right) \right] \tag{66}$$

$$i_{0,a} = i^*_{ref,H_2} \exp\left[-\frac{E_{H_2}}{R} \left(\frac{1}{T} - \frac{1}{T_{ref}} \right) \right] \frac{\left(p_{H_2} / p^*_{H_2} \right)^{1/4} \left(p_{H_2O} \right)^{3/4}}{1 + \left(p_{H_2} / p^*_{H_2} \right)^{1/2}} \tag{67}$$

$$p^*_{H_2} = \left(A_{P_{H_2}} \Gamma^2 / \gamma_0 \right) \sqrt{2\pi R T W_{H_2}} \exp\left(-E_{P_{H_2}} / RT \right) \tag{68}$$

where i^*_{ref,H_2} is an empirical factor, E_{H_2} and $E_{P_{H2}}$ are activation energies, $p^*_{H_2}$ is a function of hydrogen adsorption/desorption, $A_{P_{H2}}$ is a pre-exponential factor, Γ is the surface site density, and γ_0 is the sticking probability.

The Butler-Volmer equation can be written specifically for the SOFC cathode as [90,91]:

$$i_e = i_{0,\mathrm{c}} \left[\exp\left(\frac{\alpha_{f,c} F \eta_{act,c}}{RT} \right) - \exp\left(-\frac{\alpha_{r,c} F \eta_{act,c}}{RT} \right) \right] \tag{69}$$

$$i_{0,c} = i^*_{ref,O_2} \exp\left[-\frac{E_{O_2}}{R} \left(\frac{1}{T} - \frac{1}{T_{ref}} \right) \right] \frac{\left(p_{O_2} / p^*_{\mathrm{O}_2} \right)^{1/4}}{1 + \left(p_{O_2} / p^*_{\mathrm{O}_2} \right)^{1/2}} \tag{70}$$

$$p^*_{\mathrm{O}_2} = A_{P_{O2}} \exp\left(-E_{P_{O2}} / RT \right) \tag{71}$$

where i^*_{ref,O_2} is an empirical factor, E_{O_2} and $E_{P_{O2}}$ are activation energies, $p^*_{O_2}$ is a function of oxygen adsorption/desorption, and $A_{P_{O2}}$ is a pre-exponential factor.

For both the anode and the cathode, the activation overpotential is solved for iteratively because there is no closed form solution to the Butler-Volmer equation. The value of the overpotentials are adjusted until the calculated current densities from the equations (Eqs. (66) and (69) for the anode and cathode, respectively) are equal to the specified current density of the segment.

Mass conservation in the channels is enforced by calculating the oxygen transport across the cell based on the current density [95]:

$$\dot{m}_{O_2} = -\frac{1}{2} A_{seg} W_{O_2} [i_e/(n_e F)] \tag{72}$$

where A_{seg} is the electrolyte area of the channel segment. The channel flow is assumed to always be at equilibrium. This approach allows the model to account for complex chemistry involving H_2, H_2O, CH_4, CO, CO_2, etc. without involving complicated, multi-step chemical kinetics. This is not a trivial assumption (compared to the CPOx where a catalyst is present to enhance chemical kinetic rates), but it does represent the water-gas shift reaction that is expected to be active in the anode [23,29] and which drives the composition toward equilibrium. In each channel segment, the oxygen transport is subtracted from the cathode air flow (which has a negligible effect on equilibrium). Similarly, the oxygen is added to the anode flow resulting in production of equilibrium reaction products and heat release. The flux of species through the electrodes is found by taking the difference of the inlet and outlet compositions of a segment and assuming that the change must result from flux to/from the surface:

$$N_{k,surf} = \left(\dot{m}_{k,out} - \dot{m}_{k,in}\right)/\left(W_k A_{seg}\right) \tag{73}$$

where $\dot{m}_k$ is the channel mass flow of species k.

The percent oxidation (or percent utilization) of the fuel stream is defined as the ratio of oxygen present in the stream to the total amount necessary to fully oxidize the fuel to H_2O and CO_2. This is calculated by summing the oxygen atoms in the stream then dividing by the sum of two oxygen atoms per carbon atom and one half oxygen atom per hydrogen atom in the fuel:

$$\%Ox = \sum\left(\dot{m}_k n_{O,k}/W_k\right)/\sum\left(\dot{m}_k n^*_{O,k}/W_k\right) \tag{74}$$

where $n_{O,k}$ is the number of oxygen atoms present in species k, and $n^*_{O,k}$ is the number of oxygen atoms needed to fully oxidize species k.

The heat and pressure loss calculations are based largely on the work of Muzychka and Yovanovich [102,103] on non-circular ducts. Pressure drop is modeled using a general correlation [103] for fRe in non-circular ducts. It combines a 'short duct asymptote' and a 'long duct asymptote' into a general expression that is a function of non-dimensional duct length $L^+ = L/\sqrt{A}Re_{\sqrt{A}}$ and the duct aspect ratio ϵ. The short duct asymptote expression for fRe is valid as $L^+ \to 0$ and is independent of duct geometry [103]. The long duct asymptote expression is valid as $L^+ \to \infty$ and where the aspect ratio of the duct is $0 < \epsilon \leq 1$. Muzychka and Yovanovich found better correlations between different duct shapes by non-dimensionalizing by $\sqrt{A}$ as opposed to the more commonly used hydraulic diameter D_h. The general expression is derived by combining the asymptotic limits via the method of Churchill and Usagi [104]. The resulting expression is [103]:

$$fRe_{\sqrt{A}} = \left[\left\{3.44/\sqrt{L^+}\right\}^2 + \left\{12/\left(\sqrt{\epsilon}(1+\epsilon)\left[1 - \frac{192\epsilon}{\pi^5}\tanh\left(\frac{\pi}{2\epsilon}\right)\right]\right)\right\}^2\right]^{1/2} \quad (75)$$

The heat transfer rate from non-circular ducts was similarly modeled by Muzychka and Yovanovich [102]. That work identifies three distinct flow regimes in the simultaneously developing flow problem: fully developed flow ($L \gg L_h, L_t$), Graetz flow ($L \gg L_h, L \ll L_t$), and laminar boundary flow ($L \ll L_h, L_t$). The proposed general model is derived from the combination of these results. The average Nusselt number for uniform temperature walls is given by:

$$Nu_{\sqrt{A}} =$$

$$\left[\left(\frac{C_4}{\sqrt{z^*}}\frac{0.564}{\left[1+\left(1.664Pr^{1/6}\right)^{9/2}\right]^{2/9}}\right)^m + \left(\left\{C_2C_3\left(\frac{fRe_{\sqrt{A}}}{z^*}\right)^{1/3}\right\}^5 + \left\{C_1\left(\frac{fRe_{\sqrt{A}}}{8\sqrt{\pi}\epsilon^\gamma}\right)\right\}^5\right)^{m/5}\right]^{1/m} \quad (76)$$

where $C_1 = 3.24$ and $C_3 = 0.409$ for the uniform wall temperature condition, $C_2 = 1.5$ and $C_4 = 2$ when the average (as opposed to local) Nu is desired, and $\gamma = 0.1$ for rectangular ducts. The parameter m is a function of Prandtl number, $m = 2.27 + 1.65Pr^{1/3}$ [102]. The non-dimensional length parameter is $z^* = \left(z/\sqrt{A}\right)/\left(Re_{\sqrt{A}}Pr\right)$ [102].

Heat losses are calculated by solving a discretized finite volume problem over one quarter of the fuel cell repeating unit as illustrated in Figure 42. The interior boundaries of the defined quadrant are assumed adiabatic due to symmetry. Therefore all heat loss occurs through the insulated surface. The number and aspect ratio of the cells are inputs into the model. The flow channel temperatures are equal to the local cell average temperature.

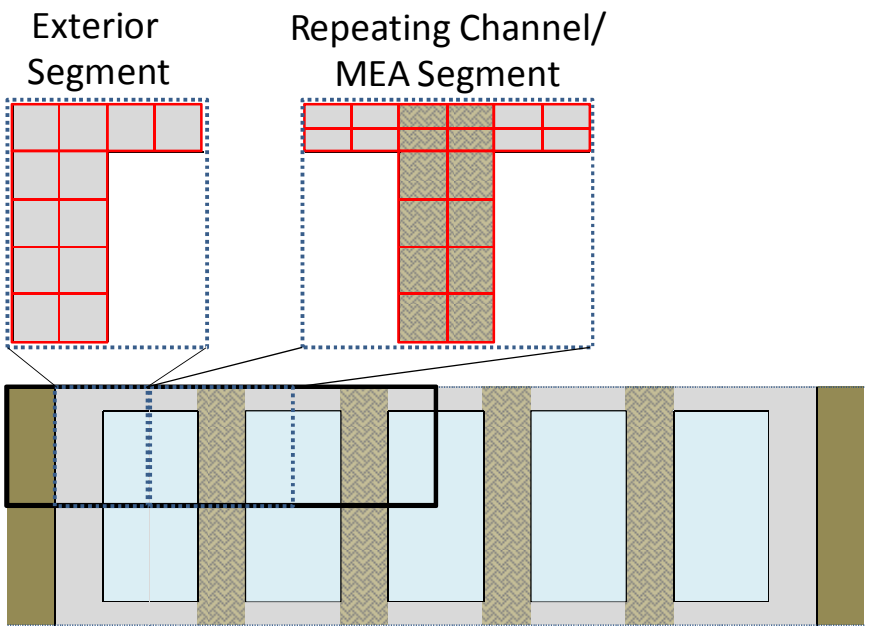

Figure 42. Heat transfer discretization of the fuel cell.

Heat transfer between cells occurs by conduction [105] and can be written between cells '1' and '2' (q'_{12}) as:

$$q'_{12} = \frac{k}{\delta_{12}} L_{12}(T_1 - T_2) \tag{77}$$

where k is the thermal conductivity of the material, δ is the distance between cell centers, and L is the length of the border between the cells. Heat transfer from the channel flow to the surface occurs by forced convection [105] using heat transfer coefficients based on the Nusselt number correlation above. Thus, the heat transfer between a channel 'c' and a surface cell '1' (q'_{c1}) is given by:

$$q'_{c1} = hL_{c1}(T_c - T_1) \tag{78}$$

where h is the convective heat transfer coefficient.

Further details of the finite volume calculation can be found in Appendix D.

The temperature distribution in the fuel cell interconnect and MEA structure is determined by iteratively calculating a new temperature for each cell by balancing the

heat transfers from the surrounding cells based on the previous iteration's temperature estimates. Repeated sweeps are performed until the heat loss estimate reaches a converged value.

There are no system level independent variables or dependent conditions for this element. However, recall that segment temperatures and activation overpotentials (both anode and cathode) are solved for internally to satisfy soot avoidance criteria and energy conservation, respectively. The heat transfer calculations also use an iterative process.

Parameters: fuel cell global air-to-fuel ratio, design operating voltage, number of identical SOFC units, number of radially stacked channels per unit, number of electrode segments for diffusion calculations, various physical and electrochemical parameters (listed below).

Table 4: Activation overpotential parameters [90,91].

Parameter	Value	Units
Anode		
Asymmetric factors, $\alpha_{f,a}, \alpha_{r,a}$	1.5, 0.5	
Exchange current factor, i^*_{ref,H_2}	8.5	A/cm^2
Apparent activation energy, E_{H_2}	120	kJ/mol
Reference temperature, T_{ref}	1073	K
$p^*_{H_2}$ pre-factor, $A_{P_{H2}}$	5.59×10^{15}	m^2/mol-s
$p^*_{H_2}$ activation energy, $E_{P_{H2}}$	88.12	kJ/mol
Surface site density, Γ	2.6×10^{-5}	mol/m^2
Sticking probability, γ_0	0.01	
Cathode		
Asymmetric factors, $\alpha_{f,c}, \alpha_{r,c}$	1.5, 0.5	
Exchange current factor, i^*_{ref,O_2}	2.4	A/cm^2
Apparent activation energy, E_{O_2}	130	kJ/mol
Reference temperature, T_{ref}	1073	K
$p^*_{O_2}$ pre-factor, $A_{P_{O2}}$	4.9×10^8	atm
$p^*_{O_2}$ activation energy, $E_{P_{O2}}$	200	kJ/mol

Table 5: Fuel cell material physical parameters [90-93].

Parameter	Value	Units
Anode		
Thickness, δ_a	900	μm
Porosity, ϕ	0.35	
Tortuosity, τ	4.8	
Average pore radius, r_p	0.2	μm
Average particle diameter, d_p	1.0	μm
Bulk density, ρ_a	4.8	g/cm^3
Thermal conductivity, k_a	11.0	W/m-K
Cathode		
Thickness, δ_c	50	μm
Porosity, ϕ	0.35	
Tortuosity, τ	4	
Average pore radius, r_p	0.25	μm
Average particle diameter, d_p	1.25	μm
Bulk density, ρ_c	4.6	g/cm^3
Thermal conductivity, k_c	6.23	W/m-K
Electrolyte		
Thickness, δ_{el}	20	μm
Bulk density, ρ_{el}	6.0	g/cm^3
Thermal conductivity, k_{el}	2.7	W/m-K
Interconnect		
Bulk density, ρ_{el}	7.8	g/cm^3
Thermal conductivity, k_{el}	30.0	W/m-K
Insulation		
Bulk density, ρ_{el}	0.25	g/cm^3
Thermal conductivity, k_{el}	0.1	W/m-K

Table 6: Ohmic overpotential parameters [90].

Parameter	Value	Units
Anode		
Conductivity pre-factor, A_a^e	9.5×10^5	K/cm-Ω
Activation energy, E_a^e	9.561	kJ/mol
Cathode		
Conductivity pre-factor, A_c^e	4.2×10^5	K/cm-Ω
Activation energy, E_c^e	9.977	kJ/mol
Electrolyte		
Conductivity pre-factor, A_{el}^i	3.6×10^5	K/cm-Ω
Activation energy, E_{el}^i	80	kJ/mol

2.3.5 Fuel Cell Inlet Element

The InletFC (hereinafter referred to as 'Fuel Cell Inlet') element is used to simulate heat transfer between the anode and cathode flow channels in an inlet region immediately upstream of the fuel cell. Because the flows are divided into narrow, thin-walled channels, the inlet essentially functions as a co-flow heat exchanger.

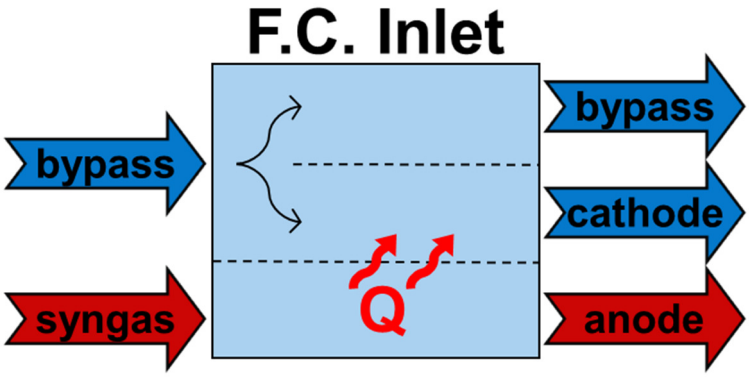

Figure 43. Fuel Cell Inlet element diagram.

Internally, the FC Inlet element separates a portion of the incoming bypass air into the cathode channel flow path. The element models a single anode/cathode pair out of many (N_{FC}) with both flows reduced proportionally ($\dot{m} = \dot{m}/N_{FC}$). Heat transfer occurs from the anode flow to the cathode flow. The single channel anode and cathode flows are multiplied by N_{FC} (implicitly assuming all channels operate identically) at the exit.

The FC Inlet element is only used in conjunction with an SOFC element. The pressure drop is calculated using a general correlation for non-circular ducts developed by Muzychka and Yovanovich [103]. This is the same correlation described in detail in the SOFC element section above. The heat transfer rate is similarly calculated from a correlation for non-circular ducts developed by Muzychka and Yovanovich [102]. The convective heat transfer coefficient is determined using the Nusselt number correlation presented in their work. The two correlations (for pressure drop and heat transfer) are restated below for convenience:

$$fRe_{\sqrt{A}} = \left[\left\{3.44/\sqrt{L^+}\right\}^2 + \left\{12/\left(\sqrt{\epsilon}(1+\epsilon)\left[1 - \frac{192\epsilon}{\pi^5}\tanh\left(\frac{\pi}{2\epsilon}\right)\right]\right)\right\}^2\right]^{1/2} \quad (79)$$

$$Nu_{\sqrt{A}} =$$

$$\left[\left(\frac{C_4}{\sqrt{z^*}}\frac{0.564}{\left[1+\left(1.664Pr^{1/6}\right)^{9/2}\right]^{2/9}}\right)^m + \left(\left\{C_2C_3\left(\frac{fRe_{\sqrt{A}}}{z^*}\right)^{1/3}\right\}^5 + \left\{C_1\left(\frac{fRe_{\sqrt{A}}}{8\sqrt{\pi}\epsilon^\gamma}\right)\right\}^5\right)^{m/5}\right]^{1/m} \quad (80)$$

Unlike in the SOFC element, no finite volume heat transfer calculation is performed in the FC Inlet element. Because of the similarity between the inlet structure and a heat exchanger, established heat exchanger analysis methods are employed. Specifically, the *effectiveness-NTU* method as described by Incropera et al. [105] is used. The dimensionless parameter 'number of transfer units' (NTU) is used to calculate a heat exchanger effectiveness,ε, which in turn is used to calculate a heat transfer, q. The heat transfer can be generally expressed as [105]:

$$q = \varepsilon C_{min}\left(T_{h,in} - T_{c,in}\right) \quad (81)$$

where $T_{h,in}$ and $T_{c,in}$ are the hot and cold side inlet temperatures and C_{min} is the lower heat capacity of the hot and cold streams. The effectiveness of a co-flow heat exchanger is given as [105]:

$$\varepsilon = \frac{1 - \exp[-\mathrm{NTU}(1 + C_{min}/C_{max})]}{1 + C_{min}/C_{max}} \quad (82)$$

where C_{max} is the higher heat capacity of the hot and cold streams. The non-dimensional NTU is defined as [105]:

$$NTU = UA/C_{min} \quad (83)$$

where A is the heat transfer surface area and U is the overall heat transfer coefficient. The overall heat transfer coefficient for the geometry of interest (Figure 44) is given as [105]:

$$U = \frac{1}{\frac{1}{h_h} + \frac{t_w}{k_w} + \frac{1}{h_c}} \tag{84}$$

where h_h and h_c are the convective heat transfer coefficients for the hot and cold streams, t_w is the wall thickness, and k_w is the wall thermal conductivity. These four equations can then be combined into one expression for the heat transfer:

$$q = (T_{h,in} - T_{c,in}) \frac{1 - \exp\left[-A\left(\frac{1}{h_h} + \frac{t_w}{k_w} + \frac{1}{h_c}\right)^{-1}\left(\frac{1}{\dot{m}_h C_{p,h}} + \frac{1}{\dot{m}_c C_{p,c}}\right)\right]}{\frac{1}{\dot{m}_h C_{p,h}} + \frac{1}{\dot{m}_c C_{p,c}}} \tag{85}$$

where $C = \dot{m}C_p$ has been substituted, $\dot{m}$ is mass flow rate, and C_p is the specific heat capacity of the flow. The distinction between C_{min} and C_{max} is unimportant in this expression because the terms are summed.

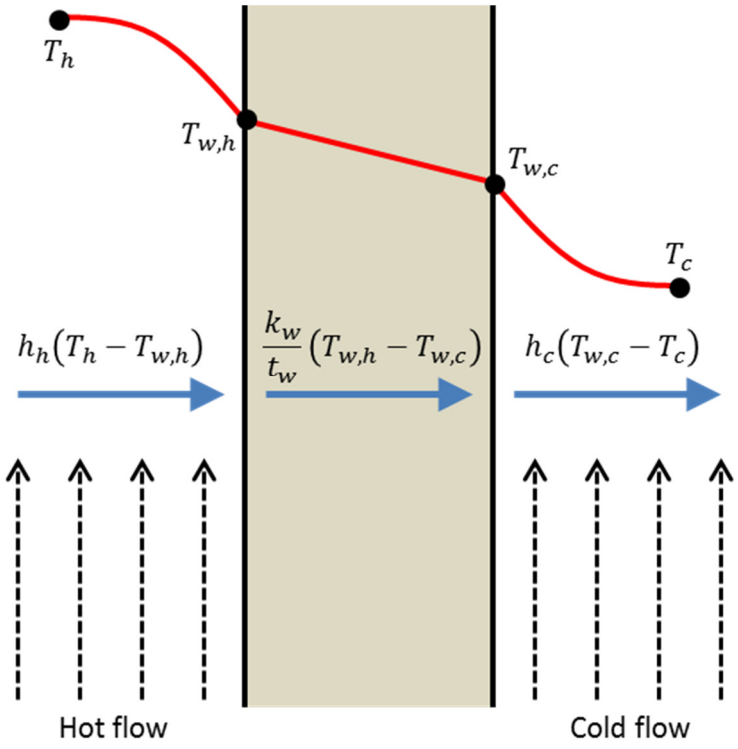

Figure 44. Illustration of temperature profiles in the FC Inlet element.

Because the expression for heat transfer assumes constant specific heats, it is subject to error when temperatures (and therefore flow properties) vary significantly

over the length of the channels. To address this, the inlet channel is divided into a number of flow-wise segments wherein flow properties are recomputed to improve accuracy.

There are no independent variables or dependent conditions for this element.

Parameters: number of flow-wise segments and several physical parameters listed below.

Table 7: Fuel cell inlet physical parameters.

Parameter	Value	Units
Dividing wall		
Thickness, t_w	0.5	mm
Thermal conductivity, k_w	30.0	W/m-K
Channels		
Length, l_{ch}	10.0	mm
Width , w_{ch}	5.0	mm
Height, h_{ch}	2.0	mm

Chapter 3: System Modeling

3.1 System Modeling in NPSS

The various standard and developed NPSS elements described in the previous chapter can be linked to generate models of any number of systems. Recall from the discussion in Section "2.1 Overview of Modeling in NPSS" that the Fluid Output Port of any component is easily linked to a Fluid Input Port using the NPSS 'linkPorts' command. Bleed, Fuel, and Shaft Ports are linked similarly. These Ports are data structures within a component which store and pass information and perform calculations. Fluid and Bleed Ports fully determine a flow state (stagnation properties and, optionally, static properties). The data structure defines mass flow temperature, pressure, enthalpy, entropy, molecular weight, etc. at the given flow location.

Recall from Figure 12 the illustration of a simple solver setup with three independent variables (air mass flow, fuel mass flow, and shaft speed (N_{shaft})) and three dependent conditions (turbine inlet temperature (TIT=target), thrust (F_n=target), and net shaft torque (ΣT=0)). The model runs and sends information about the dependents to the solver, and the solver calculates errors in the dependent conditions and makes adjustments to the independent variables to drive the error terms toward zero. It is critical when setting up a model that the solver be defined properly. Like any system to be solved, the number of unknowns (independent variables) must match the number of equations (dependent conditions). It is also essential that each dependent condition is in fact dependent on at least one independent variable. In the example, there are three dependent conditions and each is a function to some degree

on each of the three independent variables. Therefore the solver is well defined. It is of course also important to insure that the dependent conditions accurately define the desired operating state of the modeled system.

Because NPSS supports a number of thermodynamics packages, each system model must declare which package is to be used. Typically the same package is used for an entire model although it is possible to use different thermodynamics packages for different elements. In all of the system modeling presented here, the 'CEA' package is used. It performs a chemical equilibrium calculation at each flow location via an implementation of NASA's CEA code. For more information on CEA and its implementation in NPSS, see Section "1.5.4 Implementation of CEA" and Refs. [69] and [70]. The calculation by default considers all chemical species in the CEA database, but the number of species is easily reduced by supplying CEA with a modified database file. The full database contains over 2000 species which can cause calculations to be relatively slow. In this work, the database is reduced to 246 species by considering only species composed of hydrogen, nitrogen, carbon, oxygen, and argon. The computation speed is noticeably improved by using the reduced database with no loss in accuracy because only species that cannot be present are neglected. For only the SOFC element (by far the most computationally intensive), the database is further reduced to 138 species by eliminating condensed species and hydrocarbon chains longer than 3 carbons. The reduced lists of species are contained in Appendix E.

In this work, NPSS models have been assembled for three different gas turbine engine types (described in detail in the following sections). Models have also been

developed for the corresponding GT-SOFC hybrids. The primary aim of the modeling is to analyze the effects of the SOFC and its integration on the base GT system and how that translates to system level performance.

3.2 Gas Turbine Models

3.2.1 Overview

All of the gas turbine engine models developed and presented in this work are essentially 'rubber engines'. This means that the engines are 'stretched' to whatever size (or power level) is necessary for the desired study being performed. This allows great freedom in studying a wide variety of conditions, but is ultimately limited in that the modeled engines do not directly correspond to any particular engine currently available. The alternative approach would be to perform a 'fixed engine' analysis where a specific engine of a particular size and power level is assumed for all studies. This has the advantage of corresponding to an existing engine, but the disadvantage of much less flexibility. The 'rubber engine' approach is more appropriate for this study to allow the desired level of flexibility.

3.2.2 Turbojet Engine

A single spool (i.e., single shaft) turbojet engine is probably the simplest gas turbine configuration. As the earliest practical form of gas turbine engine, the turbojet was once widely used on aircraft but due to its relative inefficiency it has been largely supplanted by turboprop and turbofan engines. In recent years, the primary use of turbojets has been on cruise missiles.

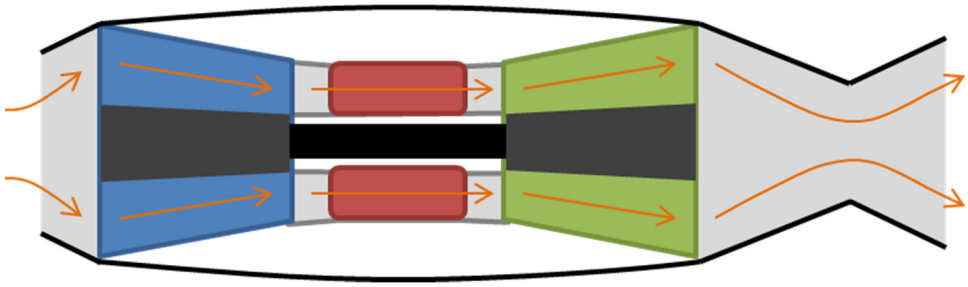

Figure 45. Illustration of (single spool) turbojet.

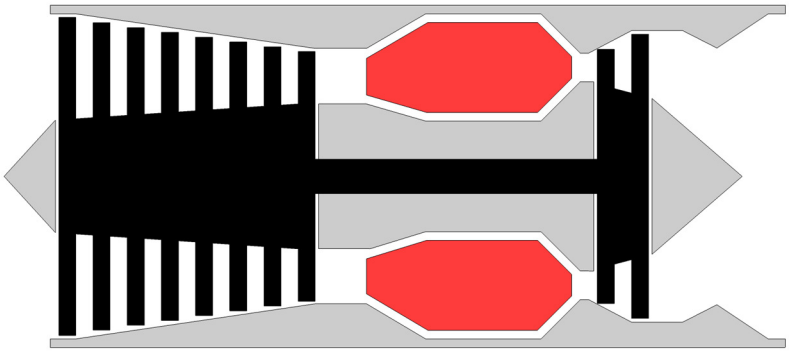

Figure 46. Illustration of (single spool) turbojet.

As illustrated in Figure 45, the turbojet engine consists of an inlet, a compressor (blue) and turbine (green) sharing a common shaft (black), a burner/combustor (red) between the compressor and turbine, and a nozzle to accelerate the exhaust. Internally, energy is added to the flow via combustion in the burner, and power extracted from the flow by the turbine drives the compressor via the common shaft. Thrust is produced primarily by the difference in flow momentum between the exhaust and inlet flows. Figure 46 presents an alternate illustration of a single spool turbojet. This second figure more accurately represents the geometry of the multistage axial compressor and turbine on a common shaft.

The NPSS model of the single spool turbojet is illustrated in Figure 47. Boxes represent flow elements, blue arrows represent flow port connections, dashed red

arrows represent bleed port connections, and dashed black lines represent shaft port connections.

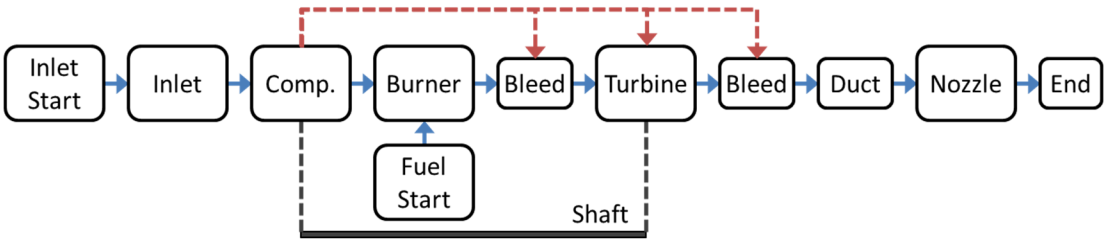

Figure 47. NPSS model schematic of turbojet.

The air flow is initiated by the Inlet Start element which communicates with an Ambient element (not pictured) to set the temperature, pressure, and speed of the incoming air. The Inlet element determines the total flow properties after an inlet pressure recovery loss is imposed. The Compressor (shown as 'Comp.') element calculates the pressure and temperature increase using a performance map, as described in the previous chapter, that relates pressure ratio and isentropic efficiency to corrected mass flow and shaft speed. Shaft speed and torque information are communicated between the Compressor and Shaft elements. The Compressor also facilitates the passage of bleed flows to downstream Bleed elements and the Turbine element. The Fuel Start element initiates a flow of fuel to the Burner element which calculates the chemistry and heat release of the fuel/air reaction. The Turbine element calculates a pressure and temperature decrease based on its performance map as described in the previous chapter. Shaft speed and torque information are communicated between the Turbine and Shaft elements. The Duct element imposes a pressure drop on the flow representing pressure losses between the turbine and nozzle. The Nozzle element calculates the acceleration of the flow assuming a

converging-diverging nozzle that is pressure matched at the nozzle exit to the ambient flow. The Flow End (shown as 'End') element simply terminates the flow.

Appendix F provides more detailed information about the model including the order of execution of elements, the list of independent variables, and the list of dependent conditions in the model.

3.2.3 Low Bypass Ratio Turbofan

A dual spool (i.e., two concentric shafts) combined exhaust turbofan engine is a more advanced gas turbine engine than the turbojet. Though more complex, the use of multiple shafts capable of rotating at different speeds allows turbomachinery to operate more efficiently by allowing low pressure and high pressure compressors (or turbines) to operate at speeds more suitable to their different operating conditions. A secondary flow that bypasses the engine core also leads to more efficient operation based on the principle that accelerating more flow by a smaller amount is inherently more efficient. The primary application of these engines (commonly referred to as low bypass ratio turbofans) is in military fighter aircraft where high thrust-to-weight, compact design, and compatibility with afterburners and supersonic flight are equally as important as efficiency.

As illustrated in Figure 48, the low bypass ratio turbofan engine consists of an inlet, a low pressure compressor (LPC, dark blue) and low pressure turbine (LPT, dark green) sharing the common inner shaft (gray), a high pressure compressor (HPC, light blue) and high pressure turbine (HPT, light green) sharing the common outer shaft (black), a burner/combustor (red) between the HPC and HPT, and a nozzle to accelerate the exhaust. The flow through the LPC is divided between a core flow that

passes to the HPC and a bypass flow that passes through a bypass duct directly to downstream of the LPT where the flow streams are recombined ahead of the nozzle. As in the turbojet, energy is added to the flow via combustion in the burner, and power extracted from the flow by the turbines drives the respective compressors via their common shafts. Thrust is produced primarily by the difference in flow momentum between the exhaust and inlet flows. Figure 49 presents an alternate illustration of a dual spool combined exhaust turbofan. This second figure more accurately represents the geometry of the multistage axial compressors and turbines sharing separate, concentric shafts.

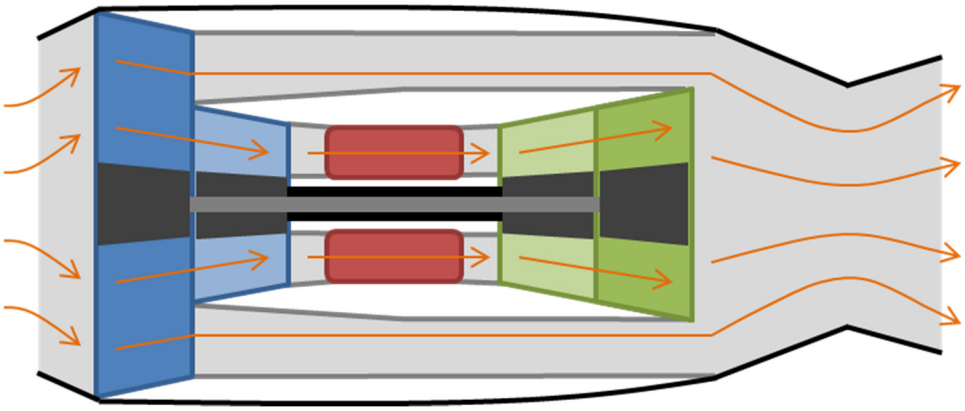

Figure 48. Illustration of low BPR (dual spool combined exhaust) turbofan.

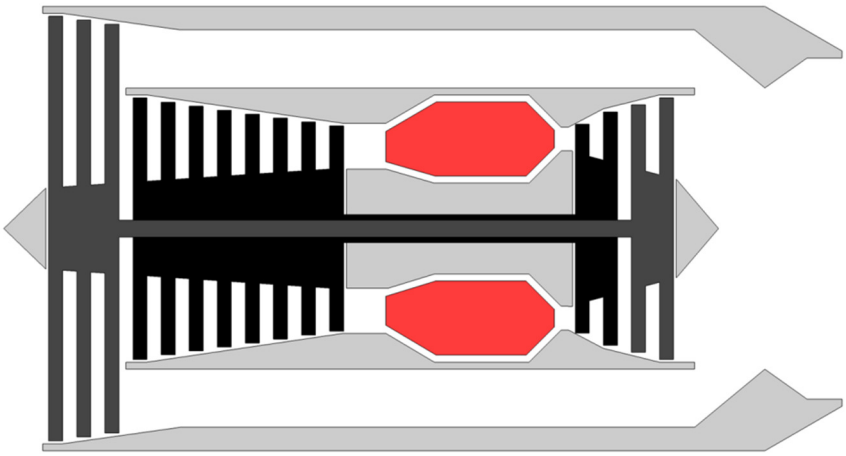

Figure 49. Illustration of low BPR (dual spool combined exhaust) turbofan.

The NPSS model of the low BPR turbofan is illustrated in Figure 50. Boxes represent flow elements, blue arrows represent flow port connections, dashed red arrows represent bleed port connections, and dashed black lines represent shaft port connections. The Inlet Start, Inlet, Shaft, Bleed, Fuel Start, Burner, Duct, Nozzle, and Flow End elements all function as they did in the turbojet model in the previous section. The LPC and HPC are Compressor elements. The HPT and LPT are Turbine elements.

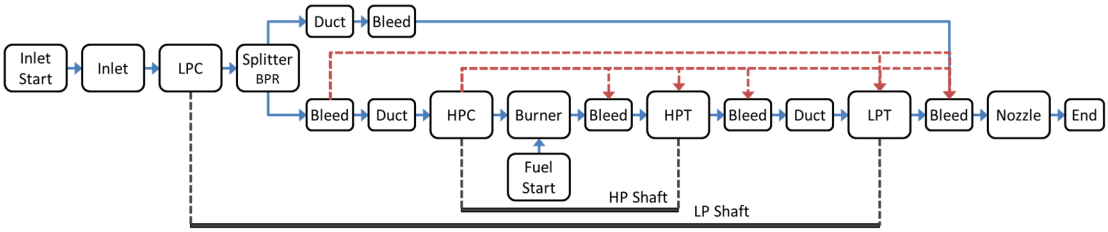

Figure 50. NPSS model schematic of low BPR turbofan.

The Inlet flow all passes to the LPC (connected to the LP Shaft) after which it is divided by the Splitter element into bypass and core flows with identical properties. The mass flow rates of the two streams are set by the bypass ratio $\left(BPR = \dot{m}_{bypass}/\dot{m}_{core}\right)$. Only the core flow passes to the HPC (connected to the high pressure (HP) Shaft), Burner, HPT (connected to HP Shaft), and LPT (connected to LP Shaft). The core and bypass flows are recombined by a Bleed element immediately downstream of the LPT. The combined flow passes to the Nozzle and Flow End elements.

Appendix G provides more detailed information about the model including the order of execution of elements, the list of independent variables, and the list of dependent conditions in the model.

3.2.4 High Bypass Ratio Turbofan

A dual spool (i.e., two concentric shafts) separate exhaust turbofan engine is similar to, but more efficient than, the combined exhaust (low BPR) turbofan above. The applications for these engines (commonly referred to as high bypass ratio turbofans) are varied and include most large commercial transport aircraft and many military aircraft where efficiency is more important than thrust-to-weight and speed.

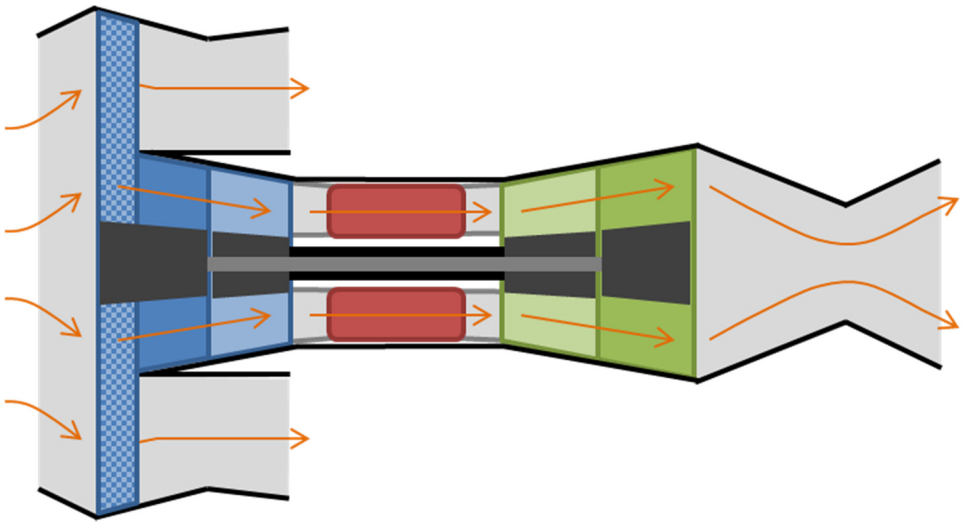

Figure 51. Illustration of high BPR (dual spool separate exhaust) turbofan.

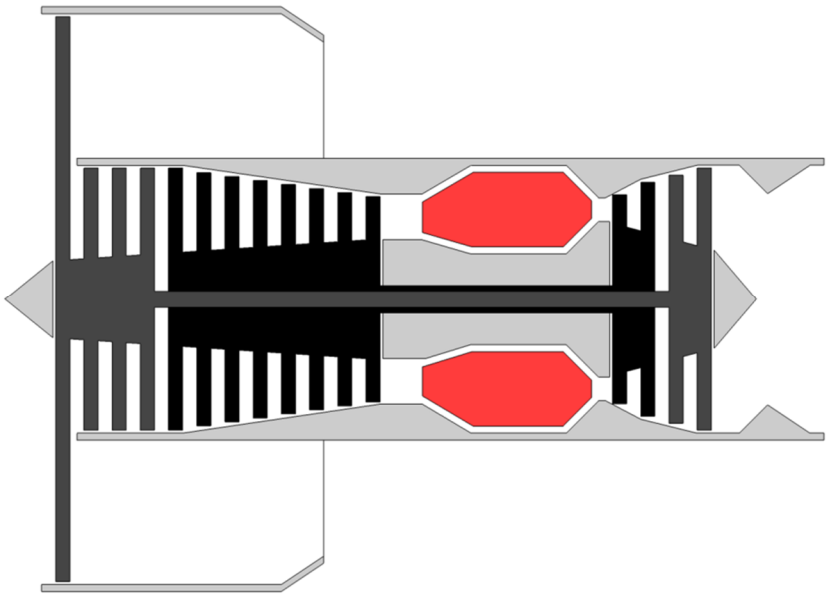

Figure 52. Illustration of high BPR (dual spool separate exhaust) turbofan.

As illustrated in Figure 51, the high bypass ratio turbofan engine consists of an inlet, a large diameter fan (checkered blue) / low pressure compressor (LPC, dark blue) and low pressure turbine (LPT, dark green) sharing the common inner shaft (gray), a high pressure compressor (HPC, light blue) and high pressure turbine (HPT, light green) sharing the common outer shaft (black), a burner/combustor (red) between the HPC and HPT, and separate bypass and core nozzles to accelerate the exhaust. The flow through the outer fan passes through a bypass duct and nozzle. The fan accelerates a large amount of air by a relatively small amount to produce the bulk of the thrust of the engine. The core flow passes through the engine and is never recombined with the bypass flow. Additional thrust is produced by the core nozzle. Figure 52 presents an alternate illustration of a dual spool combined exhaust turbofan. This second figure more accurately represents the geometry of the multistage axial compressors and turbines sharing separate, concentric shafts.

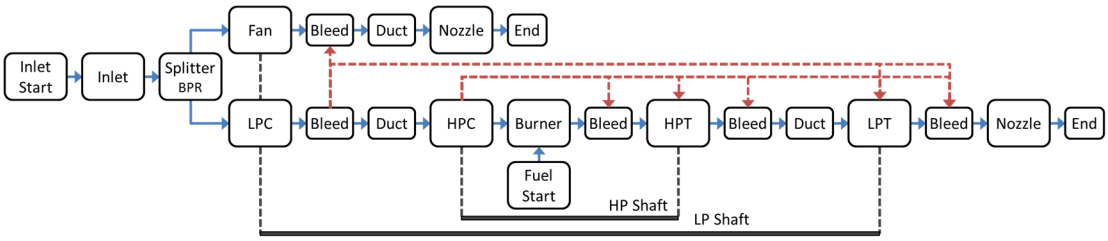

Figure 53. NPSS model schematic of high BPR turbofan.

The NPSS model of the high BPR turbofan is illustrated in Figure 53. Boxes represent flow elements, blue arrows represent flow port connections, dashed red arrows represent bleed port connections, and dashed black lines represent shaft port connections. All elements function as they did in the turbojet and low BPR turbofan models. The Fan, LPC, and HPC are Compressor elements. The HPT and LPT are Turbine elements.

The Splitter divides the Inlet flow into bypass and core flows. The bypass flow passes to the Fan (connected to LP Shaft) and then to the secondary Nozzle and Flow End elements (bypass never recombines with core flow). The core flow passes to the LPC (connected to LP Shaft), the HPC (connected to HP Shaft), Burner, HPT (connected to HP Shaft), and LPT (connected to LP Shaft). The core flow passes to the primary Nozzle and Flow End elements.

Appendix H provides more information about the model including the order of execution of elements, the list of independent variables, and the list of dependent conditions in the model.

3.3 Gas Turbine / Fuel Cell Models

3.3.1 CPOx/SOFC Assembly

The NPSS model of the CPOx/SOFC assembly is illustrated in Figure 54. The assembly is inserted into a GT model directly between the Burner element and the Compressor element immediately upstream.

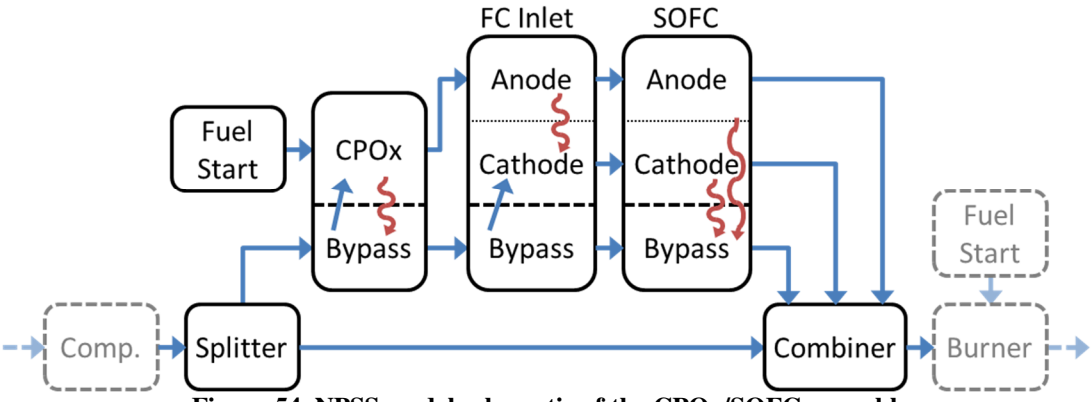

Figure 54. NPSS model schematic of the CPOx/SOFC assembly.

High pressure air exits the Compressor into a Splitter element that diverts a portion of the flow into the CPOx element. The CPOx also receives a fuel stream from a Fuel Start element (just as a Burner does). Internally, the CPOx element divides the incoming air into reaction and bypass/cooling pathways. The element models a single CPOx unit out of many (N_{CPOx}) with the reaction air and fuel flows reduced proportionally ($\dot{m} = \dot{m}/N_{CPOx}$). The air and fuel mix and participate in the catalytic partial oxidation reaction. The single unit CPOx products are multiplied by N_{CPOx} (implicitly assuming all units operate identically) and passed directly to the anode channel flow path of the FC Inlet element. Heat loss from the reacting flow path is transferred to the bypass/cooling air which passes directly to the bypass/cooling flow path of the FC Inlet. Internally, the FC Inlet element separates a portion of the incoming bypass air into the cathode channel flow path. The element models a single anode/cathode pair out of many (N_{FC}) with both flows reduced proportionally ($\dot{m} = \dot{m}/N_{FC}$). Heat transfer occurs from the anode flow to the cathode flow bringing the two closer to thermal equilibrium. The single channel anode and cathode flows are multiplied by N_{FC} and passed directly to the anode and cathode channel flow paths of the SOFC element. The exiting bypass/cooling air passes directly to the bypass/cooling flow path of the SOFC. The SOFC element also models a single anode/cathode pair with both flows reduced proportionally ($\dot{m} = \dot{m}/N_{FC}$). Electrochemistry and heat transfer are modeled down the fuel cell channels. The single channel anode and cathode flows are multiplied by N_{FC} at the exit. Heat loss from the anode and cathode channels is transferred to the bypass air. The undiverted flow from the Splitter and all three exit flows from the SOFC are passed to

the Combiner element and recombined to a single stream that then passes to the Burner.

It is essential to the operation of a physical system that the pressure losses in the CPOx/SOFC assembly be comparable in magnitude to those across the combustor. If they are not, it will be difficult or impossible to achieve the proper balance between fuel cell and combustor mass flow rates. In the present work, the estimated pressure drop across the CPOx/SOFC assembly is less than the assumed pressure drop across the burner/combustor of the GT. Pressure matching is not expected to pose a practical problem under these circumstances because adding pressure drop through the CPOx/SOFC assembly could be achieved simply via valves, grates, baffles, etc. The impact on performance if pressure drop is greater than expected is addressed in Section "7.4.3 High BPR Turbofan with Reversing Fuel Cell".

Assessing the potential impacts of the fuel cell exhaust on combustor operation are beyond the scope the current work. There are certainly important issues that will need to be considered as a topic of future study. Among these are the specifics of physical integration of SOFC exhaust into combustor design, possible impact on turbulence and instability in the combustor, and the implications of introducing highly reactive fuel species (CO, H_2) into the combustion process (although it is possible that CO and H_2 could actually benefit combustor operation).

The design, mass, and volume of the air vehicle's power management system are not addressed in the current work. All vehicles will already be equipped with some type of power management system, and it is assumed that the size of that system would be unaffected by the shift from mechanical generators to SOFCs. Since most

vehicle power systems already require conversion to multiple voltage levels in both AC and DC [2] it is not anticipated that replacing generators with SOFCs would fundamentally alter the scale of the power management system.

3.3.2 Engine / Fuel Cell Integrations

The integration of the CPOx/SOFC assembly NPSS model into the turbojet engine model is illustrated in Figure 55.

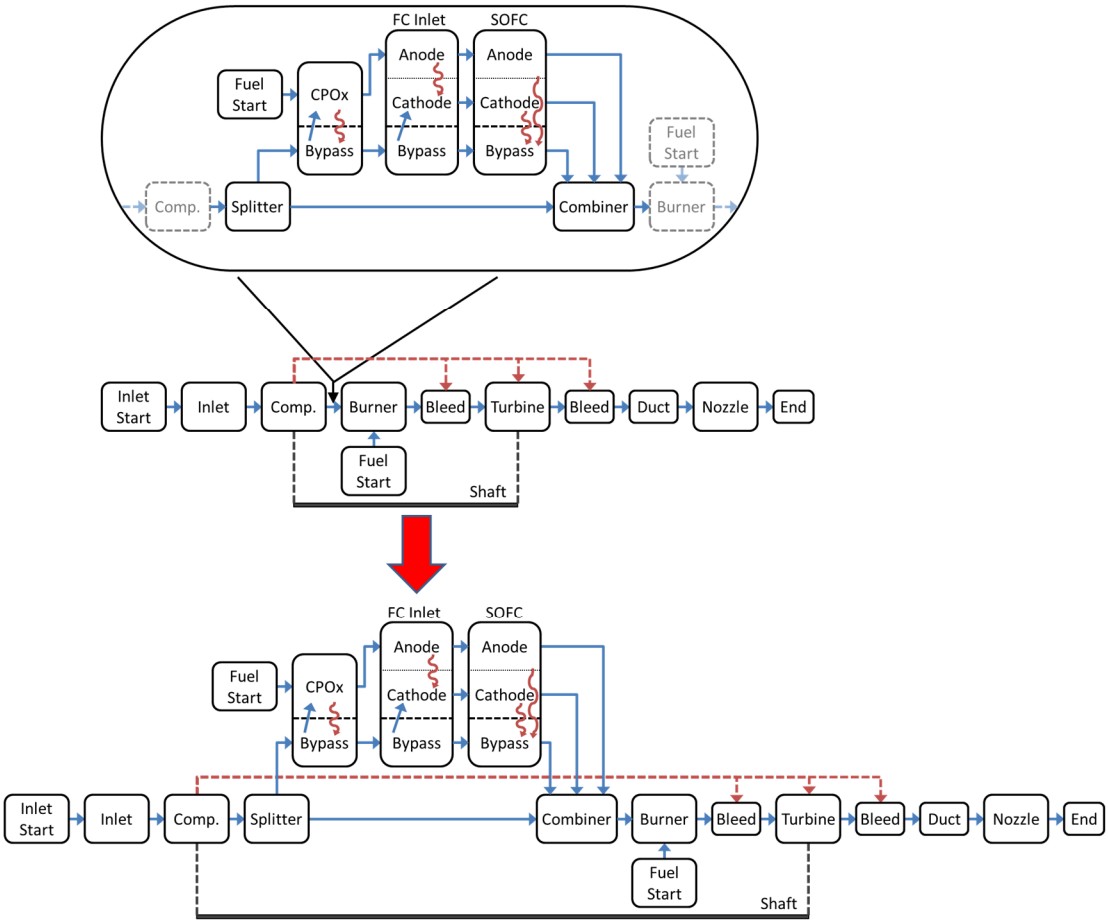

Figure 55. NPSS model schematic of turbojet based GT-SOFC system.

The upper portion of the figure shows the assembly and where it is inserted into the original turbojet model. The lower portion of the figure shows the fully integrated NPSS model for the turbojet based GT-SOFC system.

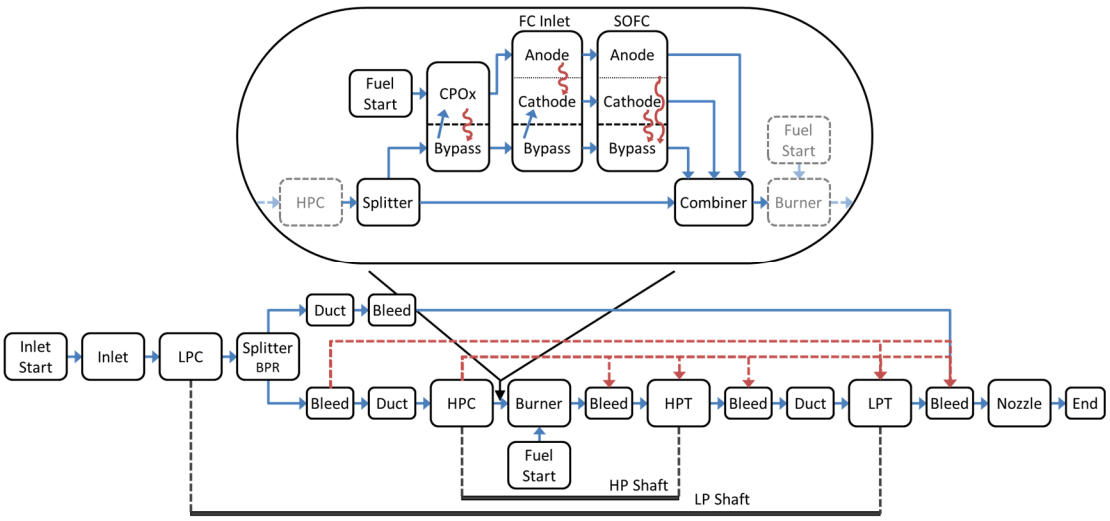

Figure 56. NPSS model schematic of low BPR turbofan based GT-SOFC system.

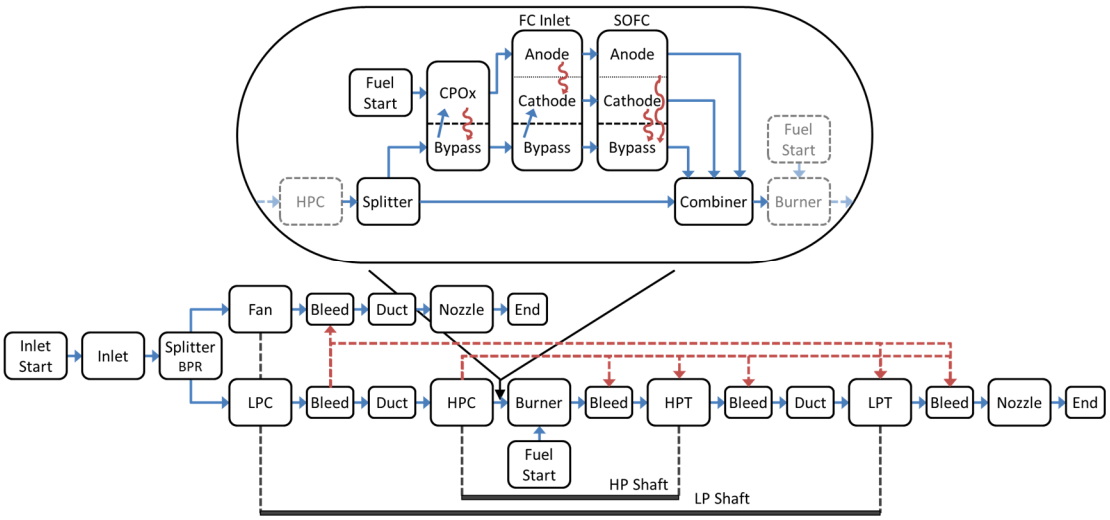

Figure 57. NPSS model schematic of high BPR turbofan based GT-SOFC system.

The NPSS models for the low BPR and high BPR turbofan based integrated GT-SOFC systems are illustrated in Figure 56 and Figure 57, respectively. To improve clarity and legibility, the integrated systems are shown as in to the top portion of Figure 55 where the CPOx/SOFC is assembly shown separately and an arrow indicates where the assembly is inserted into the original engine model.

Appendices C, D, and E contain further details of the models including the order of execution of elements, the lists of independent variables, and the lists of dependent conditions in the models.

Chapter 4: Sizing Methodologies

4.1 Sizing Challenges and Objectives

The thermodynamic benefit of incorporating a fuel cell into a gas turbine cycle has been well established in the literature (see Section "1.4 Gas Turbine / Fuel Cell Hybrid Systems"). The key to evaluating the viability of integrated GT-SOFC systems in airborne applications is accurately modeling the mass and volume of the system. This is because improved system efficiency is only beneficial if it does not come at the expense of significantly degraded specific power (W/kg) or power density (W/L). The reason for this is due to the sensitivity of vehicle performance (range/endurance) to weight and volume: Increased mass leads to increased aircraft lift coefficient, C_L, which in turns leads to increased lift-induced drag and fuel burn. Increased volume leads to increased wetted area and potentially less aerodynamic profiles which in turn leads to increased parasite drag and fuel burn. For these reasons, a highly efficient but oversized GT-SOFC system would not be an effective solution for airborne combined propulsion and power.

The need to accurately estimate mass and volume in order to accurately estimate the rate of fuel burn (as a proxy for range/endurance) presents a challenge. The number of physical dimensions explicitly accounted for varies from component to component. The SOFC model (though not a three dimensional model in the sense of a CFD simulation) requires inputs for physical size in the axial, radial, and circumferential directions. By contrast, most GT component models are 'zero dimensional' meaning that the calculations are based solely on thermodynamics,

correlations, etc. with no dependence physical size. Any dimensions not present in the initial modeling must be inferred from known model inputs/outputs and additional assumptions. Because it is crucial to accurately predict mass and volume, it is important that the inferred component sizing be based on reasonable sets of assumptions. The following sections explain the methodology employed to estimate the sizes of the various portions of the GT-SOFC system.

4.2 Gas Turbine Size Estimation

4.2.1 Overview

Estimating the mass of gas turbine engine from 'first principles' is a complex endeavor and a research topic in its own right. Fortunately, there already exists in the literature methods for accomplishing this. The mass model used here is based on the work of Onat and Klees [106] and Sanghi et al. [107] who developed a methodology for predicting the mass of a gas turbine engine based on a detailed, piece-by-piece accounting of the entire engine configuration. For example, the masses of axial turbomachinery stages are predicted based on inputs like the hub-to-tip ratio, blade aspect ratio, solidity, etc. Blade disc mass is found via a correlation. The number of compressor stages is determined by the maximum allowable pressure ratio across a single stage. The number of turbine stages is determined by the maximum allowable diameter and stage loading. The annular combustion chamber length is determined by specified flow velocity and residence time. Concentric high and low pressure shafts are sized to withstand the applied torque. Engine frame masses are found via a correlation. Further details of the estimation method are contained in the following

subsections. Section "4.2.11 Component specific assumptions" and the tables therein contain specific assumptions and parameter values for the sizing analysis.

4.2.2 Axial compressor

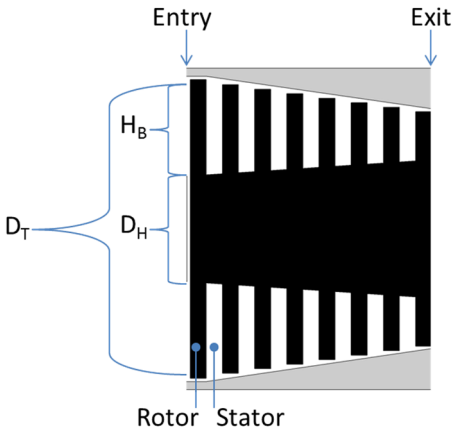

Figure 58: Axial compressor geometry.

The following parameters are inputs to the model:

π_{max} – maximum stage pressure ratio

M_{entry} – entry Mach

M_{exit} – exit Mach

HTR_{entry} – entry hub to tip ratio

α_{entry} – entry blade aspect ratio

α_{exit} – exit blade aspect ratio

$(C/S)_{entry}$ – entry blade solidity, ratio of chord length to pitch

$(C/S)_{exit}$ – exit blade solidity

K – blade volume factor

τ – blade taper ratio

t_s – spacer thickness

t_{case} – casing thickness

ρ_x – material density of component *x* (blades, disc, hardware, casing)

The following values are retrieved from the engine simulation:

$\dot{m}_{air}$ – mass flow of air through component (taken at inlet)

η_c – compressor isentropic efficiency

N_s – shaft rotation speed

h_{entry} – entry specific total enthalpy of flow

h_{exit} – exit specific total enthalpy of flow

The maximum first stage enthalpy rise, $\Delta h'_{stage}$, is estimated based on the maximum allowable pressure ratio, π_{max}:

$$\Delta h'_{stage} = -\frac{RT_{in}}{\eta_c}\left(\frac{\gamma}{1-\gamma}\right)\left(\pi_{max}^{(\gamma-1)/\gamma} - 1\right) \tag{86}$$

where R is the gas constant and γ is the ratio of specific heats. The estimated number of stages can then be calculated:

$$N'_{stages} = \left(h_{exit} - h_{entry}\right)/\Delta h'_{stage} \tag{87}$$

The raw number of stages, N'_{stages}, is rounded up to an integer value, N_{stages}. The actual enthalpy rise per stage, Δh_{stage}, is then calculated by working back using the integer number of stages. Linear variation of many parameters, x, between stages:

$$\Delta x_{stage} = \left(x_{exit} - x_{entry}\right)/N_{stages} \tag{88}$$

Linear variation of Mach number, α, and solidity (C/S) is assumed. Also, equal enthalpy change per stage is assumed. The enthalpy change across the stage (Δh_{stage})

is used to calculate the pressure rise across the stage using the isentropic efficiency, η_c [18]:

$$\pi_{stage} = \left[1 + \left(\frac{\eta_c \, \Delta h_{stage}}{RT_{in}}\right)\left(\frac{\gamma - 1}{\gamma}\right)\right]^{\gamma/(\gamma-1)} \tag{89}$$

Using an input local Mach number (interpolated from M_{entry} and M_{exit}), NPSS calculates the flow area, pressure, temperature, etc. Various geometric parameters are calculated using the following set of equations [107]:

$$A = (\pi D_T^2/4)(1 - HTR^2) \tag{90}$$

$$HTR = D_H/D_T \tag{91}$$

$$\alpha = H_B/C_B \tag{92}$$

$$H_B = (D_T - D_H)/2 \tag{93}$$

$$D_M = (D_T + D_H)/2 \tag{94}$$

where A is the flow area, D_H is the hub diameter, D_M is the mean diameter, D_T is the tip diameter, C_B is the blade chord, and α is the blade aspect ratio. For the first stage, A, HTR, and α are known. For all remaining stages, A, α, and D_M are known (D_M is held constant from the first stage). The rotor tip speed at the design state is found via the correlation presented in Refs. [106,107]. The correlation relates typical corrected tip speeds ($U_T/sqrt(T/T_{ref})$) as a function of pressure ratio. The system solver matches the shaft speed calculated from this value to the NPSS model simulation. The rotor tip speed, U_T, is calculated from the shaft speed, N_s, and tip diameter [107]:

$$U_T = \left(N_s \frac{2\pi}{60}\right)\left(\frac{D_T}{2}\right) \tag{95}$$

where the factor $2\pi/60$ converts the shaft speed from revolutions/minute to radians/second. The axial length of the rotor and stator are taken to equal the rotor

blade chord [106]. The spacing between rotor/stator and stator/rotor is taken as 17% of the blade chord [106]. Thus, the length of the entire stage:

$$L_{stage} = 2(1 + 0.17)C_B \tag{96}$$

The volume of a single rotor blade is found via [106]:

$$V_{B,r} = K(H_B^3/\alpha^2) \tag{97}$$

where K is the blade volume factor. The number of blades is calculated [106]:

$$N_{B,r} = \pi D_T \left(\frac{C}{S}\right)/C_B \tag{98}$$

The number of blades is rounded to the nearest integer. The volume and number of blades in the stator is assumed equal to the rotor. The blade pull stress is calculated via [106]:

$$\sigma_{BP} = \frac{\rho_B U_T^2}{\tau}\left(\frac{1 - HTR^2}{2} + \frac{\tau - 1}{12}(1 - HTR)(1 + 3HTR)\right) \tag{99}$$

where ρ_B is the blade density and τ is the blade taper ratio. The relative thickness of the rotor disc is found as a function of the blade pull stress and disc diameter via correlation $(t_D = func[\sigma_{BP} D_H])$ in Ref. [106]. The volume of the disc V_D, the volume of the connecting hardware V_{HW} (assuming a 0.075" thick spacer located at 75% of the hub radius) [106], and the volume of the casing (assuming 0.1" thickness) [106] can be calculated:

$$V_D = D_H^2 \cdot t_D \tag{100}$$

$$V_{HW} = (0.75\pi D_H) t_S L_{stage} \tag{101}$$

$$V_C = (\pi D_T) t_C L_{stage} \tag{102}$$

where t_S is the spacer thickness, and t_C is the casing thickness. Finally, the weight of the stage is then:

$$W_{stage} = 2V_{B,r}N_{B,r}\rho_B + V_D\rho_D + V_{HW}\rho_{HW} + V_C\rho_C \quad (103)$$

4.2.3 Axial turbine

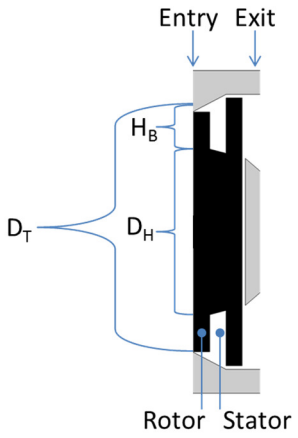

Figure 59: Axial turbine geometry.

The following parameters are inputs to the model:

Y^*_{max} – turbine loading parameter

M_{entry} – entry Mach number

M_{exit} – exit Mach number

α_{entry} – entry blade aspect ratio

α_{exit} – exit blade aspect ratio

$(C/S)_{entry}$ – entry blade solidity

$(C/S)_{exit}$ – exit blade solidity

K_r – rotor blade volume factor

K_s – stator blade volume factor

τ – blade taper ratio

t_s – spacer thickness

t_{case} – casing thickness

ρ_x – material density of component *x* (blades, disc, hardware, casing)

σ_{ref} – reference 0.2% yield strength of disc material

The following values are retrieved from the engine simulation:

$\dot{m}_{air}$ – mass flow of air through component (taken at exit)

η_t – turbine isentropic efficiency

N_s – shaft rotation speed

h_{entry} – entry specific total enthalpy of flow

h_{exit} – exit specific total enthalpy of flow

Some assumption must be made about the diameter of the last stage. This can take the form of a maximum or approximate tip, mean, or hub diameter. For specified tip diameter, the estimated mean diameter can be found from the following equations [107]:

$$A = (\pi D_T^2/4)(1 - HTR^2) \tag{104}$$

$$HTR = D_H/D_T \tag{105}$$

$$D_M = (D_T + D_H)/2 \tag{106}$$

Combining and rearranging yields the following expression for mean diameter:

$$D_M = \frac{D_T}{2}\left(1 + \sqrt{1 - \frac{4A}{\pi D_T^2}}\right) \tag{107}$$

The blade velocity at mean diameter is then estimated [107]:

$$U_M = \left(N_s \frac{2\pi}{60}\right)\left(\frac{D_M}{2}\right) \tag{108}$$

where the factor $2\pi/60$ converts the shaft speed from revolutions/minute to radians/second. The number of stages is increased incrementally until the turbine

loading parameter (Y^*) [107] is less than the maximum allowed value, Y^*_{max}. The turbine loading parameter is calculated:

$$Y^* = \frac{2\Delta h_{turbine}}{N_{stages} U_M^2} \tag{109}$$

where U_M is taken at the exit and $\Delta h_{turbine}$ is the enthalpy rise across the entire turbine. Linear variation of many parameters, *x*, between stages is:

$$\Delta x_{stage} = \left(x_{entry} - x_{exit}\right)/N_{stages} \tag{110}$$

Linear variations of Mach number, α, and solidity (C/S) are assumed. Also, equal enthalpy change per stage is assumed. The enthalpy change between stages is used to calculate the pressure rise using the isentropic efficiency, η_t [18]. The subscripts '+' and '–' denote the changes going forward and backward between stages, respectively:

$$\Delta h_+ = -\eta_t R T_{in} \left(\frac{\gamma}{1-\gamma}\right)\left(\pi_+^{(\gamma-1)/\gamma} - 1\right) = -\eta_t R T_{out} \left(\frac{\gamma}{1-\gamma}\right)\left(1 - \pi_+^{(1-\gamma)/\gamma}\right) \tag{111}$$

or equivalently:

$$-\Delta h_- = -\eta_t R T_{in} \left(\frac{\gamma}{1-\gamma}\right)\left(\pi_-^{(1-\gamma)/\gamma} - 1\right) = -\eta_t R T_{out} \left(\frac{\gamma}{1-\gamma}\right)\left(1 - \pi_-^{(\gamma-1)/\gamma}\right) \tag{112}$$

It can therefore be stated:

$$\pi_{stage} = \left[1 + \left(\frac{\Delta h_{stage}}{\eta_t R T_{out}}\right)\left(\frac{\gamma - 1}{\gamma}\right)\right]^{\gamma/(\gamma-1)} \tag{113}$$

Using an input Mach number, NPSS calculates the flow area, pressure, temperature, etc. Other geometric parameters relating the flow area, hub diameter, tip diameter, hub-to-tip ratio, mean diameter, blade height, and blade chord are calculated using Eqs. (90) – (94) in the same way as was done for the compressor stages. The area (A), aspect ratio (α), and mean diameter (D_M) are known. D_M is held

constant between stages. The aspect ratio of the stator is taken as 83% of the rotor value. The rotor tip speed is calculated from the shaft speed and tip diameter [107]:

$$U_T = \left(N_s \frac{2\pi}{60}\right)\left(\frac{D_T}{2}\right) \tag{114}$$

The axial length of the rotor and stator are taken as equal to the respective blade chords [106]. The spacing between rotor/stator and stator/rotor is taken as 17% of the blade height [106]. Thus, the length of the entire stage:

$$L_{stage} = C_{B,r}(1 + 0.17) + C_{B,s}(1 + 0.17) \tag{115}$$

where $C_{B,r}$ is the rotor blade chord and $C_{B,s}$ is the stator blade chord. The volume of a single rotor, $V_{B,r}$, or stator blade, $V_{B,s}$, is found via [106]:

$$V_{B,r} = K_r(H_B^3/\alpha^2) \tag{116}$$

$$V_{B,s} = K_s(H_B^3/(0.83\alpha)^2) \tag{117}$$

where K_r and K_s are the rotor and stator blade volume factors. The number of rotor blades, $N_{B,r}$, is calculated [106]:

$$N_{B,r} = \pi D_T \left(\frac{C}{S}\right)/C_B \tag{118}$$

The number of blades is rounded to the nearest integer. The volume and number of blades in the stator is assumed equal to the rotor. The blade pull stress can then be calculated using Eq. (99). The relative thickness of the rotor disc is found as a function of the blade pull stress, disc diameter, and the reference material strength, σ_{ref}, via correlation $\left(t_D = func\left[\sigma_{BP} D_H/\sigma_{ref}\right]\right)$ in Ref. [106]. The volume of the disc V_D, the volume of the connecting hardware V_{HW} (assuming a 0.075" thick spacer located at 75% of the hub radius) [106], and the volume of the casing (assuming 0.1" thickness) [106] can be calculated:

$$V_D = D_H^2 \cdot t_D \tag{119}$$

$$V_{HW} = (0.75\pi D_H) t_S L_{stage} \tag{120}$$

$$V_C = (\pi D_T) t_C L_{stage} \tag{121}$$

where t_S is the spacer thickness, and t_C is the casing thickness. Finally, the weight of the stage is then:

$$W_{stage} = V_{B,r} N_{B,r} \rho_B + V_{B,s} N_{B,s} \rho_B + V_D \rho_D + V_{HW} \rho_{HW} + V_C \rho_C \tag{122}$$

4.2.4 Combustor

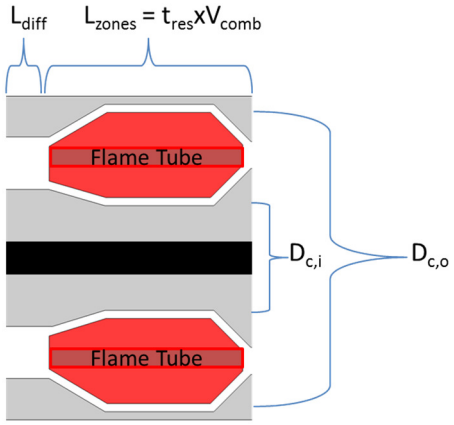

Figure 60: Annular combustor geometry.

The following parameters are inputs to the model:

AFR_{stoich} – stoichiometric air-to-fuel ratio

v_{comb} – combustion zone flow velocity

v_{pass} – passage air flow velocity

ρ_x – material density of component *x* (diffuser, casing, liner, dome)

σ_x – reference strength of material *x*

t_{res} – combustor residence time

The following values are retrieved from the engine simulation:

$\dot{m}_{fuel}$ – fuel mass flow rate

$\dot{m}_{in}$ – incoming air mass flow rate

P_{in} – incoming flow pressure

The mass estimation of the burner/combustor contained in this section does not address any modifications that may be necessary from the reintroduction of the fuel cell assembly exhaust flows. As future research on this topic defines the specifics of the flow integration, the mass estimation methods should be updated to account for new factors.

The airflow into the combustor is assumed to divide between a combustion zone flow, $\dot{m}_{comb}$, proportional to the fuel flow rate and a secondary passage flow, $\dot{m}_{pass}$, made up of the remaining air [107]:

$$\dot{m}_{comb} = AFR_{stoich}\dot{m}_{fuel} \tag{123}$$

$$\dot{m}_{pass} = \dot{m}_{in} - \dot{m}_{comb} \tag{124}$$

where AFR_{stoich} is the stoichiometric air-to-fuel ratio. Using input flow velocities, NPSS calculates the flow areas, A_{comb} and A_{pass}, which in turn are summed to calculate the combustor reference flow area, $A_{ref} = A_{comb} + A_{pass}$ [107]. The outer diameter of the combustor, $D_{C,o}$, is set as the maximum diameter of the 'engine core', $D_{core,o}$. The inner diameter of the combustor, $D_{C,i}$, is then calculated:

$$D_{C,i} = \sqrt{D_{c,o}^2 - 4A_{ref}/\pi} \tag{125}$$

The mean diameter, D_M, is the average of the inner and outer diameters. The diffuser area, A_{diff}, is estimated assuming 25% aerodynamic diffusion [107]:

$$\frac{A_{diff} - A_{HPC,out}}{A_{ref} - A_{HPC,out}} = 0.25 \tag{126}$$

where $A_{HPC,out}$ is the flow area at the HPC exit. The inner and outer diameters of the diffuser are calculated via the mean diameter and diffuser area:

$$D_{diff,i} = D_M - A_{diff}/(\pi D_M) \tag{127}$$

$$D_{diff,o} = D_M + A_{diff}/(\pi D_M) \tag{128}$$

The flame tube dimensions are calculated by subtracting the secondary passage dimension from the combustor diameter [107]:

$$D_{ft,i} = \sqrt{D_{C,i}^2 + 2A_{pass}/\pi} \tag{129}$$

$$D_{ft,o} = \sqrt{D_{C,o}^2 - 2A_{pass}/\pi} \tag{130}$$

The flame tube height is then:

$$H_{ft} = \left(D_{ft,o} - D_{ft,i}\right)/2 \tag{131}$$

Lengths (diffuser, primary, secondary, dilution zones) are defined empirically [107]:

$$L_{diff} = 1.125 H_{ft} \tag{132}$$

$$L_{zones} = v_{comb} t_{res} \tag{133}$$

$$L_C = L_{diff} + L_{zones} \tag{134}$$

where v_{comb} is the flow velocity in the combustor and t_{res} is the flow residence time. This approach takes into account typical values for known gas turbine engines, but is inherently limited in that it does not account for mixing, chemistry, or chemical kinetics. The thickness of the diffuser and combustor casings are determined by the pressure vessel stresses [106]:

$$t_{diff} = \frac{P_{in} D_{diff,o}}{2\sigma} \tag{135}$$

$$t_{case} = \frac{P_{in} D_{C,o}}{2\sigma} \tag{136}$$

The masses of diffuser, casing, and flame tube can then be calculated [106]:

$$W_{diff} = \pi\left(D_{diff,i} + D_{diff,o}\right)L_{diff}t_{diff}\rho \quad (137)$$

$$W_{case} = \pi\left(D_{C,i} + D_{C,o}\right)L_{C}t_{case}\rho \quad (138)$$

$$W_{ft} = \pi\left(D_{ft,i} + D_{ft,o}\right)L_{C}t_{ft}\rho \quad (139)$$

where the thickness of the flame tube, t_{ft}, is assumed to be 0.055" thick steel. The mass of the burner dome, fuel manifold, fuel nozzles, and other components (collectively W_{dome}) are found via correlation [106]:

$$W_{dome} = \frac{(1.5264\ lb/ft^2)}{4}\left(D_{C,o}^2 - D_{C,i}^2\right) \quad (140)$$

4.2.5 Afterburner

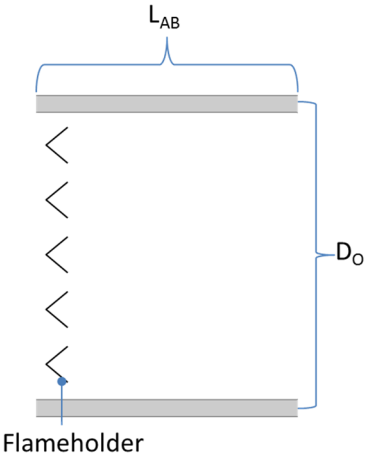

Figure 61: Afterburner geometry.

The following parameters are inputs to the model:

ρ_x – material density

σ_x – reference strength of material

The following values are retrieved from the engine simulation:

P_{in} – flow pressure

BPR – engine bypass ratio

The outer diameter, D_o, is set equal to that of the upstream component (mixer). The length of the afterburner, L_{AB}, is a function of the length to diameter ratio which is set via correlation with the BPR at sea level static (SLS) conditions [107]:

$$L_{AB} = (L/D)D_o \tag{141}$$

$$L/D = 2 - (BPR/2)_{SLS} \tag{142}$$

The thickness of the afterburner casing, t_{case}, is a function of the pressure stresses and the strength of the material [106]:

$$t_{case} = P_{in}D_o/2\sigma \tag{143}$$

The weight can then be calculated:

$$W_{AB} = \pi D_o L_{AB} t_{case} \rho \tag{144}$$

4.2.6 Duct

The following parameters are inputs to the model:

L/H – ratio of duct length to passage height

ρ_x – material density

σ_x – reference strength of material

The following values are retrieved from the engine simulation:

P_{in} – flow pressure

For the duct between the LPC and the HPC, inner and outer diameters are averages of the LPC exit and the HPC inlet values. Length is then a function of duct height [107]:

$$L_{duct,c} = (L/H)(D_o - D_i) \tag{145}$$

For a bypass duct, the outer diameter is set equal to the tip diameter of the fan/compressor [107]. The area is found by NPSS by setting the Mach number equal to the fan/compressor exit value. The inner diameter is then:

$$D_i = \sqrt{D_o^2 - 4A/\pi} \tag{146}$$

And the bypass duct length is the sum of the lengths of all the bypassed engine components:

$$L_{duct,bp} = L_{HPC} + L_C + L_{HPT} + L_{LPT} \tag{147}$$

The thickness of the duct is a function of the pressure stresses and the strength of the material [106]:

$$t_{case} = P_{in} D_o / 2\sigma \tag{148}$$

The weight can then be calculated:

$$W_{duct} = \pi(D_i + D_o) L_{duct} t_{case} \rho \tag{149}$$

4.2.7 Mixer

The following parameters are inputs to the model:

L/H – ratio of duct length to passage height

t_{case} – case thickness

ρ_x – material density

σ_x – reference strength of material

The following values are retrieved from the engine simulation:

P_{in} – flow pressure

The outer diameter is set equal to the LPT exit. The flow area is found by NPSS by setting the Mach number to the LPT exit value. The inner diameter can then be calculated:

$$D_i = \sqrt{D_o^2 - 4A/\pi} \tag{150}$$

Length is then a function of duct height [107]:

$$L_{mixer} = (L/H)(D_o - D_i) \tag{151}$$

The effective surface area (i.e., the surface area including mixing enhancers) is found via correlation [106]:

$$S_{eff} = [0.9825(D_o + D_i) + 0.75(D_o - D_i)]L_{mixer} \tag{152}$$

The weight can then be calculated [106]:

$$W_{mixer} = \pi S_{eff} t_{case} \rho \tag{153}$$

4.2.8 Nozzle

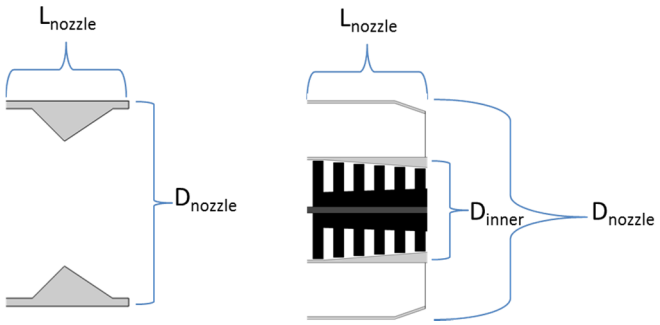

Figure 62: Primary (L) and secondary (R) nozzle geometries.

The following parameters are inputs to the model:

L/D – ratio of nozzle length to outer diameter

L/H – ratio of nozzle length to duct height

ρ_x – material density

t_{wall} – wall thickness

For the primary/core nozzle, diameter is set equal to the LPT exit diameter and the nozzle length is a function of that diameter [107]:

$$L_{nozzle} = (L/D)D_{nozzle} \tag{154}$$

For the secondary/bypass nozzle, there is an inner and an outer diameter. These are set equal to the fan flow passage upstream. The nozzle length is then a function of nozzle 'height':

$$L_{nozzle} = (L/H)(D_{nozzle} - D_{inner}) \tag{155}$$

The thickness of the wall is input, and the weight is then [106]:

$$W_{nozzle} = \pi D_{nozzle} L_{nozzle} t_{wall} \rho \tag{156}$$

To determine the throat diameter, flow Mach number is set to 1.0 and NPSS determines the flow area. The throat diameter is then:

$$D_{throat} = \sqrt{4A^*/\pi} \tag{157}$$

4.2.9 Shafts

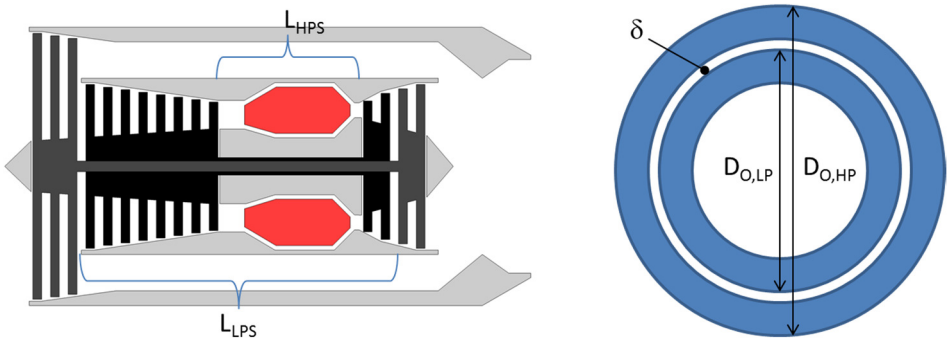

Figure 63: Concentric shaft geometry in engine (L) and cross section (R).

The following parameters are inputs to the model:

D_i/D_o – diameter ratio of the LP shaft

δ – clearance between shafts

ρ_{shaft} – material density of shaft

τ_{max} – allowable stress limit of shaft

The following values are retrieved from the engine simulation:

ΔH_T – work extracted from turbine

N_s – shaft rotation speed

The length of each shaft is determined by the sum of the lengths of the components in between [106]:

$$L_{LP} = L_{duct} + L_{HPC} + L_C + L_{HPT} \tag{158}$$

$$L_{HP} = L_C \tag{159}$$

where L_{LP} and L_{HP} are the lengths of the inner low pressure shaft and the outer high pressure shaft, respectively. The torque on each shaft (T_{LP} and T_{HP}) is determined by the work extracted from the turbines [106]:

$$T_{LP} = \Delta H_{LPT}/\omega_{LP} = \Delta H_{LPT}/(N_{LP}\, 2\pi/60) \tag{160}$$

$$T_{HP} = \Delta H_{HPT}/\omega_{HP} = \Delta H_{LPT}/(N_{HP}\, 2\pi/60) \tag{161}$$

where ΔH is the enthalpy change in the turbine, ω is the angular velocity of the shaft, and N is the shaft rotation speed in revolutions per minute. The shaft dimensions are a function of the shear stress, τ, associated with the applied torque (T). The shear stress in a hollow shaft is [106]:

$$\tau = \frac{16 T D_o}{\pi\left(D_o^4 - D_i^4\right)} \tag{162}$$

Solving for the outer diameter (in terms of the diameter ratio) [106] gives:

$$D_o = \left[\frac{16T}{\pi\tau_{max}\left(1 - D_i^4/D_o^4\right)}\right]^{1/3} \tag{163}$$

The allowable stress on the shaft, τ_{max}, should have an appropriate safety factor built in. The outer diameter of the LP shaft, $D_{o,LP}$, is found explicitly based on the input value for the diameter ratio of that shaft. The inner diameter of the HP shaft is, by necessity:

$$D_{i,HP} = D_{o,LP} + 2\delta \tag{164}$$

where δ is the clearance between the two shafts. The outer diameter of the HP shaft, $D_{o,HP}$, can then be solved for as a function of the torque and stress limit, τ_{max}. The weight of either shaft is calculated [106]:

$$W = \frac{\pi D_o^2}{4}\left(1 - D_i^2/D_o^2\right)L\rho \tag{165}$$

4.2.10 Frames

Frames make up a significant portion of the overall engine weight. Weight correlations are available in Ref. [106] for four types of frames:

(1) Single bearing frame without power takeoff

(2) Single bearing frame with power takeoff

(3) Turbine frame

(4) Intermediate 2-bearing or burner frame

A type 1 frame is assumed at the inlet. A type 4 frame is assumed at the HPC inlet and at the burner inlet. A type 3 frame is assumed at the LPT exit.

4.2.11 Component specific assumptions

The methods described above are quite sensitive to assumptions about diameter limits so some care is needed when selecting them. The best correlation with known engine masses was obtained by assuming that the combustor and turbine stages fit

into the 'engine core' diameter set by the upstream compressor. Exceptions are made subject to certain limitations (elaborated on below). The following information describes the assumptions specific to particular instances of components (i.e., the LPC as opposed to compressors in general). All of the input parameters are summarized in Table 8 through Table 17.

Fan: Hub diameter is equal to that of the first LPC stage (or first HPC stage if there is no LPC). Hub-to-tip ratio (HTR) is an output. A single stage with known pressure ratio is assumed. No stator mass is included. A gap equal to the rotor length is included behind the rotor. Blades, disc, and casing are Titanium 318. Hardware is steel.

Table 8: Fan sizing assumptions and input parameters.

Parameter	Value	Units
Entry Mach, M_{entry}	0.55	
Entry blade aspect ratio, α_{entry}	4.0	
Entry blade solidity, $(C/S)_{entry}$	1.25	
Blade volume factor, K	0.055	
Blade taper ratio, τ	1.8	
Spacer thickness, t_s	0.00625	ft
Casing thickness, t_{case}	0.00833	ft
Blade, disc, casing density	276.	lbm/ft^3
Hardware density, ρ_{HW}	512.	lbm/ft^3

LPC: Hub-to-tip ratio is an input parameter. If there is a fan stage, incoming flow state is equal to fan output. If there is no fan stage, incoming flow state is freestream. Blades, disc, and casing are Titanium 318. Hardware is steel.

HPC: Either hub-to-tip ratio or entrance diameter (tip, hub, or rotor) is an input parameter. For the first three stages, blades and disc are Titanium 685. For temperature reasons, the remaining stages' blades and discs are Inconel 718. The casing is Inconel 718. Hardware is steel. For a turbojet, the single compressor uses LPC inlet parameters and materials but HPC exit parameters.

Table 9: LPC sizing assumptions and input parameters.

Parameter	Value	Units
Max. stage pressure ratio, π_{max}	1.5	
Entry Mach, M_{entry}	0.5	
Exit Mach, M_{exit}	0.45	
Entry hub-to-tip, HTR_{entry}	0.4	
Entry blade aspect ratio, α_{entry}	4.0	
Exit blade aspect ratio, α_{exit}	3.0	
Entry blade solidity, $(C/S)_{entry}$	1.25	
Exit blade solidity, $(C/S)_{exit}$	1.25	
Blade volume factor, K	0.12	
Blade taper ratio, τ	1.2	
Spacer thickness, t_s	0.00625	ft
Casing thickness, t_{case}	0.00833	ft
Blade, disc, casing density	276.	lbm/ft^3
Hardware density, ρ_{HW}	512.	lbm/ft^3

Table 10: HPC sizing assumptions and input parameters.

Parameter	Value	Units
Max. stage pressure ratio, π_{max}	1.4	
Entry Mach, M_{entry}	0.4	
Exit Mach, M_{exit}	0.3	
Entry hub-to-tip, HTR_{entry}	0.6	
Entry blade aspect ratio, α_{entry}	3.0	
Exit blade aspect ratio, α_{exit}	1.5	
Entry blade solidity, $(C/S)_{entry}$	1.25	
Exit blade solidity, $(C/S)_{exit}$	1.25	
Blade volume factor, K	0.12	
Blade taper ratio, τ	1.2	
Spacer thickness, t_s	0.00625	ft
Casing thickness, t_{case}	0.00833	ft
Early stage blade, disc density	281.	lbm/ft^3
Late stage blade, disc density	511.	lbm/ft^3
Case density, ρ_{case}	511.	lbm/ft^3
Hardware density, ρ_{HW}	512.	lbm/ft^3

Inter-Compressor Duct: Inner and outer diameters are average of LPC exit and HPC inlet. The length is 1.5 times the height. Minimum casing thickness is 1/16" and material is Inconel 718.

LPT: Exit tip diameter is set equal to the 'maximum diameter' of the engine core (High BPR: LPC inlet tip diameter; Low BPR: LPC exit tip diameter). The diameter can be increased to satisfy limitations: HTR≥0.5; number of LPT stages, N_{LPT}≤6;

stage loading, $Y^* \leq Y^*_{max}$. Blades are a nickel based alloy. Disc and casing are Inconel 718. Hardware is steel.

Table 11: Duct sizing assumptions and input parameters.

Parameter	Value	Units
Inter-duct		
Length-to-height, L/H	1.5	
Case density, ρ_{case}	511.	lbm/ft^3
Yield stress, σ	9x10^6	lbf/ft^2
Bypass duct		
Case density, ρ_{case}	276.	lbm/ft^3
Yield stress, σ	10.4x10^6	lbf/ft^2

Table 12: LPT sizing assumptions and input parameters.

Parameter	Value	Units
Turbine loading parameter, Y^*_{max}	4.5	
Entry Mach, M_{entry}	0.45	
Exit Mach, M_{exit}	0.55	
Entry blade aspect ratio, α_{entry}	2.0	
Exit blade aspect ratio, α_{exit}	5.0	
Entry blade solidity, $(C/S)_{entry}$	1.25	
Exit blade solidity, $(C/S)_{exit}$	1.25	
Rotor blade volume factor, K_r	0.195	
Stator blade volume factor, K_s	0.144	
Blade taper ratio, τ	1.0	
Spacer thickness, t_s	0.00625	ft
Casing thickness, t_{case}	0.00833	ft
Blade density, ρ_{blade}	531.	lbm/ft^3
Disc, casing density	511.	lbm/ft^3
Hardware density, ρ_{HW}	512.	lbm/ft^3
Yield stress, σ_{ref}	18x10^6	lbf/ft^2

Table 13: HPT sizing assumptions and input parameters.

Parameter	Value	Units
Turbine loading parameter, Y^*_{max}	4.5	
Entry Mach, M_{entry}	0.3	
Exit Mach, M_{exit}	0.45	
Entry blade aspect ratio, α_{entry}	2.0	
Exit blade aspect ratio, α_{exit}	2.0	
Entry blade solidity, $(C/S)_{entry}$	1.25	
Exit blade solidity, $(C/S)_{exit}$	1.25	
Rotor blade volume factor, K_r	0.156	
Stator blade volume factor, K_s	0.144	
Blade taper ratio, τ	1.0	
Spacer thickness, t_s	0.00625	ft
Casing thickness, t_{case}	0.00833	ft
Blade, disc, casing density	511.	lbm/ft^3
Hardware density, ρ_{HW}	512.	lbm/ft^3
Yield stress, σ_{ref}	18x10^6	lbf/ft^2

HPT: If the LPC entrance tip diameter is less than 'maximum diameter' of the upstream core, then the exit mean diameter is set equal to the LPT entrance mean diameter. Otherwise, the exit tip diameter is set equal to the 'maximum diameter'. For a turbojet, the exit tip diameter is less than or equal to the HPC tip diameter. The diameter can be increased to satisfy limitations: HTR≥0.5; number of HPT stages, $N_{HPT}\leq 3$; stage loading, $Y^{*}\leq Y^{*}_{max}$. Blades are nickel based alloy. Disc and casing are Inconel 718. Hardware is steel.

Combustor: The outer diameter equals that of the core 'maximum diameter' (High BPR: LPC tip diameter; Low BPR: HPC tip diameter; Turbojet: HPC tip diameter). The inner diameter is greater than or equal to 33% of the maximum diameter. The casing and liner have minimum 1/16" thickness. The stoichiometric air-to-fuel ratio (AFR) is assumed to be 15.0. Diffuser and combustor casings are Inconel 718. Combustor liner/flame tube is Nimonic C-263.

Table 14: Combustor sizing assumptions and input parameters.

Parameter	Value	Units
Air-to-fuel ratio, AFR_{stoich}	15.0	
Combustion flow velocity, v_{comb}	100.	ft/s
Passage flow velocity, v_{pass}	100.	ft/s
Flow residence time, t_{res}	0.015	s
Case density, ρ_{case}	511.	lbm/ft^3
Yield stress, σ	9x10^6	lbf/ft^2
Flame tube density, ρ_{ft}	539.	lbm/ft^3
Flame tube thickness, t_{ft}	0.00458	ft

Bypass Duct: The inner diameter is equal to the HPC tip diameter. The outer diameter is constrained to be less than the LPC inlet. The length is the sum of that of the HPC, combustor, HPT, LPT, and mixer. Minimum case thickness is 1/16" and the material is Titanium 318.

Mixer: The outer diameter is equal to the LPT exit. The inner diameter is approximated as half the LPT hub diameter. The casing is Inconel 718.

Table 15: Mixer sizing assumptions and input parameters.

Parameter	Value	Units
Length-to-height, L/H	1.5	
Case density, ρ_{case}	511.	lbm/ft^3
Casing thickness, t_{case}	0.0083	ft
Yield stress, σ	9x10^6	lbf/ft^2

Afterburner: The outer diameter is equal to the LPT exit or the bypass duct outer diameter. Minimum case thickness is 1/16" and the material is Nimonic C-263.

Primary Nozzle: The outer diameter is equal to the LPT exit or the bypass duct outer diameter. Length is 1.1 times diameter. The casing is Nimonic C-263.

Table 16: Nozzle sizing assumptions and input parameters.

Parameter	Value	Units
Primary Nozzle		
Length-to-diameter, L/D	1.1	
Case density, ρ_{case}	539.	lbm/ft^3
Casing thickness, t_{case}	0.023	ft
Secondary Nozzle		
Length-to-height, L/H	1.1	
Case density, ρ_{case}	276.	lbm/ft^3
Casing thickness, t_{case}	0.023	ft

Secondary Nozzle: The outer diameter at the inlet is equal to the fan tip diameter. The inner diameter at the exit is equal to the LPC inlet. The length is 1.1 times height. The casing is Titanium 318.

Shafts: The LP shaft is the inner shaft. There is no outer shaft for the turbojet.

Table 17: Shaft sizing assumptions and input parameters.

Parameter	Value	Units
LP diameter ratio, D_i/D_o	0.85	
Shaft clearance, δ	0.015	ft
Allowable stress, τ	7.3x10^6	lbf/ft^2
Shaft density, ρ_{shaft}	512.	lbm/ft^3

4.3 CPOX and SOFC Size Estimation

4.3.1 Overview

The mass of the CPOx/SOFC equipment and flow passage is (like the gas turbine) estimated using a detailed piece-by-piece summation of component masses. However, the task is simpler in this case because the geometries of the configurations are known (Figure 33, Figure 38, and Figure 39) and the material properties (Table 5) are well known so far fewer inferences are required.

The anode, electrolyte, and cathode are Ni-YSZ, YSZ, and LSM-YSZ, respectively. These are common material choices in SOFC MEA's [29,92,94]. The densities are 4.8, 6.0, and 4.6 g/cm^3 [92], respectively. Ceramic interconnects are required for high temperature (>850°C) cells [92,95], but those materials are less durable than metals. Fe-Cr-Mn and Fe-Cr-W with at least 17% Cr are typical for iron based interconnects [95]. In this work, an iron based metallic interconnect material is assumed with 7.8 g/cc density (consistent with stainless steels of similar composition). An alumina silicate type insulation material is assumed with 0.25 g/cm^3 density.

The CPOx units are connected to the fuel cell inlet via short channels that divide to feed the many anode flow paths. Anode channels outnumber CPOx units roughly 10 to 1, depending on the specific operating conditions. The mass of these channels is assumed to be part of the fuel cell inlet mass.

Recall from Section "3.3.1 CPOx/SOFC Assembly" that the power management system of the air vehicle will not be considered in this work. It is not anticipated that

shifting to SOFC power would fundamentally alter the scale of the power management system.

4.3.2 CPOx

The mass of a single CPOx unit (Figure 33) is calculated by summing the masses of the catalyst, duct, and insulation. The catalyst element in a single unit is 1 inch long and 1 in^2 in cross sectional area. The wall thickness is 0.0625 inches, and the insulation thickness is 0.042 inches. These dimensions were chosen because they provide a good balance between the competing factors of pressure drop, heat removal. The length-to-height of the inlet and outlet passages is 1.0 for each such that the length of the wall is approximately 3.4 in. This leads to a CPOx unit with a mass of 3.20 g. This mass is multiplied by however many CPOx units are in the modeled system. The CPOx geometry is just one of many that could have been chosen, however because the CPOx units make up a relatively small amount of the total CPOx/SOFC assembly mass (<5%), it is not expected that changing the geometry would significantly impact performance estimates.

4.3.3 SOFC

The mass of a single SOFC unit (Figure 38 and Figure 39) is calculated by summing the masses of the anode, cathode, electrolyte, interconnect, and insulation. For example, a SOFC circumferentially repeating unit with t_{ins} =1 mm, t_{div} =1 mm, t_{ext} =1 mm, w_{act} = 5 mm, and h_{ch} = 2 mm, and one radially repeating unit (Figure 39, $N_{rep} = 1$) has a mass of 1.45 g per cm of channel length. Because the exterior interconnect wall is a major contributor to the overall mass of the system that does

not repeat when expanding radially, specific power can be improved significantly by expanding the stack radially. For example, SOFC elements with 5 and 10 radially repeating units weigh 3.20 g per cm and 5.38 g per cm. Thus, a tenfold increase in MEA area can be achieved for less than a threefold increase in mass. The mass per length of channel is multiplied by the channel length and however many repeating SOFC units are in the modeled system to get the total mass of the channels.

The fuel cell inlet is composed of a number of identical channels. The number, height, and width of channels are identical to that of the combined SOFC units. The inlet length is 10 mm and the wall thickness is 0.5 mm (deliberately as small as possible to facilitate heat transfer). The wall density is the same 7.8 g/cm^3 as the SOFC interconnect material. The inlet mass is found by summing all the individual channel segments.

4.3.4 Duct and Hardware

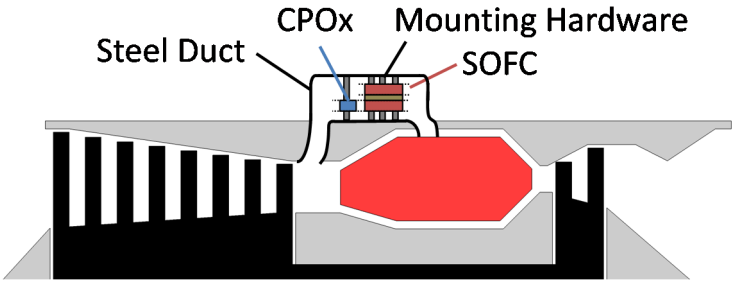

Figure 64: CPOx/SOFC assembly geometry with duct and hardware.

A steel duct is sized to contain the CPOx and SOFC units and the bypass flow channel. The wall thickness is 0.0625 inches, the material density is 511 lbm/ft^3, and the duct length is chosen to be long enough to contain the CPOx, inlet, and SOFC components. The flow area, A_{bp}, is determined in NPSS by setting the flow velocity, v_{bp}, to 10 ft/s. This area sets the outer diameter, D_o, of the duct:

$$A_{duct} = A_{bp} + A_{SOFC} = \frac{\dot{m}_{bp}}{\rho_{bp} v_{bp}} + N_{FC} A_{FC,unit} \tag{166}$$

$$D_o = \sqrt{D_i^2 + 4\frac{A_{duct}}{\pi}} \tag{167}$$

where $A_{FC,unit}$ is the cross sectional area of one SOFC unit, A_{SOFC} is the cross sectional area of the SOFC assembly, A_{duct} is the cross sectional area of the duct, $\dot{m}_{bp}$ is the bypass flow rate, and ρ_{bp} is the bypass flow density.

Also included in the mass estimate are a number of mounting bolts long enough to span the duct. The bolts are sized to support the weight of the SOFC assembly, W_{SOFC}. The yield stress of the bolts, σ, is 9x10^6 lbf/ft^2 and a safety factor of 2 is assumed. The number of bolts is initially calculated assuming a bolt diameter, D_{bolt}, of 0.25 inches:

$$N_{bolt} = \frac{(SF) W_{SOFC}}{\sigma\,(\pi D_{bolt}^2/4)} \tag{168}$$

For practical limitations, the number of bolts is constrained to between 24 and 40. If the calculated number falls below that range, it is reset to 24. If the number falls above that range, it is reset to 40 and the bolt diameter is increased to bear the additional load. The mass of the bolts is calculated:

$$W_{bolt} = N_{bolt} \frac{\pi D_{bolt}^2}{4} L_{bolt} \rho_{bolt} \tag{169}$$

An additional mass for mounting hardware is added in the form of 0.0625 inch supporting framework for the CPOx units. The framework has the length of 1 CPOx unit, the density of the duct material, and forms a series of concentric rings (one ring for each radially stacked SOFC channel) to which the CPOx units are mounted.

Chapter 5: Drag Modeling and Fuel Burn Comparison

5.1 Approach and Performance Metrics

The fuel mass flow rate is chosen as the key metric for comparing overall system performance because it is the main parameter influencing both range and endurance. It goes without explanation that if an aircraft is able to reduce the required flow of fuel while operating at the same flight conditions then that aircraft can travel farther or stay aloft longer.

The mass flow rate of fuel depends not only on the efficiency of the propulsion system but also on the thrust required. NPSS captures the thermodynamic (or efficiency) effects of any changes but additional analysis is required to capture the impact on thrust. There are two primary ways that the addition of the SOFC assembly can affect the thrust required by the vehicle at a given flight condition:

1) Increasing vehicle mass. This increases the required lift coefficient (for a given cruise speed) which in turn increases induced drag. This effect is accounted for by incorporating the vehicle drag polar in Section "5.2 Vehicle Drag Model".
2) Adding volume which can increase surface and form drag. Added volume can also increase the thrust required if it obstructs the engine's thrust producing exhaust flow(s). This effect is addressed in Section "5.3 SOFC External Aerodynamics".

5.2 Vehicle Drag Model

The selection of appropriate engine operating conditions requires some knowledge of the aerodynamic properties of the aircraft in which the engine is installed. In this study, two types of aircraft are considered: a high altitude long endurance (HALE) UAV and a regional transport jet (RTJ). The assumed properties for these aircraft are summarized in Table 18. The HALE UAV is expected to operate at high altitude (16.8 km) and relatively low Mach number (0.5). The size characteristics [5] and drag polar [12] are chosen to be consistent with a vehicle similar to the Northrop Grumman RQ-4 Global Hawk. The second aircraft is a regional transport jet (RTJ) expected to operate at high subsonic Mach numbers. The size characteristics and drag polar [12] of the regional jet are chosen to be consistent with a generic jet transport in that class.

Table 18: Simulated aircraft specifications.

Parameter	HALE	RTJ	Units
Airframe			
Wingspan, b	40.0	20.0	m
Wing area, S	64.0	50.0	m^2
Aspect ratio, AR	25.0	8.0	
Loaded airframe*	7,000	15,000	kg
Fuel capacity	7,500	4,000	kg
Aerodynamics			
C_{Dmin}	0.0195	0.016	
K	0.01725	0.09	
C_{Lmin}	0.3	0.1	
Powerplant			
Number of engines	1	2	
Total rated thrust	35.0	70.0	kN

*Loaded airframe weight includes payload but not fuel or engines

Thrust is assumed equal to drag which is calculated using standard approaches [11,108,109]. The assumed form of the drag polar is $C_D = C_{Dmin} + K(C_L - C_{Lmin})^2$ [12] where $C_L = Lift/(qS)$ is the lift coefficient, $C_D = Drag/(qS)$ is the drag

coefficient, $q = \rho_{air} v^2/2$ is the freestream dynamic pressure, v is the flight speed, and S is the wing area. C_{Lmin} is the minimum lift coefficient, and C_{Dmin} is the drag coefficient at C_{Lmin}. The additional mass of the CPOx/SOFC assembly increases the required lift coefficient which increases the thrust required to fly at the same condition. The increase in required thrust is the mechanism by which SOFC system mass influences fuel burn.

5.3 SOFC External Aerodynamics

This investigation of the integrated GT-SOFC system assumes that the CPOx/SOFC is housed in an annular ring around the hot section of the engine as illustrated in Figure 65.

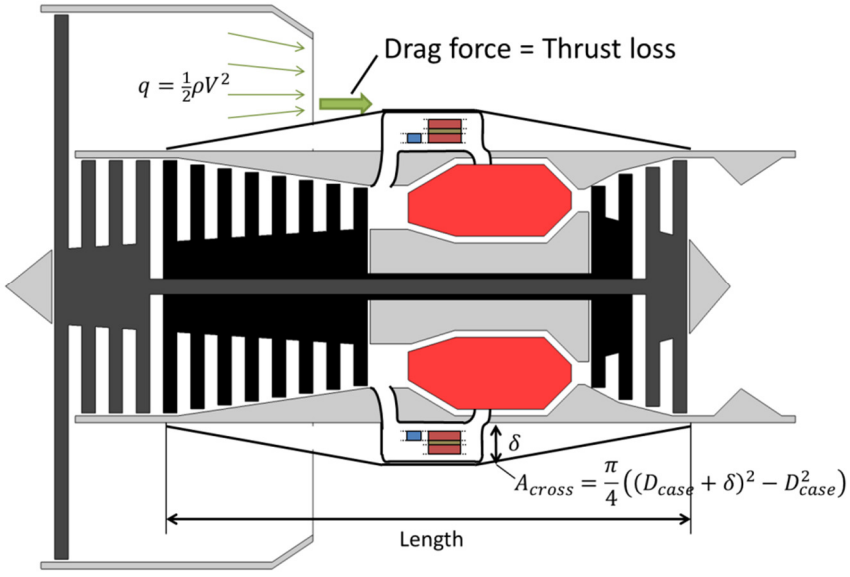

Figure 65. Illustration of drag on normal fuel cell assembly.

A major drawback of this configuration is that it blocks the secondary (bypass) flow in a separate exhaust turbofan engine. Initial investigations of integrated GT/SOFCs did not account for this effect on performance but later work showed that

it was very important. Therefore, a model for the external aerodynamic drag of the SOFC assembly is developed here.

The analysis follows the approach of Raymer Ref. [11]. Eq. (170), adapted from Raymer, gives the drag force on a component in terms of local flow dynamic pressure (q), skin friction coefficient (C_f), pressure drag form factor (FF), and wetted area (S_{wet}). The flow downstream of the fan is assumed to be turbulent and C_f is assumed to vary with local flow Reynolds number (Re) and Mach number (M) per Eq. (171) [11]. The form factor is assumed to vary with the 'fineness' ($f = length/\sqrt{(4/\pi)A_{cross}}$) of the fuel cell duct via Eq. (172) [11]. The resulting drag force is subtracted from the engine thrust to account for the external aerodynamic losses associated with the fuel cell assembly. The performance penalty increases as the fuel cell volume increases leading to increased fuel burn in the GT portion of the cycle.

$$D = qS_{wet}C_fFF \tag{170}$$

$$C_f = \frac{0.455}{(\log_{10} Re)^{2.58}(1 + 0.144M^2)^{0.65}} \tag{171}$$

$$FF = 1 + 60/f^3 + f/400 \tag{172}$$

For high BPR turbofan integrations that differ from the one illustrated in Figure 65, only the portion of the fuel cell assembly that extends out into the engine's secondary flowpath is considered. This arrangement is illustrated in Figure 66. The same principles apply as well as the same equations (above), but as can be seen in the figure, a fuel cell assembly of the same diameter protrudes a smaller distance, δ, into the flow. As a result, the drag force on the assembly will be greatly reduced.

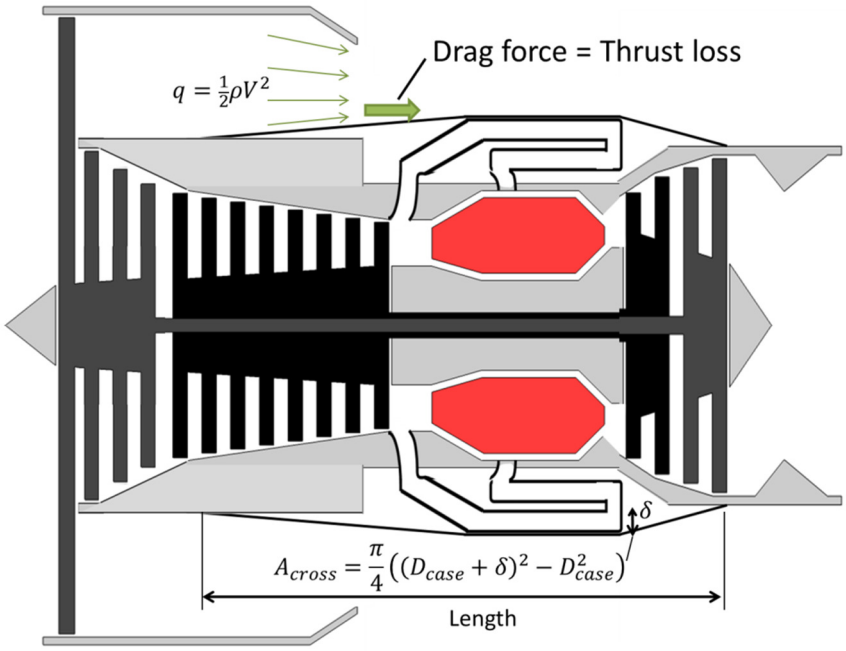

Figure 66: Illustration of drag on recessed fuel cell assembly

Chapter 6: Testing and Validation of Subsystem Models

6.1 Gas Turbine Mass Model Validation

The accuracy/reasonableness of the engine mass model is checked by comparing its predictions to the masses of actual engines from Ref [16]. This is extremely challenging since the sizing model has dozens of inputs and it is impossible to know their values for all engines in the sample. Therefore, the approach taken here is to do a comparison based on an extremely limited subset of parameters: sea level air flow rate, number of compressor stages, bypass ratio (BPR), and overall pressure ratio (OPR). Air flow, compressor stages, and BPR were available from Ref [16]. OPR was estimated by generalizing high BPR, low BPR, and turbojet engines as having OPR = 36, 24, and 8, respectively. The values selected for other parameters in the model are chosen to represent typical values (based on ranges presented in Ref. [107]) and not necessarily any specific engine. The values used were presented in Section "4.2 Gas Turbine Size Estimation" and Table 8 through Table 17. The choice of values impacts the predicted mass, but because the goal in this work is to predict mass of a 'typical' engine, using values in the typical range will deliver the desired result.

The results are plotted in Figure 67 with mass estimation error (error = (estimated mass – actual mass)/actual mass) on the vertical axis and actual engine mass on the horizontal. Although there is significant scatter, this is expected given the skeletal nature of the inputs. The figure shows that the model predicts engine mass to within ±28% for 90% of engines with little bias toward over- or under-prediction. The average error between predicted and actual engine mass for all engines is ±14%.

Average error drops to ±10% (and ±22% captures 90% of engines) when only American-built engines are considered. The reasons for this are not clear but could be because Onat and Klees only considered U.S. engines when developing their model.

While the engine mass model is not perfect, there is no single 'correct' thrust for an engine of a particular mass and BPR and the uncertainty of the mass estimate will be accounted for when predicting the performance of GT-SOFC systems. Therefore, we believe the mass model is sufficient for the purposes of the comparisons made in this work.

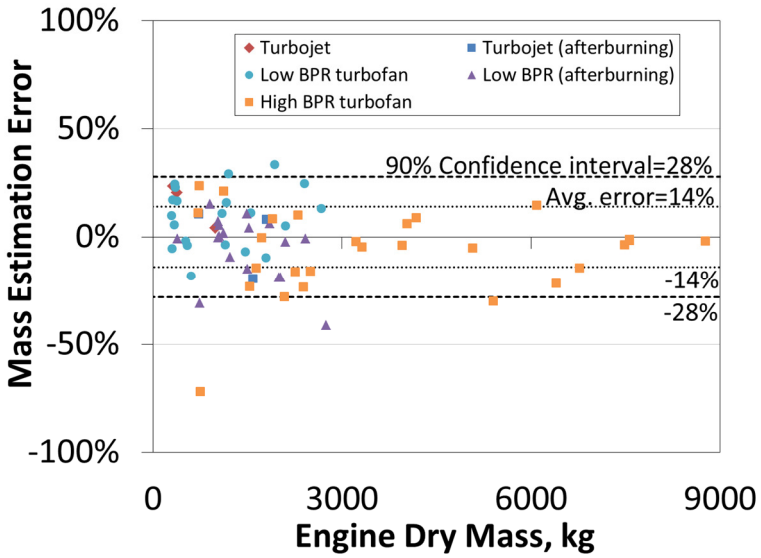

Figure 67. Gas turbine mass estimate validation.

6.2 Gas Turbine Performance Model Validation

The NPSS gas turbine models are validated via comparison to the performance of actual engines. Six configurations are considered:

(1) Turbojet, single spool, OPR=24

(2) Low BPR turbofan, combined exhaust, OPR=24, BPR=0.5

(3) High BPR turbofan, separate exhaust, OPR=24, BPR=5

(4) High BPR turbofan, separate exhaust, OPR=31.5, BPR=5

(5) High BPR turbofan, separate exhaust, OPR=40, BPR=5

(6) 'Very' High BPR turbofan, separate exhaust, OPR=40, BPR=8

Details of the engine configurations and parameters are presented in Table 19.

Table 19: Gas turbine engine parameters and performance.

	Engine					
	(1)	(2)	(3)	(4)	(5)	(6)
Design parameters,						
Bypass ratio	-	0.5	5.0	5.0	5.0	8.0
Pressure ratio	24.0	24.0	24.0	31.5	40.0	40.0
T.I.T., K	1600	1600	1600	1600	1600	1600
Fan efficiency	-	-	0.86	0.86	0.86	0.86
LPC efficiency	-	0.88	0.88	0.88	0.88	0.88
HPC efficiency	0.88	0.88	0.88	0.88	0.88	0.88
HPT efficiency	0.87	0.87	0.87	0.87	0.87	0.87
LPT efficiency	-	0.87	0.87	0.87	0.87	0.87
SLS condition:						
Mach=0, Alt.=0,						
Max. thrust, kN	35.0	35.0	35.0	35.0	35.0	35.0
Airflow, kg/s	35.97	45.31	111.81	112.85	114.35	134.99
High altitude:						
Mach=0.5, Alt.=16.8 km,						
Max. thrust, kN	5.29	5.30	3.95	3.99	4.03	3.74
Airflow, kg/s	5.58	7.26	16.24	16.51	16.87	19.91
Mid-altitude cruise:						
Mach=0.8, Alt.=10.7 km,						
Max. thrust, kN	15.25	14.36	9.98	10.02	10.04	9.06
Airflow, kg/s	17.19	21.50	50.62	51.39	52.39	62.10
Sizing,						
Dry mass, kg	590.2	676.8	587.6	578.6	578.5	603.9
Diameter, m	0.551	0.619	0.873	0.877	0.883	0.915
Length, m	1.561	2.306	1.967	1.932	1.898	2.047

The OPR of Engines (1) through (3) are held constant to allow the most meaningful comparison between engine types. All engines are sized to produce 35 kN rated thrust at sea level static (SLS) conditions in order to represent performance appropriate for a large UAV (e.g., the Northrop Grumman RQ-4 Global Hawk) or a regional transport jet (e.g., the Embraer ERJ-145). Component efficiencies are chosen to be consistent with late 20th century technology [110].

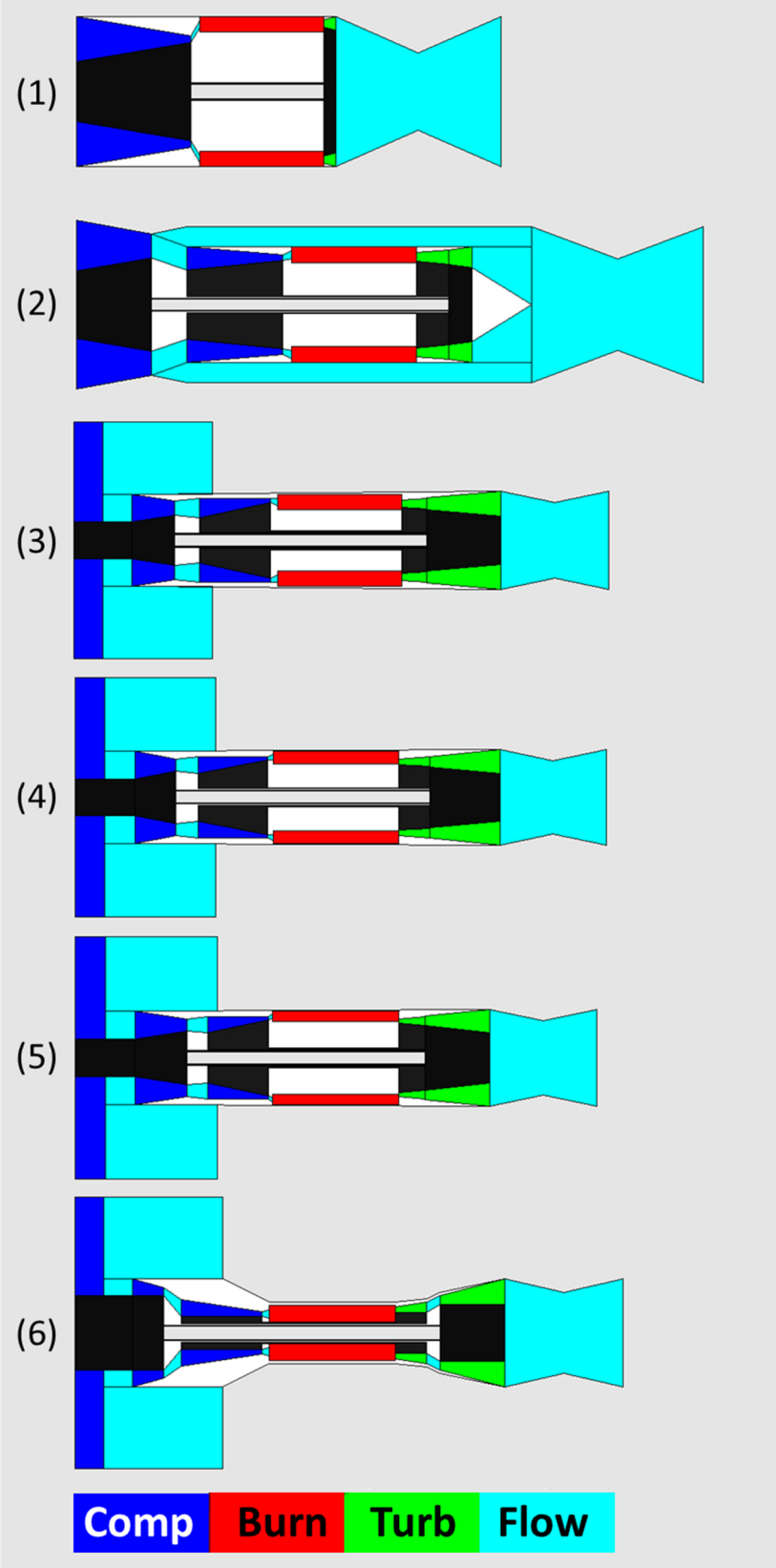

Figure 68. Scale layout view of the engines in the study: turbojet (top), low BPR turbofan (second), and four high BPR turbofan variants (bottom).

Figure 68 presents schematic illustrations of the six engines. Compressors are shown in dark blue, combustors in red, turbines in green, and flow passages in light blue. There is little difference between the geometries of (3), (4), and (5). All are BPR=5 turbofans and only vary in OPR (24, 31.5, and 40, respectively). Figure 69 shows thrust specific fuel consumption (TSFC) as a function of thrust (or power setting) for the various engine configurations. Only one curve (OPR=24) is presented for the 5.0 BPR engines because of their similarity but the higher OPR engines show slightly improved TSFC.

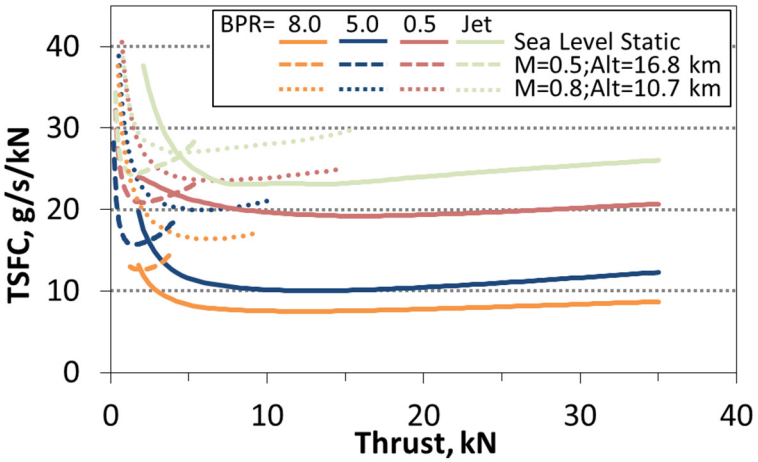

Figure 69. Thrust specific fuel consumption of three engine configurations at high altitude and sea level static conditions as thrust setting is varied.

Table 20 compares predicted TSFC to average TSFC of real engines in each of four classes: turbojets, turbofans with BPR < 1.2, turbofans with $4.8 <$ BPR < 5.2, and turbofans with $7.5 <$ BPR < 8.5. The data used to make the comparison comes from Roskam and Lan [111], Leyes and Fleming [112], and St. Peter [113].

The results show that the TSFCs predicted by the GT model fall within the known ranges for each class of engine. The low BPR turbofan deviates +1% from the sample average while the high BPR models deviate by -4% to +7% from the sample average.

The turbojet prediction deviates significantly more (-24%, below the sample average) but this is likely because the modeled turbojet OPR is 24 which is higher than a typical engine in that class. Recall that OPR was held fixed at 24 between engines (1), (2), and (3) to allow for meaningful comparisons between engine types. Modeling a more typical OPR=8 turbojet produces a TSFC within 3% of the sample average. The 'very' high BPR model differed by -15% from the only available data point, but of course one engine is not a representative sample. Overall, these results show that the GT models produce reasonable estimates of engine performance and thus are suitable for evaluating the performance of engine-integrated SOFCs.

Table 20: Comparison of predicted to actual TSFC (g/s/kN).

		Reference Engine Data		
Engine type	Model	Mean	Std.	$N_{Samples}$
Turbojet, (1)	26.0	34.3	6.8	75
Low BPR, (2)	20.7	20.5	2.9	10
High BPR, (3-5)	11.1-12.3	11.5	0.8	10
V. High BPR, (6)	8.7	10.2	-	1

6.3 CPOx Performance Model Testing

Unlike the gas turbine mass and performance models described above, experimental data are less available to make direct comparisons between predicted and observed CPOx performance. So, the model will be checked by confirming that basic principles of chemical equilibrium are upheld. While the CPOx model has 8 segments, flow-wise resolution has no impact on the results presented in this section because the exit temperature and pressure are fixed and the model calculates output compositions at equilibrium conditions.

Figure 70 and Figure 71 show CPOx reactor output composition as a function of air to fuel ratio (AFR) at different temperatures and pressures. The red curves in the figures show that the degree of conversion of fuel (JP-5) to CO and H_2 (syngas) increases as the AFR decreases. The red curve in Figure 70 shows that the degree of conversion also increases with operating temperature. However, the blue curve shows that graphite starts to form below some threshold AFR. This places a limit on the degree to which AFR can be reduced (and conversion increased) without the risk of fouling by graphite formation (coking). Raising the temperature shifts the limit to lower AFR where conversion is higher, so maximizing CPOx operating temperature is doubly favorable. In contrast, Figure 71 shows that raising the CPOx pressure is doubly unfavorable: Increasing the pressure reduces syngas production overall and shifts the limiting AFR for graphite formation to higher AFRs (i.e., leaner mixtures) where syngas production is lower still. The practical implication of this is that graphite formation places limits on the degree of conversion that is realizable.

These results are consistent with basic concepts of chemical equilibrium. In particular, they are direct consequences of Le Chatelier's principle which states that the equilibrium state of a mixture shifts to counteract any change imposed on the system. In this case, increasing the mixture temperature shifts equilibrium to compositions with more higher energy products like CO and H_2 and fewer lower energy products like CO_2, H_2O, and C at a particular AFR. This is because forming molecules containing more internal chemical energy reduces the amount of thermal energy in the mixture (counteracting the temperature increase). Increasing pressure shifts the equilibrium toward the formation of fewer moles of products. Thus as

pressure increases, the favored products shift toward CH_4, CO_2, and H_2O in place of CO, H_2, and C. This is because forming molecules containing more atoms reduces the number of moles of products (counteracting the pressure increase).

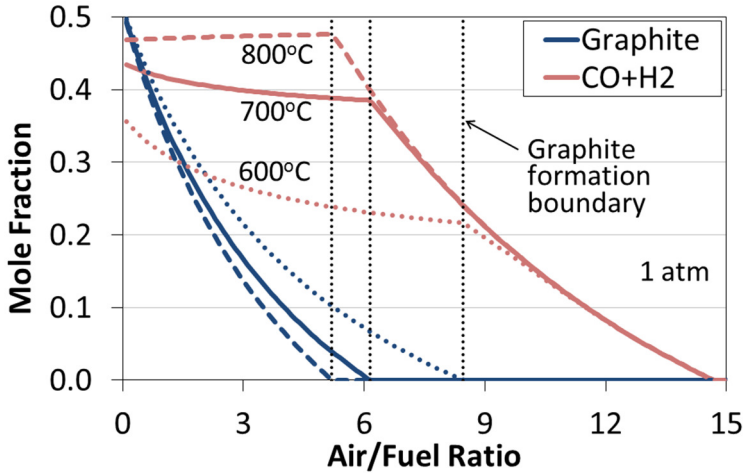

Figure 70. Formation of desired products (CO, H_2) and graphite as a function of the air to fuel ratio for various temperatures at 1 atm.

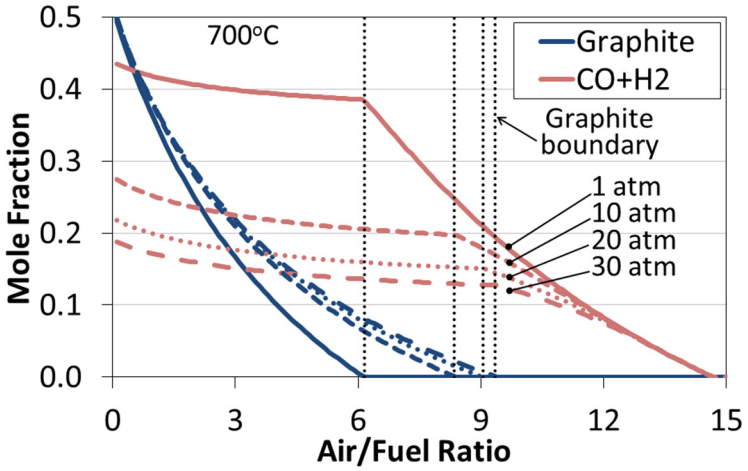

Figure 71. Formation of desired products (CO, H_2) and graphite as a function of the air to fuel ratio for various pressures at 700°C.

6.4 Fuel Cell Heat Transfer Model Testing

A series of tests have been run to examine the function of the fuel cell heat transfer model and to verify that it produces physically reasonable results. The

simulations run for this analysis correspond to t_{ins} =1 mm, t_{div} =1 mm, t_{ext} =1 mm, w_{act} = 5 mm, and h_{ch} = 2 mm (see Figure 39 in Section "2.3.4 Fuel Cell Element"). The channel temperature is 1000 K and the ambient temperature is 500 K.

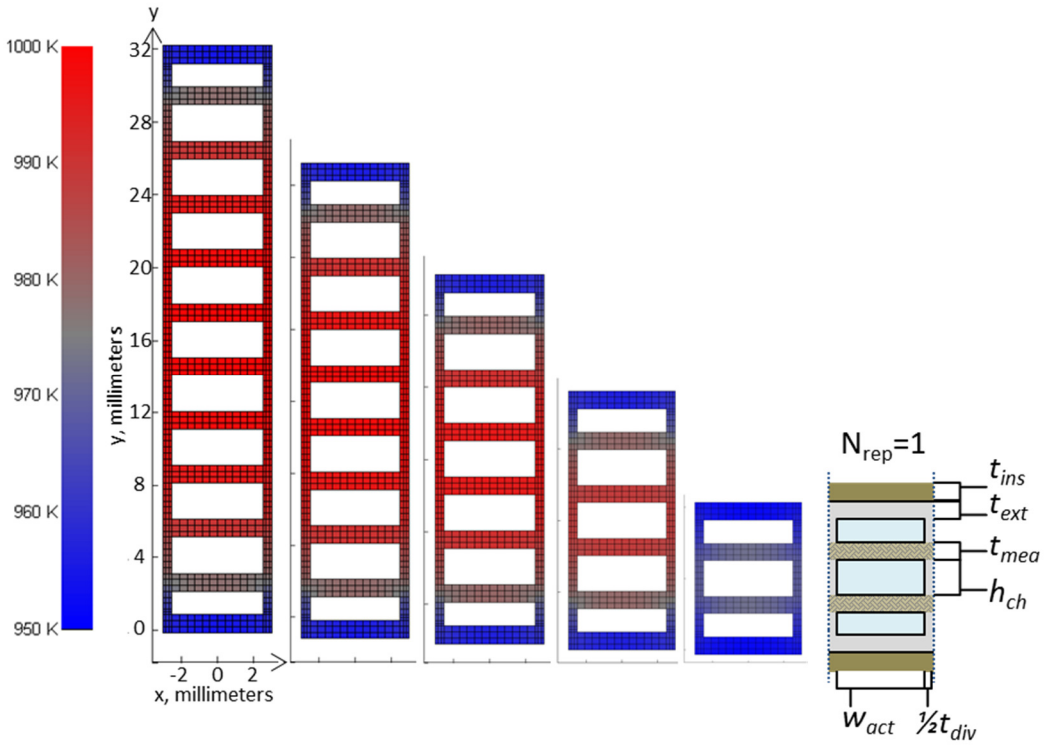

Figure 72. Temperature distribution in interconnect and MEA for various N_{rep}.

Figure 72 shows how the temperature distribution in the fuel cell stack (determined via the finite volume heat transfer model described in Section "2.3.4 Fuel Cell Element" and Appendix D) changes as the number of radially repeating fuel cell elements (N_{rep}) varies from 1 to 5. Note that blue in the temperature gradient is only relative low temperature (still quite hot). A portion of Figure 39 is reproduced at the far right to remind the reader of the meanings of the various geometric parameters of the channel/MEA assembly and to indicate the location of the insulating material. As expected, in each case temperature is greatest in the center of the assembly and lowest near the walls (top and bottom). The total temperature difference is less than 50 K

because the assembly is insulated. Recall that due to symmetry, no heat transfer occurs circumferentially (left and right). Also as expected, peak temperatures increase with N_{rep} because the larger assemblies have lower surface/volume ratios and thus retain more thermal energy. It can also be seen in the figure that for higher N_{rep} the temperatures in the outer cells (near the wall) begin to exhibit increasingly similar distributions. The importance of this is discussed below.

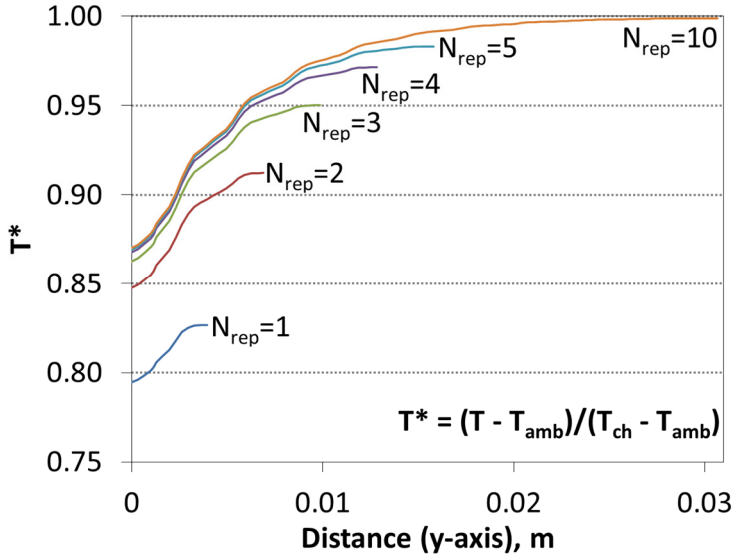

Figure 73. Heat transfer convergence at high N_{rep}.

Figure 73 illustrates temperature profiles near the insulated exterior wall as the number of repeating channel/MEA segments, N_{rep}, is increased. The temperature is plotted non-dimensionally (relative to the ambient temperature of the surrounding flow, T_{amb}, and the temperature of flow in the channels, T_{ch}) because the magnitude of ΔT between the channels and ambient does not affect the shape of the profile. The results show that the temperature profiles, and consequently the heat loss rate, quickly converge at high N_{rep}. This indicates when a large geometry (high N_{rep}) is required, a much smaller geometry (low N_{rep}) can be modeled in its place with minimal loss of

accuracy. Modeling the low N_{rep} geometry greatly reduces computation times. It is important to note that the smaller geometry is only used for calculating heat loss and not for all other fuel cell calculations. The number of required segments varies as a function of various geometric and heat transfer parameters, but any reduction in model size is constrained to require less than 0.5% error.

6.5 Fuel Cell Model Testing

The physical reasonableness of the electrochemical model is evaluated by computing fuel cell performance over a range of temperatures and pressures. The fuel stream is the CPOx output at the specified temperature and pressure with the air/fuel ratio set to the lowest possible value that does not lead to graphite formation (in order to maximize conversion in the CPOx). Figure 74 and Figure 75 show the operating voltage and power density of the MEA as functions of current density. They are analogous to button-cell results in that they isolate the electrochemical performance of the specified MEA without impact from down-the-channel effects of heat loss and reactant depletion. Figure 74 shows performance at 1 atm pressure and various temperatures. It illustrates the importance of maintaining an appropriate cell temperature as performance drops nonlinearly with decreasing temperature. Figure 75 shows performance at 700℃ and a range of pressures. While raising the pressure from 1 to 10 atm increases power density by ~50%, further increases in pressure yield progressively smaller improvements in power density. Taken together, the characterizations of the CPOx and fuel cell models suggest that there will be an

interesting system-level trade between improved fuel cell performance and degraded CPOx performance as pressure increases.

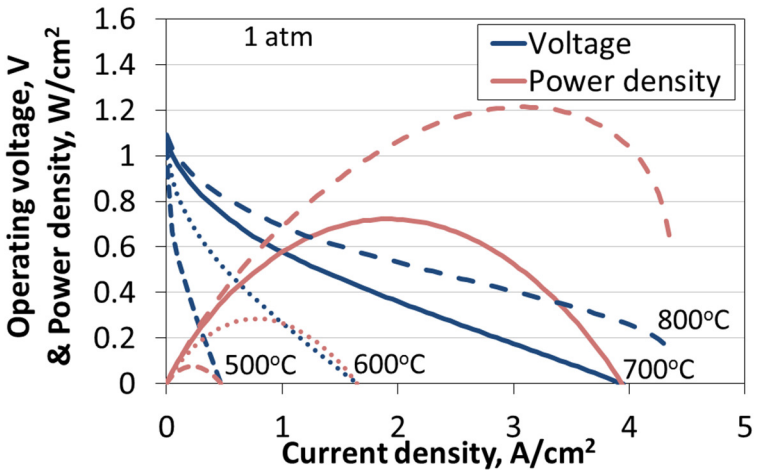

Figure 74. Performance of MEA operated at 1 atm and various temperatures.

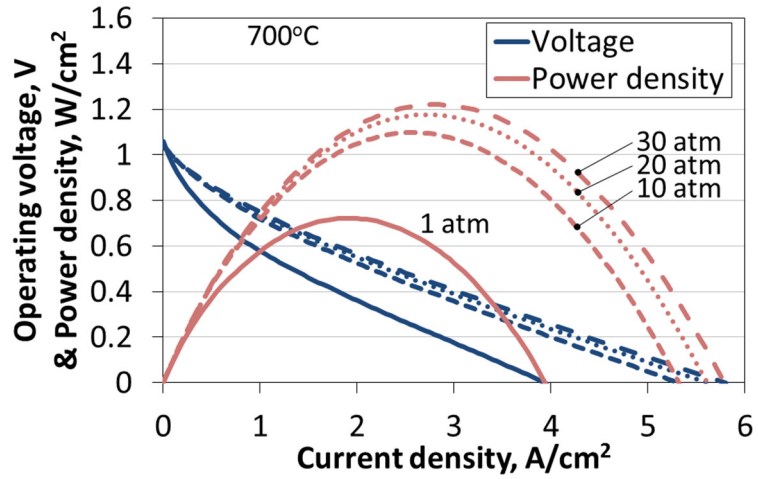

Figure 75. Performance of MEA operated at 700°C and various pressures.

Figure 76 shows how the current density, temperature, and composition vary as a function of distance down a baseline radially repeating unit cell (i.e., a single anode channel with two cathode channels; see Figure 38) at the following conditions: $T_{CPOx\ inlet} = 750$°C, $P_{CPOx\ inlet} = 1$ atm, $V_{oper} = 0.7$ V, $\dot{m}_{fuel} = 2.16 \times 10^{-7}$ kg/s, $L = 25$ cm. The finely resolved profiles are achieved by breaking the channel into 1024 flow-wise segments. The dimensions of the anode channel are 4×2 mm and

the cathode channel is 2×2 mm. The insulation thickness in this test is set to maintain an SOFC exit temperature of 750°C. The power output is 3.65 W, the flow temperature reaches a peak of 804°C, and the total percent oxidation of the fuel is 97% at the exit.

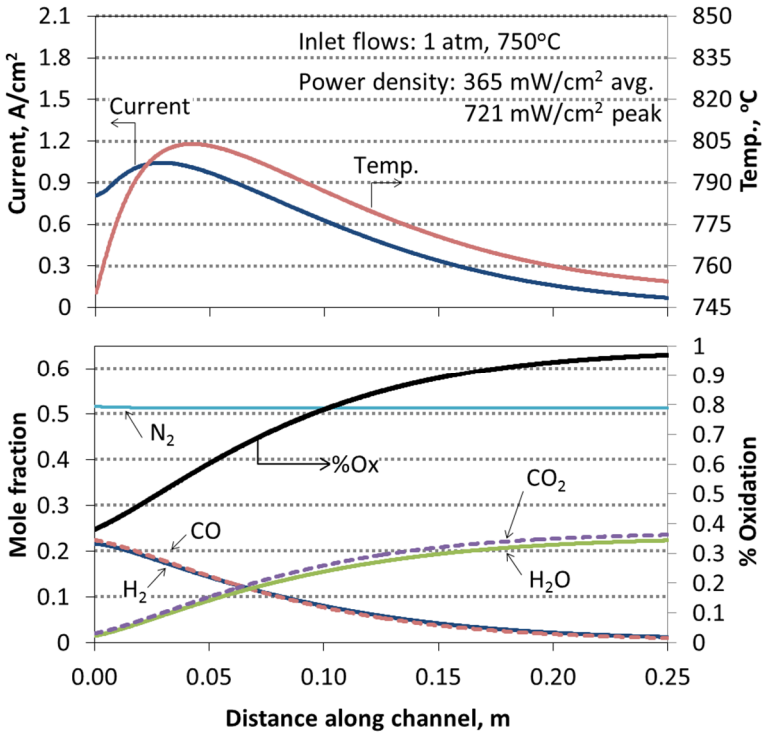

Figure 76. Temperature and species concentration profiles along the SOFC channel at 0.7 V with inlet flows at 1 atm and 750°C.

Reducing the number of flow-wise segments to 8 changes the values of all of these parameters by less than 0.5% indicating that 8 elements is sufficient to limit discretization error to acceptable levels. The results are also very similar (both quantitatively and qualitatively) to studies of CPOx/SOFC systems operating on long hydrocarbon fuels by Zhu and Kee, et al. [23,29,91]. While direct comparisons are not possible because of differences in geometry, the strong similarity inspires confidence in the accuracy of the model's predictions.

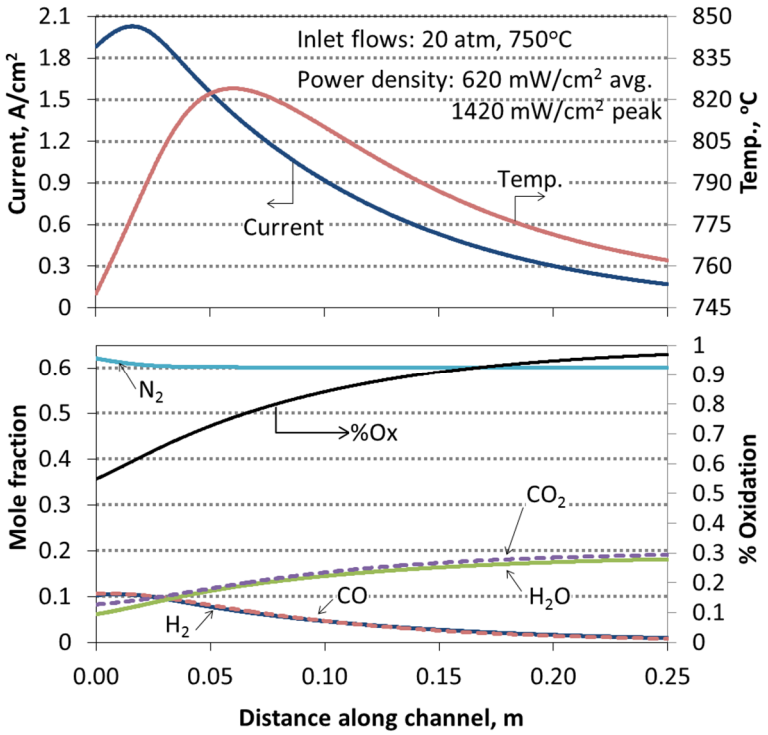

Figure 77. Temperature and species concentration profiles along the SOFC channel at 0.7 V with inlet flows at 20 atm and 750°C.

Figure 77 shows down-the-channel performance at 20 atm for the same channel configuration, physical dimensions, inlet temperature, and operating voltage as the 1 atm case. However, the fuel mass flow rate has been increased to $\dot{m}_{fuel} = 5.13 \times 10^{-7}$ kg/s in order to keep the percent oxidation at 97% and the insulation thickness is decreased to maintain the SOFC exit temperature at 750°C. The peak flow temperature increases to 824°C (because of the increased fuel consumption and reaction rate), the peak current density almost doubles, and the power output of the cell increases to 6.20 W. Reducing the number of segments from 1024 to 16 results in an acceptable (<0.05%) loss of fidelity. A further reduction in the number of segments to 8 leads to errors that are only on the order of 0.25%. Overall, the results

suggest that models based on 8 to 16 segments offer a reasonable compromise between accuracy and computational time.

Chapter 7: Results and Discussion

7.1 Sensitivity Analysis and Error Estimation

A concern when constructing models of complex nonlinear systems like this one is the possibility that uncertainties in the input parameters will lead to uncertainties in the output that are larger than the effects trying to be observed. Therefore, a sensitivity analysis is performed to quantify the influence of several important parameters on the predicted fuel mass flow rate. These are burner/fuel cell pressure drop, fuel cell assembly mass, engine mass, MEA overpotentials, fuel cell heat loss rate, compressor efficiencies, turbine efficiencies, cooling air flow rate, fuel cell global air-fuel ratio, aircraft minimum drag coefficient ($C_{d,min}$), induced drag factor (K), overall pressure ratio, fuel cell exit temperature, operating voltage, and channel width, length, and height. The sensitivity coefficient is defined as the ratio of the fractional change in fuel flow rate to the fractional change in the perturbed parameter relative to the reference configuration.

Figure 78 shows the values of the sensitivity coefficients for the parameters stated above. The reference configuration is the BPR=5, OPR=24 high bypass ratio turbofan engine with a with a 50 kW fuel cell. Two SOFC operating states are considered: 0.7 V, 90% fuel oxidation (blue) and 0.6 V, 75% fuel utilization (red). No sensitivity coefficients change sign between the two cases. Most show no significant change in magnitude with the exceptions being operating voltage, percent fuel oxidation, fuel cell air-to-fuel ratio, channel width, and channel height.

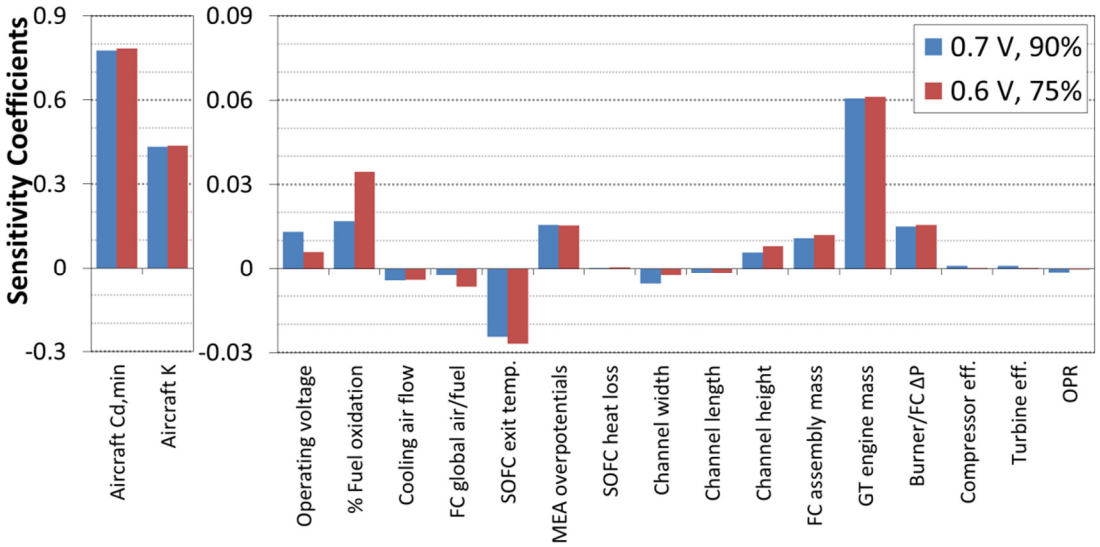

Figure 78. Sensitivity of the total fuel flow rate in BPR=5, OPR=24, 50 kW GT-SOFC hybrid on HALE UAV to several model parameters.

The figure shows that fuel flow rate is most sensitive (by an order of magnitude) to the parameters associated with aircraft drag. This illustrates the importance of identifying GT-SOFC hybridization schemes with minimum aerodynamic impact. The issues associated with drag effects of the SOFC assembly volume are more fully discussed in Section "7.4 Integrated GT-SOFC Accounting for Fuel Cell Volume".

The next largest coefficients (nearly an order of magnitude smaller) include GT engine mass (which is independent of the fuel cell assembly) and the SOFC exit temperature (set by materials limitations). The most influential parameters that are actually design choices for the fuel cell system are percent fuel oxidation, cell operating voltage, cooling air flow rate, and fuel cell global air to fuel ratio. Therefore, efforts aimed at improving the fuel cell side operation of GT-SOFC performance could target optimization of these parameters. Performance is relatively less sensitive to operating voltage and more sensitive to percent fuel oxidation at the 0.6 V, 75% operating condition. Lowering both operating voltage and percent fuel

oxidation is expected to lead to higher system level performance. Performance is also more sensitive to the air-to-fuel ratio at the 0.6 V, 75% operating condition.

The length, width, and height of the flow channels are less important than the previously mentioned parameters and also are heavily influenced by fluid dynamic and construction-related constraints that are not captured by the level of fidelity in the current modeling effort. Thus, these are less well-suited for optimization using the present model.

A major concern when attempting to predict the performance of complex systems is the degree to which uncertainties in model inputs influence/drive model outputs. To this end, the sensitivity analysis can also be used to gauge the overall reliability of the model's predictions. This is accomplished by calculating the change in system performance associated with varying key model parameter by an appropriate uncertainty level and summing the results in a root sum square (RSS) manner. The parameters considered are those in the sensitivity analysis. The uncertainty of most parameters is taken to be ±10% which is quite conservative (i.e., most parameters are known better than this). Considering all parameters directly relevant to the GT-SOFC (i.e., everything in Figure 78 except C_d and K), the RSS combined uncertainty of the fuel flow rate in the 50 kW system is only 0.74% and 0.80% for the 0.7 V, 90% and 0.6 V, 75% cases respectively. While uncertainties are larger in higher power systems because the relative size and importance of the SOFC assembly grows (i.e., ±10% mass of a 150 kW SOFC is a larger fraction of vehicle mass than that of a 50 kW SOFC), the predicted reduction in fuel burn (demonstrated in the following chapter)

also grows and remains well above the uncertainty level. Therefore, the predicted performance improvements are not artifacts of the modeling assumptions.

Variations in the aircraft minimum drag coefficient ($C_{d,min}$) and induced drag factor (K) are considered separately because they are air vehicle parameters that are presumably well known. No changes to the power/propulsion system would be expected to alter the induced drag factor. As discussed above, any SOFC assembly geometry that significantly impedes flow through or around the engine will be unacceptable. Whether bookkept as an increase in C_d or as a decrease in thrust, the result would be the same: greatly increased fuel burn. This point will be examined later in the chapter.

7.2 Importance of Engine and Flight Conditions to SOFC

7.2.1 Influence of Altitude, Mach, and OPR on Supply Air Conditions

The engine's operating state (commanded power level and internal conditions) changes significantly with the vehicle's altitude and phase of flight. The result is that conditions under which the CPOx and SOFC operate can vary widely in integrated GT-SOFC systems. Therefore, it is necessary to understand the effects of engine operating state, cycle type, and altitude/flight regime on integrated CPOx/SOFC performance.

To better understand engine/SOFC coupling, recall that the performance of the fuel cell is dependent on the flow conditions exiting the compressor. The pressure is primarily a function of OPR and altitude. The temperature is a more complicated

function of altitude, flight speed, OPR, and compression efficiency. Assuming adiabatic ram compression, the compressor exit temperature can be expressed:

$$T_{c,exit} = T_{amb}\left(1 + \frac{\gamma - 1}{2} M^2\right)\left(\left(OPR^{1-\frac{1}{\gamma}} - 1\right)/\eta_c + 1\right) \tag{173}$$

Dependence on altitude enters via the ambient temperature, T_{amb}, which is a function of altitude in a standard atmosphere [84].

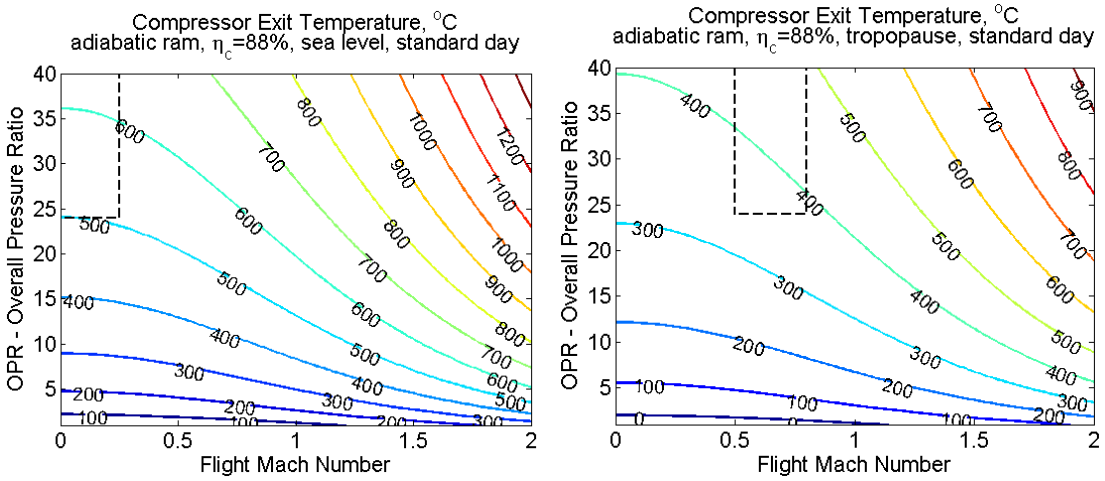

Figure 79. Compressor exit temperatures v. OPR and Mach: sea level (L), tropopause (R).

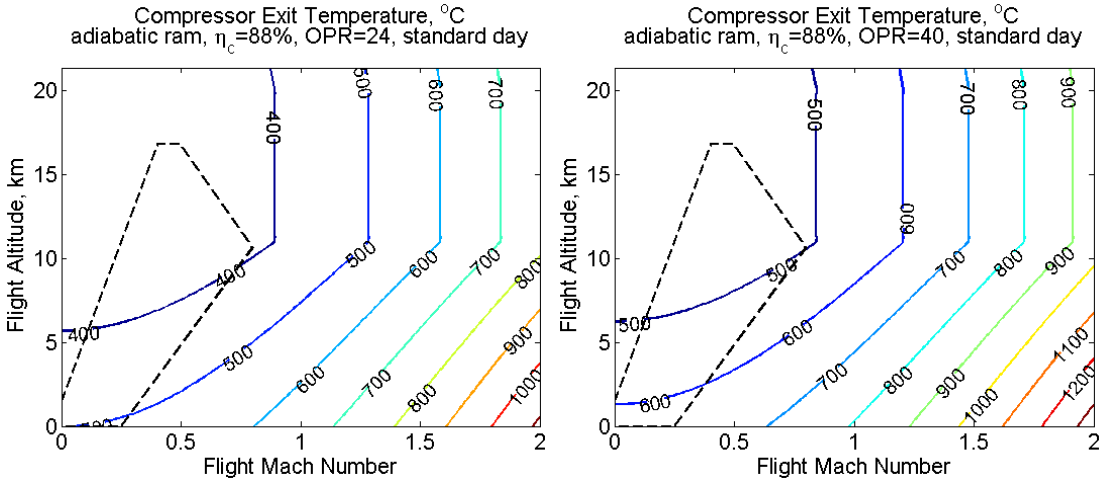

Figure 80. Compressor exit temperatures v. altitude and Mach: OPR=24 (L), OPR=40 (R).

Compressor exit temperatures are shown as a function of OPR and Mach number in Figure 79. Compressor isentropic efficiency is 88% and standard day is assumed.

The left portion of the figure shows contours of constant temperature at sea level. The dashed rectangle represents an approximate region of interest in this work corresponding to the engines considered and likely flight speeds at very low altitudes (OPR = 24-40, Mach (M) = 0-0.25). The right portion of the figure shows contours of constant temperature in the tropopause (approximately 11.3 to 19.8 km). The dashed rectangle represents an approximate region of interest in this work corresponding to the engine and flight conditions considered (OPR = 24-40, M = 0.5-0.8).

Contours of compressor exit temperature are shown as functions of altitude and Mach number in Figure 80. Compressor isentropic efficiency is 88% and standard day is assumed. The left portion of the figure shows temperatures for OPR=24. The right portion of the figure shows temperatures for OPR=40. The dashed rectangles represent an approximate region of interest in this work enclosing sea level low Mach number flight for takeoff and the two design flight conditions considered (regional jet: 0.8 Mach, 10.7 km; HALE UAV: 0.5 Mach, 16.8 km).

As expected, temperatures are greater at higher Mach, lower altitude, and higher OPR. Because the fuel cell temperature is limited to 850^{o}C due to materials limitations, compressor exit temperatures exceeding this value are unacceptable. Fortunately, the regions of current interest are well below 850^{o}C.

7.2.2 Influence of Supply Air Conditions on SOFC Performance

The influence of operating conditions on the performance of the integrated CPOx/SOFC is investigated by considering SOFC performance in a BPR=5, OPR=24 turbofan operating at four conditions:

- HALE UAV flight (Figure 81): 16.8 km / 55 kft altitude, M=0.5, full throttle

- Regional jet flight (Figure 82): 10.7 km / 35 kft altitude, M=0.8, full throttle
- Sea level 'takeoff' (Figure 83): sea level, static, full throttle
- Sea level 'idle' (Figure 84): sea level, static, 7% of rated thrust

A fifth condition studied is a BPR=5, OPR=40 turbofan engine at high altitude:

- HALE UAV flight (Figure 85): 16.8 km / 55 kft altitude, M=0.5, full throttle

Recall that the aircraft specifications were described in Section "5.2 Vehicle Drag Model" and Table 18.

An 8 segment CPOx model (catalyst length=25.4 mm, diameter=2 mm) feeds the SOFC anodes. One CPOx unit feeds approximately 10 SOFC anode channels (which could be easily implemented via a dividing flow channel or a plenum that feeds multiple flowpaths). The simple baseline repeating unit cell SOFC configuration is modeled with 16 segments and with t_{div} =1 mm, t_{ext} =1 mm, w_{act} = 5 mm, and h_{ch} = 2 mm, and N_{rep} = 1. The channel length is 20 cm. This represents only one possible geometry, but it corresponds to the modeling assumptions used for the system level analysis in the following sections. The fuel cell operates at 0.6 V, 75% fuel utilization, and 850℃ exit temperature.

Because the cathode air flow and the CPOx generated fuel flow enter the SOFC in parallel metal micro-channels (the SOFC inlet), it is assumed that sufficient heat transfer occurs between them to minimize the temperature difference between the flows. The SOFC inlet estimates the actual heat transfer between the channel flows with typical temperature differences in the 25-50^{o}C range. The temperature at which the flows come to thermal equilibrium is dependent on the system operating state. Sufficient heat transfer is important because it is unlikely that a ceramic MEA (even

the metal supported MEAs considered here) could withstand the thermal shock of a 400°C temperature difference between the adjacent flow channels.

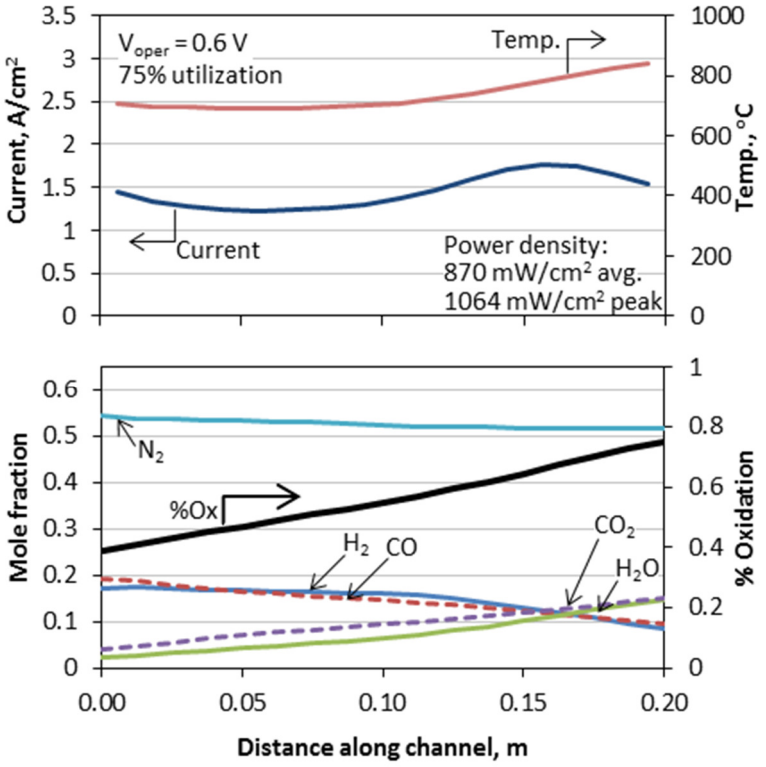

Figure 81. Temperature and species concentration profiles along an SOFC flow channel (baseline unit cell) in an OPR=24 turbofan flying at 16.8 km and M=0.5 (air: 2.9 atm, 373°C).

Figure 81 shows temperature and species concentrations along the SOFC flow path at condition 'A', the high altitude condition (16.8 km, M=0.5) of a HALE UAV. The cell operating voltage is set to 0.6 V, the insulation thickness is 2.2 mm, the fuel mass flow is 1.95 mg/s per channel, the SOFC exit temperature is 850°C, and the degree of fuel oxidation is 75%. Unlike in Figure 76 and Figure 77, the temperatures of the flows entering the anode and cathode are not fixed and are instead strongly influenced by the air conditions downstream of the compressor (373°C and 2.9 atm). The relatively lower pressure lowers conversion in the fuel cell with the net effect that the temperature through the first half of the SOFC is relatively flat at around 700°C -

below optimal for this type of cell. The current density gradually rises due to increased temperature down the channel before dropping off due to reactant depletion. While overall SOFC performance is good (870 mW/cm^2 average power density) the large difference between maximum and minimum (1064 and 736 mW/cm^2, respectively) in this example illustrates the system's sensitivity to inlet temperature and thus flight conditions.

Figure 82 shows temperature and species concentrations along the SOFC flow path at condition 'B', the middle altitude condition (10.7 km, M=0.8) of a commercial transport aircraft. The cell operating voltage, fuel oxidation, and exit temperature are the same as above (0.6 V, 75%, and 850°C, respectively). The air conditions downstream of the compressor (390°C and 8.6 atm).

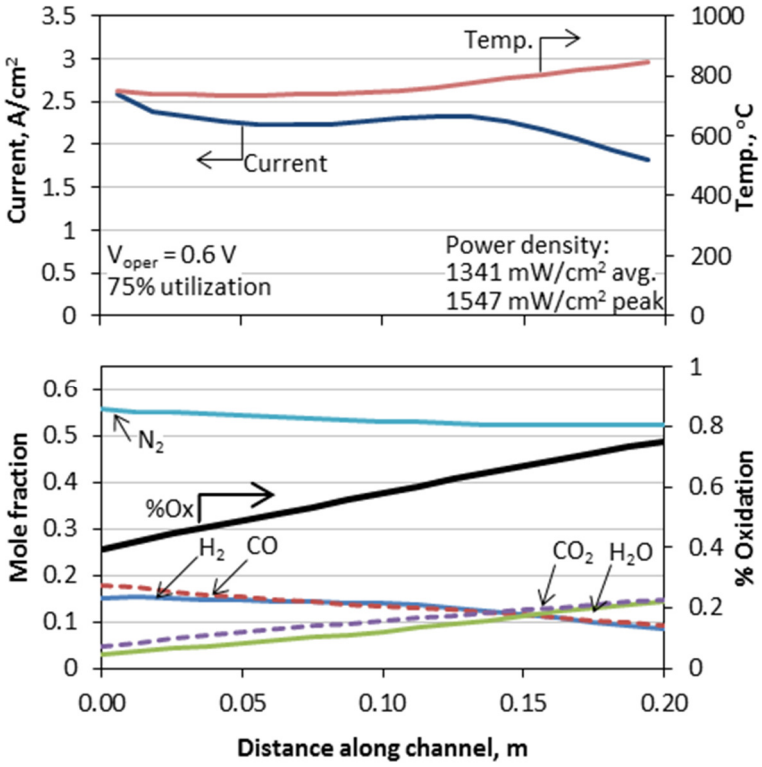

Figure 82. Temperature and species concentration profiles along an SOFC flow channel (baseline unit cell) in an OPR=24 turbofan flying at 10.7 km and M=0.8 (air: 8.6 atm, 390°C).

The insulation thickness is reduced to 1.2 mm primarily because of the increased reaction rate due to increased pressure. Of course, in a fielded system the insulation thickness could not simply be reduced to respond to changing conditions. The reduction in insulation required to maintain temperature should be interpreted as a shift to an operating condition with more thermal energy (initial energy plus heat release). The alternative to reducing insulation thickness to limit temperature would be to increase operating voltage (thereby decreasing reaction rates and heat release).

The fuel mass flow is increased to 3.08 mg/s per channel because of the reaction rates (proportional to current density) shown in the figure. Temperatures are generally higher (around 750°C) in the entry region than the previous case leading to increased current density. Overall SOFC output improves by 54% over the higher altitude condition (1341 mW/cm^2 average power density). The power density is peak at the entrance and lowest at the exit (1547 and 1089 mW/cm^2, respectively) primarily due to reactant depletion.

Figure 83 shows temperature and species concentrations along the SOFC flow path at condition 'C', the sea level, full power condition. The combination of hotter compressor exit air flow and higher pressure (430°C and 18.3 atm) leads to much higher reaction rates than either previous case. The insulation thickness is reduced to 0.27 mm because temperatures, pressures, and reaction rates are significantly higher than the previous cases. The fuel mass flow is increased to 3.56 mg/s per channel because of the high reaction rates. Temperatures are around 750°C in the entry region. The current density exhibits a steep drop in the entry region. Both previous cases showed an initial decline in current due to reactant depletion. In this case, the

effect is increased by higher initial current density (leading to faster reactant depletion) and an initial drop in temperature. Entry region effects (higher Nusselt numbers in developing flow) lead to higher heat losses in the entry. While this is true of all the simulations, the thinner insulation in this case allows the heat loss to cause a slight drop in temperature. The combination of faster reactant depletion and faster heat loss leads to a steeper decline in current density (only in the entry region). Overall SOFC output is the best of the four OPR=24 cases presented in this section (1550 mW/cm^2 average power density). The power output is 16% higher than the middle altitude and 78% higher than the high altitude cases. The power density is peak at the entrance and lowest at the exit (1940 and 1180 mW/cm^2, respectively).

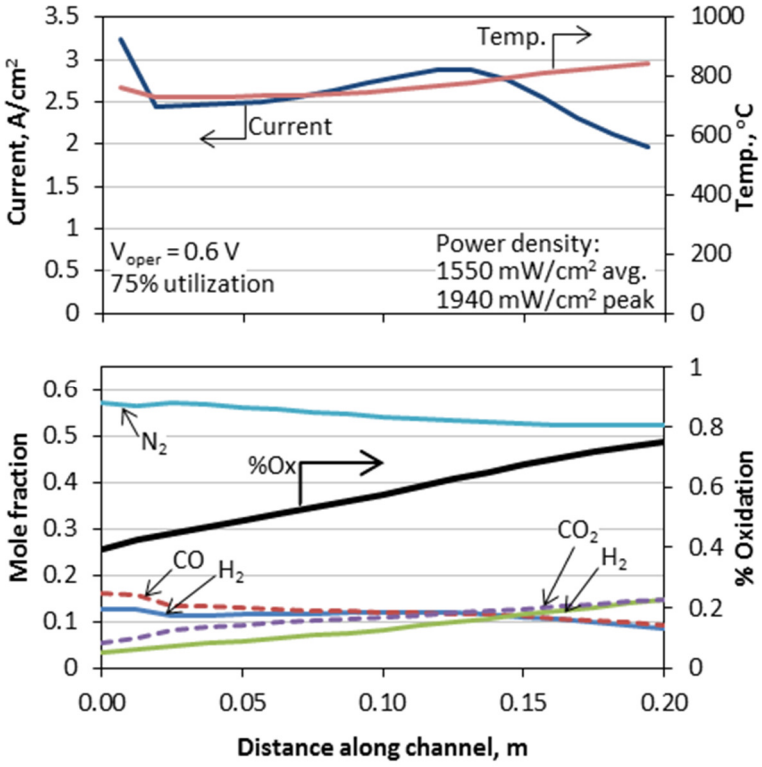

Figure 83. Temperature and species concentration profiles along an SOFC flow channel (baseline unit cell) in an OPR=24 turbofan at sea level and full throttle (air: 18.3 atm, 430°C).

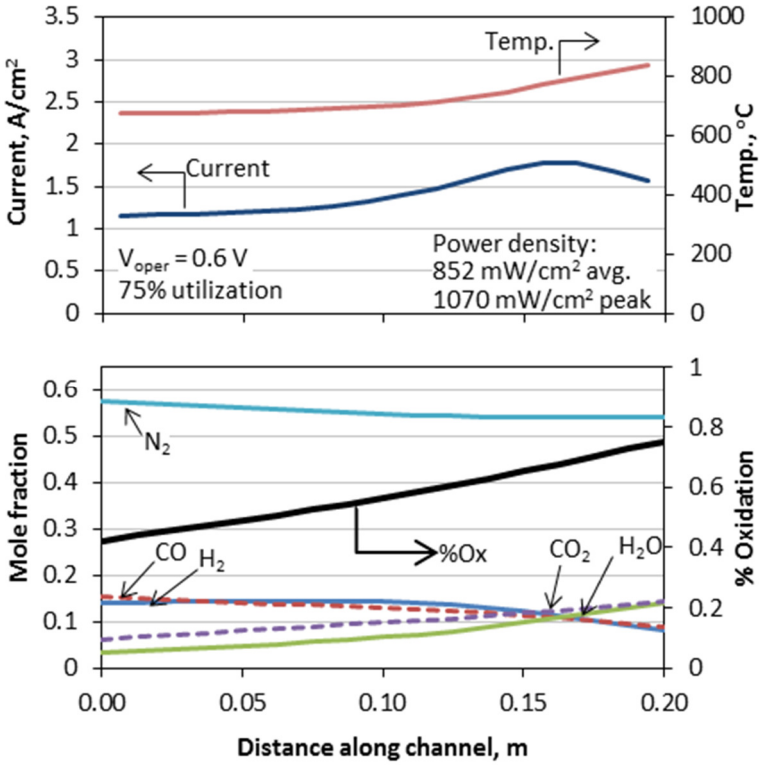

Figure 84. Temperature and species concentration profiles along an SOFC flow channel (baseline unit cell) in an OPR=24 turbofan at sea level, idle (air: 3.9 atm, 181°C).

Figure 84 shows temperature and species concentrations along the SOFC flow path at condition 'D', the sea level, idle power (7% of rated thrust) condition. This is an interesting case because the reduced throttle state of the engine leads to an effective pressure ratio of just 3.9 and the lowest incoming air temperatures of the studied cases (181°C and 3.9 atm). Temperatures are generally lower (around 675°C) in the entry region. Together with the reduced pressure, this leads to the low reaction rates (proportional to current density) shown in the figure. Due to these low reaction rates, the insulation thickness is increased significantly to 8.8 mm and the fuel mass flow is reduced to only 2.12 mg/s per channel. Overall SOFC performance is very similar to the high altitude condition in Figure 81. The average power density is 852

mW/cm^2 with the maximum and minimum at 1070 and 697 mW/cm^2, respectively (all very similar to the high altitude case).

Analogous studies performed on the low BPR turbofan and turbojet engines produce similar results showing that engine type alone does not have a strong impact on the performance of the fuel cell channels. This is because all of the engines above have the same component efficiencies and, so the conditions of the air and syngas streams entering the fuel cell are very similar.

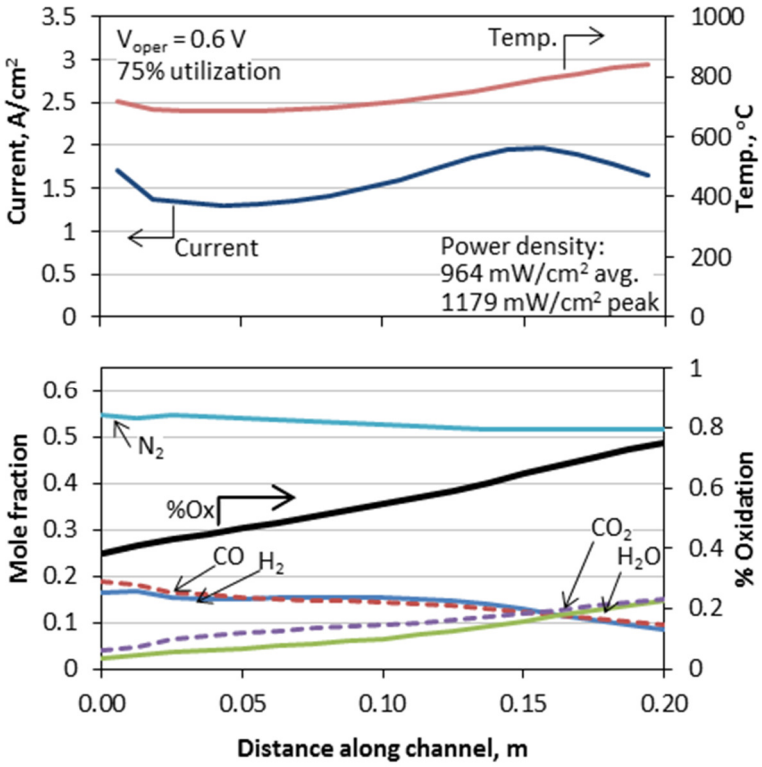

Figure 85. Temperature and species concentration profiles along an SOFC flow channel (baseline unit cell) in an OPR=40 turbofan flying at 16.8 km and M=0.5 (air: 4.1 atm, 432°C).

Figure 85 shows temperature and species concentrations along the SOFC flow path at condition 'E', the same high altitude flight condition (16.8 km, M=0.5) as the results of Figure 81. These results, however, are for a high pressure ratio (OPR=40) engine. The higher pressure ratio leads to higher incoming air temperature and

pressure than the earlier case (432℃ and 4.1 atm). The higher reaction rates that result lead to 11% higher average power density (964 mW/cm^2) and higher fuel mass flow (2.14 mg/s per channel). The insulation thickness is reduced to 0.55 mm due the increased heat release and increased cooling air temperature. Overall, the positive impact of raising OPR on fuel cell performance is evident.

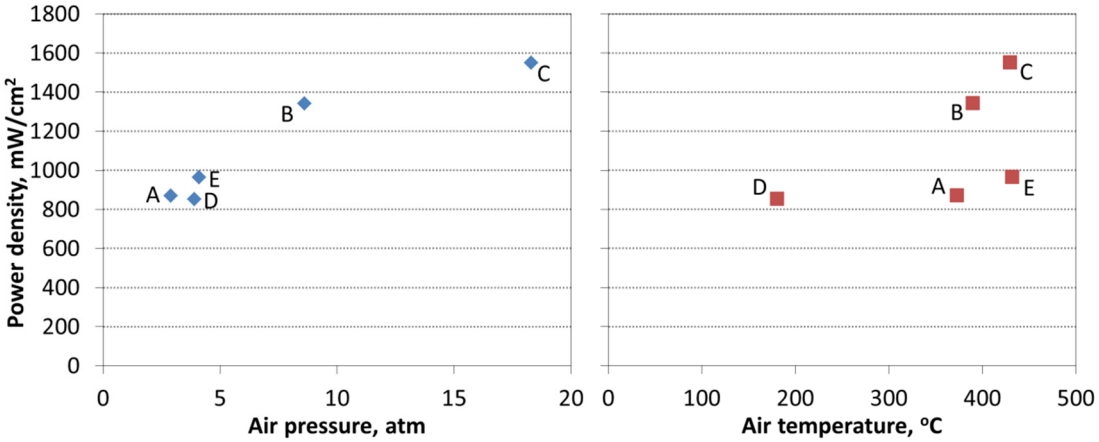

Figure 86. Power density v. delivered air pressure (L) and temperature (R).

To further investigate the impact of the conditions of the air delivered to the fuel cell, the average power density for each of the cases above has been plotted against air pressure and temperature in Figure 86. It is evident that the air pressure is the much stronger factor in determining the power density that will be achieved. Though only five data points are plotted, power density exhibits a clear correlation with pressure. The relationship to temperature is more muddled. However, this is not an indication that temperature is unimportant, only that in these cases the fuel cell has been thermally managed via the adjustment of insulation thickness which mitigates the importance of the supply temperature.

7.3 Integrated GT-SOFC with Thermodynamic and Mass Effects

7.3.1 Overview: GT-SOFC v. GT-generator

The current widely used approach for meeting vehicle electric power demands is mechanical generators driven off the high pressure engine shaft. Therefore, it is useful to compare the performance of the integrated CPOx/SOFC to that of 'conventional' shaft-driven generators. Detailed information on the sizing of these shaft and generator systems is not widely available in the literature, but every attempt has been made to represent the performance of the systems accurately.

7.3.2 Comparison by Engine Type

The potential performance improvement offered by GT-SOFC hybrids is investigated by comparing the fuel consumption of the GT-SOFC hybrid to that of a conventional system where a mechanical generator draws power off the high pressure spool. The number of radially repeating cells (described above) is increased as more power is required while the amount of insulation around the CPOx/SOFC assembly is adjusted so as to maintain a constant 850°C at the SOFC exit. If the required insulation thickness drops below 0.1 mm, a new (concentric) ring of channels is added to facilitate heat loss and avoid SOFC over-temperature. Since data describing the power densities of 'typical' aircraft generators and their associated gearboxes/mechanical generators are not available, the approach taken here is to bound the range by considering two extreme cases: generator/gearbox systems with specific powers of 1 kW/kg and 5 kW/kg, respectively.

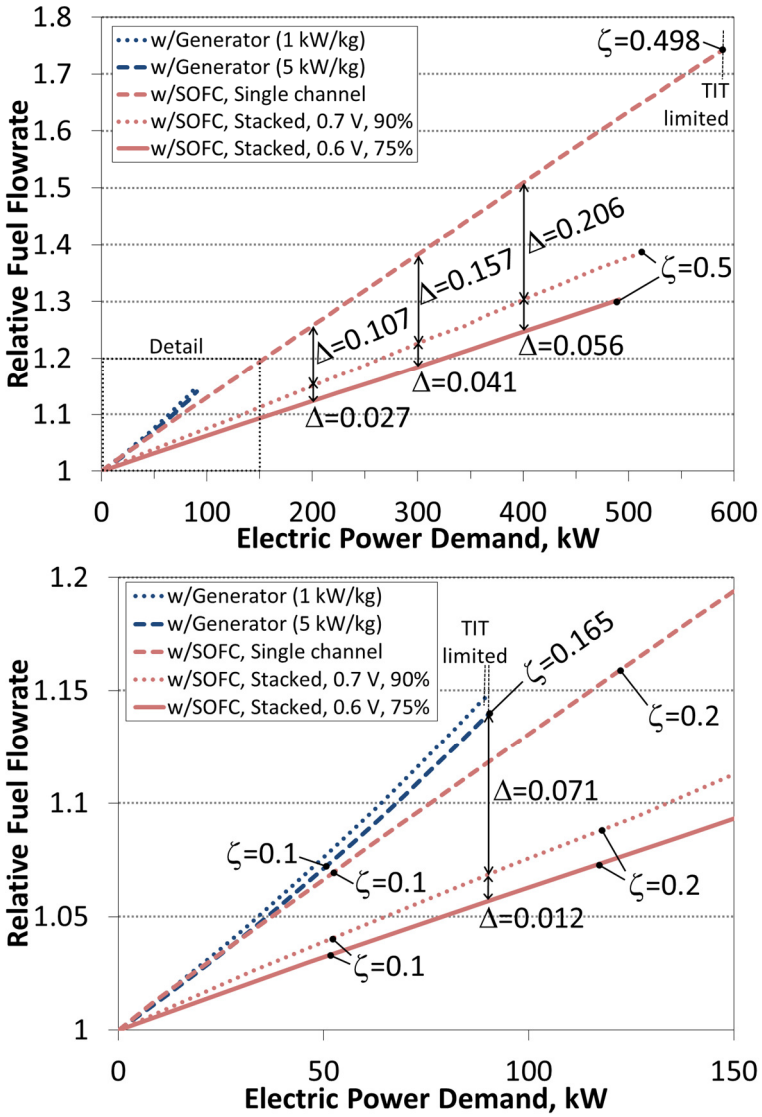

Figure 87. Comparison of relative fuel flow for BPR=5, OPR=24 engine (top). Magnified view (bottom). HALE UAV, level cruise at 16.8 km, M=0.5.

Figure 87 shows relative fuel flow rate as a function of electric power demand in the BPR=5, OPR=24 engine for three different SOFC configurations in addition to the standard engine-generator configuration. Results are presented at high altitude cruise (Mach =0.5, altitude = 16.8 km / 55 kft). The drag polar used corresponds to a HALE UAV type vehicle (Table 18). Relative fuel flow rate is defined as the ratio of the fuel flow rate to the fuel flow rate with zero electric power demand. Recall from Section "5.1 Approach and Performance Metrics" that total mass flow rate of fuel is

chosen as the key metric of performance because of its relation to range and endurance and because it captures all thermodynamic, aerodynamic, and sizing effects. Relative fuel flow rate is used here simply for the convenience of comparing percentage changes to a baseline value of unity.

The baseline flow rate of fuel (i.e., with zero electric power demand) is 52.1 g/s. The dashed blue curves correspond to the conventional engine-generator system at the two extremes of assumed generator/transmission specific power. The dashed red line ("w/SOFC, Single channel") corresponds to rings of single SOFC elements ($N_{rep} = 1$). The dotted red line ("w/SOFC, Stacked, 0.7 V, 90%") corresponds to rings of radially-stacked SOFC channels ($N_{rep} > 1$). The SOFCs in both of these cases have an operating condition of 0.7 V and 90% fuel utilization. The solid red line ("w/SOFC, Stacked, 0.6 V, 75%") show the performance of the radially stacked geometry with the SOFC operating at different, 'improved' conditions (0.6 V, 75% fuel utilization).

If fuel flow to the SOFC were held constant, a reduction in operating voltage would result in an increase in fuel utilization. Therefore, between the '0.7 V, 90%' case and the '0.6 V, 75%' case, the rate of fuel flow to the SOFC has been increased significantly to reduce utilization rates in spite of increased reaction rates. Also, it should be noted that 90% fuel utilization is probably unrealistic in practice, but it has been included here for comparison. All subsequent results beyond this section consider the more realistic 75% utilization case.

Electric power fraction (ζ) increases with electric power demand and its values at various places along the curves are indicated with solid round symbols. The same

value of ζ occurs at different electric power levels on different curves because propulsive power depends on the mass of the electrical system. The figure shows that all modeled configurations of hybrid GT-SOFCs consume less fuel than the conventional engine-generator and that the fractional improvement (i.e., reduction) in fuel consumption (Δ) over the mechanical generator increases with increasing power output (or power fraction).

The figure also shows that because the turbine inlet temperature (TIT) does not rise as quickly with electric power demand in the GT-SOFC hybrid, the hybrid is able to operate at much larger power electric power fractions – in this case $\zeta \approx 0.5$ (where electrical and propulsive power are equal) and beyond. This is much larger than the $\zeta = 0.165$ (roughly 90 kW electrical) limit of the generator-based system and suggests that GT-SOFC hybrid engines may be better suited for use in the highly electric aircraft envisioned by NASA [4].

At the 50 kW power level, the fuel flow rate of the GT-generator (5 kW/kg) is 3.2% and 3.9% larger than the 0.7 V, 90% and the 0.6 V, 75% GT-SOFCs, respectively. At the TIT limit (90 kW), the fuel flow rate is 7.1% and 8.3% larger, respectively. The arrangement consisting of rings of single-element SOFC (dashed line) performs worse than the radially stacked arrangements (solid and dotted lines) because it requires relatively more interconnect material per channel. This makes this GT-SOFC configuration heavier and thus fuel consumption is higher than in the radially stacked configurations (6.8%, 13.4%, 19.8%, and 26.2% higher than the solid curve at 100 kW, 200 kW, 300 kW, and 400 kW, respectively). The TIT limit in this configuration occurs at $\zeta = 0.498$.

The dotted and solid red lines in Figure 87 show how performance can be improved by changing the SOFC operating conditions. Here, the cell voltage has been reduced to 0.6 V (solid) from 0.7 V (dotted) and the fuel conversion percentage decreased to 75% (solid) from 90% (dotted). While this reduces the overall thermodynamic efficiency of the cell, it increases its power density which decreases the mass of the system which, in turn, decreases drag and thus the thrust requirement. Since the energy in the unreacted fuel leaving the SOFC is recovered in the gas turbine's combustor, the net result is a reduction in overall fuel consumption at the same flight conditions. This is an illustration of the synergy that can be achieved in integrated GT-SOFC systems where losses at the fuel cell level are recovered at the engine level resulting in overall improvements at the system level.

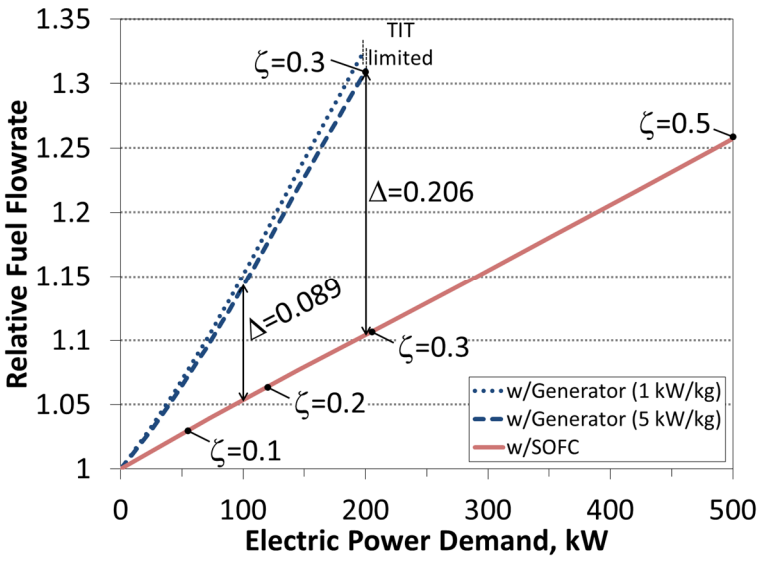

Figure 88. Comparison of relative fuel flow for 0.5 BPR engine with generator or SOFC. HALE UAV, level cruise at 16.8 km, M=0.5.

Figure 88 shows similar results for the low BPR turbofan engine. The baseline fuel flow with no electrical load is 66.2 g/s. Hybrid GT-SOFC systems with electric power fractions up to $\zeta = 0.5$ were investigated. The results show that the generator-

based system reaches the TIT limit at approximately 200 kW (corresponding to $\zeta = 0.3$). At that power level, the fractional improvement (Δ) of the GT-SOFC over the generator is 20.6%. At 100 kW, the fractional improvement is 8.9%.

The low BPR engine with mechanical generator reaches the TIT limit later than the high BPR engine did (200 kW as opposed to 90 kW) because the thrust of the high BPR configuration decreases more rapidly with altitude than the low BPR configuration. Since the engines are sized to produce the same thrust at sea level on the ground, $\zeta = 0$ at cruising altitude requires a higher throttle setting in the high BPR engine leaving less margin for increases in fuel flow rate.

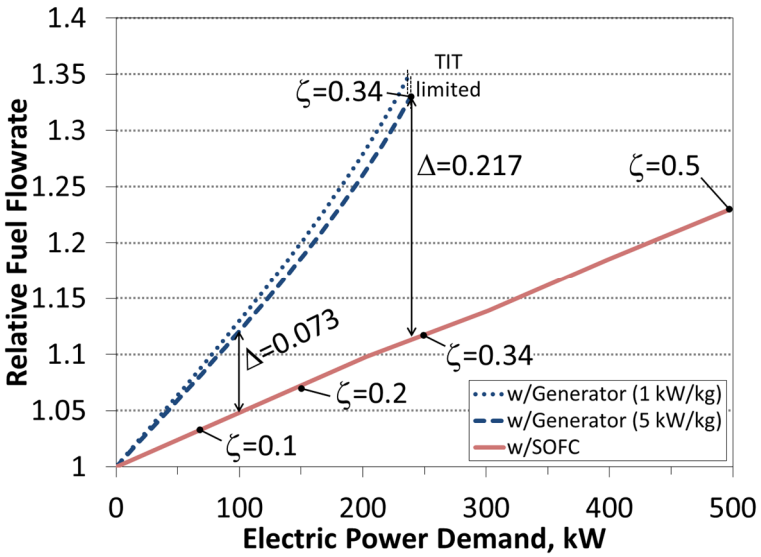

Figure 89. Comparison of relative fuel flow for turbojet engine with generator or SOFC. HALE UAV, level cruise at 16.8 km, M=0.5.

Figure 89 shows relative fuel flow rate as a function of electric power demand for the turbojet engine. The baseline fuel flow with no electrical load is 78.4 g/s. Hybrid GT-SOFC systems with electric power fractions up to $\zeta = 0.5$ were investigated. The generator-based system reaches the TIT limit at approximately 240 kW (corresponding to $\zeta = 0.34$). At 100 kW and 200 kW power levels, the fuel flow rate

improvements are 7.3% and 16.4%, respectively, compared to the GT-generator systems.

7.3.3 Comparison by Engine Pressure Ratio

The analysis of the previous section is continued by comparing the three engine configurations with BPR=5. These engines have overall pressure ratios (OPR) of 24, 31.5, and 40. The results for the OPR=24 engine have already been presented in Figure 87. It is the solid red curve in that figure (corresponding to 0.6 V, 75% fuel utilization) that is of interest in this comparison.

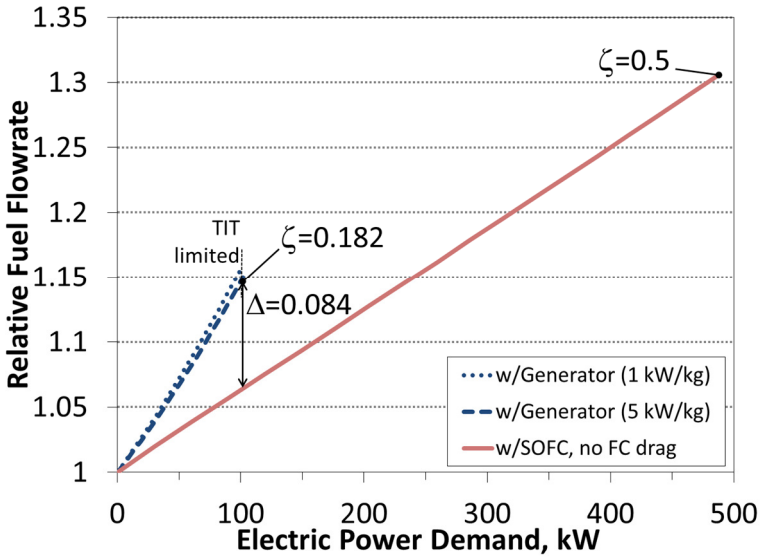

Figure 90. Comparison of relative fuel flow for BPR=5, OPR=31.5 engine. HALE UAV, level cruise at 16.8 km, M=0.5.

Figure 90 shows relative fuel flow rate as a function of electric power demand for the BPR=5, OPR=31.5 turbofan engine. The baseline fuel flow with no electrical load is 49.6 g/s. Systems with electric power fractions up to $\zeta = 0.5$ were investigated. The generator-based system reaches the TIT limit at approximately 102 kW (corresponding to $\zeta = 0.182$). At the 50 kW and 100 kW power levels, the fuel flow

rate improvements are 3.5% and 8.4%, respectively, compared to the GT-generator systems. At the 50 kW power level, the OPR=24 engine showed 3.9% improvement with the SOFC over the generator. SOFC performance improves as OPR is raised (as illustrated in Figure 85) but so does the baseline GT system as it becomes more efficient (decreasing the advantage of the SOFC). In this analysis, the higher OPR system showed relatively less improvement because the former effect is outweighed by the latter (i.e., the SOFC improves less than the GT).

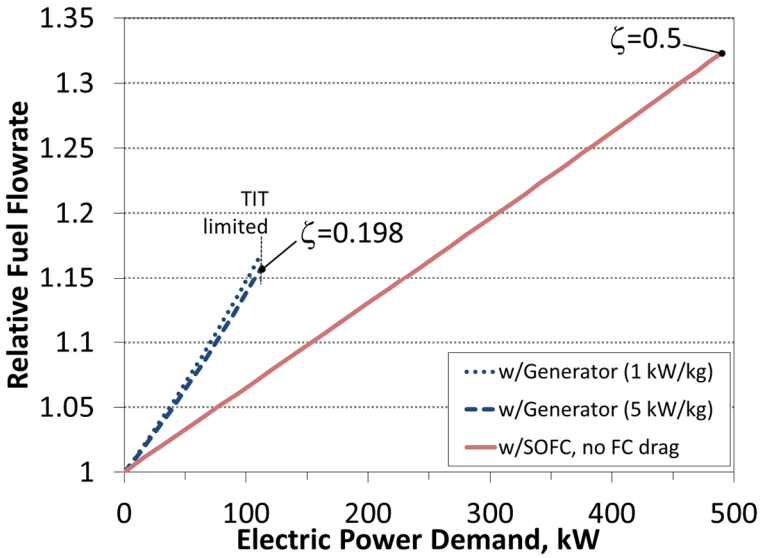

Figure 91. Comparison of relative fuel flow for BPR=5, OPR=40 engine. HALE UAV, level cruise at 16.8 km, M=0.5.

Figure 91 shows relative fuel flow rate as a function of electric power demand for the BPR=5, OPR=40 turbofan engine. The baseline fuel flow with no electrical load is 47.6 g/s. GT-SOFC systems with electric power fractions up to $\zeta = 0.5$ were investigated. The generator-based system reaches the TIT limit at approximately 113 kW (corresponding to $\zeta = 0.198$). At 50 kW and 100 kW power levels, the fuel flow rate improvements are 3.1% and 7.3%, respectively, compared to the GT-generator systems. As before, the relative improvement between the GT-SOFC and GT-

generator decreases at higher OPR because the improvement of the SOFC system is less than the improvement of the GT system. To be clear, raising OPR decreases fuel burn for both the GT-generator and GT-SOFC systems but the relative difference between the two diminishes slightly.

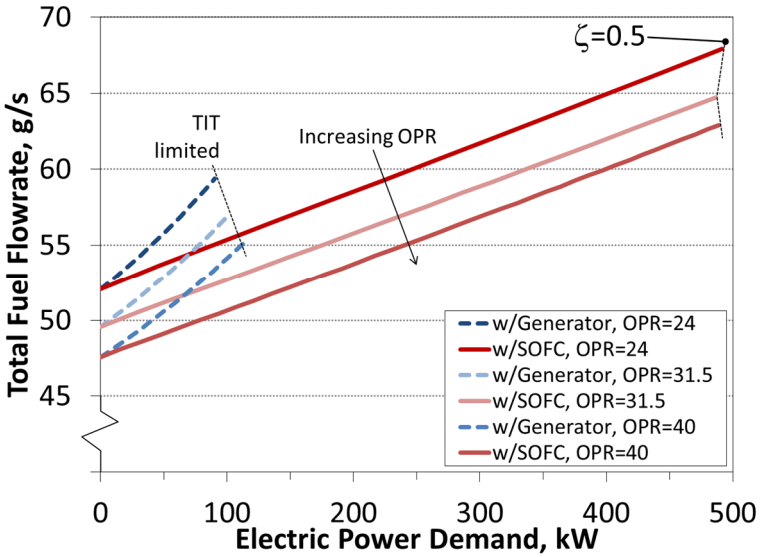

Figure 92. Comparison of total fuel flow for BPR=5 engines with different OPR. HALE UAV, level cruise at 16.8 km, M=0.5.

Figure 92 compares all three BPR=5 engines (OPR = 24, 31.5, 40) on the basis of total fuel flow rate. Note that the vertical axis does not start at zero. Only the higher specific power (5 kW/kg) generator case is shown in order to simplify the figure. Absolute fuel flow rate is used here because each engine has a different baseline fuel flow rate making it impossible to create a single relative fuel flow rate scale valid for all engines. As expected, the higher OPR engines are more fuel efficient in their baseline states. This is a direct result of the importance of pressure ratio in the Brayton cycle. The higher OPR engines with generators also hit the TIT limit at slightly higher power levels, presumably because their cycles are more efficient. While hard to see, the GT-generator curves diverge slightly (i.e., the difference

between the OPR=24 and OPR=40 engines increases as electric power output increases). The GT-SOFC systems reach $\zeta = 0.5$ at slightly lower power levels for the higher OPR engines. Again, the curves run nearly parallel, indicating no significant impact on the trend as a result of changing OPR. The higher OPR engines perform better in every investigated circumstance.

7.3.4 Comparison by Flight Condition

It is also desirable to examine the performance of GT-SOFC systems at more than a single flight condition. A condition of particular interest is a typical regional jet flight at 10.7 km altitude and M=0.8. The drag polar used for this analysis corresponds to the regional jet type vehicle defined earlier (Table 18).

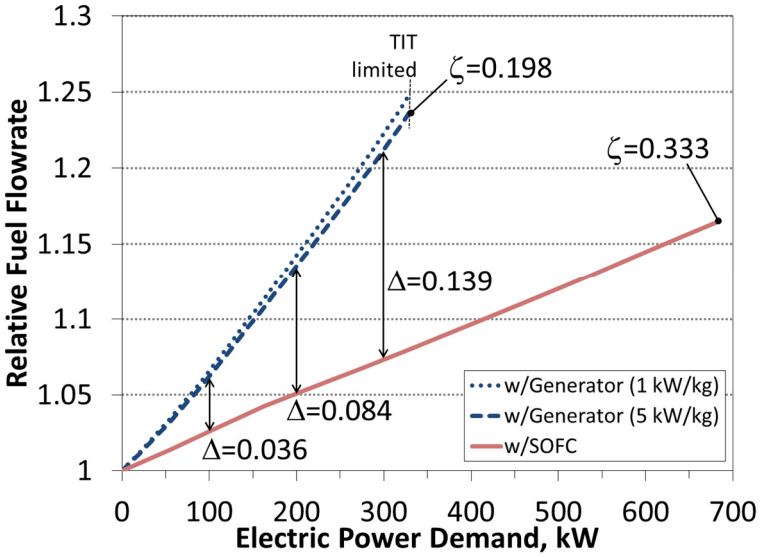

Figure 93. Comparison of relative fuel flow for BPR=5, OPR=24 engine. Regional jet, level cruise at 10.7 km, M=0.8.

Figure 93 shows relative fuel flow rate as a function of electric power demand for the BPR=5, OPR=24 turbofan engine at the regional jet type cruise condition. The baseline fuel flow with no electrical load is 111.5 g/s. The red curve represents

performance of the GT-SOFC (operating at 0.6 V, 75% fuel utilization) at power fractions up to $\zeta = 0.333$ (i.e., when the electrical demand is half the propulsive demand). The maximum power fraction investigated is lower than for the higher altitude case for two reasons. The first is that the propulsive demand is so much higher at the lower altitude that the same power fraction corresponds to a much higher net power. The second reason is that the vehicles of interest for this flight condition typically have much smaller electrical power fractions than the HALE UAV of interest at high altitude (see Figure 1). The generator-based system reaches the TIT limit at approximately 330 kW (corresponding to $\zeta = 0.198$). At 100 kW, 200 kW, and 300 kW power levels, the fuel flow rate improvements are 3.6%, 8.4%, and 13.9%, respectively, compared to the GT-generator systems. The percentage improvement in fuel flow at the same electric power level is less than what was estimated for the high altitude condition (e.g., at 50 kW the reduction is 3.9% at high altitude vs. 1.7% at the lower altitude). However, at the same electric power fraction, the percentage improvement is greater at the lower altitude condition (e.g., at $\zeta = 0.1$ the reduction is 3.9% at high altitude vs. 5.8% at the lower altitude).

7.3.5 Discussion of Power Density

It is instructive to re-visit the assertion made in many sources [59,66,114], including the introduction to this dissertation, that low specific power is a major concern when integrating engines and fuel cells because the specific power of heat engines is typically several times that of fuel cells. Consider what happens to the performance of each system at altitude: The pressure at 16.8 km (55 kft) is 0.09 atmospheres which greatly reduces engine power over sea-level performance. For

example, the high BPR engine with OPR=24 and no electric generation operates at only 775 W/kg in cruise. However, the fuel cell in the engine-integrated SOFC operates at 2.3 atmospheres enabling it to produce more power at 16.8 km than its unpressurized counterpart at sea level. The specific power of the SOFC assembly (reformer, fuel cell, ducting, and other hardware) ranges, depending on configuration, from 328 W/kg at 0.7 V with 90% utilization to 511 W/kg at 0.6 V with 75% utilization. Therefore, the specific powers of the two systems are actually of similar orders of magnitude when operating at altitude. Because increasing fuel cell performance by increasing the pressure provides a diminishing return, the specific power of the GT remains significantly larger than that of the fuel cell at sea level. Therefore, the approximate equality of GT and SOFC specific power at cruise is a result of the fact that the GT's specific power is more sensitive to changes in altitude than the pressurized SOFC.

7.4 Integrated GT-SOFC Accounting for Fuel Cell Volume

7.4.1 Overview: Importance of System Volume

The results presented in the preceding three sections implicitly assume that C_L and C_D are vehicle-level parameters that are independent of the configuration of the energy conversion system (GT-generator or GT-SOFC). However, Figure 94, which presents scale images of what such integrated configurations might look like, suggests that this may not always be a good assumption for GT-SOFC hybrids.

The figure compares the external shapes of CPOx/SOFC-equipped engines at two electric power levels (50 and 150 kW). The sizings are based on the three fuel cell

conditions investigated in Figure 87. The three SOFC configurations considered are the single channel ($N_{rep} = 1$) geometry (dashed red in Figure 87), radially stacked ($N_{rep} > 1$) channels operating at 0.7 V and 90% fuel utilization (dotted red), and radially stacked operating at 0.6 V with 75% fuel utilization (solid red). All GT engines in Figure 94 are the BPR=5, OPR=24 turbofan engine. The single channel, 150 kW system is obviously aerodynamically unacceptable as it completely blocks the bypass flow. In contrast, the 0.6 V, 75% utilization 50 kW system approaches a geometry that could be realistic for flight. Further refinements to geometry should lead to even less aerodynamically disruptive configurations. However, these results indicate that external aerodynamics are a very important issue.

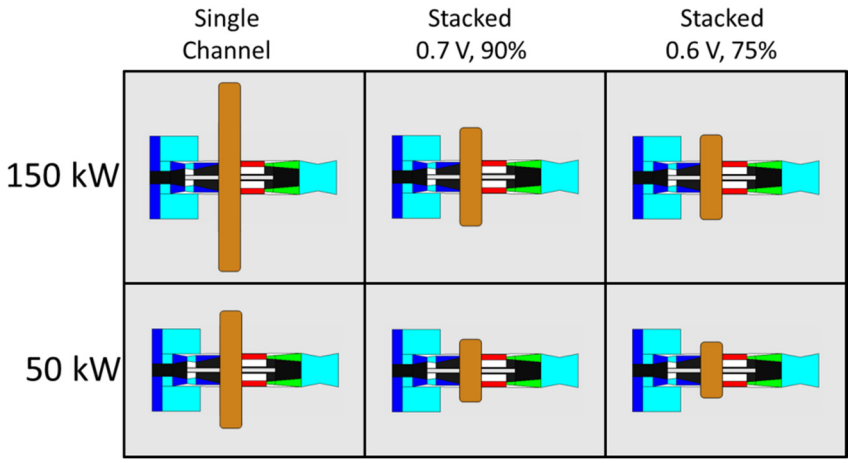

Figure 94. Approximate representation of fuel cell size on BPR=5, OPR=24 engine.

7.4.2 High BPR Turbofan with Annular Fuel Cell

So far, it has been assumed that the volume of the fuel cell assembly is unimportant because fuel cell assembly aerodynamic drag is not accounted for. However, Figure 94 showed that this is a questionable assumption, particularly at high electric power levels. For this reason, the vehicle-level analysis has been expanded to account for external aerodynamic drag on the fuel cell assembly.

Figure 95 compares relative fuel mass flow rates in a BPR=5, OPR=24 turbofan GT-SOFC at 16.8 km, M=0.5 cruise (using HALE UAV aircraft characteristics) with and without accounting for aerodynamic drag on the fuel cell assembly. Recall that 'relative fuel flow rate' is the mass flow rate of fuel divided by the mass flow rate of fuel at zero electric power.

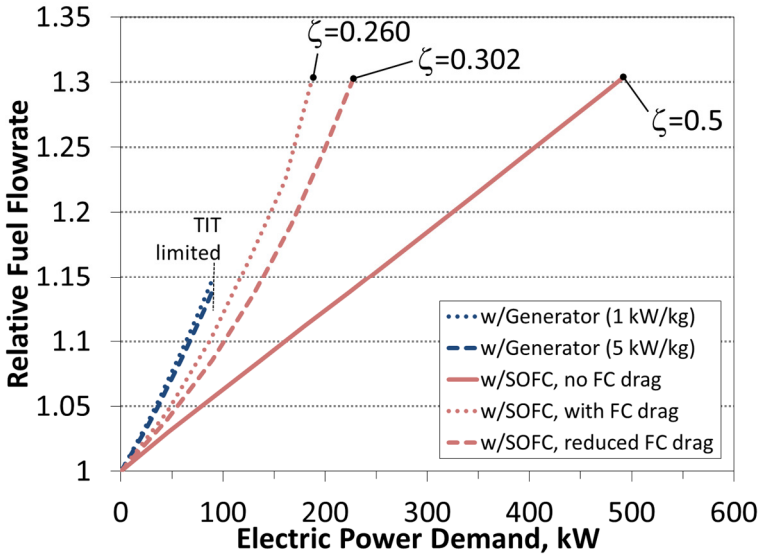

Figure 95. Comparison of relative fuel flow rate in BPR=5, OPR=24 GT-SOFC with and without SOFC external drag penalty. HALE UAV, level cruise at 16.8 km, M=0.5.

The blue curves correspond to electrical generation using shaft-driven mechanical generators with 1 and 5 kW/kg specific power (the range is to bracket possible systems). The solid red curve shows relative fuel mass flow rate when not accounting for aerodynamic drag effects on the fuel cell assembly (i.e., the original result for a BPR=5, OPR=24 turbofan coupled with a fuel cell at 0.6 V, 75% fuel oxidation). The dotted red curve shows the relative fuel flow rate when accounting for external aerodynamic drag of the fuel cell assembly. The results show that the added drag of the fuel cell volume requires the system to burn more fuel to produce the same amount of thrust, eroding a significant portion of the advantage of the GT-SOFC

system over equivalent generator based systems. This is very important because an improvement in fuel burn of only a few percent (as opposed to several percent) may not justify the added complexity of the proposed system.

While this result is not surprising given the highly intrusive nature of the particular fuel cell configuration considered in this analysis which is based on radial expansion of the stack into the external flow, it illustrates the importance of finding other more aerodynamically favorable methods for GT-SOFC integration. A first attempt at reducing drag is shown by the dashed red curve in Figure 95. The initial calculations (dotted red) were based on an air duct surrounding the SOFC channels with a design flow speed of just 10 ft/s to minimize pressure losses. The dotted curve is representative of a smaller, less externally obstructive duct with a design flow speed of 100 ft/s. The reduction in drag is evident in the figure, though performance levels still do not approach the original estimates that neglected the aerodynamic penalty. Therefore, better, less intrusive geometries are still needed.

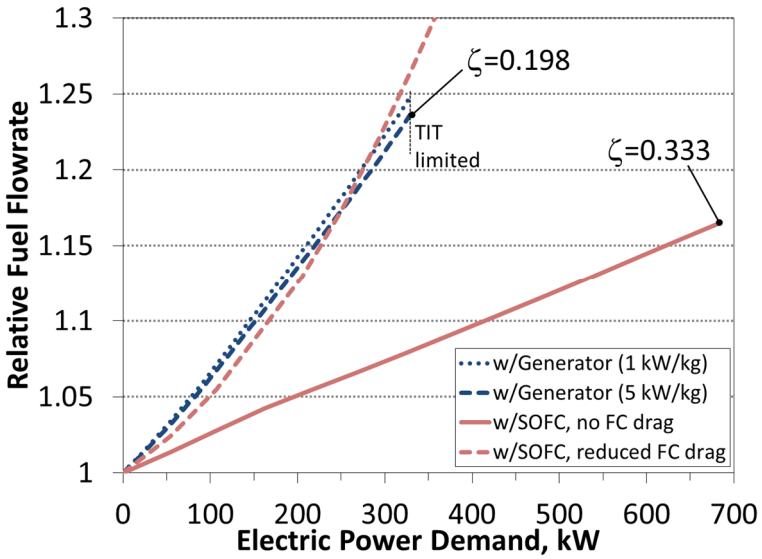

Figure 96. Comparison of relative fuel flow rate in BPR=5, OPR=24 GT-SOFC with and without SOFC external drag penalty. Regional jet, level cruise at 10.7 km, M=0.8.

Figure 96 compares relative fuel mass flow rates in a BPR=5, OPR=24 turbofan GT-SOFC at 10.7 km, M=0.8 cruise (using regional jet aircraft characteristics) with and without accounting for aerodynamic drag on the fuel cell assembly. The solid red curve shows relative fuel mass flow rate when not accounting for aerodynamic drag effects on the fuel cell assembly (i.e., the original result for a BPR=5, OPR=24 turbofan coupled with a fuel cell at 0.6 V, 75% fuel oxidation). The dashed red curve shows performance using the aerodynamically cleaner reduced size duct. The results associated with the original (larger) air duct are worse and have been omitted. As in the high altitude HALE UAV case, the drag on the fuel cell assembly cuts deeply into the originally estimated performance improvement. Even using the reduced size cooling air duct, the previously predicted fuel burn reduction is almost or completely eliminated by the drag penalty. This confirms the aerodynamic unsuitability of the stacking scheme used in this portion of the modeling and shows that the results in Figure 95 are not artifacts of a particular operating condition.

7.4.3 High BPR Turbofan with Reversing Fuel Cell

The primary difficulty with the arrangement studied above is that the fuel cell assembly extends directly into the GT engine's bypass flow as illustrated in Figure 97a. for a separate exhaust turbofan.

The aerodynamic difficulties can be mitigated by considering different geometries. Figure 97b shows what the integration might look like in a very high bypass ratio engine (such as the BPR=8, OPR=40 separate exhaust turbofan modeled in this work) where the diameters of early stage compressors and the turbines are significantly larger than the diameter of the engine core near the burner. The narrow

'waist' produced by this configuration could house the SOFC assembly with minimum drag penalty. Further advantage may be gained via the configuration in Figure 97c where the fuel cell passages extend along and even beyond the combustor and eliminates the constraint that the entire fuel cell length fit between the compressor and the combustor. This would enable one to increase the size of the fuel cell without expanding the diameter. While the 180 degree turn of the flow back to enter the combustor would introduce an internal pressure loss, the reduction in external aerodynamic drag could more than compensate for it.

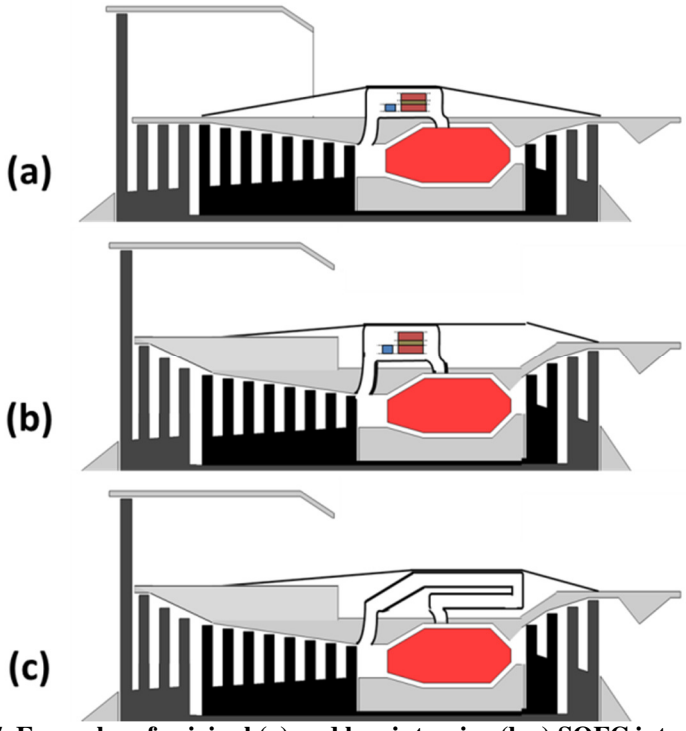

Figure 97. Examples of original (a) and less intrusive (b,c) SOFC integrations.

Figure 98 presents results for this final geometry option (Figure 97c). The fuel cell is allowed to expand axially 50 cm out and back (100 cm total). The GT engine is the BPR=8, OPR=40 turbofan and the flight condition is 16.8 km, M=0.5. The baseline fuel flow with no electrical load is 41.1 g/s. The generator-based system

(blue curves) reaches the TIT limit at approximately 81 kW (corresponding to $\zeta = 0.150$). The red curves use the standard assumption in this work of a 5% pressure drop in the combustor. The solid red curve represents performance when not accounting for fuel cell assembly drag. For this case, systems with electric power fractions up to $\zeta = 0.5$ were investigated. The dashed red curve represents performance with the drag penalty (assuming cooling duct air velocity is 100 ft/s). At 50 kW, the fuel flow rate reduction is 3.3% compared to the GT-generator systems. This is consistent with the earlier predictions for BPR=5 engines.

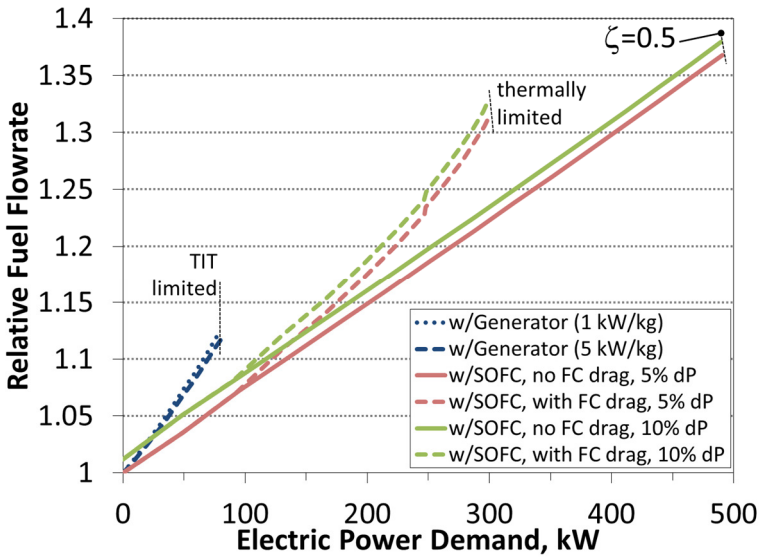

Figure 98. Comparison of relative fuel flow rate in BPR=8, OPR=40 GT-SOFC with and without SOFC external drag penalty. HALE UAV, level cruise at 16.8 km, M=0.5.

For the case with drag (dashed curve), the system reached a thermal limit at 300 kW ($\zeta = 0.37$). The system could produce no more power because the cooling duct air was heated to the point where it could no longer remove enough heat to meet the fuel cell's operating temperature limit. This thermal limit was encountered because of the increased length of the fuel cell. It is possible that the thermal limit could be extended to higher power levels by operating at higher voltage or lower fuel

conversion to reduce heat output. Increasing the air flow is also an option, but it would present a tradeoff between improved cooling and worsened drag.

The key outcome of this part of the investigation is that changing the flow path geometry and exploiting 'narrow-waisted' high bypass ratio configurations allows the full benefit of the GT-SOFC to be realized up to a power level of nearly 100 kW where the fuel cell assembly does not protrude into the GT secondary flow (as illustrated in Figure 99). The drag penalty is only 1-2% of fuel flow in the 150-200 kW power range.

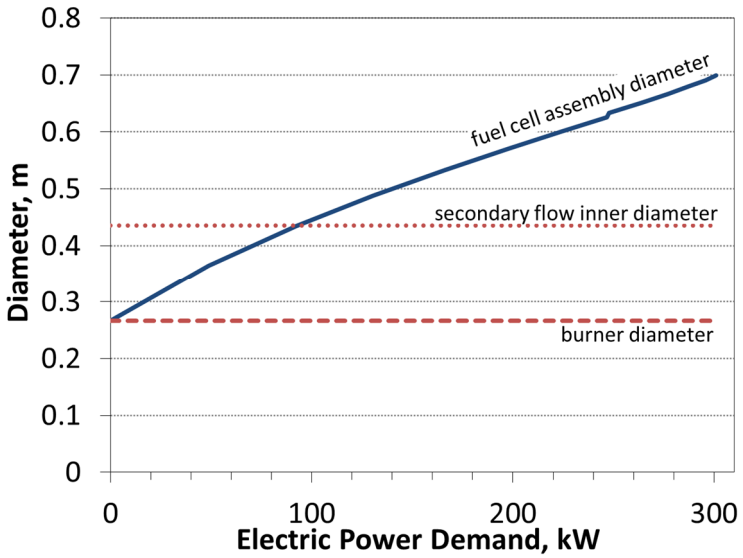

Figure 99. Fuel cell assembly diameter v. electric power.

As indicated earlier, a disadvantage of the configuration of Figure 97c is increased pressure loss. Therefore, this effect is investigated by doubling the pressure loss through the combustor and CPOx/SOFC assembly to 10%. The results are represented by the solid and dashed green curves in Figure 98. As before, the dashed curve includes external aerodynamic drag of the fuel cell and the solid curve does not. The results show that there is a fuel flow penalty of 1.2% at $\zeta = 0$ just from the increased pressure loss. This penalty remains fairly consistent at all power levels,

both with and without drag. The loss of fuel efficiency is obviously undesirable, and below 25 kW ($\zeta = 0.05$) the GT-SOFC performs worse than the generator based system. However, considering that improvements of several percent are predicted for higher power levels, the GT-SOFC system is still beneficial at high power fractions. Because the fuel cell assembly diameter relative to electric power demand does not differ significantly from the 5% pressure loss case presented earlier, only one curve for diameter is presented in Figure 99.

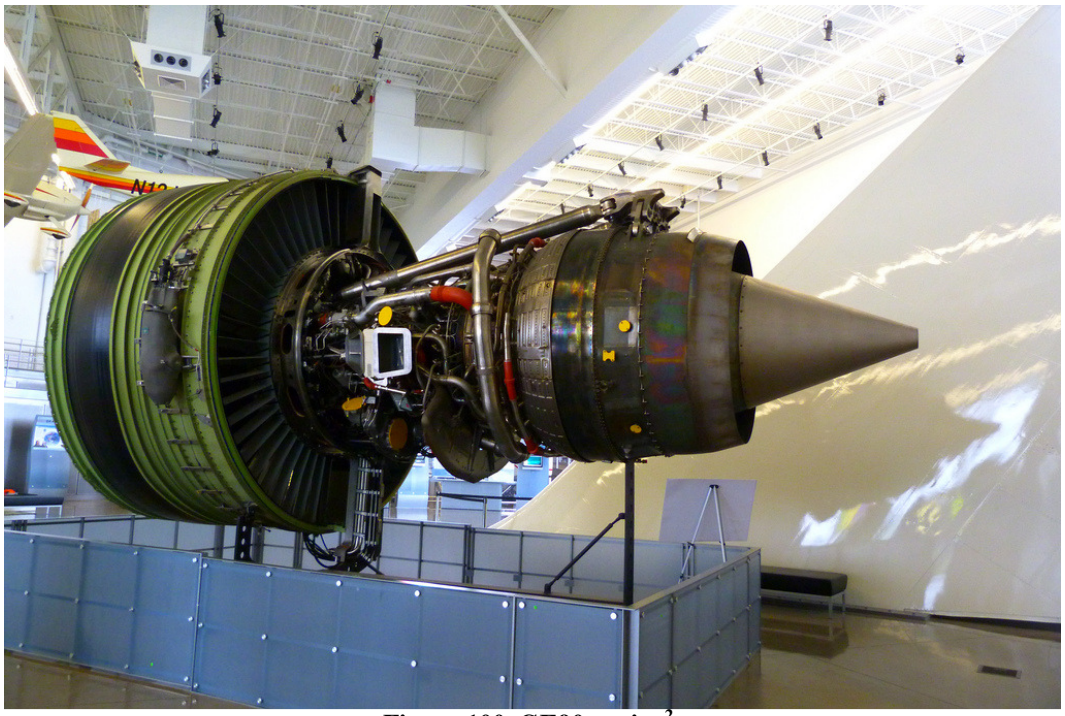

Figure 100. GE90 engine[2].

It should be noted that multiple assumptions in this analysis may prove to be overly optimistic. The first is that the entire region around the 'waist' of the engine is available for use by the fuel cell assembly. In reality, some of this space on current engines is occupied by engine accessories and attachments. It can be seen on an

[2] Image source, accessed 3/23/2015:
Photograph by Joe Kunzler, https://www.flickr.com/photos/avgeekjoe/6081507336
https://creativecommons.org/licenses/by-nc-nd/2.0/legalcode

engine like the GE90 (Figure 100) that although a number of pipes and accessories are located in the 'waist' there remains a significant amount of vacant volume.

A second assumption involves the magnitudes of the assumed pressure losses in the hot section (combustor and CPOx/SOFC). Channel flow models indicate that pressure losses in the CPOx and SOFC are indeed small (1 to 2 percent). However, a model of the pressure drop associated with turning the flow is not incorporated into the model at present (but will be in the future). These losses are currently estimated separately using a loss coefficient, $K_L = \Delta P / \left(\frac{1}{2}\rho v^2\right)$ [115]. The loss coefficient can be used to bound the magnitude of the pressure loss by evaluating it for a range of flow properties selected to span the limits of the conditions expected in the duct during flight at either HALE UAV or regional jet cruise conditions: pressure = 3-4 atm, temperature = 300-450^{o}C, molecular weight = 22-29 g/mol, velocity = 15-45 m/s, and 5 flow bends averaging loss coefficients between 0.2 and 1.1 [115] each. Under these conditions, the pressure loss ranges from negligible (0.04% for high temperature, low MW, low velocity, low K_L) up to 3.4% (low temperature, high MW, high velocity, high K_L). At sea level full throttle conditions (pressure = 18-40 atm, temperature = 400-650^{o}C, other assumptions the same), the pressure loss ranges from negligible (0.03%) up to 2.9%. Although the magnitude of pressure losses are greater, the pressure itself is also greater and the result is a percentage drop of comparable size to the higher altitude cases.

Finally, determining the pressure losses associated with extracting and reintroducing the CPOx/SOFC flow is challenging because the fluid mechanics are complex. However, one can get an idea of what these might be in Mattingly [110]

who summarizes the pressure drops associated with several gas turbine components (diffuser, burner, afterburner, and nozzle) over several eras of technology. Relatively modern (1985-present) burners and afterburners produce pressure drops of 5-6%. Since the flow paths associated with the reintroduction of SOFC exhaust are not radically different from paths in these components, assuming a pressure drop of 5-6% or less for the reintroduction seems reasonable. In addition, it is possible that existing mixing enhancement and flame holding structures in the burner could serve a dual purpose by reintroducing the SOFC flow. Also, since the SOFC exhaust will be rich in reactive low molecular weight molecules like H_2 and CO, it is even possible that flameholding could be enhanced and operating limits extended. Nevertheless, a fuller accounting of pressure losses is important and should be a focus of future research.

In summary, the results of this section's analysis indicate that there are a number of relatively simple steps that can be taken to greatly reduce the aerodynamic drag penalty enabling one to realize the full benefits of the GT-SOFC combined propulsion and power concept.

Chapter 8: Conclusions and Future Work

8.1 Summary and Key Findings

Alternative means for efficiently generating electricity on board aircraft are required to meet growing electrical demands on air vehicles. These demands are only expected to increase as hydraulic actuators and controls are replaced with electrical ones, sensor and telemetry payloads grow, and new devices like in-flight entertainment systems (or even directed energy weapons) are introduced.

This work has investigated a promising way to meet this demand that exploits fuel cells' high thermodynamic efficiency while minimizing associated balance of plant and specific power penalties. This is accomplished by integrating a catalytic partial oxidation reactor and solid oxide fuel cell directly into a gas turbine engine's flow path in a way that permits the gas turbine to absorb many of the balance of plant losses that reduce a fuel cell's specific power. Of particular importance are the use of pressurized engine air to increase fuel cell performance and the recapture by the engine cycle of heat and unreacted fuel from the fuel cell.

A review of the literature shows that while GT-SOFC hybrids have been investigated for ground-based power and as stand-alone auxiliary power units (APUs), GT-SOFC hybrids for combined propulsion and power on aircraft have not been investigated.

The efficacy of the hybrid GT-SOFC as a combined source of propulsive and electrical power is evaluated by developing models of CPOx and SOFC components and inserting them into a gas turbine cycle model implemented in an industry

standard tool called Numerical Propulsion System Simulation (NPSS). The CPOx and SOFC models account for equilibrium gas phase and electrochemical reaction, pressure losses, and heat losses in a way that captures 'down-the-channel' effects. This level of fidelity is necessary to provide meaningful estimates of the performance of integrated GT-SOFC power systems and insight into the physical factors that drive the efficacy of the integration.

The GT models are validated by confirming that model predictions are consistent with the known performance of existing GT engines. The CPOx model is tested over a range of conditions and the results are shown to be consistent with the basic principles of chemical equilibrium. The SOFC model is also tested over a range of conditions and its results are shown to be consistent with analogous modeling results in the literature.

The system model is used to investigate fuel consumption and specific power of the GT-SOFC hybrids at scales appropriate for larger GT-powered UAVS like the Northrop Grumman RQ-4 Global Hawk, General Atomics' MQ-9 Reaper, and General Atomics' Avenger, and flight conditions appropriate for high altitude long endurance (HALE) UAVs as well as for typical regional commercial aircraft. The effects of changing the engine type, bypass ratio, overall pressure ratio, and fuel cell arrangement geometry are investigated. External aerodynamic drag on the outer surface of the fuel cell assembly has been included to capture important effects of engine / fuel cell integration.

The key findings of this work are summarized below:

- Demonstrated the favorable effect of gas turbine engine operating conditions on fuel cell performance
    - Raising OPR from 24 to 40 increases FC power density by 11%
    - The rate of improvement of FC performance decreases with increasing pressure indicating that there is a diminishing return
- Showed that GT-SOFC systems can produce more electrical power than GT-generator systems because turbine inlet temperature increases more slowly with electric power production
    - Generator based systems run into the TIT limit at $\zeta = 0.15 - 0.35$
    - GT-SOFC systems are typically capable of $\zeta > 0.5$
- Performed a sensitivity and error analysis that:
    - Identified external aerodynamic drag as the main impediment to realizing the thermodynamic benefits of GT-SOFC hybridization
    - Showed that operating voltage and percent fuel oxidation are the most important fuel-cell related operating parameters
    - Showed that reductions in fuel consumption are larger than (and therefore distinguishable from) variations associated with uncertainties in model input parameters
        - Estimated uncertainty in a 50 kW system is <1% which is smaller than the predicted reduction in fuel burn (>3%)
- Showed that relatively large reductions in fuel burn rate are possible in HALE UAVs and commercial aircraft (RTJ) depending on the electric power demand, engine configuration, bypass ratio, and overall pressure ratio:

Table 21: Upper limit of fuel burn reduction (i.e., no FC drag).

Aircraft	BPR	OPR	Fuel Burn Reduction at 50 kW	100 kW	200 kW
HALE	0	24	3.5%	7.3%	16.4%
HALE	0.5	24	3.8%	8.9%	20.6%
HALE	5	24	3.9%		
RTJ	5	24	1.7%	3.6%	8.4%
HALE	5	31.5	3.5%	8.4%	
HALE	5	40	3.1%	7.3%	
HALE	8	40	3.3%		

* blank spaces indicate no comparison was possible due to TIT limit on GT-generator system

- Studied the aerodynamic drag penalty associated with large volume fuel cells integrated into high BPR turbofan engines and showed that external aerodynamic drag penalties can be reduced significantly by replacing short fuel cells that stack in the radial direction with longer fuel cells that can be contained in the narrow 'waist' section of high BPR turbofans
    - On a 35 kN rated, BPR=8, OPR=40 engine at a high altitude UAV flight condition, electric power output of nearly 100 kW is possible without encountering drag effects and 150-200 kW is possible with 1-2% fuel burn penalty from drag

8.2 Contributions

The body of work presented herein makes a number of significant contributions to the development of advanced simulation tools and propulsion systems:

- Developed the most advanced Catalytic Partial Oxidation reactor and Solid Oxide Fuel Cell models for Gas Turbine – Solid Oxide Fuel Cell studies to date, incorporating:
    - Equilibrium chemistry

    - Ability to capture ‘down the channel’ performance
    - Realistic thermal model (2-D)
    - Detailed mass and volume estimation
- Developed a methodology for estimating the mass of integrated GT-SOFC systems and quantified its level of uncertainty
    - The methodology is based on previously existing gas turbine mass models and new mass models for CPOx and SOFCs
- Developed a first of its kind, comprehensive framework to quantify the performance of a hybrid GT-SOFC engine for combined propulsion and power on aircraft
    - While focused on combined propulsion and power, the model is equally applicable for ground-based, ship-based, or auxiliary power unit applications
- Performed the first investigation of its kind into hybrid GT-SOFC systems:
    - The first study of GT-SOFCs intended for combined propulsion and power on aircraft
    - The first study of GT-SOFCs to incorporate both thermodynamic and aerodynamic factors in the evaluation of system and vehicle level performance
- Derived an analytical expression for the effect of electrical power demand and generation efficiency on the fuel consumption of a fixed wing aircraft assuming a known drag polar

- Derived an extension to the Breguet range equation to form an analytical expression for the effect of electrical power demand and generation efficiency on the range of a fixed wing aircraft assuming constant lift-to-drag
- Showed that the 'conventional wisdom' that SOFC systems' specific power is orders of magnitude smaller than that of gas turbines is untrue in integrated GT-SOFC systems at the conditions associated with high altitude cruise
    - At 16.8 km altitude, a BPR=5, OPR=24 GT operates at ambient pressures of 0.09 atm, dropping the specific power to 775 W/kg
    - Meanwhile, the SOFC is pressurized to 2.3 atm, raising the specific power to 511 W/kg

8.3 Future Work

There are many areas where this work could be advanced, expanded, and improved moving forward:

- Extending fuel cell drag modeling to the turbojet and low BPR turbofan engines:
    - The current drag modeling is directed at layouts specific to high BPR separate exhaust turbofans
    - The more extensive analysis presented for high BPR engines could be extended to the turbojet and low BPR engines with appropriate drag models
- Exploring the flight envelope for the HALE UAV and regional jet vehicles:

    - The current work is limited to a handful of the most important operating points (cruise, takeoff, idle) but performance over a wide range of operating conditions is of importance for actual missions
    - The sensitivity analysis could be extended to cover more operating points of interest
    - Characterizing the GT-SOFC performance during climb and non-standard cruising conditions would greatly expand on the scope of this study
- Incorporating more comprehensive accounting of pressure loss mechanisms in the fuel cell assembly:
    - Pressure loss estimates relating to flow extraction, turning, and reintroduction are currently not captured inside the model
    - Estimating these losses accurately will be important for developing optimal integration strategies
- Estimating the impact of using more novel MEA structures such as those proposed by Steffen et al. [62]:
    - Use of a corrugated anode support structure reduced fuel cell mass by nearly 50% (in a theoretical study)
    - Estimating the mass reduction and durability concerns associated with this and similar concepts could be of significant importance to the advancement of GT-SOFC technology
- Building and testing a bench scale GT-SOFC and accurately modeling the system using the tools developed in this work:

- A working GT-SOFC system that is capable of generating both thrust and electrical power would provide a true proof of concept
- Work is currently underway by a colleague to design a bench scale system using the modeling tools presented in this work

Appendix A:

Derivation of Fuel Flow, Range, and Endurance

A.1 General Range and Endurance

The mass flow rate of fuel in an aircraft can be related to the rate of change of vehicle mass (assuming fuel burn is the only mechanism for mass change) [10]:

$$\dot{m}_f \equiv \frac{dm_f}{dt} = -\frac{dm}{dt}$$

where m_f is the fuel mass and m is the vehicle mass. This can be rearranged to form an expression for dt:

$$dt = -\frac{dm}{\dot{m}_f}$$

Because endurance, E, can be generally expressed as the integral of time over the duration of the mission, the following general expression can be formed for a fuel burning aircraft:

$$\int_0^E dt = -\int_{m_{ini}}^{m_{fin}} \frac{dm}{\dot{m}_f} = \int_{m_{fin}}^{m_{ini}} \frac{dm}{\dot{m}_f}$$

$$\boxed{E = \int_{m_{fin}}^{m_{ini}} \frac{dm}{\dot{m}_f}}$$

where m_{ini} and m_{fin} are the initial and final vehicle mass, respectively.

To arrive at a similar expression for range, one can expand the derivative of fuel mass with respect to distance traveled, s, via the product rule:

$$\frac{dm_f}{ds} = \frac{dm_f}{dt}\frac{dt}{ds} = \frac{\dot{m}_f}{v}$$

where v is the flight velocity. This equation can then be rearranged to form an expression for ds [10]:

$$ds = v\frac{dm_f}{\dot{m}_f} = -v\frac{dm}{\dot{m}_f}$$

Because endurance, R, can be generally expressed as the integral of distance traveled over the duration of the mission, the following general expression can be formed for a fuel burning aircraft:

$$\int_0^R ds = -\int_{m_{ini}}^{m_{fin}} v\frac{dm}{\dot{m}_f} = \int_{m_{fin}}^{m_{ini}} v\frac{dm}{\dot{m}_f}$$

$$\boxed{R = \int_{m_{fin}}^{m_{ini}} v\frac{dm}{\dot{m}_f}}$$

A.2 Standard Breguet Range and Endurance

The Breguet range equation is derived by assuming level flight at constant velocity and constant lift-to-drag ratio (L/D) [11]. This represents a so-called 'cruise-climb' where the aircraft gradually increases altitude to maintain L/D as the weight of the aircraft (thus required lift) decreases. The assumption of level flight implies that lift is equal to weight ($L = mg$) and thrust is equal to drag ($F_{th} = D$). Under these circumstances, the mass flow rate of fuel can be expressed [10]:

$$\dot{m}_f = \frac{vF_{th}}{\eta_F Q_f} = v\frac{mg}{\eta_F Q_f (L/D)}$$

where η_F is the overall efficiency with which the engine produces thrust power and Q_f is the energy content of the fuel. Equivalently, the fuel flow can be expressed:

$$\dot{m}_f = (TSFC)\frac{mg}{(L/D)}$$

where TSFC is the thrust specific fuel consumption of the engine.

By plugging the mass flow rate equation into the general expressions derived above, the endurance can be found:

$$E = \int_{m_{fin}}^{m_{ini}} \left(v \frac{mg}{\eta_F Q_f (L/D)} \right)^{-1} dm = \eta_F Q_f \frac{(L/D)}{vg} \int_{m_{fin}}^{m_{ini}} \frac{dm}{m}$$

$$\boxed{E = \eta_F Q_f \frac{(L/D)}{vg} \ln\left(\frac{m_{ini}}{m_{fin}}\right)}$$

Or equivalently:

$$\boxed{E = \frac{(L/D)}{(TSFC)g} \ln\left(\frac{m_{ini}}{m_{fin}}\right)}$$

By plugging in for range:

$$R = \int_{m_{fin}}^{m_{ini}} v \left(v \frac{mg}{\eta_F Q_f (L/D)} \right)^{-1} dm = \eta_F Q_f \frac{(L/D)}{g} \int_{m_{fin}}^{m_{ini}} \frac{dm}{m}$$

$$\boxed{R = \eta_F Q_f \frac{(L/D)}{g} \ln\left(\frac{m_{ini}}{m_{fin}}\right)}$$

Or equivalently:

$$\boxed{R = v \frac{(L/D)}{(TSFC)g} \ln\left(\frac{m_{ini}}{m_{fin}}\right)}$$

A.3 Modified Breguet Range and Endurance

For a vehicle that produces thrust and electric power, the electric power fraction can be defined:

$$\zeta = \frac{\dot{W}_{elec}}{\dot{W}_{elec} + \dot{W}_{prop}}$$

where $\dot{W}_{elec}$ is the electric power and $\dot{W}_{prop} = vF_{th}$ is the propulsive power. The electric power can thus be written:

$$\dot{W}_{elec} = \left[\frac{\zeta}{1-\zeta}\right] \dot{W}_{prop} = \left[\frac{\zeta}{1-\zeta}\right] vF_{th}$$

The mass flow of fuel for the combined thrust and electricity producing engine can be expressed:

$$\dot{m}_f = \frac{vF_{th}}{Q_f \eta_F} + \frac{\dot{W}_{elec}}{Q_f \eta_{elec}}$$

Or equivalently:

$$\dot{m}_f = (TSFC)F_{th} + \frac{\dot{W}_{elec}}{Q_f \eta_{elec}}$$

where η_{elec} is the electric efficiency. Substituting for $\dot{W}_{elec}$:

$$\dot{m}_f = \frac{vF_{th}}{Q_f \eta_F} + \frac{1}{Q_f \eta_{elec}}\left[\frac{\zeta}{1-\zeta}\right] vF_{th}$$

$$\dot{m}_f = \left(\frac{1}{\eta_F} + \frac{1}{\eta_{elec}}\left[\frac{\zeta}{1-\zeta}\right]\right)\frac{vF_{th}}{Q_f}$$

Or equivalently:

$$\dot{m}_f = \left((TSFC) + \frac{v}{Q_f \eta_{elec}}\left[\frac{\zeta}{1-\zeta}\right]\right) F_{th}$$

The Breguet range equation can be extended to a vehicle that produces thrust and electric power using these expressions for mass flow rate of fuel. The same assumptions of level flight, constant velocity, and constant L/D apply here.

Because propulsive power varies throughout the flight, defining electric power in terms of the instantaneous power fraction will lead to an electrical demand that decreases in direct proportion to vehicle drag (an unrealistic assumption). The initial conditions (ζ_{ini}, $F_{th,ini}$) of the flight can be used to express a constant electric power:

$$\dot{W}_{elec} = \left[\frac{\zeta_{ini}}{1-\zeta_{ini}}\right] \dot{W}_{prop,ini}$$

$$F_{th,ini} = \frac{m_{ini} g}{(L/D)}$$

where the subscript '*ini*' denotes conditions at the start of flight. The above expressions for mass flow of fuel can thus be adapted for constant electric power 'cruise-climb':

$$\dot{m}_f = \left(\frac{m}{\eta_F} + \frac{m_{ini}}{\eta_{elec}}\left[\frac{\zeta_{ini}}{1-\zeta_{ini}}\right]\right)\frac{v}{Q_f}\frac{g}{(L/D)}$$

Or equivalently:

$$\dot{m}_f = \left((TSFC)m + \frac{v m_{ini}}{Q_f \eta_{elec}}\left[\frac{\zeta_{ini}}{1-\zeta_{ini}}\right]\right)\frac{g}{(L/D)}$$

Due to the assumptions listed above, propulsive power is dependent on instantaneous vehicle mass while electric power is only dependent on initial mass (though this could easily be expressed in terms of final or mid-flight conditions instead of initial).

The expression for mass flow can be plugged into the general equations for endurance and range, then integrated:

$$E = \int_{m_{fin}}^{m_{ini}} \frac{Q_f}{v}\frac{(L/D)}{g}\left(\frac{m}{\eta_F} + \frac{m_{ini}}{\eta_{elec}}\left[\frac{\zeta_{ini}}{1-\zeta_{ini}}\right]\right)^{-1} dm$$

$$E = \frac{Q_f \eta_F}{v}\frac{(L/D)}{g}\ln\left(\frac{\frac{m_{ini}}{\eta_F} + \frac{m_{ini}}{\eta_{elec}}\left[\frac{\zeta_{ini}}{1-\zeta_{ini}}\right]}{\frac{m_{fin}}{\eta_F} + \frac{m_{ini}}{\eta_{elec}}\left[\frac{\zeta_{ini}}{1-\zeta_{ini}}\right]}\right)$$

$$\boxed{E = \frac{Q_f \eta_F}{v}\frac{(L/D)}{g}\ln\left(\frac{\frac{1}{\eta_F} + \frac{1}{\eta_{elec}}\left[\frac{\zeta_{ini}}{1-\zeta_{ini}}\right]}{\frac{1}{\eta_F(m_{ini}/m_{fin})} + \frac{1}{\eta_{elec}}\left[\frac{\zeta_{ini}}{1-\zeta_{ini}}\right]}\right)}$$

Or equivalently:

$$\boxed{E = \frac{(L/D)}{(TSFC)g}\ln\left(\frac{(TSFC) + \frac{v}{Q_f \eta_{elec}}\left[\frac{\zeta_{ini}}{1-\zeta_{ini}}\right]}{\frac{(TSFC)}{(m_{ini}/m_{fin})} + \frac{v}{Q_f \eta_{elec}}\left[\frac{\zeta_{ini}}{1-\zeta_{ini}}\right]}\right)}$$

And then the range:

$$R = \int_{m_{fin}}^{m_{ini}} Q_f \frac{(L/D)}{g}\left(\frac{m}{\eta_F} + \frac{m_{ini}}{\eta_{elec}}\left[\frac{\zeta_{ini}}{1-\zeta_{ini}}\right]\right)^{-1} dm$$

$$R = Q_f \eta_F \frac{(L/D)}{g} \ln\left(\frac{\frac{m_{ini}}{\eta_F} + \frac{m_{ini}}{\eta_{elec}}\left[\frac{\zeta_{ini}}{1-\zeta_{ini}}\right]}{\frac{m_{fin}}{\eta_F} + \frac{m_{ini}}{\eta_{elec}}\left[\frac{\zeta_{ini}}{1-\zeta_{ini}}\right]}\right)$$

$$\boxed{R = Q_f \eta_F \frac{(L/D)}{g} \ln\left(\frac{\frac{1}{\eta_F} + \frac{1}{\eta_{elec}}\left[\frac{\zeta_{ini}}{1-\zeta_{ini}}\right]}{\frac{1}{\eta_F(m_{ini}/m_{fin})} + \frac{1}{\eta_{elec}}\left[\frac{\zeta_{ini}}{1-\zeta_{ini}}\right]}\right)}$$

Or equivalently:

$$\boxed{R = \frac{v(L/D)}{(TSFC)g} \ln\left(\frac{(TSFC) + \frac{v}{Q_f \eta_{elec}}\left[\frac{\zeta_{ini}}{1-\zeta_{ini}}\right]}{\frac{(TSFC)}{(m_{ini}/m_{fin})} + \frac{v}{Q_f \eta_{elec}}\left[\frac{\zeta_{ini}}{1-\zeta_{ini}}\right]}\right)}$$

A.4 Mass Flow Rate of Fuel with Drag Polar

An expression for the mass flow rate of fuel assuming a drag polar of the form $C_D = C_{D,min} + K\left(C_L - C_{L,min}\right)^2$ can be found for level flight. Assume that thrust is equal to drag, D:

$$F_{th} = D = \tfrac{1}{2}\rho v^2 S[C_{Dmin} + K(C_L - C_{Lmin})^2]$$

where ρ is the density and S is the aircraft wing area. C_{Dmin}, K, and C_{Lmin} are drag polar parameters. The definition of the lift coefficient, combined with the assumption that lift is equal to weight:

$$C_L = \frac{L}{\frac{1}{2}\rho v^2 S} = \frac{(m_0 + m_{elec})g}{\frac{1}{2}\rho v^2 S}$$

where m_0 is the mass of the vehicle and m_{elec} is the mass of the electric system. The thrust can thus be expressed:

$$F_{th} = \tfrac{1}{2}\rho v^2 S\left[C_{Dmin} + K\left(\frac{(m_0 + m_{elec})g}{\frac{1}{2}\rho v^2 S} - C_{Lmin}\right)^2\right]$$

Recall from the previous section:

$$\dot{m}_f = \left((TSFC) + \frac{v}{Q_f \eta_{elec}} \left[\frac{\zeta}{1-\zeta} \right] \right) F_{th}$$

Therefore, the mass flow of fuel is:

$$\boxed{\dot{m}_f = \left((TSFC) + \frac{v}{Q_f \eta_{elec}} \left[\frac{\zeta}{1-\zeta} \right] \right) \frac{1}{2} \rho v^2 S \left[C_{Dmin} + K \left(\frac{(m_0 + m_{elec})g}{\frac{1}{2}\rho v^2 S} - C_{Lmin} \right)^2 \right]}$$

The mass flow at $\zeta = 0$ is found by also setting $m_{elec} = 0$:

$$\dot{m}_f(\zeta = 0) = (TSFC) \frac{1}{2} \rho v^2 S \left[C_{Dmin} + K \left(\frac{m_0 g}{\frac{1}{2}\rho v^2 S} - C_{Lmin} \right)^2 \right]$$

The 'relative' mass flow ($\dot{m}_f{}' = \dot{m}_f / \dot{m}_f(\zeta = 0)$) is thus:

$$\dot{m}_f{}' = \frac{\left((TSFC) + \frac{v}{Q_f \eta_{elec}} \left[\frac{\zeta}{1-\zeta} \right] \right) \frac{1}{2} \rho v^2 S \left[C_{Dmin} + K \left(\frac{(m_0 + m_{elec})g}{\frac{1}{2}\rho v^2 S} - C_{Lmin} \right)^2 \right]}{(TSFC) \frac{1}{2} \rho v^2 S \left[C_{Dmin} + K \left(\frac{m_0 g}{\frac{1}{2}\rho v^2 S} - C_{Lmin} \right)^2 \right]}$$

$$\boxed{\dot{m}_f{}' = \left(1 + \frac{v}{(TSFC) Q_f \eta_{elec}} \left[\frac{\zeta}{1-\zeta} \right] \right) \frac{\left[C_{Dmin} + K \left(\frac{(m_0 + m_{elec})g}{\frac{1}{2}\rho v^2 S} - C_{Lmin} \right)^2 \right]}{\left[C_{Dmin} + K \left(\frac{m_0 g}{\frac{1}{2}\rho v^2 S} - C_{Lmin} \right)^2 \right]}}$$

Appendix B:

Iterative Methods for Nonlinear Systems

B.1 Newton's Method

The following discussion of Newton's method follows the presentation of Ortega and Rheinboldt [72] with notation modifications. The general class of 'parallel chord methods' can be described as proceeding towards the root of a function, $f(x)$, via repeated iterations of the following form:

$$x^{k+1} = x^k - m^{-1} f\left(x^k\right) \tag{174}$$

where the superscripts denote the iteration and m is the slope of some line used to approximate the function. In the case where this slope is that of the tangent to the function at x^k, Newton's method results:

$$x^{k+1} = x^k - f'\left(x^k\right)^{-1} f\left(x^k\right) \tag{175}$$

where f' is the first derivate of the function. This expression can be easily expanded to n-dimensions by introducing the Jacobian matrix [79]:

$$F'_{ij} = \frac{\partial F_i}{\partial x_j} \tag{176}$$

where F_i is the i^{th} entry in the n-dimensional array of functions and x_j is the j^{th} entry in the n-dimensional parameter vector. The n-dimensional Newton's method is thus:

$$x^{k+1} = x^k - F'\left(x^k\right)^{-1} F\left(x^k\right) \tag{177}$$

where x now represents a vector and not a scalar as before.

For problems, such as the one in this work, where the derivatives cannot be explicitly calculated, a finite difference approximation of the Jacobian can be used. Any differencing approach can be used, but a common choice [72] is the simple first order forward difference:

$$F'_{ij} \approx \left[F_i\left(x_j + \Delta x_j\right) - F_i\left(x_j\right)\right]/\Delta x_j \tag{178}$$

The finite differences are calculated through successive perturbation of each member of x^k. For the unmodified Newton's method, the Jacobian is recalculated for each iteration which requires $n + 1$ evaluations of F for each step.

B.2 Broyden's Method

The following discussion of Newton's method follows the presentation of Kelley [74,79] with notation modifications. Broyden's method is a so called quasi-Newton method (a family of methods formed from the extension of the secant method to several variables). The secant method approximates the derivative as [79]:

$$b^k = \left[f\left(x^k\right) - f\left(x^{k-1}\right)\right]/[x^k - x^{k-1}] \tag{179}$$

where b^k is the approximation. It follows that the secant method update is:

$$x^{k+1} = x^k - \left(b^k\right)^{-1} f\left(x^k\right) \tag{180}$$

The secant method can be expanded to n-dimensions:

$$x^{k+1} = x^k - \left(B^k\right)^{-1} F\left(x^k\right) \tag{181}$$

The matrix B^k must then also be updated. The form of this update differentiates Broyden's method from other multidimensional expansions of the secant method. For Broyden updates:

$$B^{k+1} = B^k + \frac{F\left(x^{k+1}\right)s^T}{s^T s} \tag{182}$$

where $s = x^{k+1} - x^k$ and the superscript 'T' denotes the transpose. The use of these updates requires carrying the previous matrix through the iteration but at the

enormous benefit of not requiring another series of perturbations to produce a new Jacobian.

Appendix C:

Compressor and Turbine Performance Maps

All of the performance maps presented and used herein are derived from General Electric's contribution to NASA's Energy Efficient Engine (E^3) program [116] and included in the NPSS software release [69].

C.1 Fan Map

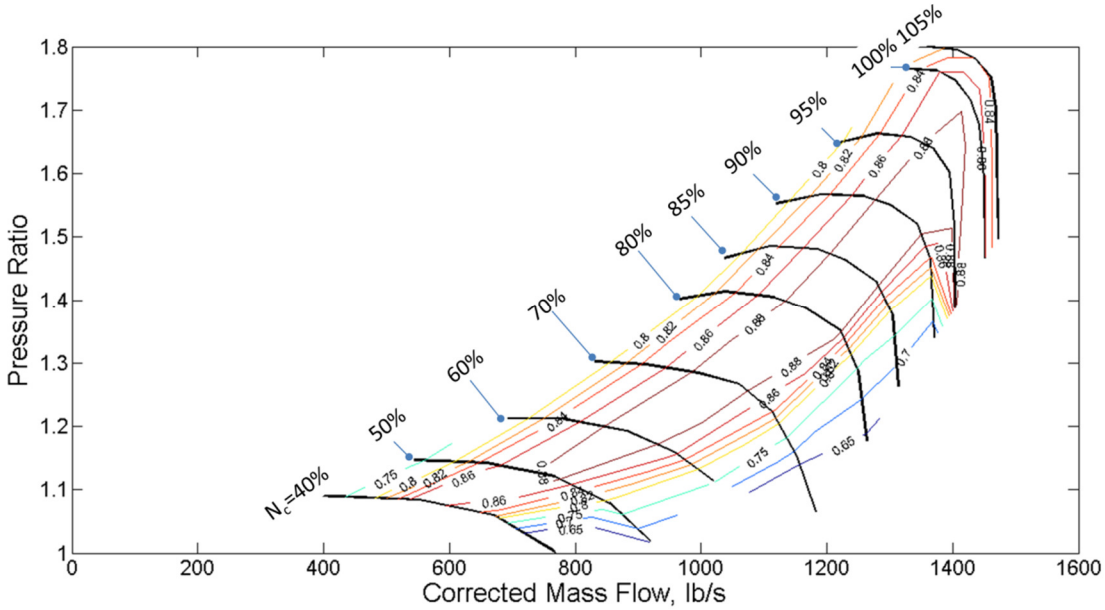

Figure 101. General Electric's fan performance map from the Energy Efficient Engine Program.

C.2 Low Pressure Compressor Map

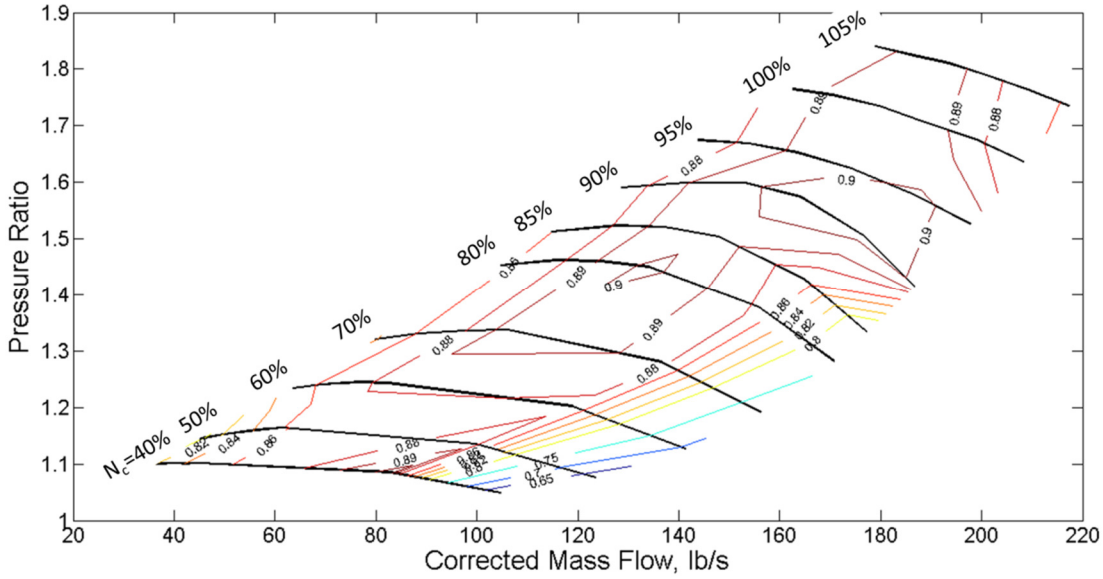

Figure 102. General Electric's LPC performance map from the Energy Efficient Engine Program.

C.3 High Pressure Compressor Map

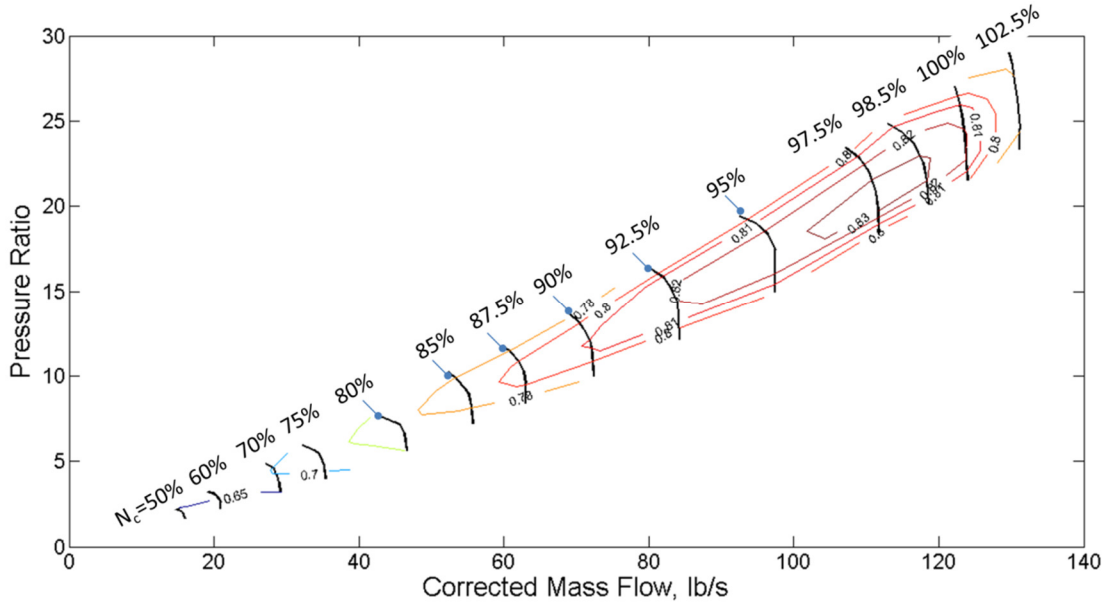

Figure 103. General Electric's HPC performance map from the Energy Efficient Engine Program.

C.4 High Pressure Turbine Map

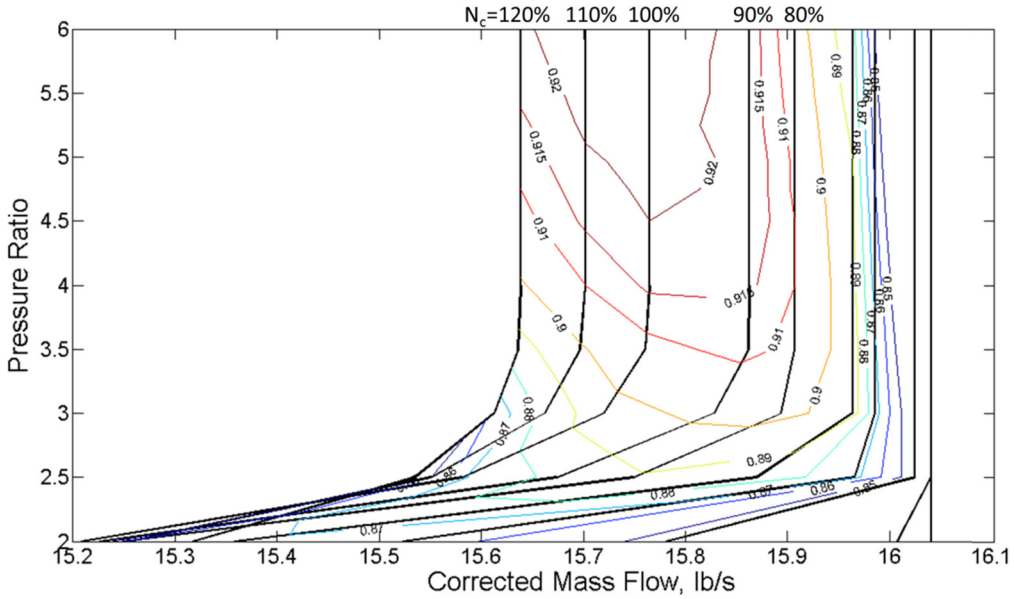

Figure 104. General Electric's HPT performance map from the Energy Efficient Engine Program.

C.5 Low Pressure Turbine Map

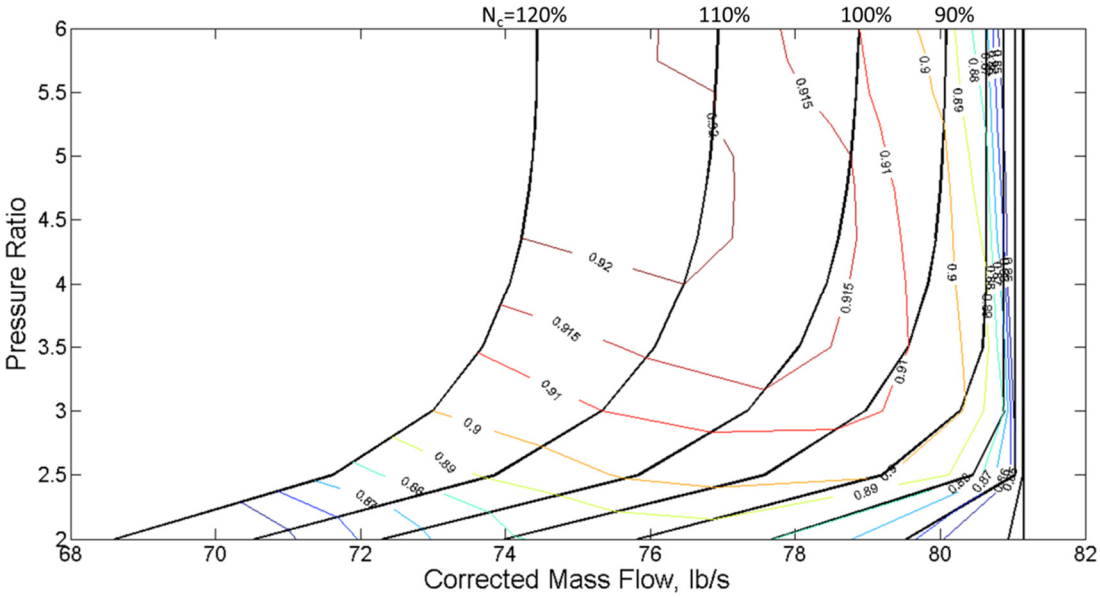

Figure 105. General Electric's LPT performance map from the Energy Efficient Engine Program.

Appendix D:

Details of Finite Volume Heat Transfer Modeling

D.1 Volume Discretization of Fuel Cell Geometry

The following is an illustration of the repeating fuel cell geometry. The center line in both directions is a plane of symmetry meaning that only one quarter of the geometry must be modeled and that no heat transfer occurs across those boundaries. The remaining quarter is divided into a unique wall geometry segment and repeating interior geometry segments. Each section of the material is divided into a number of finite volume cells (shown in red) determined by user inputs. The parameters δx_i and δy_j are the incremental cell lengths in the i/x and j/y axis directions, respectively.

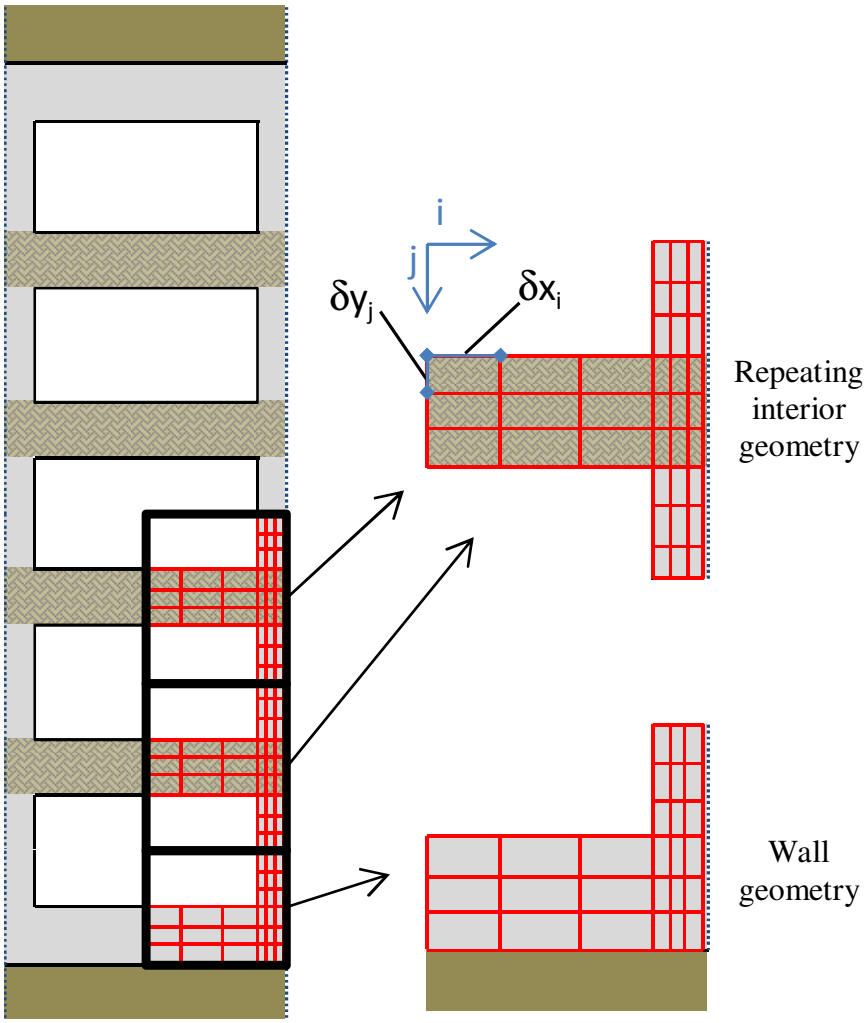

D.2 Mathematical Expressions

Interior cells (in yellow below) are finite volumes that are surrounded on four sides by other cells. Cells on the 'symmetry' boundaries are included because they are modeled with an adjacent cell assumed to be the same temperature.

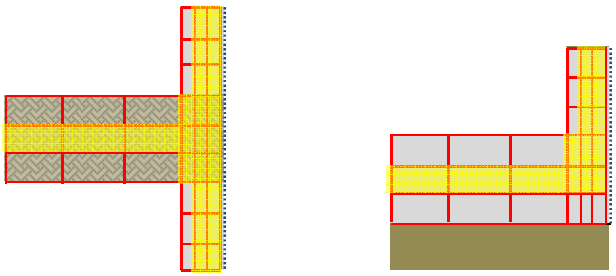

The energy balance of an interior cell is expressed by the following equations with conduction occurring between cells. In the equations, T and k denote the temperature and thermal conductivity of a cell. The subscripts indicate the location of the cell in the i and j axis directions relative to the center cell. The heat transfer code iteratively repeats the calculation of this balance for all the cells until the solution settles/ converges and no longer varies between iterations (within a user specified tolerance).

$$2\left(\frac{\delta x_{i-1}}{k_{i-1,j}}+\frac{\delta x_i}{k_{i,j}}\right)^{-1}\delta y_j\left(T_{i-1,j}-T_{i,j}\right)+2\left(\frac{\delta x_{i+1}}{k_{i+1,j}}+\frac{\delta x_i}{k_{i,j}}\right)^{-1}\delta y_j\left(T_{i+1,j}-T_{i,j}\right)$$
$$+2\left(\frac{\delta y_{j-1}}{k_{i,j-1}}+\frac{\delta y_j}{k_{i,j}}\right)^{-1}\delta x_i\left(T_{i,j-1}-T_{i,j}\right)+2\left(\frac{\delta y_{j+1}}{k_{i,j+1}}+\frac{\delta y_j}{k_{i,j}}\right)^{-1}\delta x_i\left(T_{i,j+1}-T_{i,j}\right)=0$$

$$C_1=2\left(\frac{\delta x_{i-1}}{k_{i-1,j}}+\frac{\delta x_i}{k_{i,j}}\right)^{-1}\delta y_j \qquad C_3=2\left(\frac{\delta y_{j-1}}{k_{i,j-1}}+\frac{\delta y_j}{k_{i,j}}\right)^{-1}\delta x_i$$
$$C_2=2\left(\frac{\delta x_{i+1}}{k_{i+1,j}}+\frac{\delta x_i}{k_{i,j}}\right)^{-1}\delta y_j \qquad C_4=2\left(\frac{\delta y_{j+1}}{k_{i,j+1}}+\frac{\delta y_j}{k_{i,j}}\right)^{-1}\delta x_i$$

$$T_{i,j}=\frac{T_{i-1,j}C_1+T_{i+1,j}C_2+T_{i,j-1}C_3+T_{i,j+1}C_4}{C_1+C_2+C_3+C_4}$$

Vertical channel wall cells (in yellow below) are finite volumes that are surrounded on three sides by other cells and on the fourth side by the flow channel.

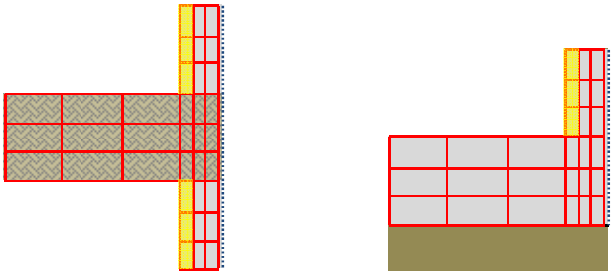

The energy balance of vertical channel wall cells is expressed by the following equations with conduction occurring between cells and forced convection occurring between the cells and the flow. In the equations, h_{ch} denotes the forced convection heat transfer coefficient and T_{ch} is the channel temperature.

$$h_{ch}\delta y_j(T_{ch}-T_{i,j})+2\left(\frac{\delta x_{i+1}}{k_{i+1,j}}+\frac{\delta x_i}{k_{i,j}}\right)^{-1}\delta y_j(T_{i+1,j}-T_{i,j})$$
$$+2\left(\frac{\delta y_{j-1}}{k_{i,j-1}}+\frac{\delta y_j}{k_{i,j}}\right)^{-1}\delta x_i(T_{i,j-1}-T_{i,j})+2\left(\frac{\delta y_{j+1}}{k_{i,j+1}}+\frac{\delta y_j}{k_{i,j}}\right)^{-1}\delta x_i(T_{i,j+1}-T_{i,j})=0$$

$$C_1=h_{ch}\delta y_j \qquad C_3=2\left(\frac{\delta y_{j-1}}{k_{i,j-1}}+\frac{\delta y_j}{k_{i,j}}\right)^{-1}\delta x_i$$

$$C_2=2\left(\frac{\delta x_{i+1}}{k_{i+1,j}}+\frac{\delta x_i}{k_{i,j}}\right)^{-1}\delta y_j \qquad C_4=2\left(\frac{\delta y_{j+1}}{k_{i,j+1}}+\frac{\delta y_j}{k_{i,j}}\right)^{-1}\delta x_i$$

$$T_{i,j}=\frac{T_{ch}C_1+T_{i+1,j}C_2+T_{i,j-1}C_3+T_{i,j+1}C_4}{C_1+C_2+C_3+C_4}$$

Top horizontal channel wall cells (in yellow below) are finite volumes that are surrounded on three sides by other cells and on the fourth side by the flow channel.

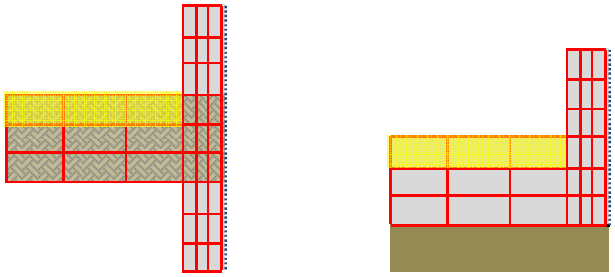

The energy balance of top horizontal channel wall cells is expressed by the following equations with conduction occurring between cells and forced convection occurring between the cells and the flow.

$$2\left(\frac{\delta x_{i-1}}{k_{i-1,j}}+\frac{\delta x_i}{k_{i,j}}\right)^{-1}\delta y_j\left(T_{i-1,j}-T_{i,j}\right)+2\left(\frac{\delta x_{i+1}}{k_{i+1,j}}+\frac{\delta x_i}{k_{i,j}}\right)^{-1}\delta y_j\left(T_{i+1,j}-T_{i,j}\right)$$
$$+h_{ch}\delta x_i\left(T_{ch}-T_{i,j}\right)+2\left(\frac{\delta y_{j+1}}{k_{i,j+1}}+\frac{\delta y_j}{k_{i,j}}\right)^{-1}\delta x_i\left(T_{i,j+1}-T_{i,j}\right)=0$$

$$C_1=2\left(\frac{\delta x_{i-1}}{k_{i-1,j}}+\frac{\delta x_i}{k_{i,j}}\right)^{-1}\delta y_j \qquad C_3=h_{ch}\delta x_i$$

$$C_2=2\left(\frac{\delta x_{i+1}}{k_{i+1,j}}+\frac{\delta x_i}{k_{i,j}}\right)^{-1}\delta y_j \qquad C_4=2\left(\frac{\delta y_{j+1}}{k_{i,j+1}}+\frac{\delta y_j}{k_{i,j}}\right)^{-1}\delta x_i$$

$$T_{i,j}=\frac{T_{i-1,j}C_1+T_{i+1,j}C_2+T_{ch}C_3+T_{i,j+1}C_4}{C_1+C_2+C_3+C_4}$$

Bottom horizontal channel wall cells (in yellow below) are finite volumes that are surrounded on three sides by other cells and on the fourth side by the flow channel.

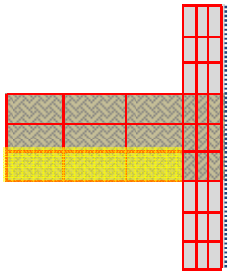

The energy balance of bottom horizontal channel wall cells is expressed by the following equations with conduction occurring between cells and forced convection occurring between the cells and the flow.

$$2\left(\frac{\delta x_{i-1}}{k_{i-1,j}}+\frac{\delta x_i}{k_{i,j}}\right)^{-1}\delta y_j\left(T_{i-1,j}-T_{i,j}\right)+2\left(\frac{\delta x_{i+1}}{k_{i+1,j}}+\frac{\delta x_i}{k_{i,j}}\right)^{-1}\delta y_j\left(T_{i+1,j}-T_{i,j}\right)$$
$$+2\left(\frac{\delta y_{j-1}}{k_{i,j-1}}+\frac{\delta y_j}{k_{i,j}}\right)^{-1}\delta x_i\left(T_{i,j-1}-T_{i,j}\right)+h_{ch}\delta x_i\left(T_{ch}-T_{i,j}\right)=0$$

$$C_1=2\left(\frac{\delta x_{i-1}}{k_{i-1,j}}+\frac{\delta x_i}{k_{i,j}}\right)^{-1}\delta y_j \qquad C_3=2\left(\frac{\delta y_{j-1}}{k_{i,j-1}}+\frac{\delta y_j}{k_{i,j}}\right)^{-1}\delta x_i$$

$$C_2=2\left(\frac{\delta x_{i+1}}{k_{i+1,j}}+\frac{\delta x_i}{k_{i,j}}\right)^{-1}\delta y_j \qquad C_4=h_{ch}\delta x_i$$

$$T_{i,j}=\frac{T_{i-1,j}C_1+T_{i+1,j}C_2+T_{i,j-1}C_3+T_{ch}C_4}{C_1+C_2+C_3+C_4}$$

Exterior cells (in yellow below) are finite volumes that are surrounded on three sides by other cells and on the fourth side by the insulated wall.

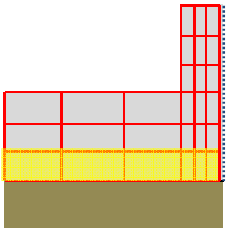

The energy balance of exterior cells is expressed by the following equations with conduction occurring between cells and conduction between the cell and the insulation. The parameters k_{ins}, δ_{ins}, and T_{amb} are the insulation thermal conductivity, insulation thickness, and ambient flow temperature, respectively. Conduction through the insulation assumes a linear temperature profile and that the outside insulation wall matches the ambient temperature.

$$2\left(\frac{\delta x_{i-1}}{k_{i-1,j}}+\frac{\delta x_i}{k_{i,j}}\right)^{-1}\delta y_j\left(T_{i-1,j}-T_{i,j}\right)+2\left(\frac{\delta x_{i+1}}{k_{i+1,j}}+\frac{\delta x_i}{k_{i,j}}\right)^{-1}\delta y_j\left(T_{i+1,j}-T_{i,j}\right)$$
$$+2\left(\frac{\delta y_{j-1}}{k_{i,j-1}}+\frac{\delta y_j}{k_{i,j}}\right)^{-1}\delta x_i\left(T_{i,j-1}-T_{i,j}\right)+\frac{k_{ins}}{\delta_{ins}}\delta x_i\left(T_{amb}-T_{i,j}\right)=0$$

$$C_1=2\left(\frac{\delta x_{i-1}}{k_{i-1,j}}+\frac{\delta x_i}{k_{i,j}}\right)^{-1}\delta y_j \qquad C_3=2\left(\frac{\delta y_{j-1}}{k_{i,j-1}}+\frac{\delta y_j}{k_{i,j}}\right)^{-1}\delta x_i$$

$$C_2=2\left(\frac{\delta x_{i+1}}{k_{i+1,j}}+\frac{\delta x_i}{k_{i,j}}\right)^{-1}\delta y_j \qquad C_4=\frac{k_{ins}}{\delta_{ins}}\delta x_i$$

$$T_{i,j}=\frac{T_{i-1,j}C_1+T_{i+1,j}C_2+T_{i,j-1}C_3+T_{amb}C_4}{C_1+C_2+C_3+C_4}$$

Appendix E:

List of Species Considered by CEA

E.1 List of 138 Species Considered in SOFC

Ar	CH3CN	HO(CO)2OH
Ar+	CH3CO,acetyl	HO2
C	CH3COOH	HO2-
C-	CH3N2CH3	N
C+	CH3O	N-
C2	CH3O2CH3	N+
C2-	CH3OCH3	N2
C2+	CH3OH	N2-
C2H	CH3OOH	N2+
C2H2,acetylene	CH4	N2H2
C2H2,vinylidene	CN	N2H4
C2H3,vinyl	CN-	N2O
C2H4	CN+	N2O+
C2H4O,ethylen-o	CNC	N2O3
C2H5	CNCOCN	N2O4
C2H5OH	CNN	N2O5
C2H6	CO	N3
C2N2	CO+	N3H
C2O	CO2	NCN
C3	CO2+	NCO
C3H3,1-propynl	COOH	NH
C3H3,2-propynl	(HCOOH)2	NH+
C3H4,allene	H	NH2
C3H4,cyclo-	H-	NH2NO2
C3H4,propyne	H+	NH2OH
C3H5,allyl	H2	NH3
C3H6,cyclo-	H2-	NH4+
C3H6,propylene	H2+	NO
C3H6O,acetone	H2O	NO+
C3H6O,propanal	H2O(cr)	NO2
C3H6O,propylox	H2O(L)	NO2-
C3H7,i-propyl	H2O+	NO3
C3H7,n-propyl	H2O2	NO3-
C3H8	H3O+	O
C3H8O,1propanol	HCCN	O-
C3H8O,2propanol	HCCO	O(CH)2O
C3O2	HCHO,formaldehy	O+
CCN	HCN	O2
CH	HCO	O2-
CH+	HCO+	O2+
CH2	HCOOH	O3
CH2CO,ketene	HNC	OCCN
CH2OH	HNCO	OH
CH2OH+	HNO	OH-
CH3	HNO2	OH+
CH3CHO,ethanal	HNO3	OHCH2COOH

E.2 List of 108 Additional Species Considered Other Components

C(gr)
C10H21,n-decyl
C10H8,naphthale
C12H10,biphenyl
C12H9,o-bipheny
C2H2(L),acetyle
C2H4(L)
C2H4O(L),ethyle
C2H5OH(L)
C2H6(L)
C2H8N2(L),UDMH
C2N2(L)
C3H6(L),propyle
C3H7NO3(L)
C3H8(L)
C4
C4H10(L),isobut
C4H10(L),n-buta
C4H10,isobutane
C4H10,n-butane
C4H2,butadiyne
C4H4,1,3-cyclo-
C4H6,1butyne
C4H6,2butyne
C4H6,butadiene
C4H6,cyclo-
C4H8(L),1-buten
C4H8,1-butene
C4H8,cis2-buten
C4H8,cyclo-
C4H8,isobutene
C4H8,tr2-butene
C4H9,i-butyl
C4H9,n-butyl
C4H9,s-butyl
C4H9,t-butyl
C(gr)
C10H21,n-decyl
C4N2
C5
C5H10,1-pentene
C5H10,cyclo-
C5H11,pentyl
C5H11,t-pentyl
C5H12(L),n-pent
C5H12,i-pentane
C5H12,n-pentane
C5H6,1,3cyclo-
C5H8,cyclo-
C6H10,cyclo-
C6H12,1-hexene
C6H12,cyclo-
C6H13,n-hexyl
C6H14(L),n-hexa
C6H14,n-hexane
C6H2
C6H5,phenyl
C6H5NH2(L)
C6H5O,phenoxy
C6H5OH,phenol
C6H6
C6H6(L)
C7H14,1-heptene
C7H15,n-heptyl
C7H16(L),n-hept
C7H16,2-methylh
C7H16,n-heptane
C7H7,benzyl
C7H8
C7H8(L)
C7H8O,cresol-mx
C8H10,ethylbenz
C8H16,1-octene
C8H17,n-octyl
C4N2
C5
C8H18(L),isooct
C8H18(L),n-octa
C8H18,isooctane
C8H18,n-octane
C8H8,styrene
C9H19,n-nonyl
(CH2)x(cr)
(CH3COOH)2
CH3C(CH3)2CH3
CH3CN(L)
CH3NO2(L)
CH3OH(L)
CH4(L)
CH6N2(L)
H2(L)
H2O2(L)
HNO3(L)
N2(L)
N2H4(L)
N2O4(L)
NH3(L)
NH4NO3(I)
NH4NO3(II)
NH4NO3(III)
NH4NO3(IV)
NH4NO3(L)
O2(L)
O3(L)
Air
Jet-A(g)
Jet-A(L)
JP-10(g)
JP-10(L)
JP-4
JP-5
RP-1
C8H18(L),isooct
C8H18(L),n-octa

Appendix F:

NPSS Details of Turbojet Model and Hybrid

F.1 Order of Execution

The model's order of execution is the order in which the elements of the model are called on to perform their calculations. It is important that the elements be ordered such that every elements run before any other element that requires a flow stream or information from that element.

Inlet Path:

1. Ambient element: AmbientNASA 'Amb
2. Inlet Start element: InletStartNASA 'InletStart'
3. Inlet element: Inlet 'InEng'
4. Compressor element: Compressor 'CmpH'

CPOx/SOFC Path (not present in the engine-only model):

5. Splitter element: SplitterNASA 'SplitFC'
6. Fuel Start element: FuelStart 'FusCpox'
7. CPOx Reactor element: CPOX 'Cpox1'
8. Fuel Cell Inlet element: InletFC 'IFC1'
9. Solid Oxide Fuel Cell element: SolideOxideFC 'SOFC1'
10. Combiner element: Combiner 'B03'

Burner and Turbine Section:

11. Fuel Start element: FuelStart 'FusEng'
12. Burner element: BurnerNASA 'BrnPri'
13. Bleed element: Bleed 'B041'
14. Turbine element: Turbine 'TrbH'

Exhaust Path:

15. Bleed element: Bleed 'B045'
16. Duct element: DuctNASA 'D043'
17. Nozzle element: NozzleNASA 'NozPri'

Flow End:

18. Flow End element: FlowEnd ‘FePri’

Shaft:

19. Shaft element: Shaft ‘ShH’

F.2 Independents

Complete list of independent variables in the system solver:

Table 22: Turbojet, GT-SOFC system independent variables.

	Independent name	Description	Controlled parameter
	Independents present in all modeling runs		
1.	TrbH.S_map.ind_parmMap	HPT performance map parameter	TrbH.parmMap
2.	ShH.ind_Nmech	HP shaft mechanical rotation speed, N	ShH. Nmech
3.	BrnFuelControl	Burner fuel mass flow, $\dot{m}_{fuel}$	BrnPri.Wfuel
	Independents present in all 'On-Design' runs		
4.	AirControl	Inlet air mass flow, $\dot{m}_{air}$	InletStart.W_in
	Independents present in all 'Off-Design' runs		
5.	InletStart.ind_W	Inlet air mass flow, $\dot{m}_{air}$	InletStart.W
6.	CmpH.S_map.ind_RlineMap	HPC performance map parameter	CmpH.RlineMap
	Independents, optional		
7.	CpoxFuelControl	CPOx fuel mass flow, $\dot{m}_{fuel}$	Cond1.Fl_O.Tt
8.	SofcIns	SOFC insulation thickness	SOFC1.t_ins
9.	SofcRep	Number of radially repeating FC units	SOFC1.Nrep

F.3 Dependents

Complete list of dependent conditions in the system solver:

Table 23: Turbojet, GT-SOFC system dependent conditions.

	Condition name	Condition description/equation
	Dependents present in all modeling runs	
1.	ShH.integrate_Nmech	Net torque on the shaft must be zero
		$\Sigma Torque = 0$
	Dependents present in all 'On-Design' runs	
2.	TIT	Turbine inlet temperature equals input value
		$TrbH.Fl\_I.Tt = TIT_{max}$
3.	Thrust	Net thrust equals input value
		$F_{net} = F_{target}$
4.	ShH_N	Shaft speed equals value predicted by correlation
		$ShH.Nmech = N_{calc}$
	Dependents present in all 'Off-Design' runs	
5.	CmpH.S_map.dep_errWc	Corrected mass flow equals calculated value from performance map
		$\dot{m}_c = \dot{m}_{c,Map}$
6.	TrbH.S_map.dep_errWp	Corrected mass flow equals calculated value from performance map
		$\dot{m}_p = \dot{m}_{p.Map}$
7.	NozPri.dep_Area	Mass flow per area equals the mass flow per area demanded by the nozzle
		$(\dot{m}/A_{throat})_{actual} = (\dot{m}/A_{throat})_{demand}$
	Dependents, optional	
8.	TIT	Same as above
9.	Thrust	Same as above
10.	DragThrust_wE	Thrust equals drag
		$F_{net} = qSC_D$
11.	DragThrust_wEwFC	Thrust equals drag (including fuel cell drag)
		$F_{net} = qSC_D + F_{FC,Drag}$
12.	PctOx_abs	Percent fuel oxidation equals input value
		$(\%Ox.)_{actual} = (\%Ox.)_{target}$
13.	SOFCtemp	Fuel cell exit temperature equals input value
		$T_{FC,out} = T_{target}$
14.	FCpower	Fuel cell power equals input value
		$\dot{W}_{FC} = \dot{W}_{target}$

Appendix G:

NPSS Details of Low Bypass Ratio Turbofan Model and Hybrid

G.1 Order of Execution

The model's order of execution is the order in which the elements of the model are called on to perform their calculations. It is important that the elements be ordered such that every elements run before any other element that requires a flow stream or information from that element.

Inlet Path:

1. Ambient element: AmbientNASA 'Amb
2. Inlet Start element: InletStartNASA 'InletStart'
3. Inlet element: Inlet 'InEng'
4. Compressor element: Compressor 'CmpL'
5. Splitter element: SplitterNASA 'SpltFan'

Bypass Path:

6. Duct element: DuctNASA 'Dfan'
7. Bleed element: Bleed 'Bsec'

Core Path:

8. Bleed element: Bleed 'B025'
9. Duct element: DuctNASA 'D025'
10. Compressor element: Compressor 'CmpH'

CPOx/SOFC Path (not present in the engine-only model):

11. Splitter element: SplitterNASA 'SplitFC'
12. Fuel Start element: FuelStart 'FusCpox'
13. CPOx Reactor element: CPOX 'Cpox1'
14. Fuel Cell Inlet element: InletFC 'IFC1'
15. Solid Oxide Fuel Cell element: SolideOxideFC 'SOFC1'
16. Combiner element: Combiner 'B03'

Burner and Turbine Section:

17. Fuel Start element: FuelStart 'FusEng'

18. Burner element: BurnerNASA ‘BrnPri’

19. Bleed element: Bleed ‘B041’

20. Turbine element: Turbine ‘TrbH’

21. Bleed element: Bleed ‘B042’

22. Duct element: DuctNASA ‘D043’

23. Turbine element: Turbine ‘TrbL’

Exhaust Path:

24. Bleed element: Bleed ‘B045’

25. Nozzle element: NozzleNASA ‘NozPri’

Flow End:

26. Flow End element: FlowEnd ‘FePri’

Shafts:

27. Shaft element: Shaft ‘ShH’, ‘ShL’

G.2 Independents

Complete list of independent variables in the system solver:

Table 24: Low BPR turbofan, GT-SOFC system independent variables.

	Independent name	Description	Controlled parameter
	Independents present in all modeling runs		
1.	TrbH.S_map.ind_parmMap	HPT performance map parameter	TrbH.parmMap
2.	TrbL.S_map.ind_parmMap	LPT performance map parameter	TrbL.parmMap
3.	ShH.ind_Nmech	HP shaft mechanical rotation speed, N	ShH. Nmech
4.	ShL.ind_Nmech	LP shaft mechanical rotation speed, N	ShL. Nmech
5.	BrnFuelControl	Burner fuel mass flow, $\dot{m}_{fuel}$	BrnPri.Wfuel
	Independents present in all 'On-Design' runs		
6.	AirControl	Inlet air mass flow, $\dot{m}_{air}$	InletStart.W_in
	Independents present in all 'Off-Design' runs		
7.	InletStart.ind_W	Inlet air mass flow, $\dot{m}_{air}$	InletStart.W
8.	CmpH.S_map.ind_RlineMap	HPC performance map parameter	CmpH.RlineMap
9.	CmpL.S_map.ind_RlineMap	LPC performance map parameter	CmpL.RlineMap
	Independents, optional		
10.	CpoxFuelControl	CPOx fuel mass flow, $\dot{m}_{fuel}$	Cond1.Fl_O.Tt
11.	SofcIns	SOFC insulation thickness	SOFC1.t_ins
12.	SofcRep	Number of radially repeating FC units	SOFC1.Nrep

G.3 Dependents

Complete list of dependent conditions in the system solver:

Table 25: Low BPR turbofan, GT-SOFC system dependent conditions.

	Condition name	Condition description/equation
	Dependents present in all modeling runs	
1.	ShH.integrate_Nmech	Net torque on the shaft must be zero
		$\Sigma Torque = 0$
2.	ShL.integrate_Nmech	Net torque on the shaft must be zero
		$\Sigma Torque = 0$
	Dependents present in all 'On-Design' runs	
3.	TIT	Turbine inlet temperature equals input value
		$TrbH.Fl\_I.Tt = TIT_{max}$
4.	Thrust	Net thrust equals input value
		$F_{net} = F_{target}$
5.	ShH_N	Shaft speed equals value predicted by correlation
		$ShH.Nmech = N_{HP,calc}$
6.	ShL_N	Shaft speed equals value predicted by correlation
		$ShL.Nmech = N_{LP,calc}$
	Dependents present in all 'Off-Design' runs	
7.	CmpH.S_map.dep_errWc	Corrected mass flow equals calculated value from performance map
		$\dot{m}_{c,HPC} = \dot{m}_{c,HPC,Map}$
8.	CmpL.S_map.dep_errWc	Corrected mass flow equals calculated value from performance map
		$\dot{m}_{c,LPC} = \dot{m}_{c,LPC,Map}$
9.	TrbH.S_map.dep_errWp	Corrected mass flow equals calculated value from performance map
		$\dot{m}_{p,HPT} = \dot{m}_{p.HPT,Map}$
10.	TrbL.S_map.dep_errWp	Corrected mass flow equals calculated value from performance map
		$\dot{m}_{p,LPT} = \dot{m}_{p.LPT,Map}$
11.	NozPri.dep_Area	Mass flow per area equals the mass flow per area demanded by the nozzle
		$(\dot{m}/A_{throat})_{actual} = (\dot{m}/A_{throat})_{demand}$

	Dependents, optional	
12.	TIT	Same as above
13.	Thrust	Same as above
14.	DragThrust_wE	Thrust equals drag
		$F_{net} = qSC_D$
15.	DragThrust_wEwFC	Thrust equals drag (including fuel cell drag)
		$F_{net} = qSC_D + F_{FC,Drag}$
16.	PctOx_abs	Percent fuel oxidation equals input value
		$(\%Ox.)_{actual} = (\%Ox.)_{target}$
17.	SOFCtemp	Fuel cell exit temperature equals input value
		$T_{FC,out} = T_{target}$
18.	FCpower	Fuel cell power equals input value
		$\dot{W}_{FC} = \dot{W}_{target}$

Appendix H:

NPSS Details of High Bypass Ratio Turbofan Model and Hybrid

H.1 Order of Execution

The model's order of execution is the order in which the elements of the model are called on to perform their calculations. It is important that the elements be ordered such that every elements run before any other element that requires a flow stream or information from that element.

Inlet Path:

1. Ambient element: AmbientNASA 'Amb'
2. Inlet Start element: InletStartNASA 'InletStart'
3. Inlet element: Inlet 'InEng'
4. Splitter element: SplitterNASA 'SpltFan'

Bypass Path:

5. Compressor element: Compressor 'CmpFSec'
6. Bleed element: Bleed 'B025in'
7. Duct element: DuctNASA 'Dfan'
8. Nozzle element: NozzleNASA 'NozSec'

Core Path:

9. Compressor element: Compressor 'CmpL'
10. Bleed element: Bleed 'B025'
11. Duct element: DuctNASA 'D025'
12. Compressor element: Compressor 'CmpH'

CPOx/SOFC Path (not present in the engine-only model):

13. Splitter element: SplitterNASA 'SplitFC'
14. Fuel Start element: FuelStart 'FusCpox'
15. CPOx Reactor element: CPOX 'Cpox1'
16. Fuel Cell Inlet element: InletFC 'IFC1'
17. Solid Oxide Fuel Cell element: SolideOxideFC 'SOFC1'
18. Combiner element: Combiner 'B03'

Burner and Turbine Section:

19. Fuel Start element: FuelStart ‘FusEng’
20. Burner element: BurnerNASA ‘BrnPri’
21. Bleed element: Bleed ‘B041’
22. Turbine element: Turbine ‘TrbH’
23. Bleed element: Bleed ‘B042’
24. Duct element: DuctNASA ‘D043’
25. Turbine element: Turbine ‘TrbL’

Exhaust Path:

26. Bleed element: Bleed ‘B045’
27. Nozzle element: NozzleNASA ‘NozPri’

Flow Ends:

28. Flow End element: FlowEnd ‘FePri’, ‘FeSec’

Shafts:

29. Shaft elements: Shaft ‘ShH’, ‘ShL’

H.2 Independents

Complete list of independent variables in the system solver:

Table 26: High BPR turbofan, GT-SOFC system independent variables.

	Independent name	Description	Controlled parameter
	Independents present in all modeling runs		
1.	TrbH.S_map.ind_parmMap	HPT performance map parameter	TrbH.parmMap
2.	TrbL.S_map.ind_parmMap	LPT performance map parameter	TrbL.parmMap
3.	ShH.ind_Nmech	HP shaft mechanical rotation speed, N	ShH. Nmech
4.	ShL.ind_Nmech	LP shaft mechanical rotation speed, N	ShL. Nmech
5.	BrnFuelControl	Burner fuel mass flow, $\dot{m}_{fuel}$	BrnPri.Wfuel
	Independents present in all 'On-Design' runs		
6.	AirControl	Inlet air mass flow, $\dot{m}_{air}$	InletStart.W_in
	Independents present in all 'Off-Design' runs		
7.	InletStart.ind_W	Inlet air mass flow, $\dot{m}_{air}$	InletStart.W
8.	SpltFan.ind_BPR	Splitter bypass ratio	SpltFan.BPR
9.	CmpH.S_map.ind_RlineMap	HPC performance map parameter	CmpH.RlineMap
10.	CmpL.S_map.ind_RlineMap	LPC performance map parameter	CmpL.RlineMap
11.	CmpFSec.S_map.ind_RlineMap	LPC performance map parameter	CmpFSec.RlineMap
	Independents, optional		
12.	CpoxFuelControl	CPOx fuel mass flow, $\dot{m}_{fuel}$	Cond1.Fl_O.Tt
13.	SofcIns	SOFC insulation thickness	SOFC1.t_ins
14.	SofcRep	Number of radially repeating FC units	SOFC1.Nrep

H.3 Dependents

Complete list of dependent conditions in the system solver:

Table 27: High BPR turbofan, GT-SOFC system dependent conditions.

	Condition name	Condition description/equation
	Dependents present in all modeling runs	
1.	ShH.integrate_Nmech	Net torque on the shaft must be zero
		$\Sigma Torque = 0$
2.	ShL.integrate_Nmech	Net torque on the shaft must be zero
		$\Sigma Torque = 0$
	Dependents present in all 'On-Design' runs	
3.	TIT	Turbine inlet temperature equals input value
		$TrbH.Fl\_I.Tt = TIT_{max}$
4.	Thrust	Net thrust equals input value
		$F_{net} = F_{target}$
5.	ShH_N	Shaft speed equals value predicted by correlation
		$ShH.Nmech = N_{HP,calc}$
6.	ShL_N	Shaft speed equals value predicted by correlation
		$ShL.Nmech = N_{LP,calc}$
	Dependents present in all 'Off-Design' runs	
7.	CmpH.S_map.dep_errWc	Corrected mass flow equals calculated value from performance map
		$\dot{m}_{c,HPC} = \dot{m}_{c,HPC,Map}$
8.	CmpL.S_map.dep_errWc	Corrected mass flow equals calculated value from performance map
		$\dot{m}_{c,LPC} = \dot{m}_{c,LPC,Map}$
9.	CmpFSec.S_map.dep_errWc	Corrected mass flow equals calculated value from performance map
		$\dot{m}_{c,Fan} = \dot{m}_{c,Fan,Map}$
10.	TrbH.S_map.dep_errWp	Corrected mass flow equals calculated value from performance map
		$\dot{m}_{p,HPT} = \dot{m}_{p.HPT,Map}$
11.	TrbL.S_map.dep_errWp	Corrected mass flow equals calculated value from performance map
		$\dot{m}_{p,LPT} = \dot{m}_{p.LPT,Map}$

12.	NozPri.dep_Area	Mass flow per area equals the mass flow per area demanded by the nozzle
		$(\dot{m}/A_{throat})_{actual} = (\dot{m}/A_{throat})_{demand}$
13.	NozSec.dep_Area	Mass flow per area equals the mass flow per area demanded by the nozzle
		$(\dot{m}/A_{throat})_{actual} = (\dot{m}/A_{throat})_{demand}$
	Dependents, optional	
14.	TIT	Same as above
15.	Thrust	Same as above
16.	DragThrust_wE	Thrust equals drag
		$F_{net} = qSC_D$
17.	DragThrust_wEwFC	Thrust equals drag (including fuel cell drag)
		$F_{net} = qSC_D + F_{FC,Drag}$
18.	PctOx_abs	Percent fuel oxidation equals input value
		$(\%Ox.)_{actual} = (\%Ox.)_{target}$
19.	SOFCtemp	Fuel cell exit temperature equals input value
		$T_{FC,out} = T_{target}$
20.	FCpower	Fuel cell power equals input value
		$\dot{W}_{FC} = \dot{W}_{target}$

Appendix I:

Example NPSS Code

I.1 High BPR Turbofan '.run' Run File

The following code is used to setup, include a model, and run a case in NPSS: the thermodynamics package is declared, relevant files are included, the model is included, various parameters are adjusted, and a '.case' file is called. For more detailed information on using NPSS, see Refs. [69] and [70].

Contents of '.run' file:

```
// Set the thermo package
string fuel = "JP-5";
real fuel_enthalpy = -1673.85;
setThermoPackage("CEA", "Air", "H2O", fuel, ...
                        "O2", "H2", "H", "O", "N", "C", "Ar" );

// File includes
//include macros
#include "bleed_macros.fnc"
//include components
#include "CPOX.int"
#include "SolidOxideFC.int"
//include viewers
#include "Viewers/summary.view"
#include "Viewers/performance.view"
#include "Viewers/fuelcell.view"
#include "Viewers/sizing_eng.view"
#include "Viewers/sizing_fc.view"
#include "Viewers/convergence.view"
#include "MassEstimation/MassEstimation_HiBPR.int"
#include "MassEstimation/MassEstimation_SOFC.int"

// Include the model file
#include "FanHigh.mdl"
int model = 2;
int it = 0;
setOption("switchTransport","EQUIL");

// Set the parameters
#include "Parameters/param_base.int"
#include "Parameters/solver_var.int"

//change BPR
SpltFan.BPRdes=5.;
//change mass flow
InletStart.W_in=112.;
//adjust pressure ratios
CmpFSec.S_map.PRdes  = 1.5;
CmpL.S_map.PRdes  = 3.0;
CmpH.S_map.PRdes  = 8.0;
//adjust efficiencies
```

```
CmpFSec.S_map.effDes = 0.86;
CmpL.S_map.effDes = 0.88;
CmpH.S_map.effDes = 0.88;
TrbH.S_map.effDes = 0.89;
TrbL.S_map.effDes = 0.89;

// Include the case file to be run
#include "Cases/Sensitivity.case"
```

I.2 Example '.case' Case File

The following code is used to set a series of cases to be run with the model. This file chooses a flight and engine condition and sets up several parameters accordingly. It then runs an 'On-Design' case which sets the model according to design parameter inputs. It continues to run multiple 'Off-Design' cases which estimate performance away from the design values. For more detailed information on using NPSS, see Refs. [69] and [70].

Contents of '.case' file:

```
string casefile = "PowerSweep.case";

// Define iteration variables and solver targets
real Fref, Wref, MNref;
Fpct=1.;
TIT_max = 2880.;        // Rankine
real Fn_req;
SOFC1.switchWrite = "OFF";
real diam, Nrings;

// Pick a flight condition
//int flight=0; //SLS;static
//int flight=1; //SLS;TO
//int flight=2; //M=0.8;Alt=35kft
int flight=3; //M=0.5;Alt=55kft

// Pick an OPR
int opr=0; //24.0
// int opr=1; //31.5
// int opr=2; //40.0

// Pick an engine
if( model==0 ){  // Jet1sp
  if( opr==0 ){
    Fn_target = 3429.34;
    CmpH.S_map.PRdes  = 24.0;
    AC.W_GT = 1301.259;
  }
  else if( opr==1 ){
    Fn_target = 3478.71;
    CmpH.S_map.PRdes  = 31.5;
    AC.W_GT = 1307.085;
  }
  else if( opr==2 ){
    Fn_target = 3518.25;
    CmpH.S_map.PRdes  = 40.0;
```

```
    AC.W_GT = 1322.493;
  }
}
else if( model==1 ){  // FanLow
  if( opr==0 ){
    Fn_target = 3229.05;
    CmpL.S_map.PRdes  = 3.0;
    CmpH.S_map.PRdes  = 8.0;
    AC.W_GT = 1492.11;
  }
  else if( opr==1 ){
    Fn_target = 3256.7;
    CmpL.S_map.PRdes  = 3.5;
    CmpH.S_map.PRdes  = 9.0;
    AC.W_GT = 1431.481;
  }
  else if( opr==2 ){
    Fn_target = 3280.3;
    CmpL.S_map.PRdes  = 4.0;
    CmpH.S_map.PRdes  = 10.0;
    AC.W_GT = 1369.871;
  }
}
else if( model==2 ){  // FanHigh
  if( opr==0 ){
    Fn_target = 2243.28;
    CmpL.S_map.PRdes  = 3.0;
    CmpH.S_map.PRdes  = 8.0;
    AC.W_GT = 1295.347;
  }
  else if( opr==1 ){
    Fn_target = 2253.24;
    CmpL.S_map.PRdes  = 3.5;
    CmpH.S_map.PRdes  = 9.0;
    AC.W_GT = 1275.621;
  }
  else if( opr==2 ){
    Fn_target = 2257.55;
    CmpL.S_map.PRdes  = 4.0;
    CmpH.S_map.PRdes  = 10.0;
    AC.W_GT = 1275.344;
  }
}

perfTitles( model );


// Design case - no SOFC

Amb.alt_in = 35000.0;
Amb.MN_in = 0.8;
Cpox1.Wfuel = 0.00000000000000000000000000001;
Cpox1.Nseg = 0.;
SOFC1.Nseg = 0.;
B03.wf = 0.;

setOption( "switchDes", "DESIGN" );
```

```
autoSolverSetup();

solver.addIndependent( "BrnFuelControl" );
solver.addDependent( "TIT" );
solver.addIndependent( "AirControl" );
solver.addDependent( "Thrust" );
solver.addIndependent( "ShH.ind_Nmech" );
solver.addDependent( "ShH_N" );
if( model ){
  solver.addIndependent( "ShL.ind_Nmech" );
  solver.addDependent( "ShL_N" );
}

cout << "\nDesign case - no SOFC:\n";
cout << "\nIndependents:\n" << solver.independentNames;
cout << "\nDependents:\n" << solver.dependentNames;
run();
cout << "Convergence? = " << solver.converged << endl;
Wref = BrnPri.Wfuel;
Fref = Perf.Fn;
MNref = Amb.MN_in;
perfPrint( model );

// Off-Design case  - no SOFC - Partial Throttle

solver.removeDependent( "TIT" );
solver.addDependent( "Thrust" );

Fn_target = Fn_req;
cout << "\nIndependents:\n" << solver.independentNames;
cout << "\nDependents:\n" << solver.dependentNames;
run();
cout << "Convergence? = " << solver.converged << endl;
converged(Amb.alt_in,Amb.MN_in," - no SOFC",Fn_req,"Thrust=");
perfPrint( model );


// Off-Design case  - with SOFC

// Solver setup
solver.removeDependent( "Thrust" );
solver.addDependent( "DragThrust_wE" );
solver.addIndependent( "CpoxFuelControl" );
solver.addDependent( "PctOx_abs" );
solver.addDependent( "SOFCtemp" );
solver.addIndependent( "SofcRep" );

// initiate variables
real units[] = {0.,186.,373.,559.,746.,932.,1119.,1305.,1492., ...
                1678.,1865.,2051.,2238.,2424.,2611.,2797.,2984.};
real init[] = {33.7161,5.1683,1.98085,1.96868,2.04233,2.60839, ...
                2.69166,18606.6,10668.3,0.106632,0.01163,16.711};
InletStart.W = init[0];
SpltFan.BPR = init[1];
CmpFSec.S_map.RlineMap = init[2];
CmpL.S_map.RlineMap = init[3];
CmpH.S_map.RlineMap = init[4];
```

```
TrbH.S_map.parmMap = init[5];
TrbL.S_map.parmMap = init[6];
ShH.Nmech = init[7];
ShL.Nmech = init[8];
BrnPri.Wfuel = init[9];
Cpox1.Wfuel = init[10];
SOFC1.Nrep = init[11];
SOFC1.t_ins = 0.0001;

SOFC1.Vdes = 0.6; //0.7; //0.6;
PctOx_des = 0.75; //0.75; //0.9;

Cpox1.Nseg = 8.;
SOFC1.Nseg = 8.;

for( Nrings=1.; Nrings<20.; Nrings++ ){
  SOFC1.Nunit = units[Nrings];

  cout << "\nNrings="<<Nrings<<"\n";
  run();
  cout << "\nNrings="<<Nrings<<" -- Done!\n";
  cout << "Convergence? = " << solver.converged << endl;
  converged(Nrings,0," - Base case",Perf.Fn,"Thrust=");
  perfPrint( model );
  sizeView2.display();
}
```

I.3 High BPR Turbofan '.mdl' Model File

The following code is used to build a system model by declaring and setting up components and then linking them together. For more detailed information on using NPSS, see Refs. [69] and [70].

Contents of '.mdl' file:

```
// Set ambient conditions
Element AmbientNASA Amb {
  switchMode = "ALDTMN";
  alt_in      = 35000.;
  dTs_in    = 0.;
  MN_in       = 0.8;
}

// Set inlet flow start
Element InletStartNASA InletStart{
  AmbientName = "Amb";
  W_in = 100.;
}

// Engine inlet
Element Inlet InEng {
  eRamBase = 0.995;
}

// Split the primary,secondary flows
Element SplitterNASA SpltFan {
  BPRdes = 5.;
}

// Low pressure compressor
Element Compressor CmpFSec {
  #include "E3maps/fanE3.map";
  S_map.PRdes  = 1.5;
  S_map.effDes= 0.8589;
  S_map.RlineMap = 2.0;
  S_map.NcDes = 1.0;
  Sh_O.inertia = 10.;
}

// Bleed B025in
Element Bleed B025in;

// Duct
Element DuctNASA Dfan;

// Secondary flow nozzle
Element NozzleNASA NozSec {
  PsExhName = "Amb.Ps";
```

```
  setOption("switchFrozen","EQUIL");
}

// Low pressure compressor
Element Compressor CmpL {
  #include "E3maps/lpcE3.map";
  S_map.PRdes  = 3.0;
  S_map.effDes= 0.872;
  S_map.RlineMap = 2.0;
  S_map.NcDes = 1.0;
  Sh_O.inertia = 10.;
}

// Bleed
Element Bleed B025;

// Duct
Element DuctNASA D025{
  switchDP="OFF";
  dPqP_in=0.002;
}

// High pressure compressor
Element Compressor CmpH {
  #include "E3maps/hpcE3.map";
  S_map.PRdes  = 10.0;
  S_map.effDes= 0.8522;
  S_map.RlineMap = 2.0;
  S_map.NcDes = 1.0;
  Sh_O.inertia = 10.;
}

// Splitter to CPOX and SOFC
Element SplitterNASA SplitFC{
  void preexecute() {
    BPRdes = 1./( Fl_I.W/(Asplit*SOFC1.AF_fcglobal*Cpox1.Wfuel)-1.);
    BPR = BPRdes;
  }
  real Asplit = 2.;
}

// FuelStart
Element FuelStart FusCpox {
  hFuel = fuel_enthalpy;
  fuelType = fuel;
}

// CPOX
Element CPOX Cpox1 {
  AF_cpox = 6.0;
  Wfuel = 0.0015625;
  length = 1.0;
  A_cross = 0.0175;
  Nseg = 8.;
  Ncells = 35.;
  kappa1 = 0.9;
  burn_eff = 1.0;
```

```
  por = 0.83;
  dp = 0.00021;
  k_wall = 0.0048;
  t_wall = 0.0052;
  k_ins = 1.6e-5;
  t_ins = 0.0035;
}

// Fuel Cell Inlet
Element InletFC IFC1{
  Nseg = 100.;
  t_div = 0.0005;
  k_int = 30.;
  length = 0.01;
  width = 0.005;
  height = 0.002;
}

// Fuel Cell
Element SolidOxideFC SOFC1{
  void preexecute() {
    system( "copy thermo_min.lib thermo.lib" );
  }

  AF_fcglobal = 15.0;
  switchWrite = "ON";
  switchMode = "CURRENT";
  switchGeom = 1;
  switchAmb = 1;
  ne = 2.0;
  Vdes = 0.7;
  deltaQ = 0.;
  deltaCOP = 0.;
  deltaAOP = 0.;
  deltaOOP = 0.;
 //adjust SOFC
  // geometry
  Nunit = 350.;
  Nrep = 1.;
  length = 0.82021;
  height_ch = 0.2;
  activeWidth = 0.5;
  t_ins = 0.001;
  t_div = 0.001;
  t_ext = 0.001;
  // thermal
  k_int = 30.;
  k_ano = 11.0;
  k_cat = 6.23;
  k_ele = 2.7;
  k_ins = 0.1;
  // numerical
  Ndiv = 3.;
  Ndiff = 16.;
  Nseg = 8.;
  kappa1 = 0.95;
  kappa2 = 0.95;
```

```
  kappa3 = 0.95;
  iDens = 1000.0;
  flagLim = 1000.;
  reltol = 1.e-8;
  finetrig = 0;
 //adjust MEA physical parameters
  // anode
  d_a = 900.0e-6;
  por_a = 0.35;
  tor_a = 4.8;
  rp_a = 0.2e-6;
  dp_a = 1.0e-6;
  // cathode
  d_c = 50.0e-6;
  por_c = 0.35;
  tor_c = 4.0;
  rp_c = 0.25e-6;
  dp_c = 1.25e-6;
  // electrolyte
  d_el = 20.0e-6;
 //adjust activation overpotential parameters
  // anode
  alphaFA = 1.5;
  alphaRA = 0.5;
  iRefH2 = 8.5e3;
  E_H2 = 120.0e3;
  Tref_act = 1073.0;
  A_pH2 = 5.59e15;
  E_pH2 = 88.12e3;
  Gamma = 2.6e-5;
  gamma0 = 0.01;
  dV_activ_an = 0.025;
  // cathode
  alphaFC = 1.5;
  alphaRC = 0.5;
  iRefO2 = 2.4e3;
  E_O2 = 130.0e3;
  A_pO2 = 4.9e8;
  E_pO2 = 200.0e3;
  dV_activ_cat = 0.025;
 //adjust ohmic overpotential parameters
  // anode
  A_ae = 9.5e5;
  E_ae = 9.5611e3;
  // cathode
  A_ce = 4.2e5;
  E_ce = 9.9768e3;
  // electrolyte
  A_el = 3.6e5;
  E_el = 80.0e3;

  void postexecute() {
    system( "copy thermo_slim.lib thermo.lib" );
  }
}

// fuel cell exit stream mixing
```

```
Element Combiner B03;

// FuelStart
Element FuelStart FusEng {
  hFuel = fuel_enthalpy;
  fuelType = fuel;
}

// Burner
Element BurnerNASA BrnPri {
  dPqPfBase         = 0.05;
  effBase           = 0.98;
  switchHotLoss   =  "input";
  switchBurn      = "FUEL";
  Wfuel = 0.35;
  tolRayleigh       = 0.0001;
}

// Bleed
Element Bleed B041;

// High pressure turbine
Element Turbine TrbH {
  #include "E3maps/hptE3.map";
  S_map.parmMapDes   = 4.975;
  S_map.parmNcDes = 100.0;
  S_map.effDes       = 0.89;
}

// Bleed
Element Bleed B042;

// Duct
Element DuctNASA D043 {
  switchDP = "INPUT";
  void preexecute() {
    dPqP_in = 0.25 * Fl_I.MN * Fl_I.MN;
  }
  Fl_I.MNdes = 0.4;
}

// Low pressure turbine
Element Turbine TrbL {
  #include "E3maps/lptE3.map";
  S_map.parmMapDes   = 4.271;
  S_map.parmNcDes = 100.0;
  S_map.effDes       = 0.8777;
}

// Bleed
Element Bleed B045;

// Primary flow nozzle
Element NozzleNASA NozPri {
  PsExhName = "Amb.Ps";
  setOption("switchFrozen","EQUIL");
}
```

```
// FlowEnds
Element FlowEnd FePri;
Element FlowEnd FeSec;

// Shafts
Element Shaft ShH {
  ShaftInputPort MeCmpH, MeTrbH;
  Nmech = 8997.43;
  inertia = .93243;
}
Element Shaft ShL {
  ShaftInputPort MeCmpFSec, MeCmpL, MeTrbL;
  Nmech = 3497.40;
  inertia = 2.73513;
}

// PerfNASA
Element PerfNASA Perf;

// Aircraft
Element Aircraft AC {
  // HALE
  Cdmin = 0.0195;
  K = 0.01725;
  Clmin = 0.3;
  W_empty = 15432.36;
  W_f = 16534.7;
  S = 688.89;
  N_eng = 1.;
  frac = 0.5;
  deltaFC = 0.;
  deltaGT = 0.;
  W_GT = 1295.347;
}

// Mass Estimation
Element MassEstimation_HiBPR MassEstEng;
Element MassEstimation_SOFC MassEstFC {
  rho_a = 300.;
  rho_c = 287.;
  rho_el = 375.;
  rho_int = 487.;
  rho_ins = 15.6;
  LoH_i = 1.;
  LoH_o = 1.;
  rho_cat = 40.;
  rho_wall = 487.;
  Vel_des = 10.;
  sigma_duct = 9.e6;
  rho_duct = 511.;
  sf_hw = 2.;
  d_hwDes = 0.0208;
  rho_hw = 512.;
  t_cpInt = 0.0052;
}
```

```
// CycleNASA Cycle
Element CycleNASA Cycle {
  EPR_numName = "CmpH.Fl_O";
  EPR_denName = "InEng.Fl_O";
  FPR_numName = "CmpFSec.Fl_O";
  FPR_denName = "InEng.Fl_O";
}

// linkPorts
linkPorts( "InletStart.Fl_O", "InEng.Fl_I",   "F0"    );
linkPorts( "InEng.Fl_O",      "SpltFan.Fl_I", "F01A"  );
linkPorts( "SpltFan.Fl_O1",   "CmpL.Fl_I",    "F025"  );
linkPorts( "CmpL.Fl_O",       "B025.Fl_I",    "F0251" );
linkPorts( "B025.Fl_O",       "D025.Fl_I",    "F0252" );
linkPorts( "D025.Fl_O",       "CmpH.Fl_I",    "F0253" );
linkPorts( "CmpH.Fl_O",       "SplitFC.Fl_I", "Fsplt1");
linkPorts( "SplitFC.Fl_O1",   "B03.Fl_I",     "F03a"  );
linkPorts( "SplitFC.Fl_O2",   "Cpox1.Fl_I",   "Fcpox" );
linkPorts( "FusCpox.Fu_O",    "Cpox1.Fu_I",   "FUcpox");
linkPorts( "Cpox1.Fl_O",      "IFC1.Fl_I1",   "IFCf"  );
linkPorts( "Cpox1.Fl_Obp",    "IFC1.Fl_I2",   "IFCa"  );
linkPorts( "IFC1.Fl_O1",      "SOFC1.Fl_I1",  "FC1"   );
linkPorts( "IFC1.Fl_O2",      "SOFC1.Fl_I2",  "FC2"   );
linkPorts( "IFC1.Fl_Obp",     "SOFC1.Fl_Ibp", "FCbp"  );
linkPorts( "SOFC1.Fl_O1",     "B03.Fl_S1",    "F03b"  );
linkPorts( "SOFC1.Fl_O2",     "B03.Fl_S2",    "F03c"  );
linkPorts( "SOFC1.Fl_Obp",    "B03.Fl_S3",    "F03d"  );
linkPorts( "B03.Fl_O",        "BrnPri.Fl_I",  "F03"   );
linkPorts( "FusEng.Fu_O",     "BrnPri.Fu_I",  "FU036" );
linkPorts( "BrnPri.Fl_O",     "B041.Fl_I",    "F041"  );
linkPorts( "B041.Fl_O",       "TrbH.Fl_I",    "F041a" );
linkPorts( "TrbH.Fl_O",       "B042.Fl_I",    "F042"  );
linkPorts( "B042.Fl_O",       "D043.Fl_I",    "F043"  );
linkPorts( "D043.Fl_O",       "TrbL.Fl_I",    "F044"  );
linkPorts( "TrbL.Fl_O",       "B045.Fl_I",    "F045"  );
linkPorts( "B045.Fl_O" ,      "NozPri.Fl_I",  "F07"   );
linkPorts( "NozPri.Fl_O",     "FePri.Fl_I",   "F09"   );
linkPorts( "SpltFan.Fl_O2",   "CmpFSec.Fl_I", "F12"   );
linkPorts( "CmpFSec.Fl_O",    "B025in.Fl_I",  "F11"   );
linkPorts( "B025in.Fl_O",     "Dfan.Fl_I",    "F16"   );
linkPorts( "Dfan.Fl_O",       "NozSec.Fl_I",  "F17"   );
linkPorts( "NozSec.Fl_O",     "FeSec.Fl_I",   "F19"   );

// Bleed Connections
// low pressure bleeds
linkBleedBB( "B025", "B025in", .00, 1., 1.,          "surge" );
linkBleedBT( "B025", "TrbL",   .00, 1., 1., 1., 0., "LPCtoLPT" );
linkBleedBB( "B025", "B045",   .00, 1., 1.,          "LPCtoExit" );
// high pressure bleeds
linkBleedCT( "CmpH", "TrbH",   .10, 1., 1., 1., 0., "ca1HPT" );
linkBleedCB( "CmpH", "B042",   .04, 1., 1.,          "ca2HPT" );
linkBleedCB( "CmpH", "B045",   .01, .5, .5,          "ca3HPT" );
linkBleedCB( "CmpH", "B041",   .00, 1., 1.,          "ca4HPT" );

// Shaft Connect Statements
linkPorts( "CmpL.Sh_O",      "ShL.MeCmpL",   "MeCmpL" );
linkPorts( "CmpFSec.Sh_O",   "ShL.MeCmpFSec","MeCmpFSec" );
```

```
linkPorts( "TrbL.Sh_O"   ,   "ShL.MeTrbL",   "MeTrbL" );
linkPorts( "CmpH.Sh_O",      "ShH.MeCmpH",   "MeCmpH" );
linkPorts( "TrbH.Sh_O",      "ShH.MeTrbH",   "MeTrbH" );
```

Bibliography

[1] Jackson, P. , Munson, K. , and Peacock, L. , *IHS Jane's All the World's Aircraft: Development & Production*, IHS Global, Inc., Alexandria, VA, 2014.

[2] Moir, I., and Seabridge, A., *Aircraft Systems: Mechanical, electrical, and avionics subsystems integration*, 3rd ed., John Wiley & Sons, Chichester, England, 2008, pp. 381-388.

[3] Isikveren, A. T., "Future of [More] Electrical Aircraft," *ICAS Biennial Workshop*, Cape Town, South Africa, 2013.

[4] Ashcraft, S. W., Padron, A. S., Pascioni, K. A., Stout, G. W., and Huff, D. L., *Review of Propulsion Technologies for N+3 Subsonic Vehicle Concepts, TM-2011-217239*, NASA, 2011.

[5] Daly, M. , and Streetly, M. , *IHS Jane's All the World's Aircraft: Unmanned*, IHS Global, Inc., Alexandria, VA, 2014-2015.

[6] Pfahler, D., "Air Force Power Requirements," AFRL, Power Division, Propulsion Directorate, Wright Patterson AFB,OH, 2006.

[7] Choudhury, A., Chandra, H., and Arora, A., "Application of solid oxide fuel cell technology for power generation - A review," *Renewable and Sustainable Energy Reviews*, Vol. 20, 2013, pp. 430-442.

[8] Rajashekara, K., Grieve, J., and Daggett, D., "Solid oxide fuel cell/gas turbine hybrid APU system for aerospace applications," *Conference Record of the IEEE Industry Applications Conference*, Vol. 5, 2006, pp. 2185-2192.

[9] Islas, J., "The gas turbine: A new technological paradigm in electricity generation," *Technological Forecasting and Social Change*, Vol. 60, 1999, pp. 129-148.

[10] Hill, P. G., and Peterson, C. R., *Mechanics and Thermodynamics of Propulsion*, 2nd ed., Addison-Wesley, Reading, MA, 1992.

[11] Raymer, D. P., *Aircraft Design: A Conceptual Approach*, 5th ed., AIAA, Reston, VA, 2012.

[12] Nicolai, L. M., and Carichner, G. E., *Fundamentals of Aircraft and Airship Design, Volume I - Aircraft Design*, AIAA, Reston, VA, 2010, pp. 733-743.

[13] Santarelli, M., Canrera, M., and Cali, M., "Solid oxide fuel based auxiliary power unit for regional jets: Design and mission simulation with different cell geometries," *Journal of Fuel Cell Science and Technology*, Vol. 7, 2010, p. 021006.

[14] Horde, T., Achard, P., and Metkemeijer, R., "PEMFC application for aviation: Experimental and numerical study of sensitivity to altitude," *International Journal of Hydrogen Energy*, Vol. 37, 2012, pp. 10818-10829.

[15] Chalk, S. G., and Miller, J. F., "Key challenges and recent progress in batteries, fuel cells, and hydrogen storage for clean energy systems," *Journal of Power Sources*, Vol. 159, 2006, pp. 73-80.

[16] Daly, M. , and Gunston, B. , *Jane's Aero Engines*, IHS Global, Inc., Alexandria, VA, 2012-2013, pp. 989-1001.

[17] Ibarreta, A. F., and Sung, C.-J., "Optimization of Jet-A fuel reforming for aerospace applications," *International Journal of Hydrogen Energy*, Vol. 31, 2006, pp. 1066-1078.

[18] Flack, R. D., *Fundamentals of Jet Propulsion with Applications*, Cambridge University Press, NY, 2005.

[19] Mattingly, J. D., *Elements of Propulsion: Gas Turbines and Rockets*, AIAA, Reston, VA, 2006.

[20] Moran, M. J., and Shapiro, H. N., *Fundamentals of Engineering Thermodynamics*, 6th ed., John Wiley & Sons, Inc., Hoboken, NJ, 2008.

[21] Haynes, W. M. , and Lide, D. R. , *CRC Handbook of Chemistry and Physics*, 91st ed., CRC Press, Internet version, http://www.hbcpnetbase.com, 2011.

[22] Li, X., *Principles of Fuel Cells*, Taylor & Francis Group, New York, 2006.

[23] Kee, R. J., Zhu, H., Sukeshini, A. M., and Jackson, G. S., "Solid oxide fuel cells: Operating principles, current challenges, and the role of syngas," *Combustion Science & Technology*, Vol. 180, No. 6, 2008, pp. 1207-1244.

[24] McLean, G. F., Niet, T., Prince-Richard, S., and Djilali, N., "An assessment of alkaline fuel cell technology," *International Journal of Hydrogen Energy*, Vol. 27, No. 5, 2002, pp. 507-526.

[25] Smitha, B., Sridhar, S., and Khan, A. A., "Solid polymer electrolyte membranes for fuel cell applications -- a review," *Journal of Membrane Science*, Vol. 259, 2005, pp. 10-26.

[26] O'Hayre, R., Cha, S.-W., Colella, W., and Prinz, F. B., *Fuel Cell Fundamentals*, 2nd ed., John Wiley & Sons, New York, 2009.

[27] Steele, B. C. H., and Heinzel, A., "Materials for fuel-cell technologies," *Nature*, Vol. 414, 2001, pp. 345-352.

[28] Trembly, J. P., Gemmen, R. S., and and Bayless, D. J., "The effect of coal syngas containing HCl on the performance of solid oxide fuel cells: Investigations into the effect of operational temperature and HCl concentration," *Journal of Power Sources*, Vol. 169, 2007, pp. 347-354.

[29] Kee, R. J., Zhu, H., and Jackson, G. S., "Solid Oxide Fuel Cells Using Syngas," *Synthesis Gas Combustion: Fundamentals and Applications*, edited by Lieuwen, T. C. , Yang, V. , and Yetter, R. , Taylor & Francis, London, 2009, ch. 11.

[30] Goodenough, J. B., and Huang, Y.-H., "Alternative anode materials for solid oxide fuel cells," *Journal of Power Sources*, Vol. 173, 2007, pp. 1–10.

[31] Sun, C., and Stimming, U., "Recent anode advances in solid oxide fuel cells," *Journal of Power Sources*, Vol. 171 , 2007, pp. 247–260.

[32] Gong, M., Liu, X., Trembly, J., and Johnson, C., "Sulfur-tolerant anode materials for solid oxide fuel cell application," *Journal of Power Sources*, Vol. 168, 2007, pp. 289–298.

[33] Kurokawa, H., Yang, L., Jacobson, C. P., DeJonghe, L. C., and Visco, S. J., "Y-doped SrTiO3 based sulfur tolerant anode for solid oxide fuel cells," *Journal of Power Sources*, Vol. 164, 2007, pp. 510–518.

[34] Sengodan, S., Liu, M., Lim, T.-H., Shin, J., Liu, M., and Kim, G., "Enhancing Sulfur Tolerance of a Ni-YSZ Anode through BaZr0.1Ce0.7Y0.1Yb0.1O3−δ Infiltration," *Journal of The Electrochemical Society*, Vol. 161, No. 5, 2014, pp. F668-F673.

[35] Ouweltjes, J. P., Aravind, P. V., Woudstra, N., and Rietveld, G., "Biosyngas Utilization in Solid Oxide Fuel Cells With Ni/GDC," *Journal of Fuel Cell Science and Technology*, Vol. 3, 2006, pp. 495-498.

[36] Kurokawa, H., Sholklapper, T. Z., Jacobson, C. P., DeJonghe, L. C., and Visco, S. J., "Ceria Nanocoating for Sulfur Tolerant Ni-Based Anodes of Solid Oxide Fuel Cells," *Electrochemical and Solid-State Letters*, Vol. 10, No. 9, 2007, pp. B135-B138.

[37] Trembly, J. P., Marquez, A. I., Ohrn, T. R., and Bayless, D. J., "Effects of coal syngas and H2S on the performance of solid oxide fuel cells: Single-cell tests," *Journal of Power Sources*, Vol. 158, 2006, pp. 263–273.

[38] Aguilar, L., Zha, S., Li, S., Winnick, J., and Liu, M., "Sulfur-Tolerant Materials for the Hydrogen Sulfide SOFC," *Electrochemical and Solid-State Letters*, Vol. 7, No. 10, 2004, pp. A324-A326.

[39] Cheng, Z., Zha, S., Aguilar, L., Wang, D., Winnick, J., and Liu, M., "A Solid Oxide Fuel Cell Running on H2S/CH4 Fuel Mixtures," *Electrochemical and Solid-State Letters*, Vol. 9, No. 1, 2006, pp. A31-A33.

[40] Chen, H.-T., Choi, Y., Liu, M., and Lin, M. C., "A First-Principles Analysis for Sulfur Tolerance of CeO2 in Solid Oxide Fuel Cells," *Journal of Physical Chemistry C*, Vol. 111, 2007, pp. 11117-11122.

[41] Cheng, Z., Zha, S., and Liu, M., "Stability of Materials as Candidates for Sulfur-Resistant Anodes of Solid Oxide Fuel Cells," *Journal of The Electrochemical Society*, Vol. 153, No. 7, 2006, pp. A1302-A1309.

[42] "Product Portfolio," Ballard Power Systems, http://www.ballard.com/files/PDF/ProductPortfolio.pdf, accessed 3/16/15.

[43] Hu, J. E., Pearlman, J. B., Jackson, G. S., and Tesluk, C. J., "Evaluating the impact of enhanced anode CO tolerance on performance of proton-exchange-membrane fuel cell systems fueled by liquid hydrocarbons," *Journal of Power Sources*, Vol. 195, 2010, pp. 1926-1935.

[44] Peng, Y., and Richardson, J. T., "Properties of ceramic foam catalyst supports: one-dimensional and two-dimensional heat transfer correlations," *Applied Catalysis A: General*, Vol. 266, 2004, pp. 235-244.

[45] Richardson, J. T., Remue, D., and Hung, J.-K., "Properties of ceramic foam catalyst supports: mass and heat transfer," *Applied Catalysis A: General*, Vol. 250, 2003, pp. 319-329.

[46] Schmidt, L. D., Klein, E. J., Leclerc, C. A., Krummenacher, J. J., and West, K. N., "Production of syngas by direct catalytic-oxidation of methane," *Chemical Engineering Science*, Vol. 58, 2003, p. 1037.

[47] Richardson, J. T., Peng, Y., and Remue, D., "Properties of ceramic foam catalyst supports: pressure drop," *Applied Catalysis A: General*, Vol. 204,

2000, pp. 19-32.

[48] Calise, F., Dentice d'Accadia, M., Vanoli, L., and von Spakovsky, M. R., "Single level optimization of a hybrid SOFC-GT power plant," *Journal of Power Sources*, Vol. 159, 2006, pp. 1169-1185.

[49] Haseli, Y., Dincer, I., and Naterer, G. F., "Thermodynamic modeling of a gas turbine cycle combined with a solid oxide fuel cell," *International Journal of Hydrogen Energy*, Vol. 33, 2008, pp. 5811-5822.

[50] Abbasi, A., and Jiang, Z., "Multidisciplinary modeling and simulation of a fuel cell/gas turbine hybrid power system," *IEEE Power & Energy Society General Meeting*, 2009, pp. 1-7.

[51] Chan, S. H., Ho, H. K., and Tian, Y., "Modelling of simple hybrid solid oxide fuel cell and gas turbine power plant," *Journal of Power Sources*, Vol. 109, 2002, pp. 111-120.

[52] Palsson, J., Selimovic, A., and Sjunnesson, L., "Combined solid oxide fuel cell and gas turbine systems for efficient power and heat generation," Journal of Power Sources," *Journal of Power Sources*, Vol. 86, 2000, pp. 442-448.

[53] Costamagna, P., Magistri, L., and Massardo, A. F., "Design and part-load performance of a hybrid system based on a solid oxide fuel cell reactor and a micro gas turbine," *Journal of Power Sources*, Vol. 96, 2001, pp. 352-368.

[54] Lim, T.-H., Song, R.-H., Shin, D.-R., Yang, J.-I., Jung, H., Vinke, I. C., and Yang, S.-S., "Operating characteristics of a 5 kW class anode-supported planar SOFC stack for a fuel cell/gas turbine hybrid system," *International Journal of Hydrogen Energy*, Vol. 33, 2008, pp. 1076-1083.

[55] Suther, T., Fung, A. S., Koksal, M., and Zabihian, F., "Effects of operating and design parameters on the performance of a solid oxide fuel cell-gas turbine system," *International Journal of Energy Research*, Vol. 35, 2011, pp. 616-632.

[56] Zhao, Y., Sadhukhan, J., Lanzini, A., Brandon, N., and Shah, N., "Optimal integration strategies for a syngas fuelled SOFC and gas turbine hybrid," *Journal of Power Sources*, Vol. 196, 2011, pp. 9516-9527.

[57] Leto, L., Dispenza, C., Moreno, A., and Calabro, A., "Simulation model of a molten carbonate fuel cell-microturbine hybrid system," *Applied Thermal Engineering*, Vol. 31, 2011, pp. 1263-1271.

[58] Veyo, S. E., Shockling, L. A., Dederer, J. T., Gillett, J. E., and Lundberg, W. L., "Tubular Solid Oxide Fuel Cell/Gas Turbine Hybrid Cycle Power Systems: Status," *Journal of Engineering for Gas Turbines and Power*, Vol. 124, 2002, pp. 845-849.

[59] Daggett, D. L., Eelman, S., and Kristiansson, G., "Fuel Cell APU for Commercial Aircraft," *AIAA/ICAS International Air and Space Symposium and Exposition*, Dayton, OH, AIAA 2003-2660, July 14-17, 2003.

[60] Freeh, J. E., Pratt, J. W., and Brouwer, J., "Development of a solid-oxide fuel cell/gas turbine hybrid system model for aerospace applications," NASA, TM-2004-213054, 2004.

[61] Tornabene, R., Wang, X.-Y., Steffen, C. J., and Freeh, J. E., "Development of

parametric mass and volume models for an aerospace SOFC/gas turbine hybrid system," NASA, TM-2005-213819, 2005.

[62] Steffen, C. J., Freeh, J. E., and Larosiliere, L. M., "Solid oxide fuel cell/gas turbine hybrid cycle technology for auxiliary aerospace power," NASA, TM-2005-213586, 2005.

[63] Freeh, J. E., Steffen, C. J., and Larosiliere, L. M., "Off-design performance analysis of a solid-oxide fuel cell/gas turbine hybrid for auxiliary aerospace power," NASA, TM-2005-213805, 2005.

[64] Eelman, S., Poza, I. d. P. y. d., and Krieg, T., "Fuel Cell APU's in Commercial Aircraft – An Assessment of SOFC and PEMFC Concepts," *24th International Congress of the Aeronautical Sciences*, 2004.

[65] Rajashekara, K., Grieve, J., and Daggett, D., "Hybrid Fuel Cell Power in Aircraft," *IEEE Industry Applications Magazine*, No. July/August, 2008, pp. 54-60.

[66] Braun, R. J., Gummalla, M., and Yamanis, J., "System Architectures for Solid Oxide Fuel Cell-Based Auxiliary Power Units in Future Commercial Aircraft Applications," *Journal of Fuel Cell Science and Technology*, Vol. 6, 2009, p. 031015.

[67] Himansu, A., Freeh, J. E., Steffen, C. J., Tornabene, R. T., and Wang, X.-Y. J., "Hybrid solid oxide fuel cell/gas turbine system design for high altitude long endurance aerospace missions," NASA, TM-2006-214328, 2006.

[68] Aguiar, P., Brett, D. J. L., and Brandon, N. P., "Solid oxide fuel cell/gas turbine hybrid system analysis for high-altitude long-endurance unmanned aerial vehicles," *International Journal of Hydrogen Energy*, Vol. 33, 2008, pp. 7214-7223.

[69] "NPSS user guide, software release 1.6.5," NASA, 2008.

[70] "NPSS developer's guide, software release 1.6.5," NASA, 2008.

[71] McBride, B., and Gordon, S., "Computer Program for Calculation of Complex Chemical Equilibrium Compositions and Applications II. User's Manual and Program Description," NASA, RP-1311-P2, 1996.

[72] Ortega, J., and Rheinboldt, W., *Iterative Solution of Nonlinear Equations in Several Variables*, Academic Press, New York, 1970.

[73] Argyros, I. K., and Szidarovszky, F., *The Theory and Application of Iteration Methods*, CRC Press, Boca Raton, 1993.

[74] Kelley, C. T., *Iterative Methods for Linear and Nonlinear Equations*, Society for Industrial and Applied Mathematics, Philadelphia, 1995.

[75] Plagianakos, V. P., Magoulas, G. D., and Vrahatis, M. N., "Improved Learning of Neural Nets Through Global Search," *Global Optimization: Scientific and Engineering Case Studies*, edited by Pintér, J. D., Springer, New York, 2006, ch. 15, pp. 361-388.

[76] Pourjafari, E., and Mojallali, H., "Solving nonlinear equations systems with a new approach based on invasive weed optimization algorithm and clustering," *Swarm and Evolutionary Computation*, Vol. 4, 2012, pp. 33-43.

[77] Ren, H., Wu, L., Bi, W., and Argyros, I. K., "Solving nonlinear equations system via an efficient genetic algorithm with symmetric and harmonious individuals," *Applied Mathematics and Computation*, Vol. 219, No. 23, 2013, pp. 10967-10973.

[78] Mastorakis, N. E., "Solving Non-linear Equations via Genetic Algorithms," *WSEAS Int. Conf. on Evolutionary Computing*, Lisbon, Portugal, 2005, pp. 24-28.

[79] Kelley, C. T., *Solving Nonlinear Equations with Newton's Method* , Society for Industrial and Applied Mathematics, Philadelphia, 2003.

[80] Wendt, J. F. , *Computational Fluid Dynamics*, 3rd ed., Springer, Berlin, 2009.

[81] Waters, D. F., "Modeling of Water-Breathing Propulsion Systems Utilizing the Aluminum-Seawater Reaction and Solid-Oxide Fuel Cells," M.S. Thesis, University of Maryland, College Park, MD, 2011.

[82] Waters, D. F., and Cadou, C. P., "Modeling a hybrid Rankine-cycle/fuel-cell underwater propulsion system based on aluminum-water combustion," *Journal of Power Sources*, Vol. 221, 2013, pp. 272-283.

[83] Waters, D. F., and Cadou, C. P., "Estimating the neutrally buoyant energy density of a Rankine-cycle/fuel-cell underwater propulsion system," *Journal of Power Sources*, Vol. 248, 2014, pp. 714-720.

[84] Sissenwine, N., Dubin, M., and Wexler, H., "The U.S. Standard Atmosphere, 1962," *Journal of Geophysical Research*, Vol. 67, No. 9, 1962, pp. 3627–3630.

[85] "Climatic Information to Determine Design and Test Requirements for Military Equipment," U.S. Department of Defense, Washington, DC, MIL-STD-210A, 1958.

[86] "Global Climatic Data for Developing Military Products," U.S. Department of Defense, Washington, DC, MIL-HDBK-310, 1997.

[87] Twigg, M. V., and Richardson, J. T., "Theory and applications of ceramic foam catalysts," *Chemical Engineering Research and Design*, Vol. 80, 2002, pp. 183-189.

[88] Twigg, M. V., and Richardson, J. T., "Fundamentals and applications of structured foam catalysts," *Industrial & Engineering Chemistry Research*, Vol. 46, 2007, pp. 4166-4177.

[89] Ergun, S., and Orning, A. A., "Fluid flow through randomly packed columns and fluidized beds," *Industrial & Engineering Chemistry*, Vol. 41, 1949, pp. 1179-1184.

[90] Zhu, H., Kee, R. J., Janardhanan, V. M., Deutschmann, O., and Goodwin, D. G., "Modeling elementary heterogeneous chemistry and electrochemistry in solid-oxide fuel cells," *Journal of the Electrochemical Society*, Vol. 152, No. 12, 2005, pp. A2427-A2440.

[91] Zhu, H., and Kee, R. J., "The influence of current collection on the performance of tubular anode-supported SOFC cells," *Journal of Power Sources*, Vol. 169, 2007, pp. 315-326.

[92] *Assessment of Solid Oxide Fuel Cell Technology: Comparison of Alternative*

Design Approaches, EPRIsolutions, Palo Alto, CA, 2002, p. 1003966.

[93] Nishino, T., Iwai, H., and Suzuki, K., "Comprehensive numerical modeling and analysis of a cell-based indirect internal reforming tubular SOFC," *Journal of Fuel Cell Science and Technology*, Vol. 3, 2006, pp. 33-44.

[94] Kee, R. J., Zhu, H., and Goodwin, D. G., "Solid-oxide fuel cells with hydrocarbon fuels," *Proceedings of the Combustion Institute*, Vol. 30, 2005, pp. 2379-2404.

[95] Zhu, W. Z., and Deevi, S. C., "Development of interconnect materials for solid oxide fuel cells," *Materials Science and Engineering A*, Vol. 348, 2003, pp. 227-243.

[96] Zhu, H., and Kee, R. J., "A general mathematical model for analyzing the performance of fuel-cell membrane-electrode assemblies," *Journal of Power Sources*, Vol. 117, 2003, pp. 61-74.

[97] Zhu, H., and Kee, R. J., "Thermodynamics of SOFC efficiency and fuel utilization as functions of fuel mixtures and operating conditions," *Journal of Power Sources*, Vol. 161, 2006, pp. 957-964.

[98] Zhu, H., and Kee, R. J., "Modeling distributed charge-transfer processes in SOFC membrane electrode assemblies," *Journal of the Electrochemical Society*, Vol. 155, No. 7, 2008, pp. B715-B729.

[99] Mason, E., and Malinauskas, A., *Gas transport in porous media: The dusty gas model*, Elsevier, New York, 1983.

[100] Bear, J., *Dynamics of fluids in porous media*, Elsevier, New York, 1972.

[101] Ferguson, J. R., Fiard, J. M., and Herbin, R., "Three-dimensional numerical simulation for various geometries of solid oxide fuel cells," *Journal of Power Sources*, Vol. 58, 1996, pp. 109-122.

[102] Muzychka, Y. S., and Yovanovich, M. M., "Laminar forced convection heat transfer in the combined entry region of non-circular ducts," *Journal of Heat Transfer*, Vol. 126, 2004, pp. 54-61.

[103] Muzychka, Y. S., and Yovanovich, M. M., "Pressure drop in laminar developing flow in noncircular ducts: A scaling and modeling approach," *Journal of Fluids Engineering*, Vol. 131, 2009, p. 111105.

[104] Churchill, S. W., and Usagi, R., "A general expression for the correlation of rates of transfer and other phenomena," *American Institute of Chemical Engineers Journal*, Vol. 126, 1972, pp. 1121-1128.

[105] Incropera, F. P., DeWitt, D. P., Bergman, T. L., and Lavine, A. S., *Fundamentals of Heat and Mass Transfer 6th ed.*, John Wiley & Sons, Hoboken, NJ, 2007, ch. 1.

[106] Onat, E., and Klees, G. W., "A method to estimate weight and dimensions of large and small gas turbine engines," NASA, CR-159481, 1979.

[107] Sanghi, V., Kishore Kumar, S., Sundararajan, V., and Sane, S. K., "Preliminary estimation of engine gas-flow-path size and weight," *Journal of Propulsion and Power*, Vol. 14, 1998, pp. 208-214.

[108] Brandt, S. A., Stiles, R. J., Bertin, J. J., and Whitford, R., *Introduction to*

Aeronautics: A Design Perspective, AIAA, Reston, VA, 1997.

[109] Eshelby, M. E., *Aircraft Performance: Theory and Practice*, AIAA, Reston, VA, 2000.

[110] Mattingly, J. D., *Elements of Propulsion: Gas Turbines and Rockets*, AIAA, Reston, VA, 2006, p. 373.

[111] Roskam, J., and Lan, C.-T., *Airplane Aerodynamics and Performance*, DARcorporation, Lawrence, KS, 1997, pp. 244-245.

[112] Leyes II, R. A., and Fleming, W. A., *The History of North American Small Gas Turbine Engines*, AIAA, Reston, VA, 1999, pp. 817-947.

[113] St. Peter, J., *The History of Aircraft Gas Turbine Engine Development in the United States… A Tradition of Excellence*, ASME, Atlanta, GA, 1999, pp. 430-567.

[114] Srinivasan, H., Yamanis, J., Welch, R., Tulyani, S., and Hardin, L., "Solid Oxide Fuel Cell APU Feasibility Study for a Long Range Commercial Aircraft Using UTC ITAPS Approach," NASA, CR-2006-214458/VOL1, 2006.

[115] Munson, B. R., Young, D. F., and Okiishi, T. H., *Fundamentals of Fluid Mechanics*, 5th ed., John Wiley & Sons, Hoboken, NJ, 2006, pp. 430-449.

[116] Ciepluch, C. C., Davis, D. Y., and Gray, D. E., "Results of NASA's Energy Efficient Engine Program," *Journal of Propulsion*, Vol. 3, No. 6, 1987, pp. 560-568.